An Engineering Approach for Elastic-Plastic Fracture Analysis

NP-1931
Research Project 1237-1

Topical Report, July 1981

Prepared by

GENERAL ELECTRIC COMPANY
Corporate Research and Development
1 River Road
Schenectady, New York 12301

Authors
V. Kumar
M. D. German
C. F. Shih

UNIVERSITÄTSBIBLIOTHEK
HANNOVER
TECHNISCHE
INFORMATIONSBIBLIOTHEK

Prepared for

Electric Power Research Institute
3412 Hillview Avenue
Palo Alto, California 94304

EPRI Project Managers
D. M. Norris, Jr.
R. L. Jones
T. U. Marston

System Integrity Program
Nuclear Power Division

SECTION 1
INTRODUCTION

Section 1
INTRODUCTION

1.1 BACKGROUND

The structural integrity of nuclear steam supply systems is presently assured by designs that adhere to the ASME Boiler and Pressure Vessel Code and various regulatory standards. The requirements imposed by these codes and standards are based on linear elastic fracture mechanics (LEFM) concepts. LEFM strictly applies only when the material behavior is dominantly elastic and the fracture response, brittle. In much or all of the working temperature regime of nuclear systems, however, the material is being stressed above the brittle-to-ductile transition temperature where the fracture response is ductile and the material capable of considerable plastic deformation. LEFM provides conservative fracture analyses for these conditions, with the net result that designs are penalized by not taking advantage of the material's full load carrying capabilities. Such design penalties are not unique to the nuclear industry, as the identical conditions prevail in others, notably power generation, chemical plant and aircraft propulsion.

Recent work in elastic-plastic fracture mechanics has demonstrated that more realistic measures of fracture behavior and design margin can be obtained through the use of elastic-plastic analyses. A number of key developments have occurred over the past several years in this field. References [1-1] - [1-10] are cited as representative of expressing these developments.

The developers of elastic-plastic fracture mechanics have been successful in identifying parameters for characterizing the ductile fracture process, developing experimental techniques for assessing fracture resistance and defining methods for fracture analysis. However, the calculations necessary to apply the developed methodology require very sophisticated analysis, usually accomplished with the aid of advanced finite element methods. This is expensive, time-consuming and requires a high degree of expertise to implement. It clearly represents a major obstacle to the potential user of elastic-plastic fracture mechanics concepts.

To overcome the above difficulties, which would greatly reduce the value and general applicability of elastic-plastic fracture mechanics, the present program was undertaken to develop an engineering approach. This approach will permit fracture evaluations of flawed structures to be carried out by personnel who are not specialists in fracture mechanics or inelastic analysis. The evaluations will not require any finite element analysis, rather only desk top calculations and simple graphical procedures. The net result is an inexpensive approach which is simple to employ for engineering design work.

1.2 FRACTURE ANALYSIS CONSIDERATIONS

Fracture analysis in the elastic-plastic regime involves a number of complications not present in the elastic regime. Foremost are the inherent nonlinearities in the material deformation and large geometry changes. A further complication is the fact that there is a significant amount of crack tip blunting prior to initiation and stable crack extension prior to final fracture. This contrasts sharply with the brittle mode of fracture (such as cleavage) in which the crack initiation and rapid crack propagation events are essentially coincident. A final complication in ductile fracture analysis involves the possibility for mixed mode separation: that is, propagation in both flat and slant modes.

The approach for ductile fracture analysis developed in this work will address all of the issues discussed above except for the mixed mode fracture possibility. It is restricted at present to the analysis of flat, ductile tearing type of fracture, such as would occur in thick-walled pressure vessels. The various stages of the ductile fracture process which can be quantified are illustrated schematically in Fig. 1-1 and enumerated below:

1. Blunting of the initially sharp crack
2. Crack initiation
3. Slow (stable) crack growth
4. Unstable crack growth.

The instability point in the ductile fracture process is highly dependent on the loading system. For a load-controlled system in which the load is monotonically increasing, the attainment of the maximum load carrying capability of the cracked structure represents the onset of unstable crack propagation, since any further applied load increment will result in rapid crack propagation. For a displacement-controlled situation, instability need not develop upon the attainment of the maximum load capacity of the flawed structure. Instability may occur at some point beyond maximum load or may not develop at all. The load-controlled and displacement-controlled situations represent the extremes of structure and system compliance. The more general situation involves a compliance between these extremes. The present approach will permit the user to incorporate the system compliance in the instability analysis.

1.3 THE ENGINEERING APPROACH

The engineering approach is based on quantifying the various stages of ductile fracture process described above through the crack tip characterizing parameter, J-integral [1-1]. The analytical foundations and limitations for employment of the J-integral in ductile fracture analysis are described in Section 2 of this report. Also included therein is a detailed description of how J is incorporated in the formation of the engineering approach. In summary the approach employs the following principal elements:

1. A handbook-style compilation of J-integral solutions for fully plastic geometries containing cracks. The compilation also includes solutions for the crack-mouth opening and load-point displacements.
2. An estimation procedure which enables the construction of elastic-plastic solutions (crack driving force estimates) for cracked geometries through the combination of results from the handbook for fully plastic conditions and existing elastic solutions.
3. Simple methods for predicting crack initiation, stable crack growth and instability by combining the crack driving force estimates with a resistance curve determined from standard specimen tests.

The catalogue of fully plastic solutions includes various laboratory specimen geometries and a number of common structural configurations. The specimens include the center-cracked plate, double-edge cracked plate, single-edge cracked plate (tension and bending) and the compact specimen. These solutions are tabulated for both plane stress and plane strain. The structural configurations include cylinders with axial and circumferential cracks, and a two-dimensional model of a nozzle corner flaw. A special incompressible finite element method is employed to develop the fully plastic solutions.

The estimation procedure essentially combines the elastic and the fully plastic solutions to produce the elastic-plastic estimates, as illustrated in Fig. 1-2. Numerous verification studies have been completed in which the estimation procedure solutions are compared with experimental data and full finite element crack solutions. In all cases examined, the estimation procedure produced solutions with sufficient accuracy.

The J-integral crack driving force obtained from the estimation procedure is used together with the experimentally determined material J-resistance curve to predict crack initiation, stable growth and instability in a flawed structure. Several different analysis diagrams are customarily generated. These are referred to as the "crack driving force diagram," the "stability assessment diagram" and the "failure assessment diagram." The crack driving force diagram allows one to analyze in detail all stages of the fracture process, from initiation to instability. The remaining two are specialized: the stability assessment diagram defines regions of loading where stable and unstable behavior exist and the failure assessment diagram allows one to perform a quick analysis to determine whether or not a fracture problem exists. The methodology used in this report is described in Fig. 1-3.

1.4 REPORT STRUCTURE

The body of the report is divided into seven sections. The first to follow, Section 2, covers the theoretical foundations which form the basis of the engineering approach. The J-integral and the concept of J-controlled crack growth are defined. Definition is also given for stability analysis in terms of the J-integral based tearing modulus. The theoretical bases for deriving the fully plastic solutions, the estimation procedure, and the various fracture analysis diagrams are briefly explained. The material in Section 2 is supplemented by Appendix A, which provides considerably more detail on estimation formulae.

Sections 3, 4 and 5 contain the fully plastic solutions obtained to date: Section 3 provides the solutions for specimen geometries, Section 4 for cylindrical geometries and Section 5 for the model of the nozzle corner flaw. Sections 4 and

5 also contain elastic solutions developed in this work because they are not readily available in the literature. The solutions are presented in tabular form in each section and in graphical form in Appendix B. Each of the sections provides technical details for constructing the fully plastic solutions and estimation formulae specific to individual configurations.

The last three sections of the report, 6, 7 and 8, present more detail on constructing the various fracture analysis diagrams as well as a number of examples demonstrating their use. A number of the examples are used to demonstrate verification of the engineering approach. Section 6 covers the crack driving force diagram, Section 7 the stability assessment diagram and Section 8 the failure assessment diagram.

Many users of the handbook may not need to, or wish to, understand all of the theoretical foundations and limitations of the approach. This being the case, the reading of much of Chapter 2 can be omitted. Use of the fully plastic solutions requires reading only Subsections 2.3, 2.4 and 2.5, and the introduction of the sections where the fully plastic solutions are tabulated. For construction of the various fracture analysis diagrams, the user should read through Section 6, 7 or 8, whichever is appropriate.

1.5 REFERENCES

[1-1] J. R. Rice, "Mathematical Analysis in the Mechanics of Fracture," in Fracture (ed. by H. Liebowitz), 1968, Vol. II, Academic Press, New York, pp. 191-311.

[1-2] J. F. Knott, Fundamentals of Fracture, John Wiley and Sons, New York, 1973.

[1-3] Elastic-Plastic Fracture, Edited by J. D. Landes, J. A. Begley and G. A. Clarke, ASTM Special Technical Publication 668, American Society for Testing and Materials, 1979.

[1-4] Fracture Mechanics, Edited by P. C. Paris, ASTM Special Technical Publication 700, American Society for Testing and Materials, 1980.

[1-5] J. W. Hutchinson, Nonlinear Fracture Mechanics, Technical University of Denmark, 1979.

[1-6] Developments in Fracture Mechanics -1, Edited by G. G. Chell, Applied Science Publishers, Ltd., London, 1979.

[1-7] Post-Yield Fracture Mechanics, Edited by D. G. H. Latzko, Applied Science Publishers, Ltd., London, 1979.

[1-8] Advances in Elasto-Plastic Fracture Mechanics, Edited by L. H. Larsson, Applied Science Publishers, Ltd., London, 1980.

[1-9] EPRI Ductile Fracture Research Review Document, Edited by T. Marston, Electric Power Research Institute, Palo Alto, California, 1978.

[1-10] EPRI Ductile Fracture Research Review Document, Edited by D. M. Norris, et al., Electric Power Research Institute, Palo Alto, California, 1980.

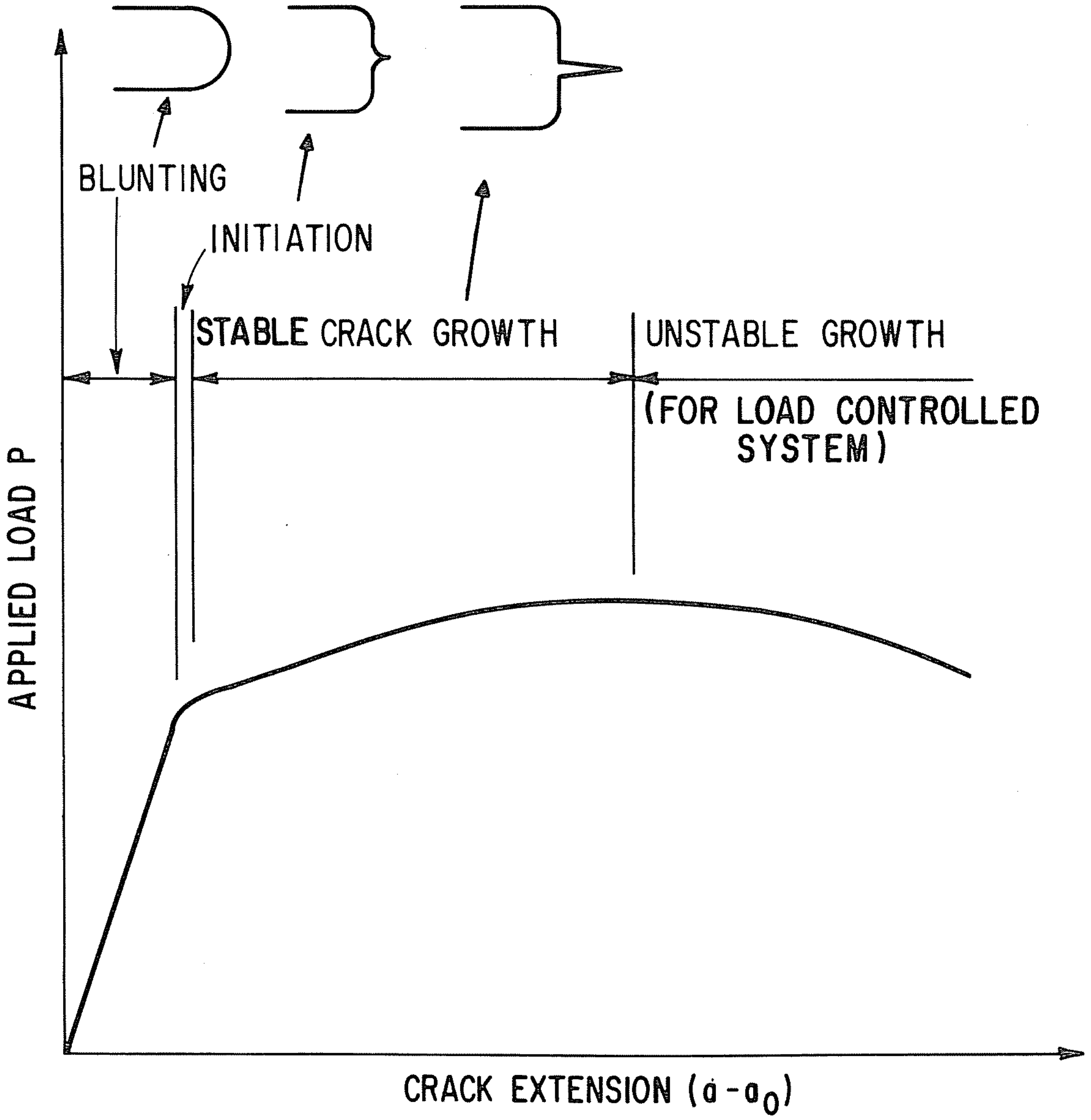

Figure 1-1. Typical crack growth behavior of ductile materials.

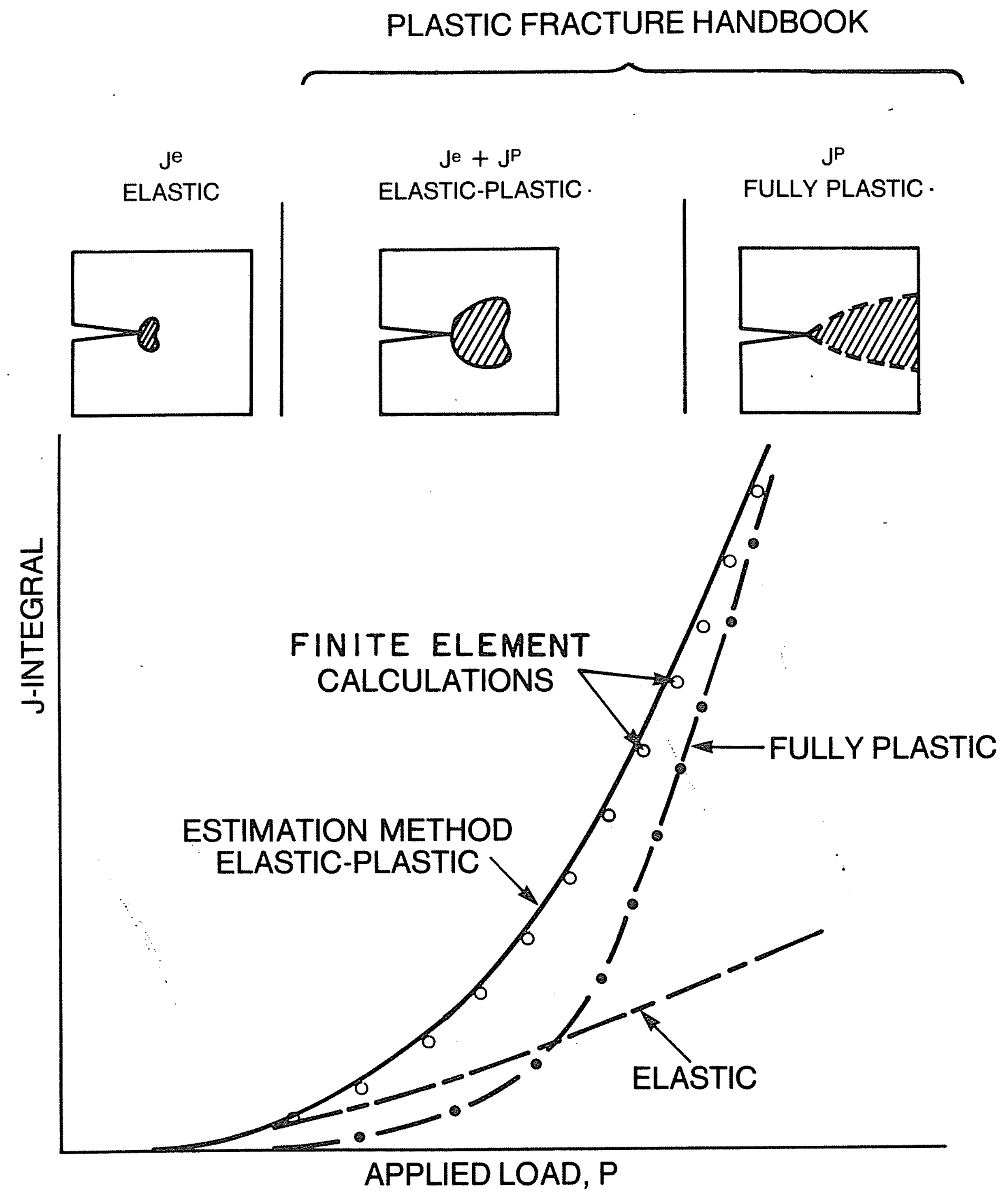

Figure 1-2. Illustration of the elastic-plastic estimation procedure.

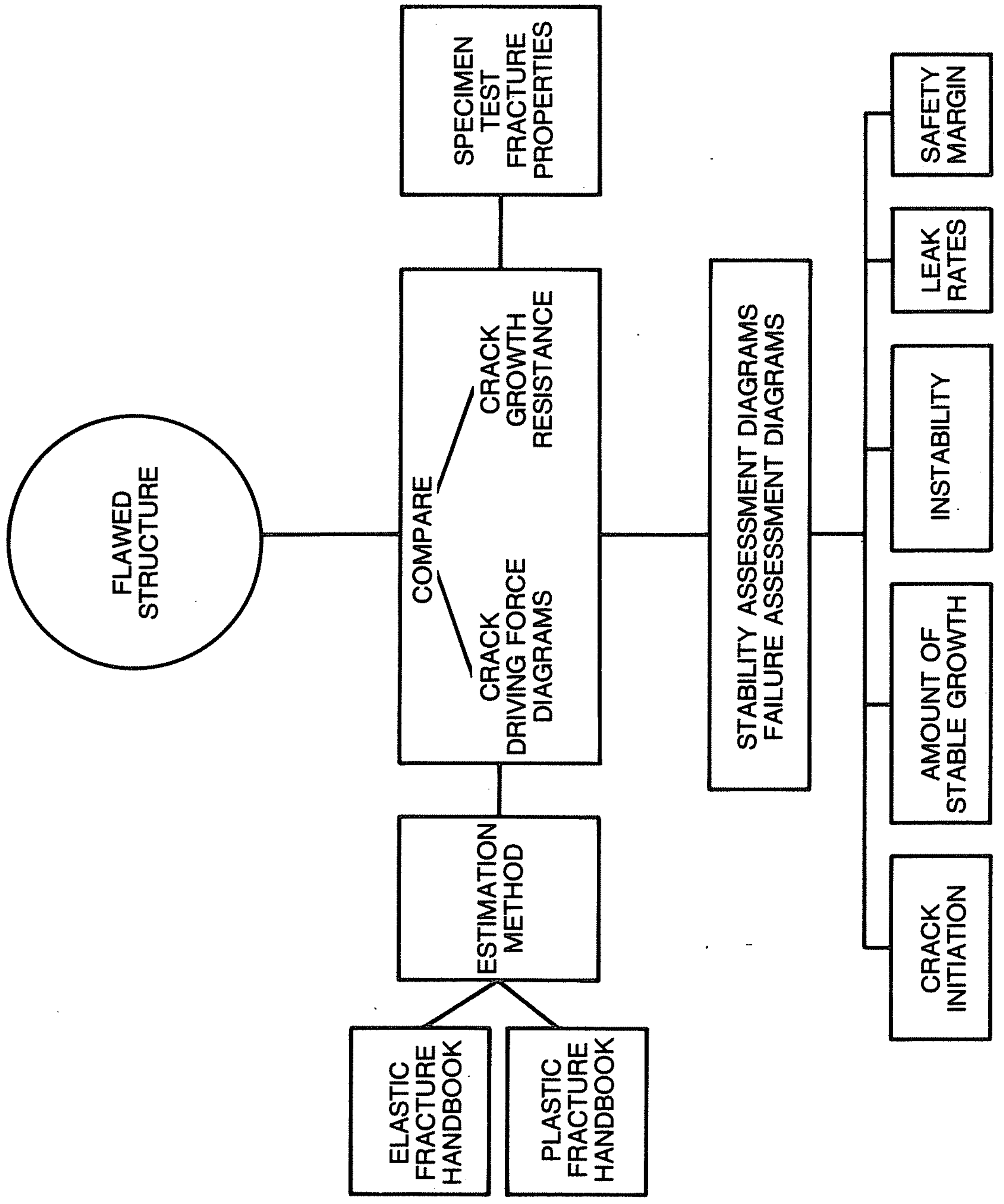

Figure 1-3. A schematic of the engineering approach for examining crack growth and stability in flawed structures.

SECTION 2
THEORETICAL BACKGROUND

Section 2
THEORETICAL BACKGROUND

2.1 INTRODUCTORY REMARKS

Three recent developments in elastic-plastic fracture mechanics have made the development of an engineering approach practical. These include the following:

1. Identification of J or COD as suitable characterizing parameters for ductile fracture, and the development of a resistance curve approach based on these parameters for crack growth predictions.
2. The development of an elastic-plastic estimation procedure for cracked bodies.
3. The development of an incompressible finite element suitable for fully plastic calculations.

The use of the J-integral [2-1, 2-2] for characterizing crack initiation in ductile materials under large-scale yielding conditions was proposed by Begley and Landes [2-3]. The suggestion that a relationship exists between the J-integral and the amount of stable crack growth was made in studies by Rice [2-4], Paris, et al. [2-5], Hutchinson and Paris [2-6] and Shih, deLorenzi and Andrews [2-7]. Considerable investigation of this possibility has since ensued. Our own work under EPRI Project RP601-2 [2-8] demonstrated such a relationship. Analyses and tests indicated that both the onset of crack extension and amount of crack extension are independent of section size and initial crack length when certain restrictions are enforced. These restrictions will be defined in the discussions to follow.

The elastic-plastic estimation procedure derives from the work of Shih and Hutchinson [2-9, 2-10], Bucci, et al. [2-11] and Rice, et al. [2-12]. The idea is to estimate the elastic-plastic solutions by interpolating in a suitable fashion between the fully plastic solutions and the elastic solutions. The elastic solutions are of course already widely tabulated in existing handbooks. The estimation procedure provides the methodology for obtaining fracture parameters pertinent to the elastic-plastic conditions normally encountered in flawed components. The present approach is based on the estimation procedure developed in References [2-9, 2-10].

The concept that fully plastic crack solutions are scalable with respect to applied load originated from the work of Goldman and Hutchinson [2-13]. The development of an incompressible element [2-14 - 2-17] has made it feasible to accurately and economically make calculations for cracked bodies in the fully plastic range. (The technical details of these developments are omitted from this report, but can be found in the references cited.) In the present work, this finite element was used to develop fully plastic plane strain, plane stress and axially symmetric solutions for a number of cracked geometries.

The basic technical approach is amplified in the subsections to follow. Details are presented on the following points:

1. Definition of the J-integral.
2. Restrictions on the application of J in analyzing crack extension.
3. Definition of the tearing modulus for stability analysis.
4. Development of fully plastic solutions.
5. Development of the estimation procedure.
6. Construction of the crack driving force diagram.
7. Construction of the stability assessment diagram.
8. Construction of the failure assessment diagram.

2.2 TECHNICAL BASIS FOR THE ENGINEERING APPROACH

The engineering approach is formulated with the J-integral serving as the crack tip characterizing parameter. Employment of the approach in elastic- plastic fracture analysis assumes the concept of J-controlled crack growth. The theoretical foundations for J and J-controlled growth are reviewed below.

2.2.1 Crack Tip Parameters

The characterization of near tip stress and strain fields by the J-integral is analogous to the use of the stress intensity factor K as the characterizing parameter in linear elastic fracture mechanics. The works of Hutchinson [2-18] and Rice and Rosengren [2-19] revealed that, for stationary cracks, the stresses and strains in the vicinity of the crack tip under yielding conditions varying from small-scale to fully plastic may be represented by

$$\sigma_{ij} = \sigma_o \left[\frac{EJ}{\sigma_o^2 I_n r} \right]^{1/n+1} \tilde{\sigma}_{ij}(\theta, n) \tag{2-1}$$

$$\varepsilon_{ij} = \varepsilon_o \left[\frac{EJ}{\sigma_o^2 I_n r} \right]^{n/n+1} \tilde{\varepsilon}_{ij}(\theta, n)$$

J = J-integral,

E = elastic modulus,

θ, r = crack tip coordinates (see Fig. 2-1),

$\tilde{\sigma}_{ij}$, $\tilde{\varepsilon}_{ij}$ = known dimensionless functions of the circumferential position θ and the hardening exponent n,

I_n = constant which is a function of n, and

ε_o, σ_o, n = yield strain, yield stress and strain hardening exponent, respectively, in the pure power stress-strain law as given in Eq. (2-2) below.

$$\frac{\varepsilon}{\varepsilon_o} = \alpha\left(\frac{\sigma}{\sigma_o}\right)^n \tag{2-2}$$

In the above α is a material constant. In Eq. (2-1), the J-integral is the amplitude of the stress and strain singularity; the latter is often referred to as the "HRR singularity." J is formally defined by the path independent line integral [2-1, 2-2]:

$$J = \int_{\Gamma} (W n_1 - \sigma_{ij}\, n_j\, u_{i,1}) ds \tag{2-3}$$

where Γ is any counterclockwise contour encircling the crack tip (Fig. 2-1), u_i is the displacement vector, n_i is the outward unit normal to Γ and ds is the length of the line element.

The crack tip field equations (Eq. (2-1)) can also be expressed in terms of the crack tip opening displacement. If the crack tip opening displacement, δ_t, is defined as the opening distance where 45° lines intercept the crack faces as illustrated in Fig. 2-2, J and δ_t are linked by the relationship

$$\delta_t = d_n \frac{J}{\sigma_o} \tag{2-4}$$

where d_n is a tabulated function of $\frac{\sigma_o}{E}$ and n [2-20]. Substituting this relationship into Eq. (2-1) will show the singularity in terms of δ_t.

When the HRR field encompasses the fracture process zone, the parameters J and δ_t are natural candidates for characterizing fracture. Thus equal values of J mean equal conditions imposed on the crack-tip region (independent of structure type, loading, crack length and extent of plastic deformation) as long as Eq. (2-1) describes the stress and strain fields around the crack tip.

Under small-scale yielding conditions the plastic zone is small compared to the crack length and other relevant geometric dimensions, so that the elastic singularity or stress intensity factor (K) field surrounds the plastic zone. More specifically, the K field is a good approximation to the actual fields in a region surrounding the crack tip. The elastic fields are given by

$$\sigma_{ij} = \frac{K}{\sqrt{2\pi r}} \tilde{\sigma}_{ij}(\theta)$$

$$(2-5)$$

$$\varepsilon_{ij} = \frac{K}{\sqrt{2\pi r}} \tilde{\varepsilon}_{ij}(\theta)$$

It is noted from Eqs. (2-1) and (2-5) that J characterizes the near-tip stresses and strains in the plastic zone as K does in the elastic zone. When small-scale

yielding prevails, J and K are related by

$$J = \frac{K^2}{E'} \tag{2-6}$$

where E' = E for plane stress and $\frac{E}{(1 - v^2)}$ for plane strain (v is Poisson's ratio).

The small-scale yielding concept is the basis for linear elastic fracture mechanics. The K field characterization is only asymptotically correct, meaning that the basis for LEFM is increasingly violated as the load increases. Under large-scale yielding conditions, there is no elastic K field and Eq. (2-5) does not characterize the crack-tip fields. However, the HRR singularity still prevails at the crack tip.

When the region of dominance of the HRR field is large enough to include the fracture process zone, the J-integral at the initiation of crack growth, denoted by J_{Ic}, can be regarded as a material property. Finite element studies have been carried out [2-21, 2-22] in an attempt to establish requirements for such a condition to exist. Initiation of the crack growth process will occur when the applied J equals the material fracture toughness J_{Ic}, expressed mathematically as

$$J(a, P) = J_{Ic} \tag{2-7}$$

2.2.2 J-Controlled Crack Growth

In crack growth situations, the near-crack tip field is far more complex than in the stationary case. To date there is no complete description of the stress and strain fields ahead of the extending crack. Some key features have evolved from a few of the studies conducted to date [2-23 - 2-27]. Because of the distinctly nonproportional plastic deformation and the strain-path dependence of elastic-plastic stress-strain relations, the deformation at the tip of an extending crack is very different from that associated with a stationary crack. The irreversible plastic strains near the tip do not refocus at the tip of the growing crack; hence it is necessary to impose additional deformation on the material to maintain a concentrated strain field at the extending crack tip. The additional deformation required to maintain the appropriate level of strain concentration at the tip of a growing crack is the source of stable crack growth.

An expression for the incremental strains during crack growth recently forwarded by Hutchinson and Paris [2-6] serves as a useful model for discussing crack growth mechanics and explaining the concept of J-controlled growth. The expression was derived assuming the deformation theory of plasticity. For an ideally plastic material, the expression is given by

$$d\varepsilon_{ij} = \frac{1}{\alpha\,\sigma_o}\,\frac{dJ}{r}\,f_{ij}(\theta) + \frac{1}{\alpha\,\sigma_o}\,J\,\frac{da}{r^2}\,\beta_{ij}(\theta) \qquad (2\text{-}8)$$

where $\beta_{ij}(\theta)$ is a dimensionless quantity of order unity. One can argue that J uniquely characterizes the crack tip field if the first term in Eq. (2-8) dominates over the second. That is, if

$$\frac{dJ}{da} \gg \frac{J}{r} \qquad (2\text{-}9)$$

The first term represents proportional increments in the strain field due to an increment in the applied load or displacement. The second term represents the nonproportional strain increments associated with the advance of the crack tip. If the first term overwhelms the second term, then the stress and strain fields in a zone which encloses the crack tip are described by Eq. (2-8). Thus J is still the appropriate characterizing parameter for limited amounts of crack growth [2-6].

Several significant features result from the concept of J-controlled growth. First, when the conditions for J-controlled growth are satisfied, the J_R curve obtained from fully yielded specimens will be the same as the J_R curve from specimens with limited yielding (or small-scale yielding). The J_R curve will also be independent of crack configuration, so that it is a material property. The common fracture toughness parameter, J_{Ic}, represents a single point on the J_R curve corresponding to the onset of crack extension. J_{Ic} is commonly related to K_{Ic} through Eq. (2-6) [2-3].

A second feature is that stable crack growth and crack growth instability can be analyzed by the R curve approach based on J, which is a generalization of Irwin's resistance curve approach for small-scale yielding based on the elastic stress intensity factor [2-28]. The J-based approach will be applicable for the complete range of elastic-plastic deformation.

As a final point, the J-integral crack driving force can be determined from analysis using the deformation theory of plasticity. The estimation method to be discussed is based on deformation theory.

2.2.3 Conditions for J-Controlled Crack Growth

A thorough discussion of the conditions which ensure the applicability of J-controlled crack growth is given in References [2-6] and [2-27]. The conditions are summarized here:

$$\Delta a \ll R \qquad (2\text{-}10)$$

and

$$D \equiv J_{Ic}/(dJ_R/da) \ll R \qquad (2\text{-}11)$$

The quantities in Eqs. (2-10) and (2-11) are defined in Fig. 2-3.

For fully yielded configurations, where the yielding is confined to the remaining ligament, R is a fraction of the ligament c. For these problems, the condition expressed by Eq. (2-9) can be restated as

$$\omega \equiv \frac{c}{J_{Ic}}\,(dJ_R/da) \gg 1 \qquad (2\text{-}12)$$

Shih, Dean and German [2-27] carried out a systematic investigation of the conditions for J-controlled growth. These studies led to quantification of the conditions given in Eqs. (2-10) through (2-12). For members subjected primarily to bending, the conditions expressed in Eqs. (2-10) and (2-12) become

$$\Delta a < 0.06c \qquad (2\text{-}13)$$

$$\omega > 10 \qquad (2\text{-}14)$$

In addition, the ligament of the member must also satisfy

$$\rho \equiv \frac{c}{(J_R/\sigma_o)} > 25 \qquad (2\text{-}15)$$

Plane strain constraints are met by the following requirement on the relevant structure dimensions B and c, where B is the thickness:

$$B \geq c \tag{2-16}$$

For configurations subjected to tensile loads, it appears that the conditions for J-controlled growth are more stringent. The analyses in Reference [2-27] suggest the following conditions (conservatively stated):

$$\begin{aligned} \omega &> 80 \\ \rho &> 200 \end{aligned} \tag{2-17}$$

2.2.4 Crack Growth and Stability Analysis with the J-Integral

When J-controlled crack growth is applicable, the condition for continued crack growth is [2-5, 2-6]

$$J(a,P) = J_R(a - a_o) \tag{2-18}$$

For any given configuration, the crack driving force J is a function of crack length a and load per unit thickness P. The J_R curve is a function of the amount of crack growth, $a - a_o$, and is obtained experimentally. Therefore, crack growth is unstable if

$$(\partial J/\partial a)_{\Delta_T} \geq dJ_R/da \tag{2-19}$$

The subscript in Eq. (2-19) denotes a partial derivative with the total displacement Δ_T held fixed, where Δ_T is defined by

$$\Delta_T = \Delta + C_M P \tag{2-20}$$

C_M is the compliance of a linear spring placed in series with the cracked body, as shown in Fig. 2-4. Treating the crack driving force J and load point displacement as functions of P and a only, the role of system compliance C_M is

revealed through

$$\left(\frac{\partial J}{\partial a}\right)_{\Delta_T} = \left(\frac{\partial J}{\partial a}\right)_P - \left(\frac{\partial J}{\partial P}\right)_a \left(\frac{\partial \Delta}{\partial a}\right)_P \left[C_M + \left(\frac{\partial \Delta}{\partial P}\right)_a\right]^{-1} \tag{2-21}$$

It is convenient in examining stability to introduce nondimensional tearing moduli after Paris, et al. [2-5]:

$$T_J = \frac{E}{\sigma_o^2}\left(\frac{\partial J}{\partial a}\right)_{\Delta_T} \quad \text{and} \quad T_{JR} = \frac{E}{\sigma_o^2}\frac{dJ_R}{da} \tag{2-22}$$

The instability criterion, Eq. (2-19), is then simply phrased in terms of these tearing moduli as

$$T_J \geq T_{JR} \tag{2-23}$$

The stability assessment diagram is based on Eqs. (2-22) and (2-23).

The stability of crack growth can also be analyzed through the use of the crack opening displacement parameter [2-20, 2-27] by utilizing Eq. (2-4).

2.3 FULLY PLASTIC SOLUTIONS

As indicated earlier, the key to developing the engineering approach rests in the ability to tabulate fully plastic crack solutions for a broad range of representative structural configurations. Such tabulations are of course already available for linear elasticity [2-29, 2-30]. It will be discussed later in this section that it is also feasible to tabulate fully plastic solutions for the crack tip parameters corresponding to specific values of crack length to width ratio and strain hardening exponent.

In linear elasticity, crack parameters like the J-integral, the crack or mouth opening displacement δ and the load line displacement Δ_c (due to crack) can be scaled with respect to load according to

$$J/(\sigma_o\ \varepsilon_o\ a) = \left[P/P_o\right]^2 \hat{J}^e(a/b)$$

$$\delta/(\varepsilon_o\, a) = \left[P/P_o\right] \hat{\delta}^e(a/b) \tag{2-24}$$

$$\Delta_c/(\varepsilon_o\, a) = \left[P/P_o\right] \hat{\Delta}_c^e(a/b)$$

where the superscript e denotes elastic quantities. In Eq. (2-24) P is a generalized load per unit thickness, a/b is the crack length to width ratio, σ_o is the yield stress, reference stress or in some applications the flow stress and ε_o is the corresponding strain (the connection $\sigma_o = E\, \varepsilon_o$ can always be made, but is not necessary). The quantities J, δ and Δ_c are functions of a/b only. P_o is the limit or reference load per unit thickness based on the stress σ_o, defined by

$$P_o = \Lambda\, c\, \sigma_o \tag{2-25}$$

where Λ is the constraint factor which may depend on the ratios of relevant structure dimensions, and c is the length of the uncracked ligament.

Consider now an incompressible nonlinear or fully plastic material where the strain is related to the stress in uniaxial tension by Eq. (2-2). Generalization of Eq. (2-2) to multiaxial stress states using J_2 deformation theory gives

$$\frac{\varepsilon_{ij}}{\varepsilon_o} = \frac{3}{2}\, \alpha \left[\sigma_e/\sigma_o\right]^{n-1} \frac{S_{ij}}{\sigma_o} \tag{2-26}$$

where S_{ij} and $\sigma_e = (\frac{3}{2} S_{ij} S_{ij})^{1/2}$ are the stress deviator and effective stress, respectively. Ilyushin [2-31] noted that solution of the boundary value problems based on Eq. (2-26) and involving only a single load or displacement parameter which is increasing monotonically has two important properties. First, the field quantities increase in direct proportion to the load or displacement parameter raised to some power dependent on n. For example, if the applied load or stress is σ^∞, then the field solution has the simple functional forms

$$\frac{\sigma_{ij}}{\sigma_o} = \left[\sigma^\infty/\sigma_o\right] \hat{\sigma}_{ij}(\underline{x}, n)$$

$$\frac{\varepsilon_{ij}}{\varepsilon_o} = \alpha\left[\sigma^\infty/\sigma_o\right]^n \hat{\varepsilon}_{ij}(\underline{x}, n) \tag{2-27}$$

$$\frac{u_i}{\varepsilon_o\, l} = \alpha\left[\sigma^\infty/\sigma_o\right]^n \hat{u}_i(\underline{x}, n)$$

where u_i is the displacement, l is a length parameter, and σ_{ij}, ε_{ij}, and u_i are dimensionless functions of spatial position $\underline{x}$ and strain hardening exponent n.

The second property follows from the first two equations of Eq. (2-27). Since the stress and strain at every point increase in exact proportion, the fully plastic solution based on the deformation plasticity theory is also the exact solution to the same problem posed for flow theory of plasticity.

The simple functional dependence of the field quantities on the applied load or displacement also means that quantities such as the J-integral, the crack opening displacement δ, and other crack parameters have the following forms [2-13]:

$$\frac{J}{\alpha\, \sigma_o\, \varepsilon_o\, a} = \left[P/P_o\right]^{n+1} \hat{J}^p(a/b, n)$$

$$\frac{\delta}{\alpha\, \varepsilon_o\, a} = \left[P/P_o\right]^{n} \hat{\delta}^p(a/b, n) \tag{2-28}$$

$$\frac{\Delta_c}{\alpha\, \varepsilon_o\, a} = \left[P/P_o\right]^{n} \hat{\Delta}_c^p(a/b, n)$$

where the applied load appears explicitly in the manner shown and the superscript p denotes fully plastic quantities. The dimensionless quantities J^p, δ^p and Δ_c^p are functions <u>only</u> of a/b and n and are independent of the applied load.

The functional forms in Eq. (2-28) are similar to those for linear elasticity, Eq. (2-24), except for the additional dependence on n. Consequently, it is feasible to tabulate the fully plastic solutions J^p, δ^p, and Δ_c^p corresponding to specific values of a/b and n for crack configurations similar to those tabulated in handbooks based on elastic conditions. The fully plastic solutions in plane stress are readily obtained from conventional finite element techniques as discussed in References [2-9] and [2-15]. In plane strain, the incompressible deformation introduces constraints on the displacement gradients, and special techniques are required to handle fully plastic problems. An efficient technique for solving incompressible nonlinear problems is given in References [2-14] -

[2-17]; this technique was used in the present work. Fully plastic solutions for a wide range of crack configurations are presented in later sections in this report.

2.4 ELASTIC-PLASTIC ESTIMATION PROCEDURE

Fully plastic crack solutions and analyses are applicable to situations where the cracked configurations are completely yielded, i.e., the plastic strains are large compared to elastic strains everywhere in the body. Most crack problems of practical interest are in the elastic-plastic regime; in this regime an estimation procedure is employed.

By exploiting the functional forms of the fully plastic solutions, Eq. (2-28), and the linear elastic solutions, Eq. (2-24), simple approximate formulae are obtained for quantities such as J, δ, and Δ_c which allow interpolation over the range from small-scale yielding to fully plastic conditions. For a Ramberg-Osgood material characterized by

$$\frac{\varepsilon}{\varepsilon_o} = \frac{\sigma}{\sigma_o} + \alpha\left(\frac{\sigma}{\sigma_o}\right)^n \tag{2-29}$$

the interpolation formulae combine in essence the linear elastic and the fully plastic conditions and are of the form [2-9, 2-10]

$$\begin{aligned} J &= J^e(a_e) + J^p(a, n) \\ \delta &= \delta^e(a_e) + \delta^p(a, n) \\ \Delta_c &= \Delta_c^e(a_e) + \Delta_c^p(a, n) \end{aligned} \tag{2-30}$$

$J^e(a_e)$, $\delta^e(a_e)$ and $\Delta_c^e(a_e)$ are the elastic contributions based on an adjusted crack length a_e; the latter is Irwin's effective crack length modified to account for strain hardening. a_e is given by [2-32]

$$a_e = a + \phi\, r_y \tag{2-31}$$

where

$$r_y = \frac{1}{\beta\pi}\left[\frac{n-1}{n+1}\right]\left(\frac{K_I}{\sigma_o}\right)^2 \tag{2-32}$$

and

$$\phi = \frac{1}{1 + (P/P_o)^2} \tag{2-33}$$

For plane stress β = 2 and for plane strain β = 6.
$J^p(a, n)$, $\delta^p(a, n)$ and $\Delta_c^p(a, n)$ in Eq. (2-29) are the plastic contributions based on the material hardening exponent n. Using the quantities defined in Eqs. (2-24) and (2-28), a detailed expression for the estimation method, Eq. (2-29), can be readily obtained. Such formulae for various crack configurations will be given in the following sections.

In small-scale yielding, the plastic contribution is small compared to the elastic contribution and hence Eq. (2-30) reduces to the well-known elastic solutions adjusted by Irwin's effective crack length. At the other extreme in the fully plastic range, the plastic contribution is the dominant term. Analyses employing Eq. (2-30) have been found to be in good agreement with finite element calculations and experimental results for the complete range of elastic-plastic deformation and material hardening properties for a number of crack configurations. Example comparisons are presented in subsequent sections of this report.

The user of the Handbook may desire to express the material flow properties in a form other than that given by Eq. (2-29). Estimation formulae can be derived for other representations of the stress-strain law. A number of these are developed in Appendix A.

2.5 FRACTURE ANALYSIS USING THE ENGINEERING APPROACH

In employing the engineering approach for fracture analysis of a flawed body, the crack driving force in terms of "applied" J (or COD) is computed by combining the elastic and fully plastic solutions via the estimation method as discussed above. Following the crack growth and stability conditions as posed by Eqs. (2-18) and (2-19), this is then compared with the material resistance to crack growth (the J_R curve) determined experimentally to obtain predictions for crack initiation, stable growth, instability and other quantities relevant to the overall fracture behavior. Depending upon the application, several different analysis diagrams can be generated. These are customarily referred to as the crack driving force diagram, the stability assessment diagram and the failure assessment diagram.

The crack driving force diagram allows one to perform a comprehensive analysis of the crack growth process, from initiation to instability. This diagram is actually the graphical solution to crack growth stability as posed by Eqs. (2-18) and (2-19). The strain hardening properties of the material and the system compliance are accounted for in the driving force term. A detailed discussion of this diagram with several illustrative examples will be presented in Section 6.

The stability assessment diagram is typically employed if one desires to analyze whether a flawed structure is stable or unstable. This diagram is basically a compression of the information contained in the crack driving force diagram via Eqs. (2-22) and (2-23). The customary plot is made on coordinates of J-integral versus the tearing modulus T_J. Further details on this diagram and examples of its use will be given in Section 7.

The failure assessment diagram is convenient in a preliminary investigation of the safety margin of a flawed structure. The concept of a failure assessment diagram has mainly evolved from work at the Central Electricity Generating Board (CEGB) of the United Kingdom; and is based on the "two criteria" approach of Dowling and Townley [2-33]. The present form, also referred to as the R-6 diagram, is due to Harrison, Loosemore and Milne [2-34]. Recently, Shih, Kumar and German [2-35 - 2-36] employed the estimation procedure and the J-controlled crack growth approach to derive a failure assessment curve which accounts for, in a rational manner, the geometry of a cracked body, the type of loading and material flow properties. Similar developments have also been carried out by Bloom [2-37]. Further discussion of this subject with several examples is given in Section 8.

2.6 REFERENCES

[2-1] J. R. Rice, "A Path Independent Integral and the Approximate Analysis of Strain Concentration by Notches and Cracks," Journal of Applied Mechanics, Vol. 35, 1968, pp. 379-386.

[2-2] J. R. Rice, "Mathematical Analysis in the Mechanics of Fracture," in Fracture (ed. by H. Liebowitz), 1968, Vol. II, Academic Press, NY, pp. 191-311.

[2-3] J. A. Begley and J. D. Landes, "The J-Integral as a Fracture Criterion in Fracture Toughness Testing," in Fracture Toughness, ASTM Special Technical Publication 514, 1972, pp. 1-23, 24-39.

[2-4] J. R. Rice, "Elastic-Plastic Models for Stable Crack Growth," in Mechanics and Mechanism of Crack Growth, (Proc. at Cambridge, England, April 1973) Ed. M. J. May, British Steel Corporation Physical Metallurgy Centre Publication, 1975, pp. 14-39.

[2-5] P. C. Paris, H. Tada, A. Zahoor, and H. Ernst, "The Theory of Instability of the Tearing Mode of Elastic-Plastic Crack Growth," in Elastic-Plastic Fracture, ASTM Special Technical Publication 668, 1979, pp. 5-36, pp. 251-265.

[2-6] J. W. Hutchinson and P. C. Paris, "Stability Analysis of J-Controlled Crack Growth," in Elastic-Plastic Fracture, ASTM Special Technical Publication 668, 2979, pp. 37-64.

[2-7] C. F. Shih, H. G. deLorenzi, and W. R. Andrews, "Studies on Crack Initiation and Stable Crack Growth," in Elastic-Plastic Fracture, ASTM Special Technical Publication 668, 1979, pp. 65-120.

[2-8] C. F. Shih, W. R. Andrews, H. G. deLorenzi, M. D. German, R. H. Van Stone, and D. F. Mowbray, "Methodology for Plastic Fracture," Final Report to EPRI, Contract No. RP601-2, General Electric Company, Schenectady, New York, August 1980.

[2-9] C. F. Shih, "J-Integral Estimates for Strain Hardening Materials in Antiplane Shear Using Fully Plastic Solutions," in Mechanics of Crack Growth, ASTM Special Technical Publication 590, 1976, pp. 3-22.

[2-10] C. F. Shih and J. W. Hutchinson, "Fully Plastic Solutions and Large-Scale Yielding Estimates for Plane Stress Crack Problems," Transactions of ASME, Journal of Engineering Materials and Technology, Series H, Vol.

98, No. 4, October 1976, pp. 289-295.

[2-11] R. J. Bucci, P. C. Paris, J. D. Landes, and J. R. Rice, "J-Integral Estimation Procedures," in Fracture Toughness, ASTM Special Technical Publication 514, 1972, pp. 40-69.

[2-12] J. R. Rice, P. C. Paris, and J. G. Merkle, "Some Further Results on J-Integral Analysis and Estimates," in Progress in Flaw Growth and Fracture Toughness Testing, ASTM Special Technical Publication 536, 1973, pp. 231-245.

[2-13] N. L. Goldman and J. W. Hutchinson, "Fully Plastic Crack Problems: The Center-Cracked Strip Under Plane Strain," International Journal of Solids and Structures, Vol. 11, 1975, pp. 575-591.

[2-14] A. Needleman and C. F. Shih, "Finite Element Method for Plane Strain Deformations of Incompressible Solids," Computer Methods in Applied Mechanics and Engineering, 1978, pp. 223-240.

[2-15] C. F. Shih and V. Kumar, "Estimation Technique for the Prediction of Elastic-Plastic Fracture of Structural Components of Nuclear Systems," 1st Semiannual Report to EPRI, Contract No. RP1237-1, General Electric Company, Schenectady, New York, July 1, 1978 - January 31, 1979.

[2-16] V. Kumar, M. D. German, and C. F. Shih, "Estimation Techniques for the Prediction of Elastic-Plastic Fracture of Structural Components of Nuclear Systems," Combined 2nd and 3rd Semiannual Report to EPRI, Contract No. RP1237-1, General Electric Company, Schenectady, New York, February 1, 1979 - January 31, 1980.

[2-17] V. Kumar, H. G. deLorenzi, W. R. Andrews, C. F. Shih, M. D. German, and D. F. Mowbray, "Estimation Technique for the Prediction of Elastic-Plastic Fracture of Structural Components of Nuclear Systems, 4th Semiannual Report to EPRI, Contract No. RP1237-1, General Electric Company, Schenectady, New York, July 1, 1980 - January 31, 1981.

[2-18] J. W. Hutchinson, "Singular Behavior at End of Tensile Crack in Hardening Material," Journal of the Mechanics and Physics of Solids, Vol. 16, No. 1, January 1968, pp. 13-31; also "Plastic Stress and Strain Fields at Crack Tip," Journal of the Mechanics and Physics of Solids, Vol. 16, No. 4, September 1968, pp. 337-347.

[2-19] J. R. Rice and G. F. Rosengren, "Plane Strain Deformation Near Crack Tip in Power-Law Hardening Material," Journal of the Mechanics and Physics of Solids, Vol. 16, No. 1, January 1968, pp. 1-12.

[2-20] C. F. Shih, "Relationships Between the J-Integral and the Crack Opening Displacement for Stationary and Extending Cracks," General Electric Company TIS Report No. 79CRD075, April 1979; to appear in Journal of the Mechanics and Physics of Solids.

[2-21] R. M. McMeeking and D. M. Parks, "On Criteria for J-Dominance of Crack Tip Fields in Large-Scale Yielding," in Elastic-Plastic Fracture, ASTM Special Technical Publication 668, 1979, pp. 175-194.

[2-22] C. F. Shih and M. D. German, "Requirements for a One Parameter Characterization of Crack Tip Fields by the HRR Singularity," General Electric Company TIS Report No. 79CRD076, 1979; International Journal of Fracture, in press.

[2-23] A. D. Chitaley and F. A. McClintock, "Elastic-Plastic Mechanics of Steady Crack Growth Under Anti-Plane Shear," Journal of the Mechanics and Physics of Solids, Vol. 19, 1971, pp. 147-163.

[2-24] J. C. Amazigo and J. W. Hutchinson, "Crack-Tip Fields in Steady Crack-Growth with Linear Strain-Hardening," Journal of the Mechanics and Physics of Solids, Vol. 25, 1977, pp. 81-97.

[2-25] J. R. Rice, W. J. Drugan, and T. L. Sham, "Elastic-Plastic Analysis of Growing Cracks," in Fracture Mechanics, ASTM Special Technical Publication 700, 1980, pp. 189-221.

[2-26] R. H. Dean and J. W. Hutchinson, "Quasi-Static Steady Crack Growth in Small-Scale Yielding," in *Fracture Mechanics,* ASTM Special Technical Publication 700, 1980, pp. 383-405.

[2-27] C. F. Shih, R. H. Dean, and M. D. German, "On J-Controlled Crack Growth: Evidence, Requirements and Applications," General Electric Company TIS Report (to be submitted).

[2-28] *Fracture Toughness Evaluation by R-Curve Methods,* ASTM Special Technical Publication 527, 1973, p. 118.

[2-29] H. Tada, P. C. Paris, and G. R. Irwin, "The Stress Analysis of Cracks Handbook," Del Research Corporation, Hellertown, Pennsylvania, 1973.

[2-30] D. P. Rooke and J. C. Cartwright, *Compendium of Stress Intensity Factors,* Her Majesty's Stationary Office, London, 1976.

[2-31] A. A. Ilyushin, "The Theory of Small Elastic-Plastic Deformations," *Prikadnaia Matematika i Mekhanika,* P. M. M., Vol. 10, 1946, p. 347.

[2-32] V. Kumar and C. F. Shih, "Fully Plastic Crack Solutions, Estimation Scheme and Stability Analyses for Compact Specimen," in *Fracture Mechanics,* ASTM Special Technical Publication 700, 1980, pp. 406-438.

[2-33] A. R. Dowling and C. H. A. Townley, "The Effects of Defects on Structural Failures: A Two-Criteria Approach," *International Journal of Pressure Vessel and Piping,* Vol. 3, 1975, pp. 77-137.

[2-34] R. P. Harrison, L. Loosemore, and I. Milne, "Assessment of the Integrity of Structures Containing Defects," CEGB Report No. R/H/R6, Central Electricity Generating Board, United Kingdom, 1976.

[2-35] C. F. Shih, M. D. German, and V. Kumar, "An Engineering Approach for Examining Crack Growth and Stability in Flawed Structures," presented at the OECD-CSNI Specialist Meeting at Washington University, St. Louis, Missouri, September 1979, NUREG CP-0010; *International Journal of Pressure Vessels and Piping,* in press.

[2-36] C. F. Shih, V. Kumar, and M. D. German, "Studies on the Failure Assessment Diagram Using the Estimation Scheme and J-Controlled Crack Growth Approach," General Electric Company TIS Report, 1981, to appear.

[2-37] J. M. Bloom, "Prediction of Ductile Tearing Using a Proposed Strain Hardening Failure Assessment Diagram," *International Journal of Fracture,* Vol. 6, 1980, pp. R73-R77.

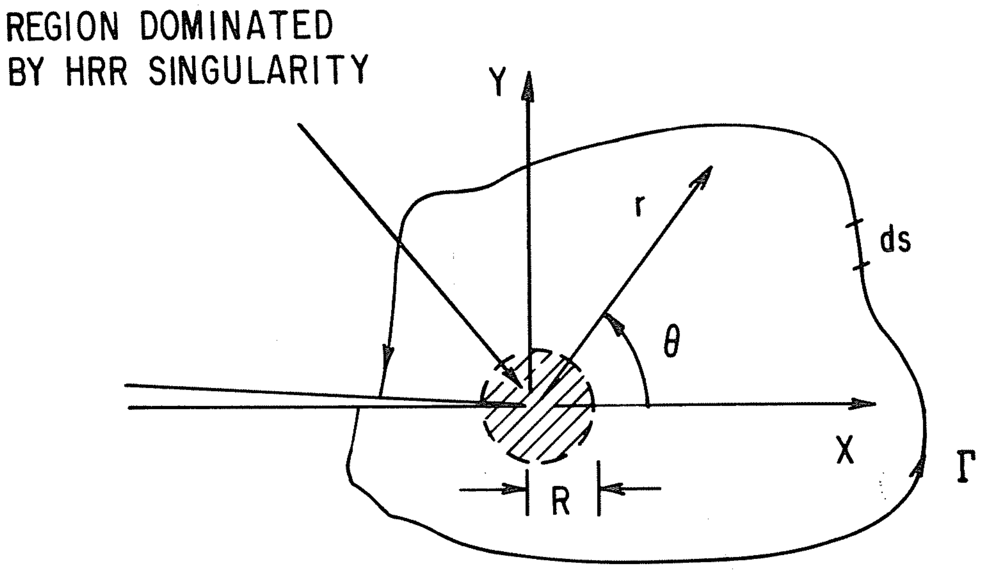

Figure 2-1. Definition of crack tip coordinates.

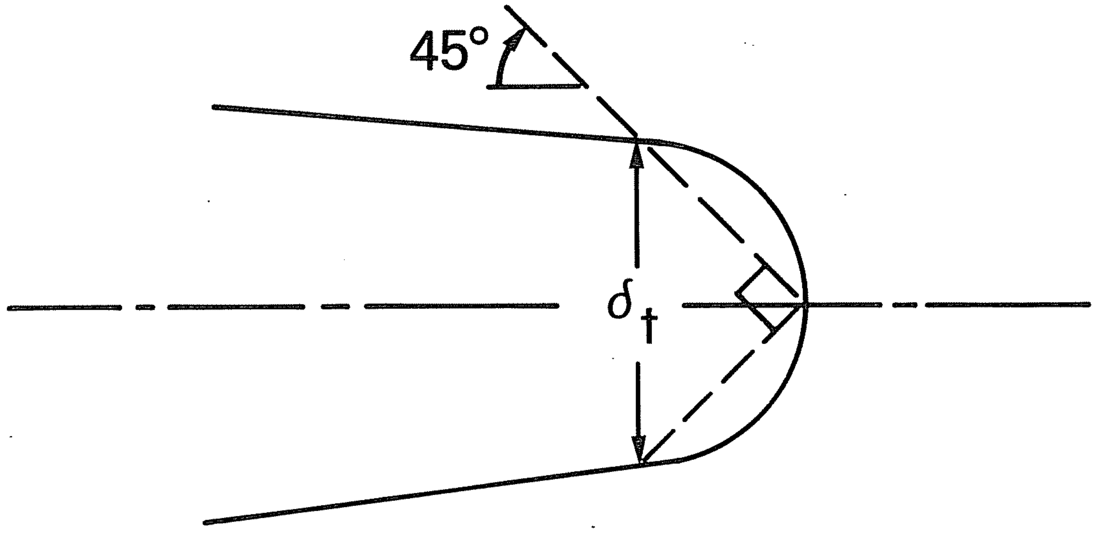

Figure 2-2. Definition of the crack tip opening displacement (CTOD) denoted by δ_t.

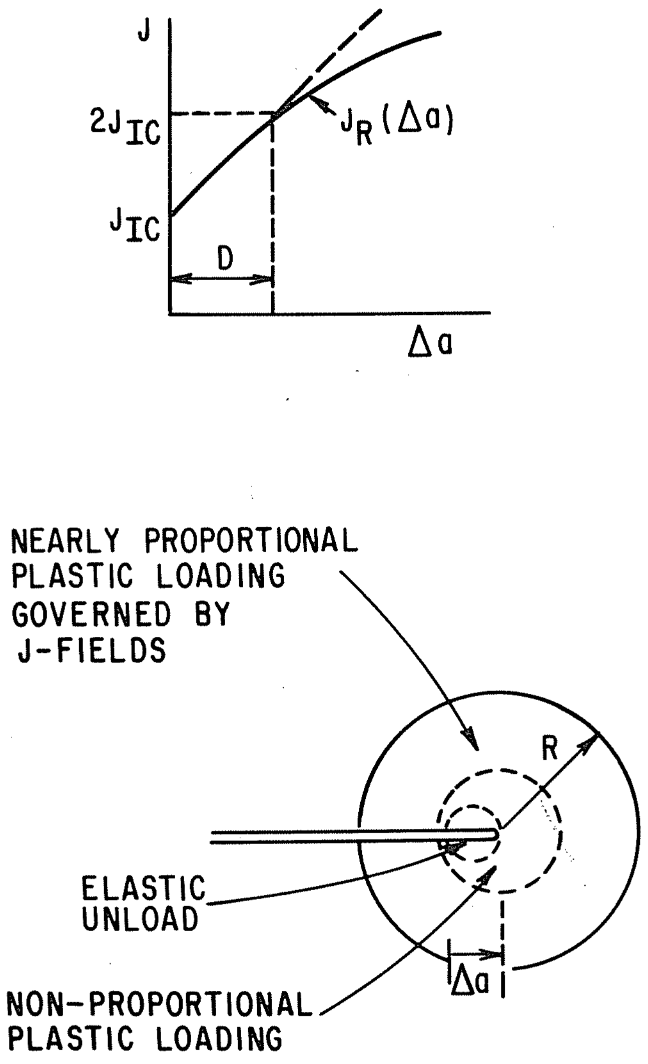

Figure 2-3. Definition of terms in conditions for J-controlled crack growth.

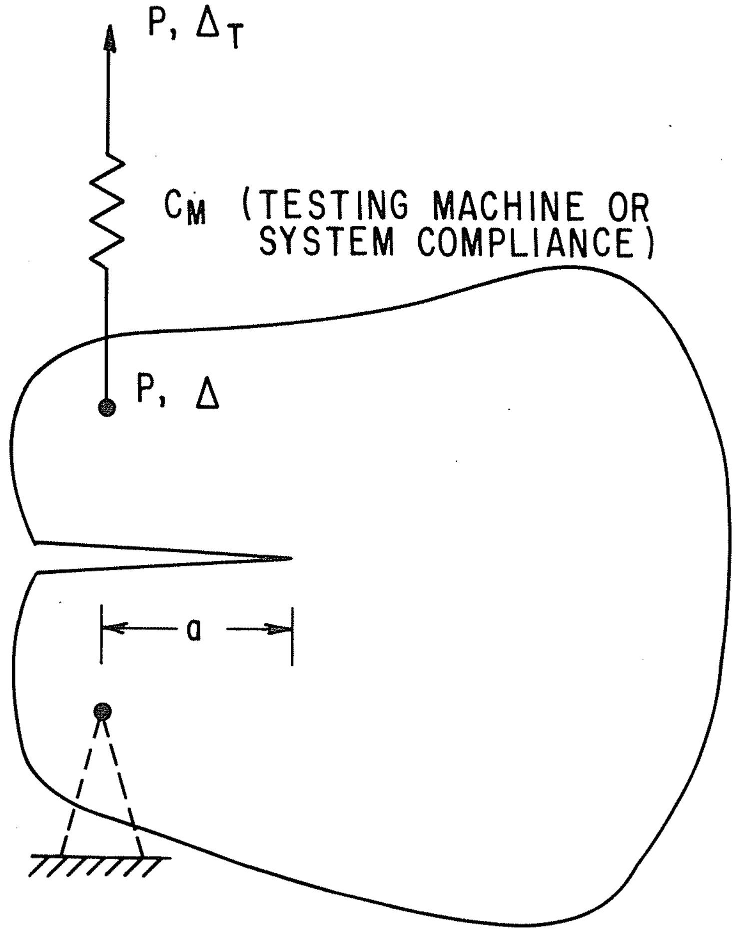

Figure 2-4. Schematic of a cracked boy. The spring represents compliance of the system.

SECTION 3
FULLY PLASTIC SOLUTIONS FOR TEST SPECIMEN
CONFIGURATIONS

Section 3
FULLY PLASTIC SOLUTIONS FOR TEST SPECIMEN CONFIGURATIONS

3.1 INTRODUCTION

The fully plastic crack solutions for common fracture toughness test specimen configurations are presented in this section. The solutions cover a wide range of values of crack length-to-specimen width ratio, a/b, and strain hardening exponent, n. Both plane stress and plane strain conditions are considered. The solutions are presented in tabular form here; graphs are provided in Appendix C. For given crack length to width ratios, uniaxial stress-strain properties (E, ν, α, σ_o and n), and applied loadings, fully plastic solutions for the J-integral, crack mouth opening displacement and load-point displacement can be readily computed by simply using the relevant formulae and values of functions from the tables or graphs.

The solutions were obtained numerically by employing the incompressible finite element computer code INFEM. This code was developed specifically for the fully plastic crack analyses conducted in this program [3-1 - 3-4]. The finite element meshes and other pertinent details are discussed in References [3-2] - [3-4]. Results for the elastic cases ($n = 1$) were compared with solutions available in literature, such as the handbooks of elastic stress intensity factors [3-5, 3-6]. These comparisons are briefly summarized here with further details given in References [3-2] - [3-4].

Elastic-plastic solutions for J and the other parameters are obtained by combining elastic and fully plastic contributions as discussed in Section 2. The LEFM handbooks typically contain solutions for the stress-intensity factor K_I; these can be converted to J via the relationship given in Eq. (2-6):

$$J^e = \frac{K_I^2}{E'}$$

where $E' = E$ for plane stress and $E' = E/(1 - \nu^2)$ for plane strain. Using detailed expressions for elastic and fully plastic contributions, one can arrive at explicit forms of estimation formulae. These are provided in this section. Example problems illustrating applications and verification of the estimation procedure and fully plastic solutions will be discussed in Section 6.

Although fully plastic solutions for the crack tip opening displacement parameter δ_t are not catalogued here, these can be calculated from the J solutions using Eq. (2-4). Under fully plastic conditions Eq. (2-4) can be conveniently rewritten as

$$h_4 = d_n h_1 \tag{3-1}$$

d_n in the above equation can be obtained from Figs. 3-1 and 3-2. h_4 and h_1 are the fully plastic solutions corresponding to J and δ_t and will be defined in subsequent parts of this section.

3.2 COMPACT SPECIMEN

3.2.1 Fully Plastic Solutions

Consider the standard ASTM compact specimen (CS) as shown in Fig. 3-3. The fully plastic solutions for this test specimen are given in [3-7],

$$J = \alpha \sigma_o \varepsilon_o c h_1(a/b, n)(P/P_o)^{n+1} \tag{3-2}$$

$$\delta = \alpha \varepsilon_o a h_2(a/b, n)(P/P_o)^n \tag{3-3}$$

$$\Delta_L = \alpha \varepsilon_o a h_3(a/b, n)(P/P_o)^n \tag{3-4}$$

$$\delta_t = \alpha \varepsilon_o c h_4(a/b, n)(P/P_o)^{n+1} \tag{3-5}$$

where P is the applied load per unit thickness, a is the crack length, b the specimen width and c = b - a is the uncracked ligament. It is noted that h_1, h_2 and h_3 in the above expressions are functions of a/b and n alone. P_o is the limit load per unit thickness and is given by

$$P_o = 1.455 \eta c \sigma_o \tag{3-6}$$

for plane strain and by

$$P_0 = 1.071 \eta c \sigma_o \tag{3-7}$$

for plane stress. In the above, η is defined as

$$\eta = \left[(2a/c)^2 + 2(2a/c) + 2\right]^{1/2} - \left[2a/c + 1\right] \tag{3-8}$$

In Eq. (3-3), δ is the mouth opening displacement of the crack at the outer edge, i.e., $\delta = U_y(0, 0^+) - U_y(0, 0^-)$. In Eq. (3-4) the COD at the load line is given by $\Delta_L = U_y(d, 0^+) - U_y(d, 0^-)$. The crack tip opening displacement CTOD denoted by δ_t in Eq. (3-5) was defined earlier in Section 2.

The functions h_1, h_2 and h_3 in Eqs. (3-2) - (3-4) are presented for a wide range of a/b and n values in Table 3-1 for plane strain and Table 3-2 for plane stress.

The function h_4 is obtained from h_1 by using Eq. (3-1). For the purposes of interpolation and extrapolation, plots of h_1, h_2 and h_3 versus n with a/b as the parameter are given in Appendix C.

The fully plastic solutions tabulated above were obtained by using the incompressible finite element program INFEM. The present results for K, δ and Δ_L for the elastic case corresponding to n = 1 were found to be within 2% of the results by Newman [3-8], except for extreme a/b ratios where the difference was of the order of 4%. The numerical accuracy of the above solutions for $n \geq 3$ was assessed by comparing the present results with the J-integral expressions for deep cracks by Merkle and Corten [3-9] and Rice, Paris and Merkle [3-10]. It was concluded that for $a/b \geq 3/8$ and $n \geq 3$ the present solutions for J are within 3% of the Merkle and Corten analysis. For further details, the reader is referred to the Reference [3-7].

3.2.2 Elastic-Plastic Estimation Formulae

As discussed in Section 2, for material fitting the Ramberg-Osgood stress-strain law, Eq. (2-2), the fracture parameters J, δ and Δ_L are given by the sum of the adjusted linear elastic and the fully plastic contributions.

The elastic solutions are available from several elastic crack handbooks and are generally tabulated in the following format:

$$J = \frac{a\,F_1^2(a/b)}{E'\,b}\,P^2,\quad \delta = \frac{1}{E'}\,V_1(a/b)P,\quad \Delta_L = \frac{1}{E'}\,V_2(a/b)P$$

where E' = E for plane stress and $E' = E/(1 - \nu^2)$ for plane strain. The functions F_1, V_1 and V_2 are tabulated for example in Reference [3-5]. For purposes here these expressions are more conveniently written as

$$J = f_1(a)\,\frac{P^2}{E'} \tag{3-9}$$

$$\delta = f_2(a)\,\frac{P}{E'} \tag{3-10}$$

$$\Delta_L = f_3(a)\,\frac{P}{E'} \tag{3-11}$$

where $f_1 = \frac{a\,F_1^2}{b^2}$, $f_2 = V_1$ and $f_3 = V_2$.

Using the quantities defined in Eqs. (3-2) - (3-5) and (3-9) - (3-11), the estimation formulas for the entire range of elastic-plastic deformation have the specific forms:

$$J = f_1(a_e)\,\frac{P^2}{E'} + \alpha\,\sigma_o\,\varepsilon_o\,c\,h_1(a/b,\,n)(P/P_o)^{n+1} \tag{3-12}$$

$$\delta = f_2(a_e)\,\frac{P}{E'} + \alpha\,\varepsilon_o\,a\,h_2(a/b,\,n)(P/P_o)^{n} \tag{3-13}$$

$$\Delta_L = f_3(a_e)\,\frac{P}{E'} + \alpha\,\varepsilon_o\,a\,h_3(a/b,\,n)(P/P_o)^{n}. \tag{3-14}$$

Here a_e is effective crack length as defined by Eqs. (2-31) - (2-33). The above equations have been used successfully in a variety of test situations involving elastic-plastic stable crack growth, and these are discussed later in Section 6 and in Reference [3-7].

3.3 CENTER-CRACKED PLATE IN TENSION

3.3.1 Fully Plastic Solutions

Consider a center-cracked plate (CCP) of width 2b with a crack of length 2a as shown in Fig. 3-4. A uniform stress distribution

$$\sigma_{yy}(x, \pm L) = P/2b \tag{3-15}$$

is imposed at the ends where P is the load per unit thickness carried by the strip. c = b − a denotes the uncracked ligament on either end of the crack. The fully plastic solutions for this crack configuration are given by

$$J = \alpha\, \sigma_o\, \varepsilon_o\, a(c/b)\, h_1(a/b,\, n)(P/P_o)^{n+1} \tag{3-16}$$

$$\delta = \alpha\, \varepsilon_o\, a\, h_2(a/b,\, n)(P/P_o)^{n} \tag{3-17}$$

$$\Delta_c = \alpha\, \varepsilon_o\, a\, h_3(a/b,\, n)(P/P_o)^{n} \tag{3-18}$$

$$\delta_t = \alpha\, \varepsilon_o\, a(c/b)\, h_4(a/b,\, n)(P/P_o)^{n+1} \tag{3-19}$$

where $\delta = U_y(0, 0^+) - U_y(0, 0^-)$ is the mouth opening displacement at the center of the crack. In the above, Δ_c is the load-point displacement due to the crack and is defined as

$$\Delta_c = \Delta(L) - \Delta(L)_{\text{no crack}} \tag{3-20}$$

Here Δ is the remote load-point displacement defined by

$$\Delta(L) = \frac{1}{2b} \int_{-b}^{b} \left[U_y(x,\, L) - U_y(x,\, -L)\right] dx \tag{3-21}$$

$\Delta(L)_{\text{no crack}}$ is the load-point displacement in the absence of a crack and is given by

$$\Delta(L)_{\text{no crack}} = \sqrt{3}\, \alpha\, \varepsilon_o\, L \left[\sqrt{3}\, \frac{P}{4\, b\, \sigma_o}\right]^n \tag{3-22}$$

for plane strain and by

$$\Delta(L)_{\text{no crack}} = 2\, \alpha\, \varepsilon_o\, L\left[P/2\, b\, \sigma_o\right]^n \tag{3-23}$$

for plane stress. In Eqs. (3-16) − (3-19), P_o is the limit load per unit thickness and is given by the following:

$$P_o = 4c\, \sigma_o/\sqrt{3} \text{ for plane strain} \tag{3-24}$$

and

$$P_o = 2c\, \sigma_o \text{ for plane stress.} \tag{3-25}$$

The expressions for h in Eqs. (3-16) − (3-19) are functions of a/b and n only, and are catalogued for several values of a/b and n in Table 3-3 for plane strain and Table 3-4 for plane stress. As before, the function h_4 is obtained from h_1 by using the Eq. (3-1). For ease in obtaining the h's for desired a/b and n values by interpolation or extrapolation, plots of h versus n with a/b as a parameter are presented in Appendix C.

The CCP solutions were also obtained using INFEM. For the elastic case (n = 1), the results were found to agree with solutions given in Reference [3-5] by a factor less than 3%. The numerical accuracy of these solutions for large values of n can be assessed by a comparison with the J-integral expression by Rice, Paris and Merkle [3-10] for deeply-cracked situations. These comparisons are discussed in detail in References [3-2], [3-3], [3-11] and [3-12].

3.3.2 Elastic-Plastic Estimation Formulae

In the linear elastic range, the simple functional dependence of J, δ and Δ_c on the applied load per unit thickness P for the CCP is expressed explicitly by

$$J = \frac{\pi\, a}{E'\, 4b^2}\, F^2(a/b)P^2 \tag{3-26}$$

$$\delta = \frac{2a}{E'\, b}\, V_1(a/b)P \tag{3-27}$$

$$\Delta_c = \frac{2a}{E'\, b}\, V_2(a/b)P \tag{3-28}$$

where the dimensionless functions, F, V_1 and V_2, are tabulated in elastic handbooks such as [3-5]. For the convenience of introducing Eqs. (3-26) - (3-28) into the estimation procedure, the above equations are expressed alternately by

$$J = f_1(a)\,\frac{P^2}{E'} \qquad (3\text{-}29)$$

$$\delta = f_2(a)\,\frac{P}{E'} \qquad (3\text{-}30)$$

$$\Delta_c = f_3(a)\,\frac{P}{E'} \qquad (3\text{-}31)$$

where $f_1 = \frac{\pi a}{4b^2} F^2$, $f_2 = \frac{2a}{b} V_2$ and $f_3 = \frac{2a}{b} V_2$.

In the fully plastic state, Eqs. (3-16) - (3-19) apply. In the elastic- plastic deformation range the estimation formulae are expressed as follows:

$$J = f_1(a_e)\,\frac{P^2}{E'} + \alpha\,\sigma_o\,\varepsilon_o\,a(c/b)\,h_1(a/b,\,n)(P/P_o)^{n+1} \qquad (3\text{-}32)$$

$$\delta = f_2(a_e)\,\frac{P}{E'} + \alpha\,\varepsilon_o\,a\,h_2(a/b,\,n)(P/P_o)^{n} \qquad (3\text{-}33)$$

$$\Delta_c = f_3(a_e)\,\frac{P}{E'} + \alpha\,\varepsilon_o\,a\,h_3(a/b,\,n)(P/P_o)^{n} \qquad (3\text{-}34)$$

where a_e is again the adjusted crack length as defined by Eqs. (2-31) - (2-33). Illustrative examples demonstrating the application and verification of these equations are discussed in References [3-2], [3-11] and [3-13].

3.4 SINGLE-EDGE CRACKED PLATE IN THREE-POINT BENDING

3.4.1 Fully Plastic Solutions

Next, consider a single-edge cracked plate (SECP) of length 2L, width b and with a crack of length a. The plate is subjected to three-point bending as shown in Fig. 3-5. The various crack parameters in the fully plastic state are expressed as follows:

$$J = \alpha\,\sigma_o\,\varepsilon_o\,c\,h_1(a/b,\,n)(P/P_o)^{n+1} \qquad (3\text{-}35)$$

$$\delta = \alpha\,\varepsilon_o\,a\,h_2(a/b,\,n)(P/P_o)^{n} \qquad (3\text{-}36)$$

$$\Delta_c = \alpha\,\varepsilon_o\,a\,h_3(a/b,\,n)(P/P_o)^{n} \qquad (3\text{-}37)$$

$$\delta_t = \alpha\,\varepsilon_o\,c\,h_4(a/b,\,n)(P/P_o)^{n+1} \qquad (3\text{-}38)$$

Here P is the load per unit thickness and c = b - a is the remaining ligament. P_o is the limit load per unit thickness for perfectly plastic material corresponding to $n = \infty$. For plane strain the Green and Hundy solution [3-14] gives P_o as

$$P_o = 0.728\,\sigma_o\,c^2/L \qquad (3\text{-}39)$$

P_o for plane stress conditions is obtained from the Lord and Lianis slip-line field solution [3-15] and is expressed as

$$P_o = 0.536\,\sigma_o\,c^2/L \qquad (3\text{-}40)$$

In Eq. (3-36), $\delta = U_y(0,\,0^+) - U_y(0,\,0^-)$ is the mouth opening displacement at the edge of the specimen. Δ_c in Eq. (3-37) is the load-point displacement due to crack and is defined as

$$\Delta_c = \Delta - \Delta_{nc} \qquad (3\text{-}41)$$

where Δ_{nc} is the load-point displacement of an uncracked bar. For the linear elastic case (n = 1) Δ^e_{nc} is given by [3-16]

$$\Delta^{e}_{nc} = \frac{PL^{3}}{6E'I} + \frac{PL}{b}\left[\frac{3}{4G} - \frac{3}{10E'} - 3\frac{v}{4E'}\right] - \frac{0.21P}{E'} \tag{3-42}$$

where $G = E/2(1 + v)$ is the shear modulus and $I = b^{3}/12$. It is noted that the shear deformation effects are included in this equation as these may be quite significant for small L/b values, particularly for the L/b = 2 case considered in this work.

The functions h_1, h_3 and h_3 in Eqs. (3-35) - (3-38) are presented here for L/b = 2 covering a wide range of a/b and n values. The plane strain solutions are catalogued in Table 3-5 and the plane stress solutions in Table 3-6. Again, h_4 is obtained from h_1 by using Eq. (3-1). Plots of these functions are illustrated in Appendix C.

The SECP solutions were obtained by using the finite element code INFEM. In the elastic case (n = 1) these solutions are within 5% of the results given in Reference [3-5], except for a/b = 3/4, where the difference was about 8%. (This suggests that deep cracks under three-point bending require finer meshes than used here.) For larger values of n, the numerical accuracy of the solutions reported herein was assessed by a comparison with the J-integral expression for deep cracks given in Reference [3-10]. For further details, one is referred to References [3-2] and [3-3].

3.4.2 Elastic-Plastic Estimation Formulae

The estimation formulae for SECP crack parameters in the elastic-plastic range are presented below. The parameters J, δ and Δ_c in the linear elastic range are commonly given by

$$J = \frac{9\ \pi\ a\ L^{4}}{E'\ b^{4}}\, f^{2}(a/b)P^{2} \tag{3-43}$$

$$\delta = \frac{12a\ L}{E'\ b^{2}}\, V_{1}(a/b)P \tag{3-44}$$

$$\Delta_{c} = \frac{6L^{2}}{E'b^{2}}\, V_{2}(a/b)P \tag{3-45}$$

where F, V_1 and V_2 are as tabulated in Reference [3-5]. These expressions are rewritten as

$$J = f_{1}(a)\,\frac{P^{2}}{E'} \tag{3-46}$$

$$\delta = f_{2}(a)\,\frac{P}{E'} \tag{3-47}$$

$$\Delta_{c} = f_{3}(a)\,\frac{P}{E'} \tag{3-48}$$

where $f_{1} = \frac{9\ \pi\ a\ L^{2}}{b^{4}} F^{2}$, $f_{2} = \frac{12a\ L}{b^{2}} V_{1}$ and $f_{3} = \frac{6L^{2}}{b^{2}} V_{2}$.

Substituting the elastic relationships, Eqs. (3-46) - (3-48), and the fully plastic formulae, Eqs. (3-35) - (3-37), into the estimation formulae, Eqs. (2-30), one gets the following expressions:

$$J = f_{1}(a_{e})\,\frac{P^{2}}{E'} + \alpha\ \sigma_{o}\ \varepsilon_{o}\ c\ h_{1}(a/b,\ n)(P/P_{o})^{n+1} \tag{3-49}$$

$$\delta = f_{2}(a_{e})\,\frac{P}{E'} + \alpha\ \varepsilon_{o}\ a\ h_{2}(a/b,\ n)(P/P_{o})^{n} \tag{3-50}$$

$$\Delta_{c} = f_{3}(a_{e})\,\frac{P}{E'} + \alpha\ \varepsilon_{o}\ a\ h_{3}(a/b,\ n)(P/P_{o})^{n} \tag{3-51}$$

where a_e is again the effective crack length defined by Eqs. (2-31) - (2-33). Examples showing the application and verification of these formulae are discussed in Reference [3-2].

3.5 SINGLE-EDGE CRACKED PLATE IN UNIFORM TENSION

3.5.1 Fully Plastic Solutions

A SECP specimen under remotely applied uniform tension is illustrated in Fig. 3-6. The crack length is denoted by a, the plate width by b and the length of the plate by 2L. The plate is subjected to a uniform stress field at its ends given by

$$\sigma_{yy}(x, \pm L) = \sigma^{\infty} = P/b \tag{3-52}$$

where P is the load per unit thickness. The fully plastic solutions for this crack configuration are given by the following expressions:

$$J = \alpha\, \sigma_o\, \varepsilon_o\, c(a/b)\, h_1(a/b,\ n)(P/P_o)^{n+1} \tag{3-53}$$

$$\delta = \alpha\, \varepsilon_o\, a\, h_2(a/b,\ n)(P/P_o)^{n} \tag{3-54}$$

$$\Delta_c = \alpha\, \varepsilon_o\, a\, h_3(a/b,\ n)(P/P_o)^{n} \tag{3-55}$$

$$\delta_t = \alpha\, \varepsilon_o\, c(a/b)\, h_4(a/b,\ n)(P/P_o)^{n+1} \tag{3-56}$$

$$\Theta_c = \alpha\, \varepsilon_o\, h_5(a/b,\ n)(P/P_o)^{n}$$

where Θ_c is the relative rotation at the ends due to crack. Here c = b − a is the remaining ligament and P_o is the limit load per unit thickness for the perfectly plastic case (n = ∞). A limit load analysis of this configuration is discussed in some detail in Reference [3-2]. It is found that P_o for this case is given by

$$P_o = 1.455\ \eta\ c\ \sigma_o;\ \text{plane strain} \tag{3-57}$$

$$P_o = 1.072\ \eta\ c\ \sigma_o;\ \text{plane stress} \tag{3-58}$$

where η is defined as

$$\eta = \left[1 + (a/c)^2\right]^{1/2} - a/c \tag{3-59}$$

In Eq. (3-54) $\delta = U_y(0, 0^+) - U_y(0, 0^-)$ is the mouth opening displacement at the edge of the specimen and Δ_c is the remote load point displacement due to the crack along the centerline of the specimen width (i.e., x = b/2, y = L). Δ_c is defined by

$$\Delta_c = \Delta - \Delta_{nc} \tag{3-60}$$

where Δ_{nc} is the load point displacement in the absence of crack and is given by

$$\Delta_{nc} = \sqrt{3}\ \alpha\ \varepsilon_o\ L\left[\frac{\sqrt{3}\ P}{2b\ \sigma_o}\right]^n \tag{3-61}$$

for plane strain and by

$$\Delta_{nc} = 2\ \alpha\ \varepsilon_o\ L\left[\frac{P}{b\ \sigma_o}\right]^n \tag{3-62}$$

for plane stress.

The functions h_1, h_2, h_3 and h_5 in Eqs. (3-53) − (3-55) are tabulated for a broad range of a/b and n values in Table 3-7 for plane strain and Table 3-8 for plane stress. Appendix C provides plots of the h functions.

The fully plastic solutions tabulated above were computed by employing the incompressible finite element program INFEM. For the linear elastic case corresponding to n = 1 these results compare within 6% of the solution given in Reference [3-5]. A detailed discussion on the numerical accuracy of the above solutions for n ≥ 1 is provided in References [3-2] and [3-3].

3.5.2 Elastic-Plastic Estimation Formulae

In the linear elastic range, the fracture parameters are commonly expressed by

$$J = \frac{\pi\ a\ F^2}{b^2\ E'}\ P^2 \tag{3-63}$$

$$\delta = \frac{4a\ V_1}{b\ E'}\ P \qquad (3\text{-}64)$$

$$\Delta_c = \frac{4a\ V_2}{b\ E'}\ P \qquad (3\text{-}65)$$

where the dimensionless functions F, V_1 and V_2 are tabulated functions [3-5]. On rewriting the above relationships in the alternate form, used here, one gets

$$J = f_1(a)\ \frac{P^2}{E'} \qquad (3\text{-}66)$$

$$\delta = f_2(a)\ \frac{P}{E'} \qquad (3\text{-}67)$$

$$\Delta_c = f_3(a)\ \frac{P}{E'} \qquad (3\text{-}68)$$

where $f_1 = \frac{\pi\ a\ F^2}{b^2}$, $f_2 = \frac{4a\ V_1}{b}$ and $f_3 = \frac{4a\ V_2}{b}$.

The elastic solutions, Eqs. (3-66) - (3-68), and the fully plastic solutions, Eqs. (3-53) - (3-55), are substituted into the estimation formulae to give the following elastic-plastic formulae for a Ramberg-Osgood stress-strain law:

$$J = f_1(a_e)\ \frac{P^2}{E'} + \alpha\ \sigma_o\ \varepsilon_o\ c(a/b)\ h_1(a/b,\ n)(P/P_o)^{n+1} \qquad (3\text{-}69)$$

$$\delta = f_2(a_e)\ \frac{P}{E'} + \alpha\ \varepsilon_o\ a\ h_2(a/b,\ n)(P/P_o)^{n} \qquad (3\text{-}70)$$

$$\Delta_c = f_3(a_e)\ \frac{P}{E'} + \alpha\ \varepsilon_o\ a\ h_3(a/b,\ n)(P/P_o)^{n} \qquad (3\text{-}71)$$

a_e is the effective crack length given by Eqs. (2-31) - (2-33).

3.6 DOUBLE-EDGE CRACKED PLATE IN TENSION

3.6.1 Fully Plastic Solutions

Figure 3-7 shows a double-edge cracked plate (DECP) specimen with crack length a, width 2b, length 2L and remaining ligament 2c = 2b - 2a. A uniform stress field is applied at the ends and is given by

$$\sigma_{yy}(x,\ \pm\ L) = \sigma\infty = P/2b \qquad (3\text{-}72)$$

where P is the load per unit thickness. In the fully plastic state, the crack parameters are given by

$$J = \alpha\ \sigma_o\ \varepsilon_o\ c\ h_1(a/b,\ n)(P/P_o)^{n+1} \qquad (3\text{-}73)$$

$$\delta = \alpha\ \varepsilon_o\ c\ h_2(a/b,\ n)(P/P_o)^{n} \qquad (3\text{-}74)$$

$$\Delta_c = \alpha\ \varepsilon_o\ c\ h_3(a/b,\ n)(P/P_o)^{n} \qquad (3\text{-}75)$$

$$\delta_t = \alpha\ \varepsilon_o\ c\ h_4(a/b,\ n)(P/P_o)^{n+1} \qquad (3\text{-}76)$$

where P_o is the limit load per unit thickness. The limit load is given below and derived in Reference [3-4]. It is given by

$$P_o = (0.72 + 1.82\ \frac{c}{b})\sigma_o\ b \qquad (3\text{-}77)$$

for plane strain and

$$P_o = \frac{4}{\sqrt{3}}\ c\ \sigma_o \qquad (3\text{-}78)$$

for plane stress.

In Eq. (3-74), $\delta = U_y(b,\ 0^+) - U_y(b,\ 0^-)$ is the mouth opening displacement of the crack at the edge of the plate. Δ_c in Eq. (3-75) is the load-point displacement due to the crack along the centerline of the specimen (i.e., x = 0, y = L) and is defined by

$$\Delta_c = \Delta - \Delta_{nc} \qquad (3\text{-}79)$$

The load point displacement in the absence of crack is given by

$$\Delta_{nc} = \sqrt{3}\ \alpha\ \varepsilon_o\ L \left[\frac{\sqrt{3}\ P}{4b\ \sigma_o}\right]^n \text{; plane strain} \qquad (3\text{-}80)$$

$$\Delta_{nc} = 2\ \alpha\ \varepsilon_o\ L \left[\frac{P}{2b\ \sigma_o}\right]^n \text{; plane stress} \qquad (3\text{-}81)$$

The h functions in Eqs. (3-73) - (3-75) are listed in Tables 3-9 and 3-10 for plane strain and plane stress, respectively. In the linear elastic case, n = 1, these solutions compare within less than 5% of those given in Reference [3-5]. An assessment of the accuracy of the above results for large a/b and n values is given in Reference [3-3]. Solutions presented here were obtained by using the code INFEM. Plots of h_1, h_2 and h_3 versus n are shown in Appendix C.

3.6.2 Elastic-Plastic Estimation Formulae

The linear elastic solutions for the DECP are given by

$$J = \frac{\pi\ a\ F^2}{4b^2\ E'} P^2 \qquad (3\text{-}82)$$

$$\delta = \frac{2a\ V_1}{b\ E'} P \qquad (3\text{-}83)$$

$$\Delta_c = \frac{2a\ V_2}{b\ E'} P \qquad (3\text{-}84)$$

where the functions F, V_1 and V_2 are given in [3-5]. After the customary recasting they appear as:

$$J = f_1(a)\ \frac{P^2}{E'} \qquad (3\text{-}85)$$

$$\delta = f_2(a)\ \frac{P}{E'} \qquad (3\text{-}86)$$

$$\Delta_c = f_3(a)\ \frac{P}{E'}$$

where $f_1 = \frac{\pi\ a\ F^2}{4b^2}$, $f_2 = \frac{2a\ V_1}{b}$ and $f_3 = \frac{2a\ V_2}{b}$.

Combining the linear elastic solutions with the fully plastic solutions in accordance with the estimation procedure, the following expressions are obtained:

$$J = f_1(a_e)\ \frac{P^2}{E'} + \alpha\ \sigma_o\ \varepsilon_o\ c\ h_1(a/b,\ n)(P/P_o)^{n+1} \qquad (3\text{-}87)$$

$$\delta = f_2(a_e)\ \frac{P}{E'} + \alpha\ \varepsilon_o\ c\ h_2(a/b,\ n)(P/P_o)^n \qquad (3\text{-}88)$$

$$\Delta_c = f_3(a_e)\ \frac{P}{E'} + \alpha\ \varepsilon_o\ c\ h_3(a/b,\ n)(P/P_o)^n \qquad (3\text{-}89)$$

In the above, a_e is the effective crack length as defined in Eqs. (2-31) - (2-33).

3.7 REFERENCES

[3-1] A. Needleman and C. F. Shih, "Finite Element Method for Plane Strain Deformations of Incompressible Solids," Computer Methods in Applied Mechanics and Engineering, 1978, pp. 223-240.

[3-2] C. F. Shih and V. Kumar, "Estimation Technique for the Prediction of Elastic-Plastic Fracture of Structural Components of Nuclear Systems," 1st Semiannual Report to EPRI, Contract No. RP1237-1, General Electric Company, Schenectady, New York, July 1, 1978 - January 31, 1979.

[3-3] V. Kumar, M. D. German, and C. F. Shih, "Estimation Techniques for the Prediction of Elastic-Plastic Fracture of Structural Components of Nuclear Systems," Combined 2nd and 3rd Semiannual Report to EPRI, Contract No. RP1237-1, General Electric Company, Schenectady, New York, February 1, 1979 - January 31, 1980.

[3-4] V. Kumar, H. G. deLorenzi, W. R. Andrews, C. F. Shih, M. D. German, and D. F. Mowbray, "Estimation Technique for the Prediction of Elastic-Plastic Fracture of Structural Components of Nuclear Systems," 4th Semiannual Report to EPRI, Contract No. RP1237-1, General Electric Company,

Schenectady, New York, July 1, 1980 - January 31, 1981.

[3-5] H. Tada, P. C. Paris, and G. R. Irwin, "The Stress Analysis of Cracks Handbook," Del Research Corporation, Hellertown, Pennsylvania, 1973.

[3-6] D. P. Rooke and J. C. Cartwright, Compendium of Stress Intensity Factors, Her Majesty's Stationary Office, London, 1976.

[3-7] V. Kumar and C. F. Shih, "Fully Plastic Crack Solutions, Estimation Scheme and Stability Analyses for Compact Specimen," in Fracture Mechanics, ASTM Special Technical Publication 700, 1980, pp. 406-438.

[3-8] J. C. Newman, Jr., "Stress Analysis of the Compact Specimen Including the Effects of Pin Loading," Fracture Analysis, ASTM Special Technical Publication 560, 1974, pp. 105-121.

[3-9] J. G. Merkle and H. T. Corten, "A J-Integral Analysis for the Compact Specimen, Considering Axial Force as Well as Bending Effects," Journal of Pressure Vessel and Technology, Trans. ASME, Vol. 96, 1974, pp. 286-292.

[3-10] J. R. Rice, P. C. Paris, and J. G. Merkle, "Some Further Results of J-Integral Analysis and Estimates," in Progress in Flaw Growth and Fracture Toughness Testing, ASTM Special Technical Publication 536, 1973, pp. 231-245.

[3-11] C. F. Shih and J. W. Hutchinson, "Fully Plastic Solutions and Large-Scale Yielding Estimates for Plane Stress Crack Problems," Transactions of ASME, Journal of Engineering Materials and Technology, Series H, Vol. 98, No. 4, October 1976, pp. 289-295.

[3-12] J. W. Hutchinson, A. Needleman, and C. F. Shih, "Fully Plastic Crack Problems in Bending and Tension," Fracture Mechanics, Ed. by N. Perrone, et al., University Press of Virginia, Charlottesville, North Carolina, 1978, pp. 515-528.

[3-13] C. F. Shih, W. R. Andrews, H. G. deLorenzi, M. D. German, R. H. Van Stone, and D. F. Mowbray, "Methodology for Plastic Fracture," Final Report to EPRI, Contract No. RP601-2, General Electric Company, Schenectady, New York, August 1980.

[3-14] A. P. Green and B. B. Hundy, "Initial Plastic Yielding in Notch Bend Bars," Journal of the Mechanics and Physics of Solids, Vol. 4, 1956, pp. 128-144.

[3-15] H. Ford and G. Lianis, Agnew. Math. Phys., 1957, Vol. 8, pp. 360-382.

[3-16] S. P. Timoshenko and J. N. Goodier, Theory of Elasticity, 3rd Edition, McGraw-Hill, New York, 1970, p. 121.

Table 3-1

h_1, h_2 and h_3 for the compact specimen in plane strain.

		n = 1	n = 2	n = 3	n = 5	n = 7	n = 10	n = 13	n = 16	n = 20
a/b = 1/4	h_1	2.23	2.05	1.78	1.48	1.33	1.26	1.25	1.32	1.57
	h_2	17.9	12.5	11.7	10.8	10.5	10.7	11.5	12.6	14.6
	h_3	9.85	8.51	8.17	7.77	7.71	7.92	8.52	9.31	10.9
a/b = 3/8	h_1	2.15	1.72	1.39	0.970	0.693	0.443	0.276	0.176	0.098
	h_2	12.6	8.18	6.52	4.32	2.97	1.79	1.10	0.686	0.370
	h_3	7.94	5.76	4.64	3.10	2.14	1.29	0.793	0.494	0.266
a/b = 1/2	h_1	1.94	1.51	1.24	0.919	0.685	0.461	0.314	0.216	0.132
	h_2	9.33	5.85	4.30	2.75	1.91	1.20	0.788	0.530	0.317
	h_3	6.41	4.27	3.16	2.02	1.41	0.888	0.585	0.393	0.236
a/b = 5/8	h_1	1.76	1.45	1.24	0.974	0.752	0.602	0.459	0.347	0.248
	h_2	7.61	4.57	3.42	2.36	1.81	1.32	0.983	0.749	0.485
	h_3	5.52	3.43	2.58	1.79	1.37	1.00	0.746	0.568	0.368
a/b = 3/4	h_1	1.71	1.42	1.26	1.033	0.864	0.717	0.575	0.448	0.345
	h_2	6.37	3.95	3.18	2.34	1.88	1.44	1.12	0.887	0.665
	h_3	4.86	3.05	2.46	1.81	1.45	1.11	0.869	0.686	0.514
a/b → 1	h_1	1.57	1.45	1.35	1.18	1.08	0.950	0.850	0.730	0.630
	h_2	5.39	3.74	3.09	2.43	2.12	1.80	1.57	1.33	1.14
	h_3	4.31	2.99	2.47	1.95	1.79	1.44	1.26	1.07	0.909

Table 3-2

h_1, h_2 and h_3 for the compact specimen in plane stress.

		n = 1	n = 2	n = 3	n = 5	n = 7	n = 10	n = 13	n = 16	n = 20
a/b = 1/4	h_1	1.61	1.46	1.28	1.06	0.903	0.729	0.601	0.511	0.395
	h_2	17.6	12.0	10.7	8.74	7.32	5.74	4.63	3.75	2.92
	h_3	9.67	8.00	7.21	5.94	5.00	3.95	3.19	2.59	2.023
a/b = 3/8	h_1	1.55	1.25	1.05	0.801	0.647	0.484	0.377	0.284	0.220
	h_2	12.4	8.20	6.54	4.56	3.45	2.44	1.83	1.36	1.02
	h_3	7.80	5.73	4.62	3.25	2.48	1.77	1.33	0.990	0.746
a/b = 1/2	h_1	1.40	1.08	0.901	0.686	0.558	0.436	0.356	0.298	0.238
	h_2	9.16	5.67	4.21	2.80	2.12	1.57	1.25	1.03	0.814
	h_3	6.29	4.15	3.11	2.09	1.59	1.18	0.938	0.774	0.614
a/b = 5/8	h_1	1.27	1.03	0.875	0.695	0.593	0.494	0.423	0.370	0.310
	h_2	7.47	4.48	3.35	2.37	1.92	1.54	1.29	1.12	0.928
	h_3	5.42	3.38	2.54	1.80	1.47	1.18	0.988	0.853	0.710
a/b = 3/4	h_1	1.23	0.977	0.833	0.683	0.598	0.506	0.431	0.373	0.314
	h_2	6.25	3.78	2.89	2.14	1.78	1.44	1.20	1.03	0.857
	h_3	4.77	2.92	2.24	1.66	1.38	1.12	0.936	0.800	0.666
a/b → 1	h_1	1.13	1.01	0.775	0.680	0.650	0.620	0.490	0.470	0.420
	h_2	5.29	3.54	2.41	1.91	1.73	1.59	1.23	1.17	1.03
	h_3	4.23	2.83	1.93	1.52	1.39	1.27	0.985	0.933	0.824

Table 3-3

h_1, h_2 and h_3 for CCP in plane strain under remote tension.

		n = 1	n = 2	n = 3	n = 5	n = 7	n = 10	n = 13	n = 16	n = 20
a/b = 1/8	h_1	2.80	3.61	4.06	4.35	4.33	4.02	3.56	3.06	2.46
	h_2	3.05	3.62	3.91	4.06	3.93	3.54	3.07	2.60	2.06
	h_3	0.303	0.574	0.840	1.30	1.63	1.95	2.03	1.96	1.77
a/b = 1/4	h_1	2.54	3.01	3.21	3.29	3.18	2.92	2.63	2.34	2.03
	h_2	2.68	2.99	3.01	2.85	2.61	2.30	1.97	1.71	1.45
	h_3	0.536	0.911	1.22	1.64	1.84	1.85	1.80	1.64	1.43
a/b = 3/8	h_1	2.34	2.62	2.65	2.51	2.28	1.97	1.71	1.46	1.19
	h_2	2.35	2.39	2.23	1.88	1.58	1.28	1.07	0.890	0.715
	h_3	0.699	1.06	1.28	1.44	1.40	1.23	1.05	0.888	0.719
a/b = 1/2	h_1	2.21	2.29	2.20	1.97	1.76	1.52	1.32	1.16	0.978
	h_2	2.03	1.86	1.60	1.23	1.00	0.799	0.664	0.564	0.466
	h_3	0.803	1.07	1.16	1.10	0.968	0.796	0.665	0.565	0.469
a/b = 5/8	h_1	2.12	1.96	1.76	1.43	1.17	0.863	0.628	0.458	0.300
	h_2	1.71	1.32	1.04	0.707	0.524	0.358	0.250	0.178	0.114
	h_3	0.844	0.937	0.879	0.701	0.522	0.361	0.251	0.178	0.115
a/b = 3/4	h_1	2.07	1.73	1.47	1.11	0.895	0.642	0.461	0.337	0.216
	h_2	1.35	0.857	0.596	0.361	0.254	0.167	0.114	0.0810	0.0511
	h_3	0.805	0.700	0.555	0.359	0.254	0.168	0.114	0.0813	0.0516
a/b = 7/8	h_1	2.08	1.64	1.40	1.14	0.987	0.814	0.688	0.573	0.461
	h_2	0.889	0.428	0.287	0.181	0.139	0.105	0.0837	0.0682	0.0533
	h_3	0.632	0.400	0.291	0.182	0.140	0.106	0.0839	0.0683	0.0535

Table 3-4

h_1, h_2 and h_3 for CCP in plane stress under remote tension.

		n = 1	n = 2	n = 3	n = 5	n = 7	n = 10	n = 13	n = 16	n = 20
a/b = 1/8	h_1	2.80	3.57	4.01	4.47	4.65	4.62	4.41	4.13	3.72
	h_2	3.53	4.09	4.43	4.74	4.79	4.63	4.33	4.00	3.55
	h_3	0.350	0.661	0.997	1.55	2.05	2.56	2.83	2.95	2.92
a/b = 1/4	h_1	2.54	2.97	3.14	3.20	3.11	2.86	2.65	2.47	2.20
	h_2	3.10	3.29	3.30	3.15	2.93	2.56	2.29	2.08	1.81
	h_3	0.619	1.01	1.35	1.83	2.08	2.19	2.12	2.01	1.79
a/b = 3/8	h_1	2.34	2.53	2.52	2.35	2.17	1.95	1.77	1.61	1.43
	h_2	2.71	2.62	2.41	2.03	1.75	1.47	1.28	1.13	0.988
	h_3	0.807	1.20	1.43	1.59	1.57	1.43	1.27	1.13	0.994
a/b = 1/2	h_1	2.21	2.20	2.06	1.81	1.63	1.43	1.30	1.17	1.00
	h_2	2.34	2.01	1.70	1.30	1.07	0.871	0.757	0.666	0.557
	h_3	0.927	1.19	1.26	1.18	1.04	0.867	0.758	0.668	0.560
a/b = 5/8	h_1	2.12	1.91	1.69	1.41	1.22	1.01	0.853	0.712	0.573
	h_2	1.97	1.46	1.13	0.785	0.617	0.474	0.383	0.313	0.256
	h_3	0.975	1.05	0.970	0.763	0.620	0.478	0.386	0.318	0.273
a/b = 3/4	h_1	2.07	1.71	1.46	1.21	1.08	0.867	0.745	0.646	0.532
	h_2	1.55	0.970	0.685	0.452	0.361	0.262	0.216	0.183	0.148
	h_3	0.929	0.802	0.642	0.450	0.361	0.263	0.216	0.183	0.149
a/b = 7/8	h_1	2.08	1.57	1.31	1.08	0.972	0.862	0.778	0.715	0.630
	h_2	1.03	0.485	0.310	0.196	0.157	0.127	0.109	0.0971	0.0842
	h_3	0.730	0.452	0.313	0.198	0.157	0.127	0.109	0.0973	0.0842

Table 3-5

h_1, h_2 and h_3 for SECP in plane strain under three-point bending.

		n = 1	n = 2	n = 3	n = 5	n = 7	n = 10	n = 13	n = 16	n = 20
a/b = 1/8	h_1	0.936	0.869	0.805	0.687	0.580	0.437	0.329	0.245	0.165
	h_2	6.97	6.77	6.29	5.29	4.38	3.24	2.40	1.78	1.19
	h_3	3.00	22.1	20.0	15.0	11.7	8.39	6.14	4.54	3.01
a/b = 1/4	h_1	1.20	1.034	0.930	0.762	0.633	0.523	0.396	0.303	0.215
	h_2	5.80	4.67	4.01	3.08	2.45	1.93	1.45	1.09	0.758
	h_3	4.08	9.72	8.36	5.86	4.47	3.42	2.54	1.90	1.32
a/b = 3/8	h_1	1.33	1.15	1.02	0.084	0.695	0.556	0.442	0.360	0.265
	h_2	5.18	3.93	3.20	2.38	1.93	1.47	1.15	0.928	0.684
	h_3	4.51	6.01	5.03	3.74	3.02	2.30	1.80	1.45	1.07
a/b = 1/2	h_1	1.41	1.09	0.922	0.675	0.495	0.331	0.211	0.135	0.0741
	h_2	4.87	3.28	2.53	1.69	1.19	0.773	0.480	0.304	0.165
	h_3	4.69	4.33	3.49	2.35	1.66	1.08	0.669	0.424	0.230
a/b = 5/8	h_1	1.46	1.07	0.896	0.631	0.436	0.255	0.142	0.084	0.0411
	h_2	4.64	2.86	2.16	1.37	0.907	0.518	0.287	0.166	0.0806
	h_3	4.71	3.49	2.70	1.72	1.14	0.652	0.361	0.209	0.102
a/b = 3/4	h_1	1.48	1.15	0.974	0.693	0.500	0.348	0.223	0.140	0.0745
	h_2	4.47	2.75	2.10	1.36	0.936	0.618	0.388	0.239	0.127
	h_3	4.49	3.14	2.40	1.56	1.07	0.704	0.441	0.272	0.144
a/b = 7/8	h_1	1.50	1.35	1.20	1.02	0.855	0.690	0.551	0.440	0.321
	h_2	4.36	2.90	2.31	1.70	1.33	1.00	0.782	0.613	0.459
	h_3	4.15	3.08	2.45	1.81	1.41	1.06	0.828	0.649	0.486

Table 3-6

h_1, h_2 and h_3 for SECP in plane stress under three-point bending.

		n = 1	n = 2	n = 3	n = 5	n = 7	n = 10	n = 13	n = 16	n = 20
a/b = 1/8	h_1	0.676	0.600	0.548	0.459	0.383	0.297	0.238	0.192	0.148
	h_2	6.84	6.30	5.66	4.53	3.64	2.72	2.12	1.67	1.26
	h_3	2.95	20.1	14.6	12.2	9.12	6.75	5.20	4.09	3.07
a/b = 1/4	h_1	0.869	0.731	0.629	0.479	0.370	0.246	0.174	0.117	0.0593
	h_2	5.69	4.50	3.68	2.61	1.95	1.29	0.897	0.603	0.307
	h_3	4.01	8.81	7.19	4.73	3.39	2.20	1.52	1.01	0.508
a/b = 3/8	h_1	0.963	0.797	0.680	0.527	0.418	0.307	0.232	0.174	0.105
	h_2	5.09	3.73	2.93	2.07	1.58	1.13	0.841	0.626	0.381
	h_3	4.42	5.53	4.48	3.17	2.41	1.73	1.28	0.948	0.575
a/b = 1/2	h_1	1.02	0.767	0.621	0.453	0.324	0.202	0.128	0.0813	0.0298
	h_2	4.77	3.12	2.32	1.55	1.08	0.655	0.410	0.259	0.0974
	h_3	4.60	4.09	3.09	2.08	1.44	0.874	0.545	0.344	0.129
a/b = 5/8	h_1	1.05	0.786	0.649	0.494	0.357	0.235	0.173	0.105	0.0471
	h_2	4.55	2.83	2.12	1.46	1.02	0.656	0.472	0.286	0.130
	h_3	4.62	3.43	2.60	1.79	1.26	0.803	0.577	0.349	0.158
a/b = 3/4	h_1	1.07	0.786	0.643	0.474	0.343	0.230	0.167	0.110	0.0442
	h_2	4.39	2.66	1.97	1.33	0.928	0.601	0.427	0.280	0.114
	h_3	4.39	3.01	2.24	1.51	1.05	0.680	0.483	0.316	0.129
a/b = 7/8	h_1	1.086	0.928	0.810	6.46	0.538	0.423	0.332	0.242	0.205
	h_2	4.28	2.76	2.16	1.56	1.23	0.922	0.702	0.561	0.428
	h_3	4.07	2.93	2.29	1.65	1.30	0.975	0.742	0.592	0.452

Table 3-7

h_1, h_2, h_3 and h_5 for SECP in plane strain under remote uniform tension.

		n = 1	n = 2	n = 3	n = 5	n = 7	n = 10	n = 13	n = 16	n = 20
a/b = 1/8	h_1	4.95	6.93	8.57	11.5	13.5	16.1	18.1	19.9	21.2
	h_2	5.25	6.47	7.56	9.46	11.1	12.9	14.4	15.7	16.8
	h_3	26.6	25.8	25.2	24.2	23.6	23.2	23.2	23.5	23.7
	h_5	0.0	0.558	0.807	1.26	1.62	1.98	2.19	2.33	0.0
a/b = 1/4	h_1	4.34	4.77	4.64	3.82	3.06	2.17	1.55	1.11	0.712
	h_2	4.76	4.56	4.28	3.39	2.64	1.81	1.25	0.875	0.552
	h_3	10.3	7.64	5.87	3.70	2.48	1.50	0.970	0.654	0.404
	h_5	0.0	1.14	1.11	0.833	0.604	0.375	0.237	0.153	0.0894
a/b = 3/8	h_1	3.88	3.25	2.63	1.68	1.06	0.539	0.276	0.142	0.0595
	h_2	4.54	3.49	2.67	1.57	0.946	0.458	0.229	0.116	0.048
	h_3	5.14	2.99	1.90	0.923	0.515	0.240	0.119	0.060	0.0246
	h_5	0.0	1.43	1.10	0.643	0.380	0.179	0.0879	0.0442	0.0181
a/b = 1/2	h_1	3.40	2.30	1.69	0.928	0.514	0.213	0.0902	0.0385	0.0119
	h_2	4.45	2.77	1.89	0.954	0.507	0.204	0.0854	0.0356	0.0110
	h_3	3.15	1.54	0.912	0.417	0.215	0.085	0.0358	0.0147	0.00448
	h_5	0.0	1.60	1.11	0.562	0.300	0.121	0.0511	0.0213	0.00657
a/b = 5/8	h_1	2.86	1.80	1.30	0.697	0.378	0.153	0.0625	0.0256	0.0078
	h_2	4.37	2.44	1.62	0.0806	0.423	0.167	0.0671	0.0272	0.00823
	h_3	2.31	1.08	0.681	0.329	0.171	0.067	0.0268	0.0108	0.00326
	h_5	0.0	1.80	1.21	0.604	0.318	0.126	0.0509	0.0207	0.00626
a/b = 3/4	h_1	2.34	1.61	1.25	0.769	0.477	0.233	0.116	0.059	0.0215
	h_2	4.32	2.52	1.79	1.03	0.619	0.296	0.146	0.0735	0.0267
	h_3	2.02	1.10	0.765	0.435	0.262	0.125	0.0617	0.0312	0.0113
	h_5	0.0	2.17	1.55	0.895	0.539	0.258	0.127	0.0639	0.0232
a/b = 7/8	h_1	1.91	1.57	1.37	1.10	0.925	0.702			
	h_2	4.29	2.75	2.14	1.55	1.23	0.921			
	h_3	2.01	1.27	0.988	0.713	0.564	0.424			
	h_5	0.0	2.601	2.203	1.47	1.16	0.875			

Table 3-8

h_1, h_2, h_3 and h_5 for SECP in plane stress under remote uniform tension.

		n = 1	n = 2	n = 3	n = 5	n = 7	n = 10	n = 13	n = 16	n = 20
a/b = 1/8	h_1	3.58	4.55	5.06	5.30	4.96	4.14	3.29	2.60	1.92
	h_2	5.15	5.43	6.05	6.01	5.47	4.46	3.48	2.74	2.02
	h_3	26.1	21.6	18.0	12.7	9.24	5.98	3.94	2.72	2.0
	h_5	0.296	0.490	0.627	0.748	0.720	0.586	0.450	0.345	0.255
a/b = 1/4	h_1	3.14	3.26	2.92	2.12	1.53	0.960	0.615	0.400	0.230
	h_2	4.67	4.30	3.70	2.53	1.76	1.05	0.656	0.419	0.237
	h_3	10.1	6.49	4.36	2.19	1.24	0.630	0.362	0.224	0.123
	h_5	0.904	1.05	0.932	0.631	0.433	0.258	0.160	0.103	0.0583
a/b = 3/8	h_1	2.81	2.37	1.94	1.37	1.01	0.677	0.474	0.342	0.226
	h_2	4.47	3.43	2.63	1.69	1.18	0.762	0.524	0.372	0.244
	h_3	5.05	2.65	1.60	0.812	0.525	0.328	0.223	0.157	0.102
	h_5	1.73	1.40	1.10	0.720	0.510	0.332	0.229	0.164	0.108
a/b = 1/2	h_1	2.46	1.67	1.25	0.776	0.510	0.286	0.164	0.0956	0.0469
	h_2	4.37	2.73	1.91	1.09	0.694	0.380	0.216	0.124	0.0607
	h_3	3.10	1.43	0.871	0.461	0.286	0.155	0.088	0.0506	0.0247
	h_5	2.41	1.58	1.12	0.652	0.417	0.229	0.130	0.0748	0.0395
a/b = 5/8	h_1	2.07	1.41	1.105	0.755	0.551	0.363	0.248	0.172	0.107
	h_2	4.30	2.55	1.84	1.16	0.816	0.523	0.353	0.242	0.150
	h_3	2.27	1.13	0.771	0.478	0.336	0.215	0.146	0.100	0.0616
	h_5	3.02	1.88	1.36	0.861	0.606	0.388	0.262	0.179	0.111
a/b = 3/4	h_1	1.70	1.14	0.910	0.624	0.447	0.280	0.181	0.118	0.0670
	h_2	4.24	2.47	1.81	1.15	0.798	0.490	0.314	0.203	0.115
	h_3	1.98	1.09	0.784	0.494	0.344	0.211	0.136	0.0581	0.0496
	h_5	3.44	2.12	1.56	0.986	0.686	0.421	0.270	0.174	0.0987
a/b = 7/8	h_1	1.38	1.11	0.962	0.792	0.677	0.574			
	h_2	4.22	2.68	2.08	1.54	1.27	1.04			
	h_3	1.97	1.25	0.969	0.716	0.591	0.483			
	h_5	3.91	2.53	1.96	1.45	1.19	0.973			

Table 3-9

h_1, h_2, and h_3 for DECP in plane strain under remote tension.

		n = 1	n = 2	n = 3	n = 5	n = 7	n = 10	n = 13	n = 16	n = 20
a/b = 1/8	h_1	0.572	0.772	0.922	1.13	1.35	1.61	1.86	2.08	2.44
	h_2	0.732	0.852	0.961	1.14	1.29	1.50	1.70	1.94	2.17
	h_3	0.063	0.126	0.200	0.372	0.571	0.911	1.30	1.74	2.29
a/b = 1/4	h_1	1.10	1.32	1.38	1.65	1.75	1.82	1.86	1.89	1.92
	h_2	1.56	1.63	1.70	1.78	1.80	1.81	1.79	1.78	1.76
	h_3	0.267	0.479	0.698	1.11	1.47	1.92	2.25	2.49	2.73
a/b = 3/8	h_1	1.61	1.83	1.92	1.92	1.84	1.68	1.49	1.32	1.12
	h_2	2.51	2.41	2.35	2.15	1.94	1.68	1.44	1.25	1.05
	h_3	0.637	1.05	1.40	1.87	2.11	2.20	2.09	1.92	1.67
a/b = 1/2	h_1	2.22	2.43	2.48	2.43	2.32	2.12	1.91	1.60	1.51
	h_2	3.73	3.40	3.15	2.71	2.37	2.01	1.72	1.40	1.38
	h_3	1.26	1.92	2.37	2.79	2.85	2.68	2.40	1.99	1.94
a/b = 5/8	h_1	3.16	3.38	3.45	3.42	3.28	3.00	2.54	2.36	2.27
	h_2	5.57	4.76	4.23	3.46	2.97	2.48	2.02	1.82	1.66
	h_3	2.36	3.29	3.74	3.90	3.68	3.23	2.66	2.40	2.19
a/b = 3/4	h_1	5.24	6.29	7.17	8.44	9.46	10.9	11.9	11.3	17.4
	h_2	9.10	7.76	7.14	6.64	6.83	7.48	7.79	7.14	11.1
	h_3	4.73	6.26	7.03	7.63	8.14	9.04	9.40	8.58	13.5
a/b = 7/8	h_1	14.2	24.8	39.0	78.4	140.0	341.0	777.0	1570.0	3820.0
	h_2	20.1	19.4	22.7	36.1	58.9	133.0	294.0	585.0	1400.0
	h_3	12.7	18.2	24.1	40.4	65.8	149.0	327.0	650.0	1560.0

Table 3-10

h_1, h_2, and h_3 for DECP in plane stress under remote tension.

		n = 1	n = 2	n = 3	n = 5	n = 7	n = 10	n = 13	n = 16	n = 20
a/b = 1/8	h_1	0.583	0.825	1.02	1.37	1.71	2.24	2.84	3.54	4.62
	h_2	0.853	1.05	1.23	1.55	1.87	2.38	2.96	3.65	4.70
	h_3	0.0729	0.159	0.26	0.504	0.821	1.41	2.18	3.16	4.73
a/b = 1/4	h_1	1.01	1.23	1.36	1.48	1.54	1.58	1.59	1.59	1.59
	h_2	1.73	1.82	1.89	1.92	1.91	1.85	1.80	1.75	1.70
	h_3	0.296	0.537	0.770	1.17	1.49	1.82	2.02	2.12	2.20
a/b = 3/8	h_1	1.29	1.42	1.43	1.34	1.24	1.09	0.970	0.873	0.674
	h_2	2.59	2.39	2.22	1.86	1.59	1.28	1.07	0.922	0.709
	h_3	0.658	1.04	1.30	1.52	1.55	1.41	1.23	1.07	0.830
a/b = 1/2	h_1	1.48	1.47	1.38	1.17	1.01	0.845	0.732	0.625	0.208
	h_2	3.51	2.82	2.34	1.67	1.28	0.944	0.762	0.630	0.232
	h_3	1.18	1.58	1.69	1.56	1.32	1.01	0.809	0.662	0.266
a/b = 5/8	h_1	1.59	1.45	1.29	1.04	0.882	0.737	0.649	0.466	0.0202
	h_2	4.56	3.15	2.32	1.45	1.06	0.790	0.657	0.473	0.0277
	h_3	1.93	2.14	1.95	1.44	1.09	0.809	0.665	0.487	0.0317
a/b = 3/4	h_1	1.65	1.43	1.22	0.979	0.834	0.701	0.630	0.297	
	h_2	5.90	3.37	2.22	1.30	0.966	0.741	0.636	0.312	
	h_3	3.06	2.67	2.06	1.31	0.978	0.747	0.638	0.318	
a/b = 7/8	h_1	1.69	1.43	1.22	0.979	0.845	0.738	0.664	0.614	0.562
	h_2	8.02	3.51	2.14	1.27	0.971	0.775	0.663	0.596	0.535
	h_3	5.07	3.18	2.16	1.30	0.980	0.779	0.665	0.597	0.538

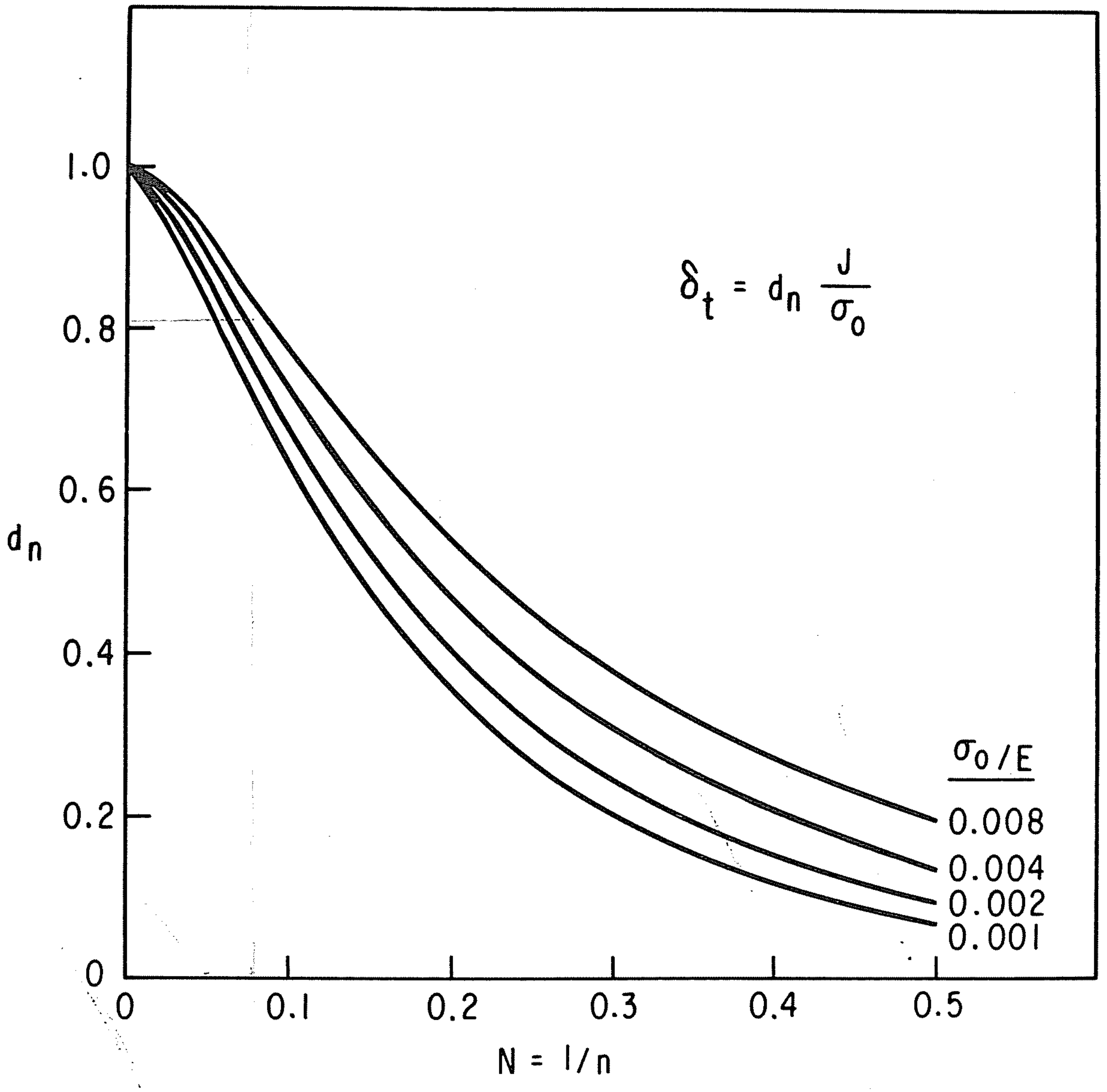

Figure 3-1. Variation of d_n with n and σ_o/E for plane strain with $\alpha = 1$. For $\alpha \neq 1$, $d_n(\alpha \neq 1) = \alpha^{1/n} d_n(\alpha = 1)$.

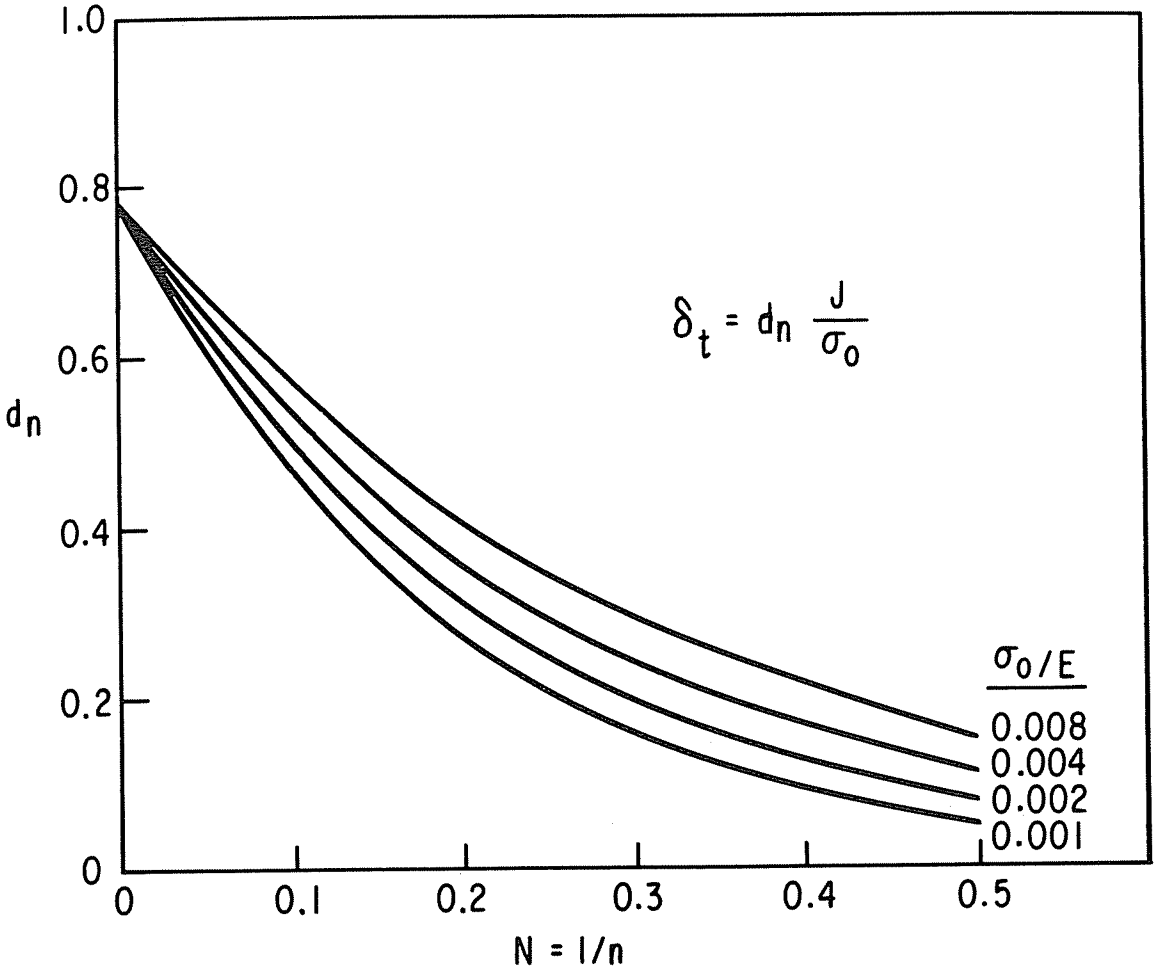

Figure 3-2. Variation of d_n with n and σ_o/E for plane stress with $\alpha = 1$. For $\alpha \neq 1$, $d_n(\alpha \neq 1) = \alpha^{1/n} d_n(\alpha = 1)$.

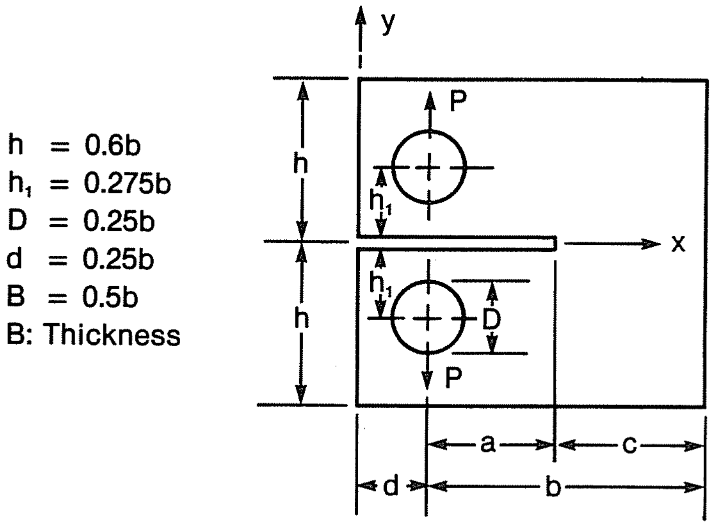

Figure 3-3. Geometry of standard ASTM compact specimen.

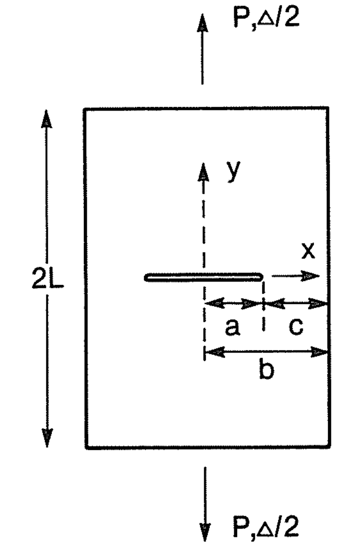

Figure 3-4. Center-cracked plate in tension.

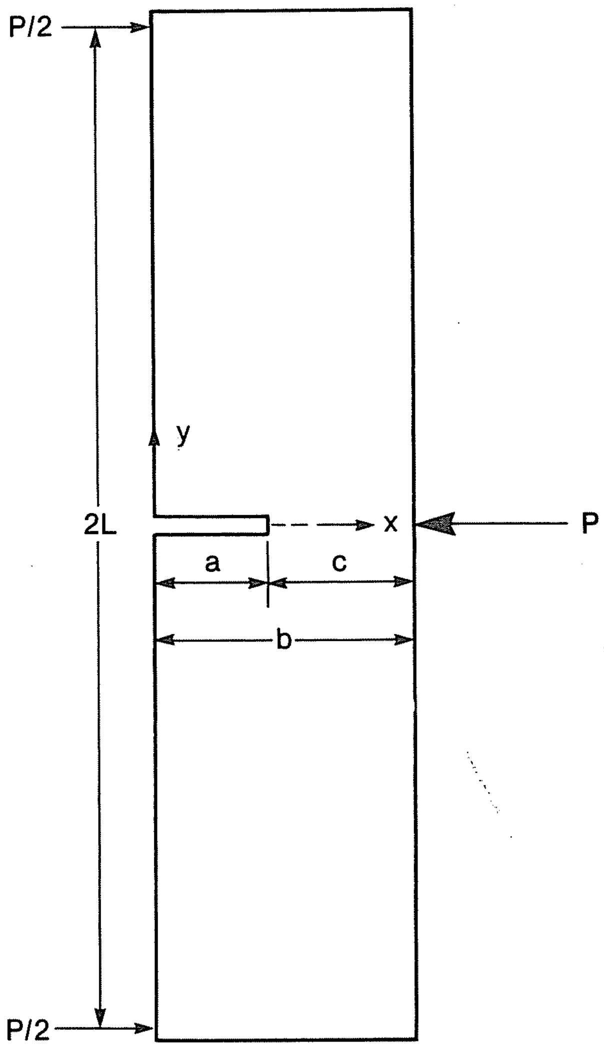

Figure 3-5. Schematic of a single-edge cracked panel under three-point bending.

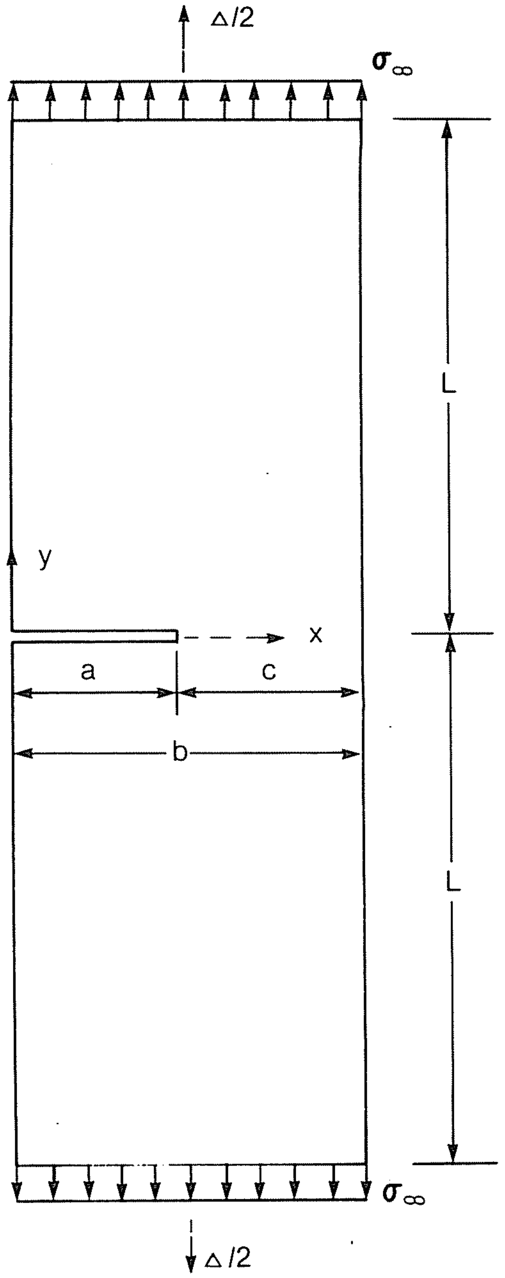

Figure 3-6. Single-edge cracked plate under remote uniform tension.

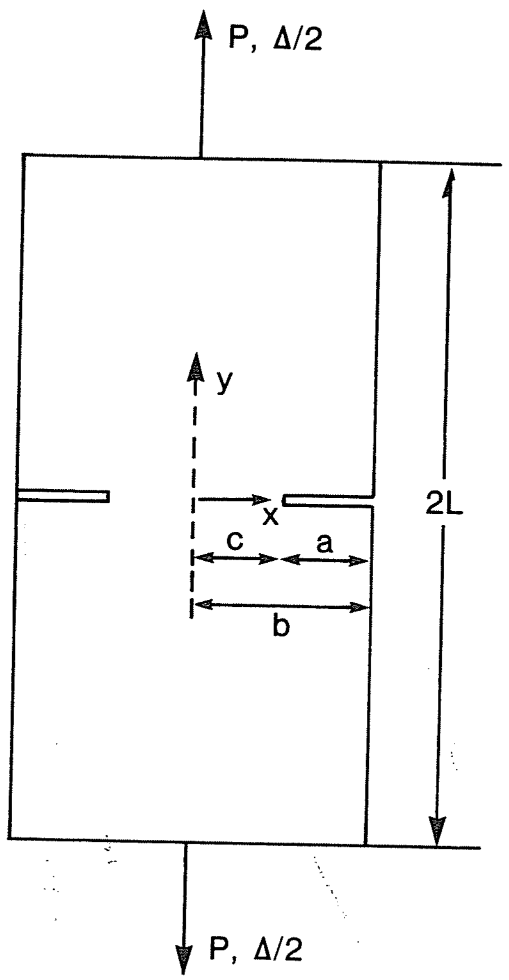

Figure 3-7. Double-edge cracked plate in tension.

SECTION 4
ELASTIC AND FULLY PLASTIC SOLUTIONS FOR FLAWED
CYLINDERS

Section 4
ELASTIC AND FULLY PLASTIC SOLUTIONS FOR FLAWED CYLINDERS

4.1 INTRODUCTION

This section presents elastic and fully plastic solutions for cylindrical configurations containing two-dimensional axial and circumferential flaws. In the case of the axially cracked cylinder shown in Fig. 4-1, the loading is due to internal pressure, which also acts on the crack face. This crack geometry is analyzed as a two-dimensional plane strain problem. The circumferentially cracked cylinder is loaded by applying uniform tension at its ends, as illustrated in Fig. 4-2. This is treated as an axisymmetric problem. It is noted that the formulation of the J-integral for these crack problems, which involve either crack face loading or axisymmetric deformation, are different from the conventional two-dimensional expression, Eq. (2-2) [4-1, 4-2]. Modifications accounting for these effects are summarized in Appendix B and discussed in greater detail in References [4-3] - [4-6]. The solutions reported in this section are calculated using these modified forms of J-integral; this point should be kept in mind when applying the material given here to specific problems.

The solutions cover a broad range of values for inside radius-to-wall thickness ratio R_i/b, crack length-to-wall thickness ratio a/b and strain hardening exponent n. The results reported here were obtained using the incompressible finite element code INFEM [4-7 - 4-10]. Solution details, such as the finite element meshes employed, are described in Reference [4-10]. Since elastic solutions for the present crack geometries are not available in the literature for all the values of R_i/b and a/b examined, the elastic results obtained from INFEM are also compiled here. These solutions were compared with literature solutions when available; in some cases comparisons were made with alternate finite element calculations from the ADINA computer code [4-10]. Accuracy of the elastic solutions was thus assessed through these comparisons and other consistency checks obtained in Reference [4-10].

For given material properties following the Ramberg-Osgood stress-strain law and structure dimensions R_i/b and a/b, the elastic and fully plastic solutions can readily be obtained by using the relevant formulae, and tables given in this section. (For convenience' sake the solutions tabulated in the present section are plotted against $1/n$ in Appendix C.) Elastic-plastic solutions can then be obtained by superposing the elastic and fully plastic contributions according to the estimation procedure, Eq. (2-30). Other representations of uniaxial stress-strain properties can be utilized and estimation formulae for a number of others are given in Appendix A. Various illustrative examples are discussed in Section 6 and in Reference [4-10]. Using the material presented here, stability and failure assessment diagrams can be easily constructed as described with several examples in Sections 7 and 8.

4.2 INTERNALLY PRESSURIZED CYLINDER WITH AN INTERNAL AXIAL CRACK

4.2.1 Elastic Solutions

Fig. 4-1 describes a long, thin-walled cylinder containing an internal radial axial crack of length a, with internal radius R_i and outer radius R_o. The crack front is parallel to the axis of the cylinder. A uniform pressure p acts on the inside of the cylinder and on the crack face. The wall thickness is denoted by $b = R_o - R_i$, and $c = b - a$ is the uncracked ligament. The configuration is assumed to be in plane strain. In the linear elastic range, the stress intensity factor K_I, the J-integral and the mouth opening displacement δ can be written as

$$K_I = \frac{2p\, R_o^2 \sqrt{\pi a}}{R_o^2 - R_i^2}\, F(a/b,\ R_i/R_o) \tag{4-1}$$

$$\delta = \frac{8p\, R_o^2\, a}{(R_o^2 - R_i^2)E'}\, V_1(a/b,\ R_i/R_o) \tag{4-2}$$

$$J = K_1^2/E' \tag{4-3}$$

where $E' = E/(1 - \nu^2)$. It is noted that the dimensionless functions F and V_1 depend upon two ratios, a/b and R_i/R_o.

Elastic analyses of the above problem were carried out using the finite element code INFEM. The pertinent details are presented in Reference [4-10]. The solutions for F and V_1 thus obtained are catalogued in Table 4-1. Three values of the wall thickness-to-inside radius ratio b/R_i are considered, namely 1/5, 1/10 and 1/20. For each b/R_i, the crack length-to-wall thickness ratio a/b is taken to be 1/8, 1/4, 1/2 and 3/4.

For some combinations of a/b and b/R_i the results for K_I and therefore F have also been reported by Bowie and Freese [4-11], Rooke and Cartwright [4-12], Buchalet and Bamford [4-13] and Labbens, et al. [4-14]. The results given here were compared with these solutions at the available reference points. As discussed in Reference [4-10] the numerical error in the presented solutions is assessed to be in the range of 1% - 4%.

4.2.2 Fully Plastic Solutions

The fully plastic solutions for J and δ are expressed as*

$$J = \alpha\, \sigma_o\, \varepsilon_o\, c(a/b)\, h_1(a/b,\ n;\ R_i/R_o)(p/p_o)^{n+1} \tag{4-4}$$

$$\delta = \alpha\, \varepsilon_o\, a\, h_2(a/b,\ n;\ R_i/R_o)(p/p_o)^{n} \tag{4-5}$$

where p_o is the limit pressure for this geometry in the perfectly plastic case ($n = \infty$). A lower bound value for this is given by

$$p_o = \frac{2}{\sqrt{3}}\, \frac{c\, \sigma_o}{R_c} \tag{4-6}$$

where $R_c = R_i + a$ is the radial distance from the centerline to the crack tip.

The dimensionless functions h_1 and h_2 in Eqs. (4-4) and (4-5) are functions of a/b and n with R_i/R_o as the parameter. The computed h functions are catalogued for a wide range of a/b and n values in Tables 4-2 - 4-4 for b/R_i = 1/5, 1/10 and 1/20, respectively. Plots of h_1 and h_2 versus $1/n$ are shown in Appendix C. These figures are useful for interpolating and extrapolating the values of h for

---

* Solutions for the CTOD δ_t are not catalogued here since the relationship between J and δ_t is not completely established in the presence of crack face loading.

required value.

4.2.3 Elastic-Plastic Estimation Formulae

The elastic and fully plastic solutions can be readily incorporated into the estimation procedure. For a material governed by Ramberg-Osgood stress-strain representation in uniaxial tension, this procedure gives the following expressions for J and δ:

$$J = f_1(a_e;\ R_i/R_o)\ \frac{p^2}{E'} + \alpha\ \sigma_o\ \varepsilon_o\ c(a/b)\ h_1(a/b,\ n;\ R_i/R_o)(p/p_o)^{n+1} \tag{4-7}$$

$$\delta = f_2(a_e;\ R_i/R_o)\ \frac{p}{E'} + \alpha\ \varepsilon_o\ a\ h_2(a/b,\ n;\ R_i/R_o)(p/p_o)^{n} \tag{4-8}$$

a_e is the effective crack length defined by Eqs. (2-31) - (2-33). The functions f_1 and f_2 in Eqs. (4-7) and (4-8) are related to F and V_1 defined in Eqs. (4-1) and (4-2) in the following manner:

$$f_1(a/b,\ R_i/R_o) = 4\pi a \left[\frac{R_o^2}{R_o^2 - R_i^2}\right]^2 F^2(a/b,\ R_i/R_o) \tag{4-9}$$

$$F_2(a/b,\ R_i/R_o) = 8a \left[\frac{R_o^2}{R_o^2 - R_i^2}\right] V_1(a/b,\ R_i/R_o) \tag{4-10}$$

Results obtained using the above elastic-plastic formulae (Eqs. (4-7) and (4-8)) compare favorably with detailed finite element elastic-plastic computations of the J-integral for an axially cracked cylinder. The comparison and further applications of the above are given in Section 6 and Reference [4-10].

4.3 CYLINDER WITH AN INTERNAL CIRCUMFERENTIAL CRACK UNDER REMOTE TENSION

4.3.1 Elastic Solutions

Consider a cylinder with inner radius R_i, outer radius R_o, wall thickness $b = R_o - R_i$ and length 2L, containing an internal axisymmetric part-through crack of length a (Fig. 4-2). $b = R_o - R_i$ denotes the wall thickness and $c = b - a$ the uncracked ligament. The cylinder is subjected to a uniform tensile stress field

at its ends given by

$$\sigma_{zz}(r,\ \pm L) = \sigma^\infty = P/\pi(R_o^2 - R_i^2) \tag{4-11}$$

where P is the total tensile load carried by the cylinder. In the linear elastic case, the fracture parameters K_I, δ and Δ_c are given by

$$K_I = \sigma^\infty \sqrt{\pi a}\ F(a/b,\ R_i/R_o) \tag{4-12}$$

$$\delta = \frac{4\sigma^\infty a}{E'}\ V_1(a/b,\ R_i/R_o) \tag{4-13}$$

$$\Delta_c = \frac{4\sigma^\infty a}{E'}\ V_2(a/b,\ R_i/R_o) \tag{4-14}$$

where $E' = E/(1 - \nu^2)$ and F, V_1, V_2 are dimensionless functions of a/b and R_i/R_o. Sneddon and Lowengrub [4-15] and Rice [4-2] have shown that the singular stress and strain fields in the crack-tip vicinity of an axisymmetric crack correspond to those in plane strain. Consequently, J is related to K_I via the plane strain relationship, namely

$$J = (1 - \nu^2)\ K_I^2/E \tag{4-15}$$

The finite element code INFEM with axisymmetric elements was employed to perform the analysis of this problem. The mesh used and other computational aspects of the analysis are described in [4-10]. Similar to the axially cracked cylinder of the previous section, three values of the wall thickness-to-inside radius ratio b/R_i were chosen, namely 1/5, 1/10 and 1/20. For each b/R_i, the crack length-to-wall thickness ratio a/b is taken to be 1/8, 1/4, 1/2 and 3/4. The calculated values F, V_1 and V_2 are presented in Table 4-5.

The accuracy of the above solution for F can be assessed by comparing with a solution by Buchalet and Bamford [4-13] for $b/R_i = 1/10$. This is carried out in Reference [4-10]. For other values of b/R_i, the accuracy was assessed by a comparison with independent finite element calculations using the computer code ADINA. As described in Reference [4-10] the error in the above results for F is estimated to be less than 1% - 4%.

4.3.2 Fully Plastic Solutions

The fully plastic solutions are given by

$$J = \alpha\, \sigma_o\, \varepsilon_o\, c(a/b)\, h_1(a/b,\ n;\ R_i/R_o)(P/P_o)^{n+1} \tag{4-16}$$

$$\delta = \alpha\, \varepsilon_o\, a\, h_2(a/b,\ n;\ R_i/R_o)(P/P_o)^{n} \tag{4-17}$$

$$\Delta_c = \alpha\, \varepsilon_o\, a\, h_3(a/b,\ n;\ R_i/R_o)(P/P_o)^{n} \tag{4-18}$$

$$\delta_t = \alpha\, \varepsilon_o\, c(a/b)\, h_4(a/b,\ n;\ R_i/R_o)(P/P_o)^{n+1} \tag{4-19}$$

where P_o is the limit load for perfectly plastic material ($n = \infty$). A lower bound expression for this is

$$P_o = \frac{2}{\sqrt{3}}\, \sigma_o\, \pi(R_o^2 - R_c^2) \tag{4-20}$$

Here $R_c = R_i + a$ is the radial distance from the centerline to the crack tip.

In Eq. (4-17), $\delta = U_z(R_i,\ 0^+) - U_z(R_i,\ 0^-)$ is the mouth opening displacement. δ_t in Eq. (4-19) is the crack-tip opening displacement as defined by Eq. (2-4). Δ_c in Eq. (4-18) is the load-point displacement due to the crack and is given by

$$\Delta_c = \Delta - \Delta_{nc} \tag{4-21}$$

where Δ_{nc} is the load-point displacement in the absence of crack. It is written as

$$\Delta_{nc} = 2\alpha\, \varepsilon_o\, L\left[P/\pi(R_o^2 - R_i^2)\sigma_o\right]^n \tag{4-22}$$

The functions h_1, h_2, h_3 and h_4 depend upon a/b, n and R_i/R_o. These were computed using INFEM; details of the analysis are given in Reference [4-10].

The calculated h functions are presented in Tables 4-6 – 4-8 for $b/R_i = 1/5$, 1/10 and 1/20, respectively. h_4 is obtained from h_1 through the relationship

$$h_4 = d_n\, h_1 \tag{4-23}$$

where d_n corresponds to the plane strain value as given in Fig. 3-1. Plots of h_1, h_2 and h_3 versus 1/n as the parameter are given in Appendix C.

4.3.3 Elastic-Plastic Estimation Formulae

The elastic-plastic formulae obtained through the estimation procedure are as follows:

$$J = f_1(a_e,\ R_i/R_o)\, \frac{P^2}{E'} + \alpha\, \sigma_o\, \varepsilon_o\, c(a/b)\, h_1(a/b,\ n;\ R_i/R_o)(P/P_o)^{n+1} \tag{4-24}$$

$$\delta = f_2(a_e,\ R_i/R_o)\, \frac{P}{E'} + \alpha\, \varepsilon_o\, a\, h_2(a/b,\ n;\ R_i/R_o)(P/P_o)^{n} \tag{4-25}$$

$$\Delta_c = f_3(a_e,\ R_i/R_o)\, \frac{P}{E'} + \alpha\, \varepsilon_o\, a\, h_3(a/b,\ n;\ R_i/R_o)(P/P_o)^{n} \tag{4-26}$$

In the above, a_e is the effective crack length as defined by Eqs. (2-31) – (2-33). The functions f_1, f_3 and f_3 in Eqs. (4-24) – (4-26) are obtained from F, V_1 and V_2 as follows:

$$f_1(a/b,\ R_i/R_o) = \frac{a\, F^2(a/b,\ R_i/R_o)}{\pi(R_o^2 - R_i^2)^2} \tag{4-27}$$

$$f_2(a/b,\ R_i/R_o) = \frac{4a}{\pi(R_o^2 - R_i^2)}\, V_1(a/b,\ R_i/R_o) \tag{4-28}$$

$$f_3(a/b,\ R_i/R_o) = \frac{4a}{\pi(R_o^2 - R_i^2)}\, V_2(a/b,\ R_i/R_o) \tag{4-29}$$

Examples illustrating the application and verification of the above elastic-plastic formulae are described in Section 6 and Reference [4-10].

4.4 REFERENCES

[4-1] J. R. Rice, "A Path Independent Integral and the Approximate Analysis of Strain Concentration by Notches and Cracks," Journal of Applied Mechanics, Vol. 35, 1968, pp. 379-386.

[4-2] J. R. Rice, "Mathematical Analysis in the Mechanics of Fracture," in Fracture (Ed. by H. Liebowitz), 1968, Vol. II, Academic Press, New York, pp. 191-311.

[4-3] M. A. Astiz, M. Elices, and V. Sanchez Galvez, "On Energy Release Rates in Axisymmetric Problems," in Fracture 1977 (Ed. by D. M. R. Taplin), ICF4, Waterloo, Canada, June 19-24, 1977, pp. 395-400.

[4-4] H. Bergkvist and G.-L. Lan Huong, "J-Integral Related Quantities in Axisymmetric Cases," International Journal of Fracture, Vol. 13, 1977, pp. 556-558.

[4-5] H. Bergkvist and G.-L. Lan Huong, "Energy Release Rates in Cases of Axial Symmetry," in Fracture Mechanics and Technology (Ed. by G. C. Sih and C. L. Chow), International Conference on Fracture Mechanics and Technology, Hong Kong, March 21-25, 1977, pp. 1053-1066.

[4-6] A. Karlsson and J. Backlund, "J-Integral at loaded Crack Surfaces," International Journal of Fracture, Vol. 14, 1978, pp. R311-R314.

[4-7] A. Needleman and C. F. Shih, "Finite Element Method for Plane Strain Deformations of Incompressible Solids," Computer Methods in Applied Mechanics and Engineering, 1978, pp. 223-240.

[4-8] C. F. Shih and V. Kumar, "Estimation Technique for the Prediction of Elastic-Plastic Fracture of Structural Components of Nuclear Systems," 1st Semiannual Report to EPRI, Contract No. RP1237-1, General Electric Company, Schenectady, New York, January 31, 1978.

[4-9] V. Kumar, M. D. German, and C. F. Shih, "Estimation Techniques for the Prediction of Elastic-Plastic Fracture of Structural Components of Nuclear Systems," Combined 2nd and 3rd Semiannual Report to EPRI, Contract No. RP1237-1, General Electric Company, Schenectady, New York, February 1, 1979 - January 31, 1980.

[4-10] V. Kumar, H. G. deLorenzi, W. R. Andrews, C. F. Shih, M. D. German, and D. F. Mowbray, "Estimation Techniques for the Prediction of Elastic-Plastic Fracture of Structural Components of Nuclear Systems," 4th Semiannual Report to EPRI, Contract No. RP1237-1, General Electric Company, Schenectady, New York, July 1, 1980 - January 31, 1981.

[4-11] O. L. Bowie and C. E. Freese, "Elastic Analysis for a Radial Crack in a Circular Ring," Engineering Fracture Mechanics, Vol. 4, 1972, pp. 315-321.

[4-12] D. P. Rooke and Cartwright, Compendium of Stress Intensity Factors, Her Majesty's Stationary Office, London, 1976.

[4-13] C. B. Buchalet and W. H. Bamford, "Stress Intensity Factor Solutions for Continuous Surface Flaws in Reactor Pressure Vessels," in Mechanics of Crack Growth, ASTM Special Technical Publication 590, 1976, pp. 385-402.

[4-14] R. Labbens, A. Pellissier-Tanon, and J. Heliot, "Practical Method for Calculating Stress-Intensity Factors Through Weight Function," in Mechanics of Crack Growth, ASTM Special Technical Publication 590, 1976, pp. 368-384.

[4-15] I. N. Sneddon and M. Lowengrub, Crack Problems in Classical Theory of Elasticity, John Wiley and Sons, New York, 1969.

Table 4-1

F and V_1 for an axially cracked cylinder under internal pressure.

		a/b = 1/8	a/b = 1/4	a/b = 1/2	a/b = 3/4
$b/R_i = 1/5$	F	1.19	1.38	2.10	3.30
	V_1	1.51	1.83	3.44	7.50
$b/R_i = 1/10$	F	1.20	1.44	2.36	4.23
	V_1	1.54	1.91	3.96	10.4
$b/R_i = 1/20$	F	1.20	1.45	2.51	5.25
	V_1	1.54	1.92	4.23	13.5

Table 4-2

h_1 and h_2 for an axially cracked cylinder under internal pressure with $b/R_i = 1/5$.

		n = 1	n = 2	n = 3	n = 5	n = 7	n = 10
a/b = 1/8	h_1	6.32	7.93	9.32	11.5	13.12	14.94
	h_2	5.83	7.01	7.96	9.49	10.67	11.96
a/b = 1/4	h_1	7.00	8.34	9.03	9.59	9.71	9.45
	h_2	5.92	8.72	7.07	7.26	7.14	6.71
a/b = 1/2	h_1	9.79	10.37	9.07	5.61	3.52	2.11
	h_2	7.05	6.97	6.01	3.70	2.28	1.25
a/b = 3/4	h_1	11.00	5.54	2.84	1.24	0.83	0.493
	h_2	7.35	3.86	1.86	0.556	0.261	0.129

Table 4-3

h_1 and h_2 for an axially cracked cylinder under internal pressure with $b/R_i = 1/10$.

		n = 1	n = 2	n = 3	n = 5	n = 7	n = 10
a/b = 1/8	h_1	5.22	6.64	7.59	8.76	9.34	9.55
	h_2	5.31	6.25	6.88	7.65	8.02	8.09
a/b = 1/4	h_1	6.16	7.49	7.96	8.08	7.78	6.98
	h_2	5.56	6.31	6.52	6.40	6.01	5.27
a/b = 1/2	h_1	10.5	11.6	10.7	6.47	3.95	2.27
	h_2	7.48	7.72	7.01	4.29	2.58	1.37
a/b = 3/4	h_1	16.1	8.19	3.87	1.46	1.05	0.787
	h_2	9.57	5.40	2.57	0.706	0.370	0.232

Table 4-4

h_1 and h_2 for an axially cracked cylinder under internal pressure with $b/R_i = 1/20$.

		n = 1	n = 2	n = 3	n = 5	n = 7	n = 10
a/b = 1/8	h_1	4.50	5.79	6.62	7.65	8.07	7.75
	h_2	4.96	5.71	6.20	6.82	7.02	6.66
a/b = 1/4	h_1	5.57	6.91	7.37	7.47	7.21	6.53
	h_2	5.29	5.98	6.16	6.01	5.63	4.93
a/b = 1/2	h_1	10.8	12.8	12.8	8.16	4.88	2.62
	h_2	7.66	8.33	8.13	5.33	3.20	1.65
a/b = 3/4	h_1	23.1	13.1	5.87	1.90	1.23	0.883
	h_2	12.1	7.88	3.84	1.01	0.454	0.240

Table 4-5

F, V_1 and V_2 for a circumferentially cracked cylinder in tension.

		a/b = 1/8	a/b = 1/4	a/b = 1/2	a/b = 3/4
$b/R_i = 1/5$	F	1.16	1.26	1.61	2.15
	V_1	1.49	1.67	2.43	3.76
	V_2	0.117	0.255	0.743	1.67
$b/R_i = 1/10$	F	1.19	1.32	1.82	2.49
	V_1	1.55	1.76	2.84	4.72
	V_2	0.180	0.290	0.885	2.09
$b/R_i = 1/20$	F	1.22	1.36	2.03	2.89
	V_1	1.59	1.81	3.26	5.99
	V_2	0.220	0.315	1.04	2.74

Table 4-6

h_1, h_2 and h_3 for a circumferentially cracked cylinder in tension with $b/R_i = 1/5$.

		n = 1	n = 2	n = 3	n = 5	n = 7	n = 10
a/b = 1/8	h_1	3.78	5.00	5.94	7.54	8.99	11.1
	h_2	4.56	5.55	6.37	7.79	9.10	11.0
	h_3	0.369	0.700	1.07	1.96	3.04	4.94
a/b = 1/4	h_1	3.88	4.95	5.64	6.49	6.94	7.22
	h_2	4.40	5.12	5.57	6.07	6.28	6.30
	h_3	0.673	1.25	1.79	2.79	3.61	4.52
a/b = 1/2	h_1	4.40	4.78	4.59	3.79	3.07	2.34
	h_2	4.36	4.30	3.91	3.00	2.26	1.55
	h_3	1.33	1.93	2.21	2.23	1.94	1.46
a/b = 3/4	h_1	4.12	3.03	2.23	1.546	1.30	1.11
	h_2	3.46	2.19	1.36	0.638	0.436	0.325
	h_3	1.54	1.39	1.04	0.686	0.508	0.366

Table 4-7

h_1, h_2 and h_3 for a circumferentially cracked cylinder in tension with $b/R_i = 1/10$.

		n = 1	n = 2	n = 3	n = 5	n = 7	n = 10
a/b = 1/8	h_1	4.00	5.13	6.09	7.69	9.09	11.1
	h_2	4.71	5.63	6.45	7.85	9.09	10.9
	h_3	0.548	0.733	1.13	2.07	3.16	5.07
a/b = 1/4	h_1	4.17	5.35	6.09	6.93	7.30	7.41
	h_2	4.58	5.36	5.84	6.31	6.44	6.31
	h_3	0.757	1.35	1.93	2.96	3.78	4.60
a/b = 1/2	h_1	5.40	5.90	5.63	4.51	3.49	2.47
	h_2	4.99	5.01	4.59	3.48	2.56	1.67
	h_3	1.555	2.26	2.59	2.57	2.18	1.56
a/b = 3/4	h_1	5.18	3.78	2.57	1.59	1.31	1.10
	h_2	4.22	2.79	1.67	0.725	0.48	0.300
	h_3	1.86	1.73	1.26	0.775	0.561	0.360

Table 4-8

h_1, h_2 and h_3 for a circumferentially cracked cylinder in tension with $b/R_i = 1/20$.

		n = 1	n = 2	n = 3	n = 5	n = 7	n = 10
a/b = 1/8	h_1	4.04	5.23	6.22	7.82	9.19	11.1
	h_2	4.82	5.69	6.52	7.90	9.11	10.8
	h_3	0.680	0.759	1.17	2.13	3.23	5.12
a/b = 1/4	h_1	4.38	5.68	6.45	7.29	7.62	7.65
	h_2	4.71	5.56	6.05	6.51	6.59	6.39
	h_3	0.818	1.43	2.03	3.10	3.91	4.69
a/b = 1/2	h_1	6.55	7.17	6.89	5.46	4.13	2.77
	h_2	5.67	5.77	5.36	4.08	2.97	1.88
	h_3	1.80	2.59	2.99	2.98	2.50	1.74
a/b = 3/4	h_1	6.64	4.87	3.08	1.68	1.30	1.07
	h_2	5.18	3.57	2.07	0.808	0.472	0.316
	h_3	2.36	2.18	1.53	0.772	0.494	0.330

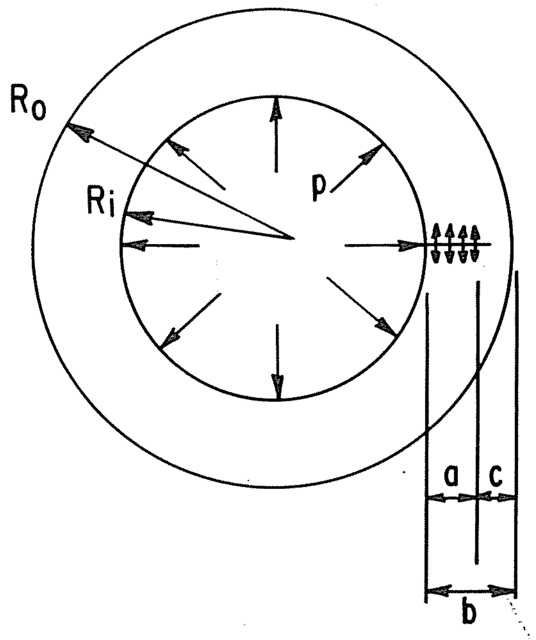

Figure 4-1. Axially cracked cylinder under internal pressure.

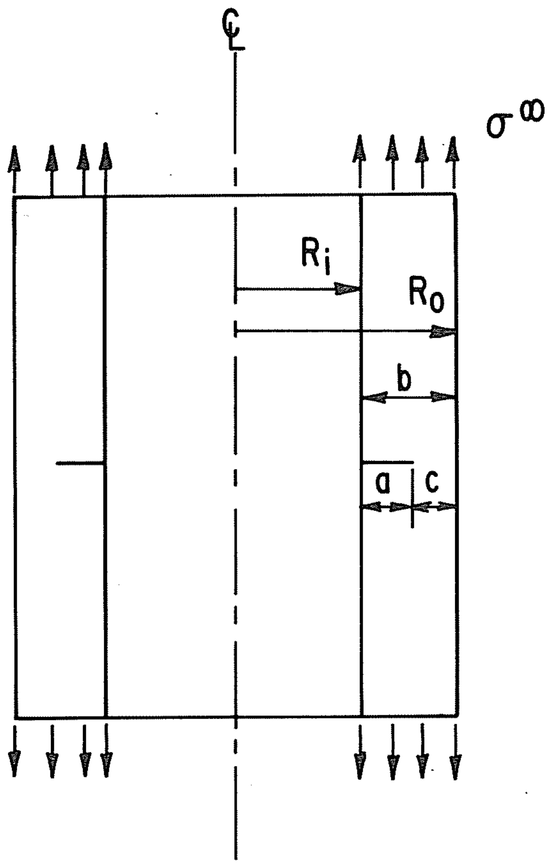

Figure 4-2. Circumferentially cracked cylinder in tension.

SECTION 5
TWO-DIMENSIONAL FLAT PLATE MODEL OF A NOZZLE CORNER FLAW

Section 5

TWO-DIMENSIONAL FLAT PLATE MODEL OF A NOZZLE CORNER FLAW

5.1 INTRODUCTION

In this section fully plastic solutions are presented for a nozzle corner flaw modeled by a flat plate with a central hole and a single radial crack. This model is due to Yukawa [5-1] and is illustrated in Figs. 5-1 - 5-2. The analysis assumes plane stress conditions. The plate is subjected to uniform stress distributions of different magnitude in the x and y directions. This crack configuration may be employed for two-dimensional modeling of a nozzle corner flaw if the hoop and axial stresses are simulated by imposing appropriate boundary conditions on the plate. In many situations, especially for relatively thin reactor vessels, the axial stress is typically half the hoop stress; therefore, in the present study applied stress in the x direction was taken to be one-half the y direction stress.

It is recognized that the nozzle corner flaw problem is truly three-dimensional in nature. However, a two-dimensional model such as the one analyzed here may be utilized for preliminary investigations, especially when three-dimensional elastic-plastic calculations are extremely complicated and not available to date.

5.2 FULLY PLASTIC SOLUTIONS

The plate is of width 2b containing a hole of radius R and radial crack of length a (Fig. 5-2). The loading consists of a uniform stress distribution of magnitude σ^∞ in the y direction and $\lambda\,\sigma^\infty$ in the x direction. The fully plastic solutions are given by the following expressions:

$$J = \alpha\,\sigma_o\,\varepsilon_o\,a\,h_1(a/R,\ n;\ \lambda)(\sigma^\infty/\sigma_L^\infty)^{n+1} \tag{5-1}$$

$$\delta = \alpha\,\varepsilon_o\,a\,h_2(a/R,\ n;\ \lambda)(\sigma^\infty/\sigma_L^\infty)^{n} \tag{5-2}$$

$$\delta_t = \alpha\ \varepsilon_o\ a\ h_3(a/R,\ n;\ \lambda)(\sigma^\infty/\sigma_L^\infty)^n \tag{5-3}$$

where $\delta = U_y(a,\ 0^+) - U_y(a,\ 0^-)$ is the crack mouth opening displacement at the hole. δ_t denotes the crack tip opening displacement as before. σ_L^∞ and $\lambda\ \sigma_L^\infty$ are the stresses corresponding to the limit load situation. From a lower bound analysis σ_L^∞ is given by

$$\sigma_L^\infty = \frac{(2b - 2R - a)\ \sigma_o\ \sqrt{3}}{4b} \tag{5-4}$$

For a given λ, the h functions in Eqs. (5-1) - (5-3) are functions of a/R and n only. In the present analysis λ was taken to be 0.5 and plane stress assumed.

The solutions in this example were obtained employing the ADINA [5-2] computer code. In the elastic case (n = 1), results presented here were found to agree within 0.5% - 3% in K_I with those given in Reference [5-3]. Finite element meshes and other solution details can be found in Reference [5-4].

The functions h_1 and h_2 are catalogued for several values of a/R and n in Table 5-1. Using the relationship between J and δ_t discussed in Section 2, h_3 can be calculated from h_1 as follows:

$$h_3 = d_n\ h_1 \tag{5-5}$$

where d_n is obtained from Fig. 3-2.

5.3 ELASTIC-PLASTIC ESTIMATION FORMULAE

In the linear elastic range, J and δ can be written as

$$J = \frac{\pi a}{E}\ F^2(a/R;\ \lambda)\sigma^{\infty 2} \tag{5-6}$$

$$\delta = \frac{a}{E}\ V_1(a/R;\ \lambda)\sigma^\infty \tag{5-7}$$

where the dimensionless function F is given in reference [5-3]. V_1 as a function of a/R for $\lambda = 0.5$ can be obtained from Table 5-2. For convenience, the above equations are rewritten in the form

$$J = f_1(a;\ \lambda)\ \frac{\sigma^{\infty 2}}{E} \tag{5-8}$$

$$\delta = f^2(a;\ \lambda)\ \frac{\sigma^\infty}{E} \tag{5-9}$$

where $f_1 = \pi\ a\ F^2$ and $f_2 = a\ V_1$.

By combining elastic terms given by Eqs. (5-8) - (5-9) and fully plastic solutions given by Eqs. (5-1) - (5-2), one obtains the following forms for elastic-plastic formulae:

$$J = f_1(a_e;\ \lambda)\ \frac{\sigma^{\infty 2}}{E} + \alpha\ \sigma_o\ \varepsilon_o\ a\ h_1\ (\tfrac{a}{b},\ n;\ \lambda)(\sigma^\infty/\sigma_L^\infty)^{n+1} \tag{5-10}$$

$$\delta = f_2(a_e;\ \gamma)\ \frac{\sigma^\infty}{E} + \alpha\ \varepsilon_o\ a\ h_2(\tfrac{a}{b},\ n;\ \lambda)(\sigma^\infty/\sigma_L^\infty)^n \tag{5-11}$$

where a_e is the adjusted crack length as defined by Eqs. (2-31) - (2-33).

5.4 REFERENCES

[5-1] PVRC Recommendations on Toughness Requirements for Ferritic Materials, WRC Bulletin No. 175, August 1975.

[5-2] H. G. deLorenzi, "3-D Elastic-Plastic Fracture Mechanics with ADINA," Journal of Computers and Structures, Special Issue, June 1981, to appear. Also General Electric Company TIS Report No. 80CRD242, November 1980.

[5-3] H. Tada, P. C. Paris, and G. R. Irwin, "The Stress Analysis of Cracks Handbook," Del Research Corporation, Hellertown, Pennsylvania, 1973.

[5-4] V. Kumar, H. G. deLorenzi, W. R. Andrews, C. F. Shih, M. D. German, and D. F. Mowbray, "Estimation Technique for the Prediction of Elastic-Plastic Fracture of Structural Components of Nuclear Systems," 4th Semi-annual Report to EPRI, Contract No. RP1237-1, General Electric Company, Schenectady, New York, July 1, 1980 - January 31, 1981.

Table 5-1

h_1 and h_2 for the two-dimensional model of nozzle corner flaw.

		n = 1	n = 2	n = 3	n = 5
a/R = 1/8	h_1	10.2	11.9	10.5	9.0
	h_2	9.50	10.8	10.1	8.80
a/R = 1/4	h_1	7.71	8.38	7.50	6.85
	h_2	8.30	8.73	7.59	6.74
a/R = 1/2	h_1	4.91	5.39	4.30	2.73
	h_2	6.51	6.17	4.94	3.01
a/R = 3/4	h_1	3.63	3.82	3.03	1.88
	h_2	5.48	4.84	3.80	2.23
a/R = 1	h_1	2.93	3.04	2.41	1.48
	h_2	4.78	4.06	3.14	1.80

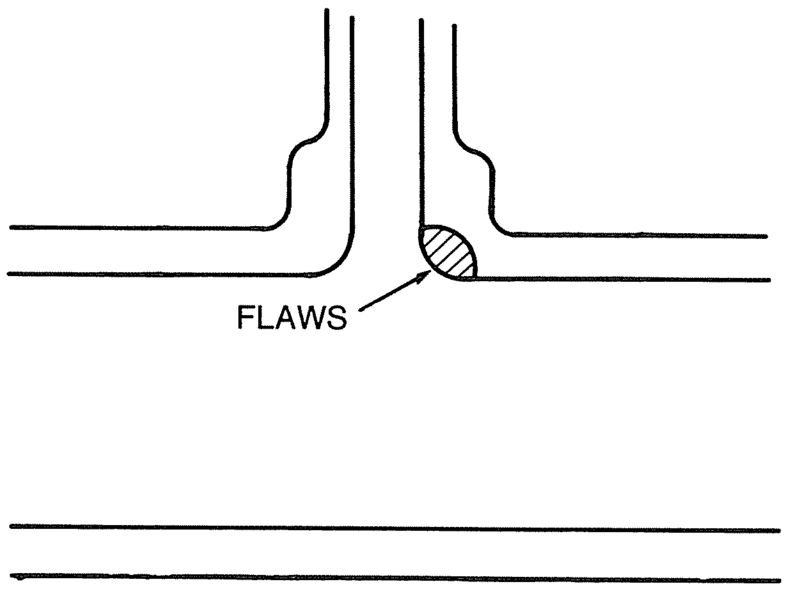

Figure 5-1. Schematic of a nozzle corner flaw.

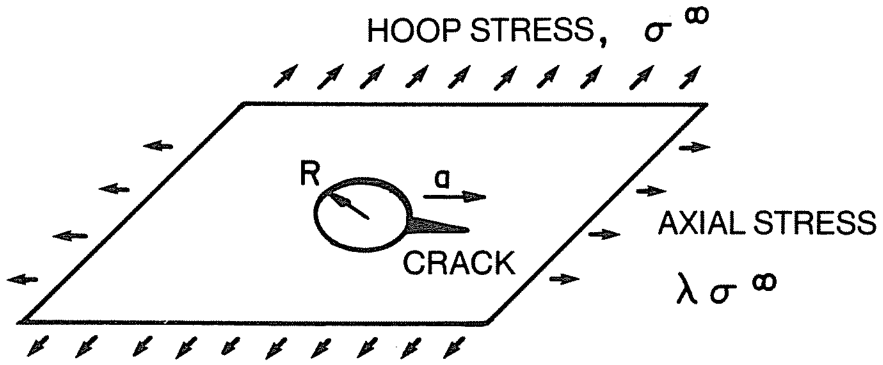

Figure 5-2. Two-dimensional flat plate model of a nozzle corner flaw.

SECTION 6

CRACK DRIVING FORCE DIAGRAM: APPLICATIONS AND VERIFICATION OF THE ENGINEERING APPROACH

SECTION 6
CRACK DRIVING FORCE DIAGRAM: APPLICATIONS AND
VERIFICATION OF THE ENGINEERING APPROACH

Section 6

CRACK DRIVING FORCE DIAGRAM: APPLICATIONS AND VERIFICATION OF THE ENGINEERING APPROACH

6.1 INTRODUCTION

As discussed in the earlier sections, the J-integral crack driving force for a given flawed body can be obtained by superposing the elastic and fully plastic solutions according to the estimation procedure. By comparing the crack driving force with the material resistance to crack growth, one can predict various quantities of interest associated with the fracture behavior. As indicated in Section 2, several different types of diagrams can be computed depending upon the specific application. In this section attention will be focused on the crack driving force diagram, which is basically a plot of the J-integral or the CTOD versus crack length and applied load (or displacement). In this section attention will be focused on the crack driving force diagram. Construction of the diagram and applications will be discussed in detail. In most cases, predicted results obtained from analyses using the diagram are compared with experimental data and/or detailed finite element calculations. Hence, the material presented serves to provide a verification of the engineering approach.

When the crack driving force diagram is used together with the material J-resistance (J_R) curve, a complete history of deformation and crack growth behavior is predicted. This includes a prediction of the load at crack initiation (i.e., onset of crack propagation), extent of stable growth prior to instability, load at instability, maximum load carrying capacity and load-displacement behavior. In many instances a complete analysis is not necessary, in which case one can use the estimation formulae to calculate specific quantities of interest. This point will also be addressed here in some detail.

The crack driving force diagram can also be used to estimate J_R curves given the load-displacement test record. This procedure will be explained and a comparison of predicted and experimental J_R curves is given.

It is important to note that conditions for instability of crack growth and the effect of system compliance discussed in Section 2 can be incorporated in crack driving force diagrams in a convenient manner. Examples of this will be presented here; it will be shown in the section to follow that results thus obtained are consistent with those from stability diagrams.

6.2 EXAMPLE CRACK DRIVING FORCE DIAGRAM FOR A COMPACT SPECIMEN

An example crack driving force diagram will be presented for a compact specimen of A533B steel. Typical input required for this analysis consists of material deformation properties in terms of the uniaxial stress-strain curve, specimen size, crack length and applied loading. When constructing a crack driving force diagram one is usually interested in a range of values for crack length, applied load and/or displacement, rather than specific values. For test specimens this range may be chosen on the basis of the test data being simulated; in other cases the ranges should be broad enough to encompass the crack growth and deformation behavior being predicted. This may come from past experience, intuition or other considerations. However, if no a priori knowledge is available, the trial and error procedure can be used to arrive at the range of interest.

The uniaxial stress-strain curve for A533B steel at 93°C (200°F) and its characterization by the Ramberg-Osgood law are given in Fig. 6-1. Values for E, ν and σ_o are taken to be 30 x 10^6 psi, 0.3 and 60 x 10^3 psi, respectively. The least squares curve fitting method yields values for α of 1.12 and n, 9.7.

The specimen size analyzed corresponds to the 4T (4 in. thick) ASTM standard compact specimen with a 25% side-groove (see Fig. 3-3). The objective in constructing the crack driving force diagram in this case is to simulate the load-displacement behavior of a test described in Reference [6-1] for specimen T-52. The initial crack length in this case is 4.615 in. (b = 8.0 in.). The ranges of values for a, P and Δ_L were selected on the basis of observed crack growth test data. Plane strain behavior is assumed in the analyses.

Elastic-plastic estimation formulae for a compact specimen were given earlier in Section 3.2 and are repeated below.

$$J = f_1(a_e)\,\frac{P^2}{E'} + \alpha\,\sigma_o\,\varepsilon_o\,c\,h_1(a/b,\,n)[P/P_o]^{n+1} \qquad (6\text{-}1)$$

$$\delta = f_2(a_e)\,\frac{P}{E'} + \alpha\,\varepsilon_o\,a\,h_2\,(a/b,\,n)[P/P_o]^{n} \qquad (6\text{-}2)$$

$$\Delta_L = f_3(a_e)\,\frac{P}{E'} + \alpha\,\varepsilon_o\,a\,h_3(a/b,\,n)[P/P_o]^{n}. \qquad (6\text{-}3)$$

For a given value of n, values of h_1, h_2 and h_3 are read from Table 3-1 for a range of a/b. On substituting the values of h in the above formulae, J, δ and Δ_L can easily be computed for the range of a and P of interest. These quantities provide the ingredients for the crack driving force diagram.

The diagram in the present case is expressed in terms of J vs. a. Such curves with P as the parameter are shown in Fig. 6-2. These curves are calculated directly from Eq. (6-1). The calculation of J versus a curves with Δ_L as the parameter is performed in a different manner. For a given Δ_L, Eq. (6-3) is solved numerically, by Newton's method for example, to obtain P corresponding to various values of a. From the a and P values the J-integral can then be computed directly from Eq. (6-1), thus yielding J versus a curves for a fixed Δ_L. Curves thus generated are shown in Fig. 6-3. Since the intent here is predict P-Δ_L behavior as the crack grows, it is convenient to combine the two families of curves into one diagram, as illustrated in Fig. 6.4. The solid lines indicate fixed load and the dashed lines, fixed Δ_L.

An experimentally determined J-resistance curve [6-1, 6-2] is superimposed on Figs. 6-2 - 6-4 at the initial crack length of 4.615 inches as indicated by the thicker solid line. Equilibrium of crack growth requires that the applied crack driving force in terms of J equals the material resistance to crack growth, J_R. Thus, a fixed load line (solid line) and fixed displacement line (dashed line) that intersect at a point on the J_R curve yields the respective values of P and Δ_L which are in equilibrium at that crack length. By examining for this condition at different points along the J_R curve, the complete load-displacement behavior is obtained for the range of deformation and crack growth occurring in the test.

Figure 6-5 shows the load-displacement behavior obtained by the foregoing procedure together with the experimental data and finite element calculations for the same configuration based on J_2 flow theory of plasticity. (Note that the load/unit thickness from the crack driving force diagram is multiplied by the net thickness, 3 in this case, to obtain the total load used in this figure.) The point corresponding to the onset of crack propagation (customarily termed crack initiation) is indicated. The agreement between all three sets of results is very good; in fact the estimated curve completely follows the trends of test measurements and the detailed finite element solution. Further details on the experimental data and finite element crack growth calculations are given in References [6-1] and [6-2].

It is noted from Figs. 6-2 - 6-4 that the response of this specimen under dead load (curves corresponding to P held constant) is markedly different from its behavior with displacement held fixed. The J-integral crack driving force increases with crack length when load is held constant and it decreases with crack length in the case of fixed displacement. However, for a sufficiently compliant loading system the crack driving force for fixed total displacement will increase with crack length; this feature will be illustrated later in another example.

Other information on crack growth behavior can also be obtained from these figures. For example, the load at the onset of crack growth is given by the intersection of the constant P curve with the J_R curve at the defined value of J_{Ic}. The maximum attainable load during crack growth is defined at the point of tangency of a constant P curve and the J_R curve. This is illustrated on Figs. 6-2 and 6-4.

In view of the condition defining instability, Eq. (2-19), the onset of instability and corresponding load is characterized by the point at which a constant total displacement curve becomes tangent to the J_R curve. It is evident immediately that the maximum load also gives the instability load for an infinitely compliant system (dead load for example), in which case constant load and total displacement curves coincide with each other. However, in the present example it is clear from either Fig. 6-3 or 6-4 that constant displacement curves have negative slope, whereas the J_R curve has positive slope. There is no constant displacement curve tangent to the J_R curve and therefore the instability condition cannot be met. Crack growth in this example will therefore be stable.

The amount of stable crack extension can be determined from the crack length. The deformation and crack growth behavior of configurations and different initial crack lengths can be predicted by simply sliding the J_R curve along the crack length axis.

Following the procedures described above, the load-displacement behavior of several other compact specimens have been determined as shown in Figs. 6-6 - 6-8. The material in each example is A533B steel and plane strain conditions were assumed. The initial crack length, amount of side-groove and other pertinent analysis details are indicated on the figures. Again comparisons of the predicted results are made with experimental data and/or finite element calculations. Close agreement is observed between results in all cases. Examples presented in this section and another example on plane stress are discussed in Reference [6-3].

6.3 INSTABILITY ANALYSIS USING THE CRACK DRIVING FORCE DIAGRAM

Stability of crack growth can be examined within the framework of the crack driving force diagram. This will be illustrated here with the example of the 4T, T-52 compact specimen previously discussed but now including test machine compliance.

Reviewing the previous discussion, the instability condition on the crack driving force diagram is characterized by the point of tangency between the J_R curve and a J versus crack length curve with the total displacement Δ_T held constant ($\Delta_T = \Delta + C_M P$). There are two limiting situations of applied loading: (1) the load controlled or dead load system (i.e., $C_M = \infty$) and, (2) the displacement controlled system ($C_M = 0$). Internal pressure on a flawed cylinder is an example of the dead load system and a test machine typically represents the latter example. The instability condition is sensitive to the actual compliance, and an analysis using the crack driving force diagram should employ the value of C_M corresponding to the actual crack configuration/applied loading system.

First consider the J-integral crack driving force diagram for the 4T compact specimen subjected to fixed grip loading as shown in Fig. 6-9a (i.e., $C_M = 0$, $\Delta_T = \Delta_L$; values of Δ_T are indicated on the figure). The material J-resistance curve is superposed on this diagram as indicated. Note that this figure is identical to Fig. 6-3 and is reproduced here for convenience of example. Crack growth will clearly be stable in this case since the driving force decreases with increase of crack length and the J_R curve rises with crack growth. That is, the instability condition, Eq. (2-19) is never met for this combination of crack configuration and imposed loading. One can readily observe this by sliding the J_R curve along the crack length axis to correspond to different initial crack sizes.

Figure 6-9b shows the crack driving force diagram for a soft loading system ($C_M = 3.3 \times 10^{-5}$ in./lb.) acting on the compact specimen. The driving force curves in this case correspond to Δ_T held fixed at the values indicated. For an initial crack length of 4.615 in., the diagram indicates that an unstable condition will develop after about 0.4 in. of stable growth. The instability point is clearly demonstrated on the figure. The value of J at this point is 12,000 in.-lb./in.^{2}, the corresponding critical load P_{cr} at instability can be determined from Eq. (6-1) by using this J and the associated crack length a = 4.615 in. + 0.4 inch. In this case P_{cr} = 42 kips/unit thickness.

The case of a dead load system ($C_M = \infty$) is illustrated in Fig. 6-9c. It is noted that constant total displacement curves in this situation are identical to constant load curves as shown. It is easily seen from this diagram that a crack with initial length of 4.615 in. will grow about 0.12 in. before instability occurs at an applied load of about 47 kips/unit thickness and applied J of about 6,000 in.-lb./in.^{2}. The corresponding tearing modulus is given by the slope of the J_R curve at the instability point. As stated earlier, the instability load for a dead load situation is also the maximum load carrying capacity of the structure.

The above examples illustrate that the extent of stable crack growth and the instability load are strongly dependent on the loading system and the material properties. The amount of stable growth decreases with increasing compliance; the values of J, T_J and applied load also depend upon the compliance of the loading system. The crack driving force diagram is in essence a graphical solution to crack growth stability as posed by Eq. (2-19). In this approach the material strain-hardening properties and the system compliance are implicitly accounted for in the crack driving force term. Furthermore, the extent of stable growth prior to instability, the value of J (and T_J) at instability and the load carrying capacity of the configuration at various stages of growth are explicitly given by the graphical solution.

In some applications, it is convenient to explicitly plot tearing modulus T_J versus various parameters such as J, crack length or applied load. This will be discussed in detail in Section 7.

6.4 CRACK DRIVING FORCE DIAGRAM FOR A CIRCUMFERENTIALLY CRACKED CYLINDER IN TENSION

This example will consider the crack growth and stability behavior of the circumferentially cracked cylinder under remote tension shown schematically in Fig. 4-2. The material properties chosen correspond to 304 stainless steel. The Ramberg-Osgood law is used to characterize the uniaxial stress-strain data as shown in Fig. 6-10. A least squares fit of the experimental data gives the relevant material parameters as $\alpha = 1.69$ and $n = 5.42$. Values of E, ν and σ_o (yield stress) are taken to be 30×10^6 psi, 0.3 and 30×10^3 psi, respectively. The material J_R curve for 304 stainless steel given in Reference [6-14] is utilized in the present analysis.

Geometrical dimensions of the cylinder are taken to be as follows: Inside radius R_i = 90 in., outside radius R_o = 99 in., wall thickness $b = R_o - R_i$ = 9 in., and length 2L = 180 inches. The initial crack size a_o is assumed to be 2.25 in., which corresponds to $a_o/b = 1/4$. Although these dimensions are rather unrealistic for 304 SS, it is not of great concern since the objective here is only to illustrate the methodology.

Following the procedure described in Section 6.2 and using the relevant elastic-plastic estimation formulae (Eqs. 4-24 - 4-26) and tables from Section 4, the J-integral crack driving force diagram is constructed as shown in Fig. 6-11. The solid lines indicate the variation of J with crack length for applied stress held fixed and the dashed lines for displacement held constant. The material J_R curve is superposed at the initial crack length of 2.25 inch. Values of load and displacement associated with various points on the J_R curve yield the load displacement behavior during crack growth. Other quantities of interest such as maximum load, values of load at crack initiation and instability and the extent of stable growth are predicted in the same manner as in the compact specimen example, Section 6.2. Also, sliding the J_R curve along the crack length axis will yield the crack growth and deformation behavior corresponding to different initial crack sizes.

The predicted results for applied stress versus remote displacement are illustrated in Fig. 6-12. Load at the onset of crack propagation is clearly indicated, and the instability phenomenon is denoted by a break of the curve at its terminal point. It is noted that in this case load at instability coincides with the maximum load. This is consistent with discussion in Section 6.3 because constant load and constant displacement in Fig. 6-11 are close to each other.

Fig. 6-13 shows the crack driving force diagram plotted in an alternate form of J-integral versus applied load with crack depth, a/b, as the parameter. Such curves are often convenient when making instability predictions from stability diagrams; this will be discussed further in Section 7. For a/b = 1/4, the engineering approach results are also compared with finite element computations based on both the flow and deformation theories of plasticity. Agreement between results is excellent. Similar agreement between predicted and finite element results is also observed for the other fracture parameters, namely mouth opening displacement δ and load-point displacement Δ. These are shown in Figs. 6-14 and 6-15, respectively.

6.5 CRACK DRIVING FORCE DIAGRAM FOR AN AXIALLY CRACKED CYLINDER UNDER INTERNAL PRESSURE

This example considers the problem of an axial crack in an internally pressurized cylinder, examined as shown in Fig. 5-1. The analysis is for A533B steel. The stress-strain properties (E, ν, σ_o, α and n) and J_R-curve are the same as those used in Section 6.2. The selected dimensions of the cylinder correspond to the size of a typical reactor pressure vessel and are as follows: Inside radius R_i = 90 in., external radius R_o = 99 in., wall thickness b = $R_o - R_i$ = 9 inches. The initial crack length a_o is taken to be 2.25 in. so that $a_o/b = 1/4$. It is assumed that the cylinder is sufficiently long that plane strain conditions are applicable.

The relevant elastic-plastic estimation formulae are given by Eqs. (4-7) and (4-8). Using these equations in conjunction with elastic and fully plastic solutions catalogued in Section 4.2, a J-integral driving force diagram is generated as shown in Fig. 6-16. The procedural details are similar to those of the examples discussed earlier. The diagram plots J versus crack length with internal pressure p as the parameter. The J_R curve is superimposed on this diagram at the initial crack length of 2.25 inch. The instability pressure is determined from the constant pressure line which is tangent to the J_R curve. The extent of stable growth is calculated by subtracting the initial crack length from the crack length associated with the instability point. Since internal pressure in the cylinder acts as a dead load (i.e., $C_M = \infty$), the instability pressure also

gives the maximum load carrying capacity. Sliding the J_R curve along the crack length axis allows straightforward predictions of structural response corresponding to different initial crack sizes.

Figure 6-17 shows a recasting of the crack driving force diagram on J-integral versus internal pressure coordinates, with a/b varying. For a/b = 1/4, results obtained from finite element calculations (based on deformation theory of plasticity) are compared with the engineering approach predictions. Observed discrepancy between the two solutions at higher values of pressure is due to the fact that the mesh employed in finite element calculations was not the most appropriate one to model this problem. This point is elaborated upon in Reference [6-7]. In any case, the two results do exhibit a consistent trend without any serious concern.

6.6 FURTHER APPLICATIONS OF THE ENGINEERING APPROACH

6.6.1 Prediction of Load-Displacement Behavior

As discussed in the preceeding material, a crack driving force diagram can be used together with the J_R curve to determine the complete crack growth and deformation behavior of a cracked body. However, it may not be necessary to construct the diagram if the objective is to predict only some specific rather than detailed aspects of the overall structure response. In many problems, for example, one is interested only in the load-displacement behavior. This can be obtained by using the J_R curve and the estimation formulae, and does not require constructing a detailed crack driving force diagram. This application will be described next.

Given the material J_R (Δa) curve and the initial crack length a_o, the crack length associated with a point on the J_R curve during the crack growth process is simply $a = a_o + \Delta a$. Since equilibrium of crack growth requires that J(a, P) equals J_R $(a - a_o)$, Eq. (2-18), it gives the value of applied J associated with the crack length a for the specific crack configuration under consideration. These values of J and a are used in Eq. (6-1) to solve for the corresponding value of P numerically, for example, by Newton's method. The values of a and P thus obtained are then employed in Eq. (6-3) to determine the load-line displacement. By repeating this process at various points along the J_R curve, a complete load versus load-line displacement curve can be generated.

The example geometries discussed in the previous material were also analyzed by employing the procedure described above. The resulting load versus load-line displacement curves in all cases were identical to those obtained from crack driving force diagrams. Further examples are presented in References [6-3] and [6-5] - [6-8].

6.6.2 Determination of J_R Curves from Load-Displacement Records

There are often examples in experimental test programs where it is practical to measure the load-displacement behavior, but not the J-resistance response. Tests on irradiated material present a common example of this situation. The engineering approach can be applied to "back-out" the J-resistance curve for an extended interval of stable crack growth. This application was first developed in Reference [6-3] and will be outlined below.

The example of the 4T compact specimen of A533B steel with initial crack length of 4.615 in. is again used. Since the specimen has 25% side-groove, the fracture behavior is approximated by plane strain conditions. Using the material constants corresponding to the Ramberg-Osgood stress-strain law for A533B steel as determined in Section 6.2, and the respective fully plastic solutions from Section 3, the J-integral crack driving force diagram is generated using Eqs. (6-1) and (6-3) and the procedure described in Section 6.2. Figs. 6-18 and 6-19 show the experimental load-displacement curve and the calculated crack driving force diagram, respectively. In Fig. 6-19 the solid (load) and dashed (displacement) lines are identified which correspond to respective measured values of load and load-line displacement on Fig. 6-18 (that is, the values of P and Δ_L for a point on the P-Δ_L curve). The intersection of these two lines gives the values of J and crack length a that satisfy the given P and Δ_L for this particular crack configuration. By repeating this process for other measured values of load and load-line displacement (that is, other points on the P-Δ_L curve), the J_R curve may be constructed. The procedure is clearly demonstrated by the data points on the two figures.

Figure 6-20 shows a comparison of the J_R curve estimated from the above procedure and actual experimental data. Results for another 4T specimen (a_o/b = 0.615 in. and 12.5% side-groove) are also included. The good agreement between the predicted and measured curves clearly suggests that the J_R can be estimated to a fair degree of accuracy by the procedure outlined.

Construction of the crack driving force diagram can be bypassed in this application by proceeding directly with Eqs. (6-1) and (6-3). For any load-displacement pair from the P-Δ_L curve, the nonlinear equation (6-3) is solved numerically by Newton's method, for example, to obtain a and thus Δa. Knowing P and a, the corresponding J is calculated from Eq. (6-1). This yields the J-Δa pair corresponding to the particular P-Δ_L pair. By repeating this procedure for various points on the P-Δ_L curve, the J_R curve is determined as a function of Δa. The J_R curves obtained by the above two procedures are identical, as they should be.

A note of caution must be made. The J_R curve obtained from a specimen load-displacement record using the above procedures or other procedures will be the proper material curve only if the conditions for J-controlled growth [6-9, 6-10] are satisfied by the specimen being analyzed. If not, the estimated J_R curve may not be conservative.

6.7 SUMMARY

The examples presented in this section illustrate that fracture behavior of flawed structures under elastic-plastic and fully plastic conditions can be reliably predicted employing the engineering approach together with conditions for crack growth and instability. For a comprehensive analysis of a given crack problem, a crack driving force diagram may be generated which allows straightforward predictions of various fracture quantities of interest, such as load at the onset of crack propagation, extent of stable growth prior to instability, load at instability, maximum load carrying capacity and load-deformation behavior. Accuracy of the methodology was assessed by comparing the predicted results with experimental data and detailed finite element calculations for a variety of crack problems.

Some other applications of the crack driving force diagram were also discussed, an example being the estimation of the J_R curve from load-displacement records. It was also shown that the compliance of a loading system has a significant influence on the crack growth and instability behavior. The effect of system compliance is treated by the crack driving force diagram in a very material and systematic fashion.

When applying the engineering approach to a fracture problem of interest, the conditions for J-controlled crack growth [6-9, 6-10] as summarized in Section 2 should be kept in mind. Although such conditions impose certain limitations on the approach, a limited study carried out in Reference [6-8] suggests that the conservative predictions will result for non-J-controlled growth conditions. Also, it was shown in Reference [6-3] that the effect of scatter in the experimental J_r-curve data is relatively small on the overall load-displacement behavior. These topics are treated in much greater detail in the references cited above.

6.8 REFERENCES

[6-1] C. F. Shih, H. G. deLorenzi, and W. R. Andrews, "Studies on Crack Initiation and Stable Crack Growth," in Elastic-Plastic Fracture, ASTM Special Technical Publication 668, 1979, pp. 65-120.

[6-2] W. R. Andrews and C. F. Shih, "Thickness and Side-Groove Effects on J and δ Resistance Curves for A533B Steel at 93°C," in Elastic-Plastic Fracture, ASTM Special Technical Publication 668, 1979, pp. 426-450.

[6-3] V. Kumar and C. F. Shih, "Fully Plastic Crack Solutions, Estimation Scheme and Stability Analyses for Compact Specimen," in Fracture Mechanics, ASTM Special Technical Publication 700, 1980, pp. 406-438.

[6-4] M. F. Kanninen, C. W. Marschall, I. S. Abou-Sayed, A. Zahoor, G. M. Wilkowski, J. Ahmad, H. C. Rhee, and S. G. Sampath, "Instability Predictions for Circumferentially Cracked Large-Diameter Type 304 Stainless Steel Piping Under Dynamic Loading," 3rd Semiannual Report to EPRI, Contract No. T118-2, Battelle Columbus Laboratory, Columbus, Ohio, January 31, 1981.

[6-5] C. F. Shih and V. Kumar, "Estimation Technique for the Prediction of Elastic-Plastic Fracture of Structural Components of Nuclear Systems," 1st Semiannual Report to EPRI, Contract No. RP1237-1, General Electric Company, Schenectady, New York, July 1, 1978 - January 31, 1979.

[6-6] V. Kumar, M. D. German, and C. F. Shih, "Estimation Techniques for the Prediction of Elastic-Plastic Fracture of Structural Components of Nuclear Systems," Combined 2nd and 3rd Semiannual Report to EPRI, Contract No. RP1237-1, General Electric Company, Schenectady, New York, February 1, 1979 - January 31, 1980.

[6-7] V. Kumar, H. G. deLorenzi, W. R. Andrews, C. F. Shih, M. D. German, and D. F. Mowbray, "Estimation Techniques for the Prediction of Elastic-Plastic Fracture of Structural Components of Nuclear Systems," 4th Semiannual Report to EPRI, Contract No. RP1237-1, General Electric Company, Schenectady, New York, July 1, 1980 - January 31, 1981.

[6-8] C. F. Shih, M. D. German, and V. Kumar, "An Engineering Approach for Examining Crack Growth and Stability in Flawed Structures," presented at the OECD-CSNI Specialist Meeting at Washington University, St. Louis, Missouri, September 1979, NUREG CP-0010; International Journal of Pressure Vessels and Piping, in press.

[6-9] J. W. Hutchinson and P. C. Paris, "Stability Analysis of J-Controlled Crack Growth," in Elastic-Plastic Fracture, ASTM Special Technical Publication 668, 1979, pp. 37-64.

[6-10] C. F. Shih, R. H. Dean, and M. D. German, "On J-Controlled Crack Growth: Evidence, Requirements and Applications," General Electric Company TIS Report (to be submitted).

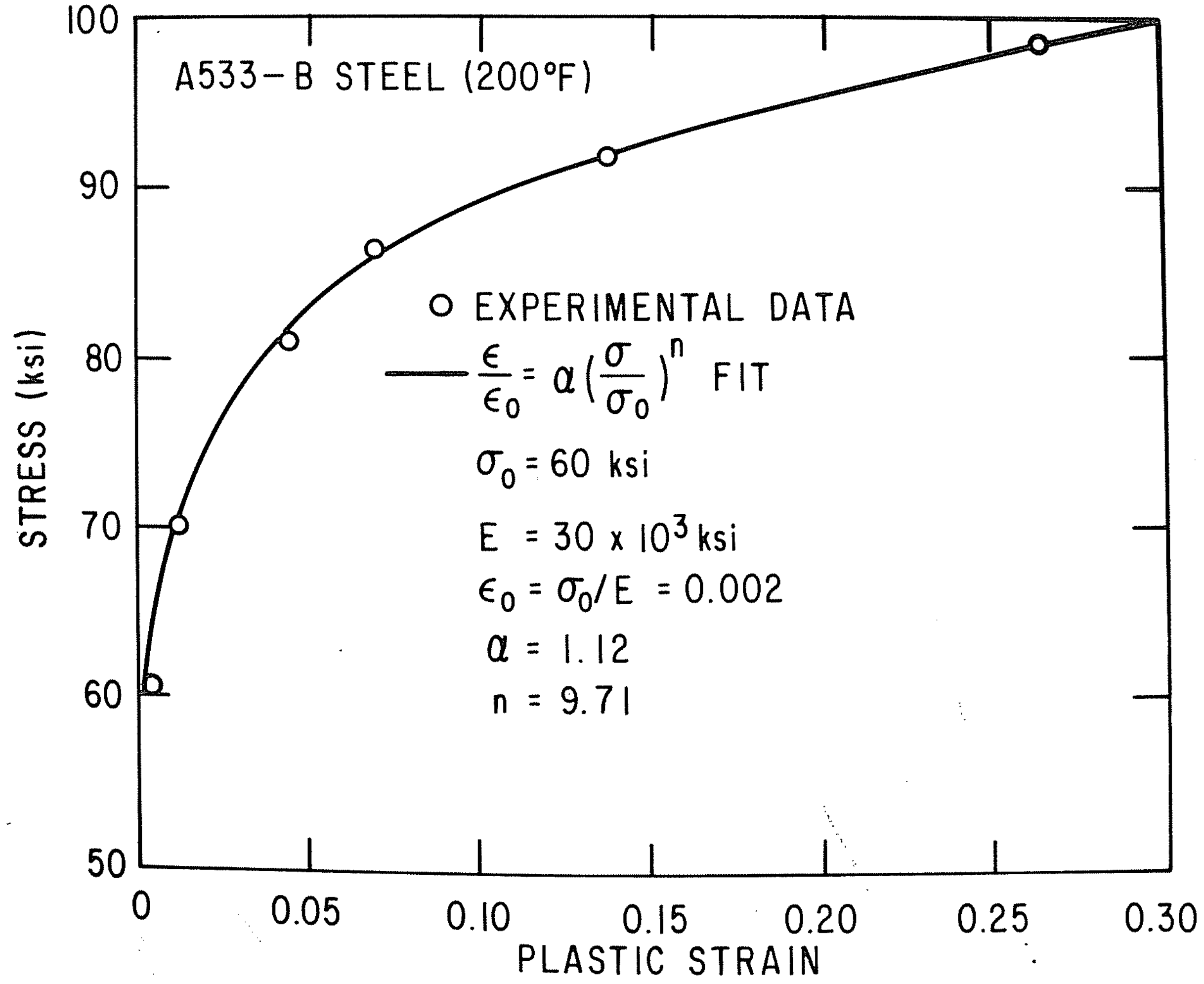

Figure 6-1. Stress-strain curve for A533B steel at 200°F and its representation by the Ramberg-Osgood law.

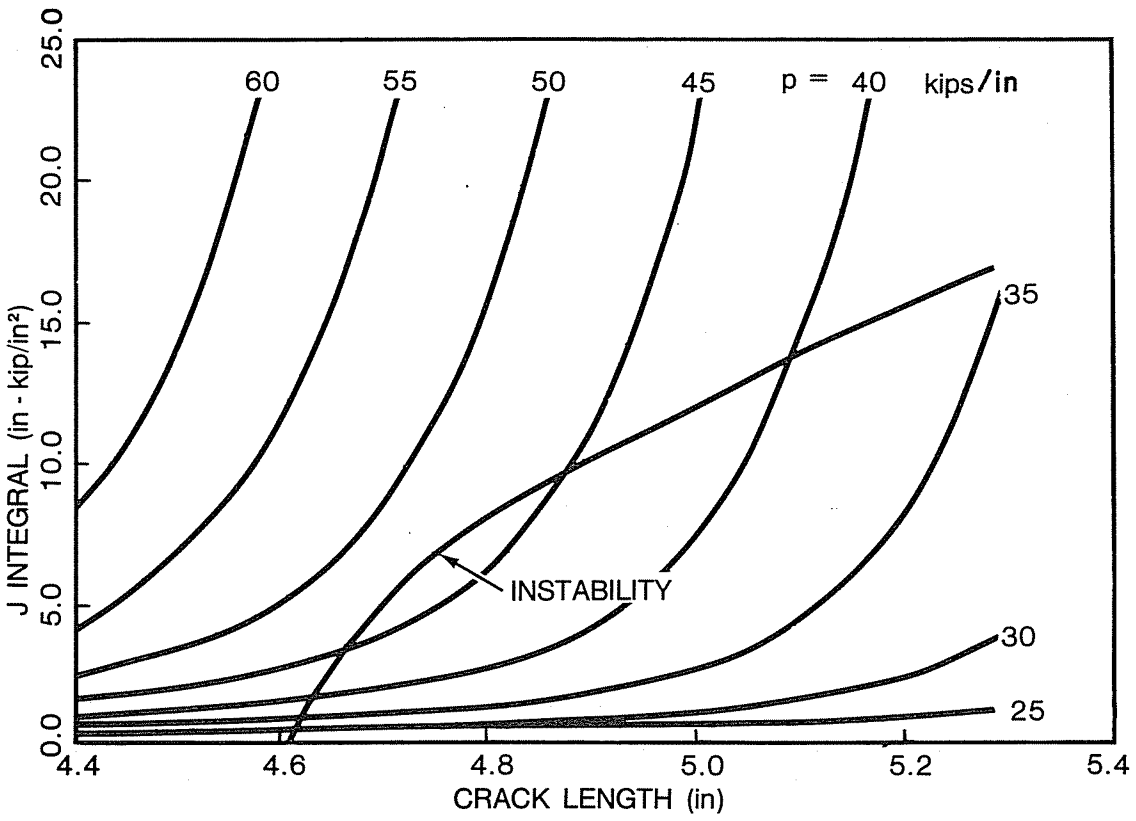

Figure 6-2. J-integral versus crack length curves with load as the parameter for a 4T, T-52, plane strain compact specimen of A533B steel. The material J_R curve is indicated by the heavy solid line at the initial crack length of 4.615 inches.

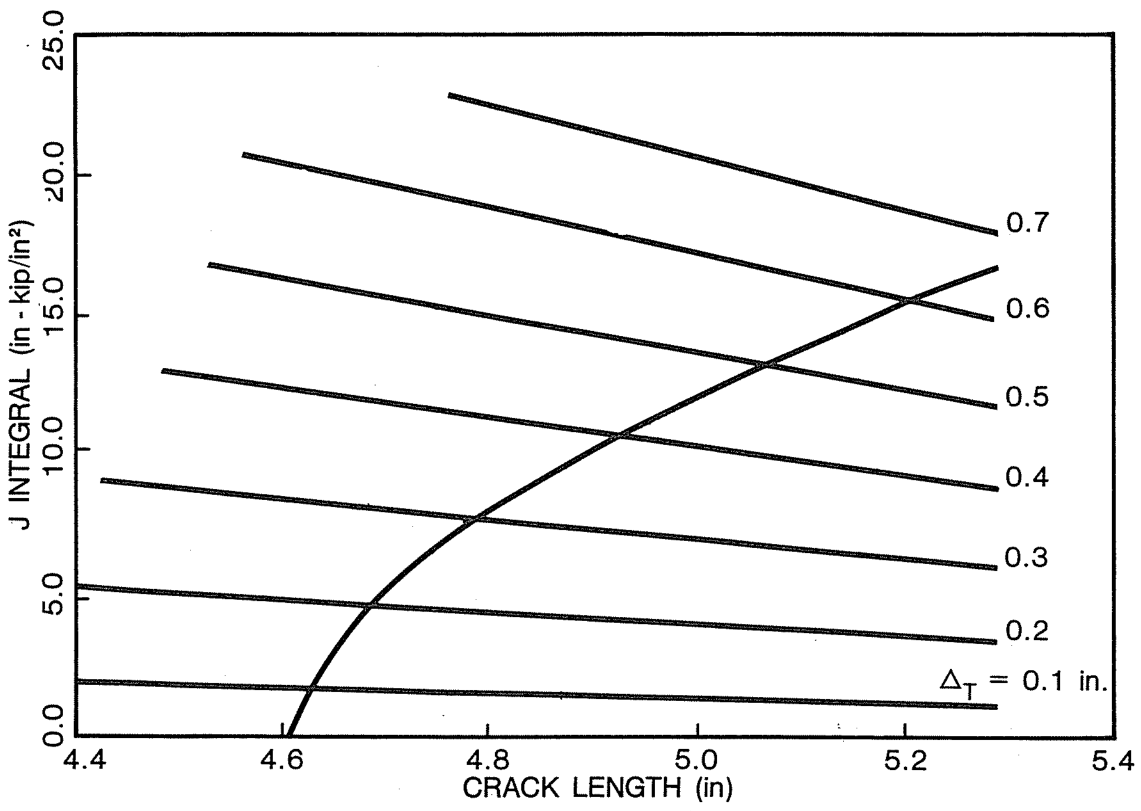

Figure 6-3. J-integral versus crack length curves with displacement as the parameter for a 4T, T-52, plane strain compact specimen of A533B steel. The material J_R curve is indicated by the heavy solid line at the initial crack length of 4.615 inches.

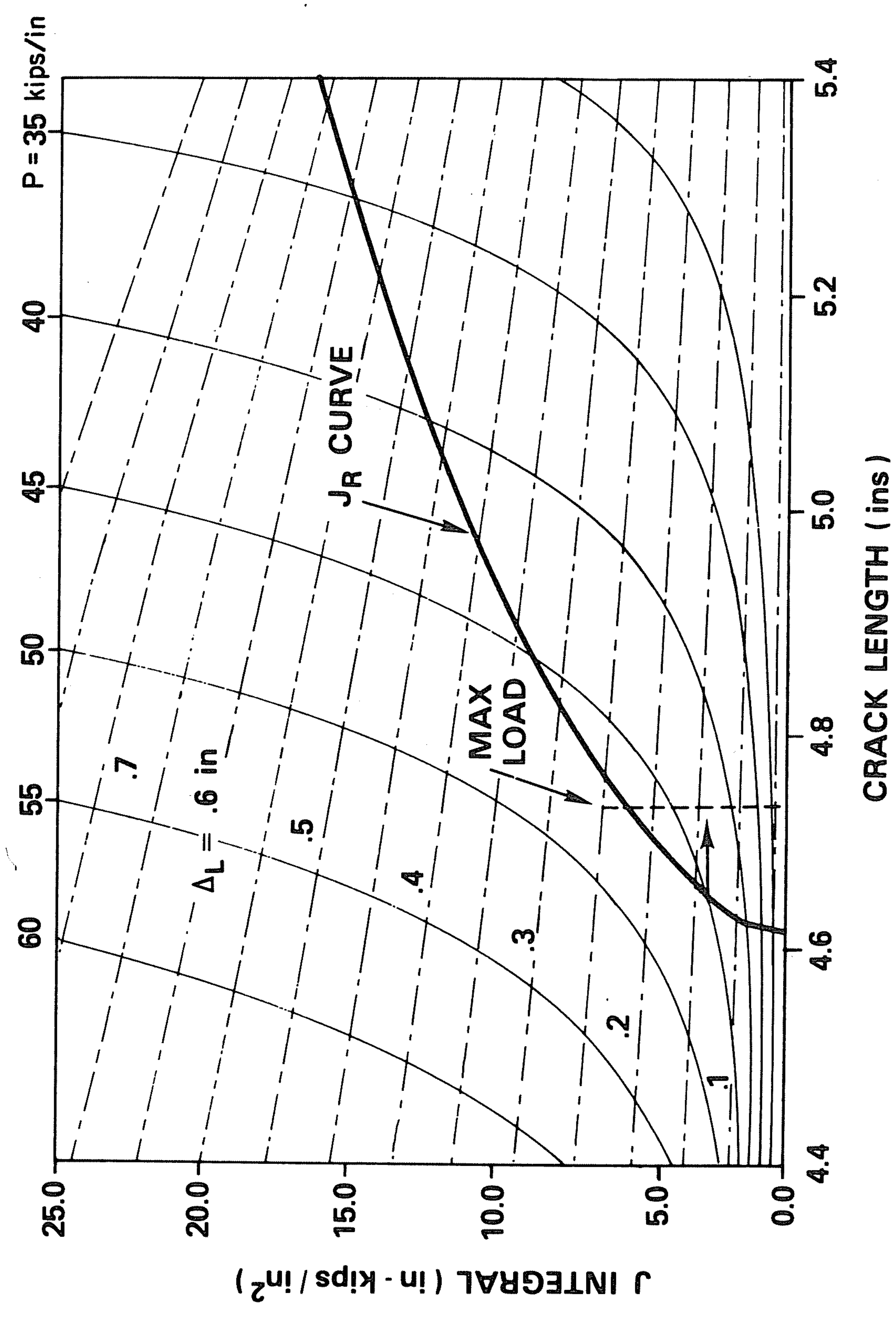

Figure 6-4. A J-integral crack driving force diagram for a 4T, T-52, plane strain compact specimen of A533B steel. The constant load curves are shown by solid lines and the constant displacement curves by dashed lines. The material J_R curve, indicated by the heavy solid lines, is superimposed at the initial crack length of 4.615 inches.

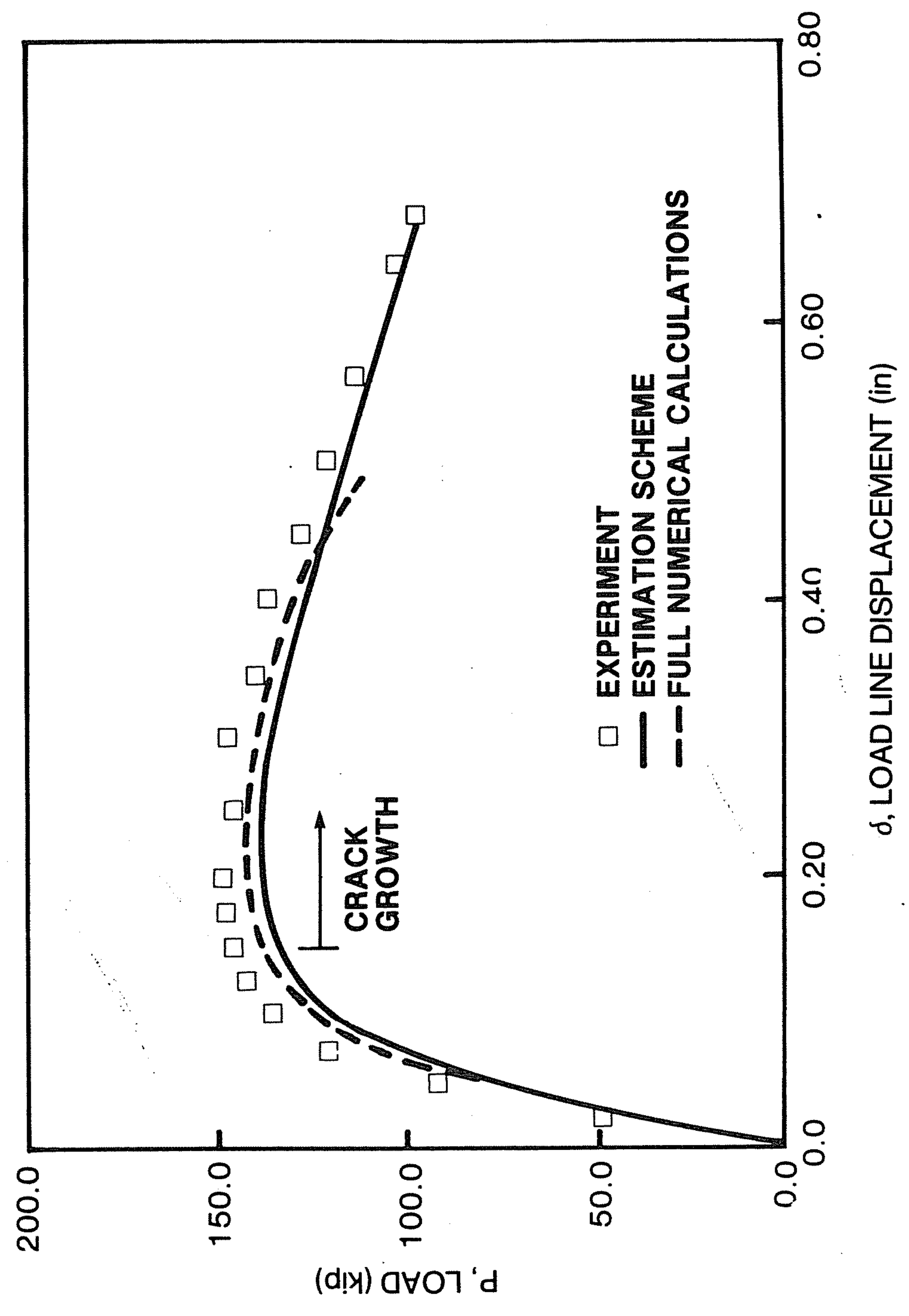

Figure 6-5. Comparison of predicted and experimentally measured load-displacement relationship for 4T, T-52, A533B steel, 25% side-grooves plane strain compact specimen with initial crack length of 4.615 inches. Results from full numerical calculations based on J_2 flow theory of plasticity are also included.

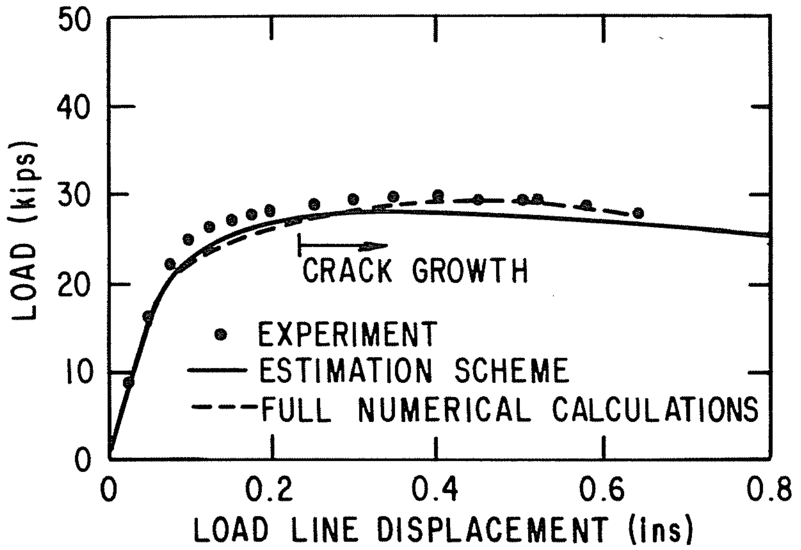

Figure 6-6. Comparison of predicted and experimentally measured behavior for 4T, T-61, 25% side-grooves, plane strain compact specimen with $a_o/b = 0.8$, b = 8 inches. Results from full numerical calculations based on J_2 flow theory of plasticity are also included.

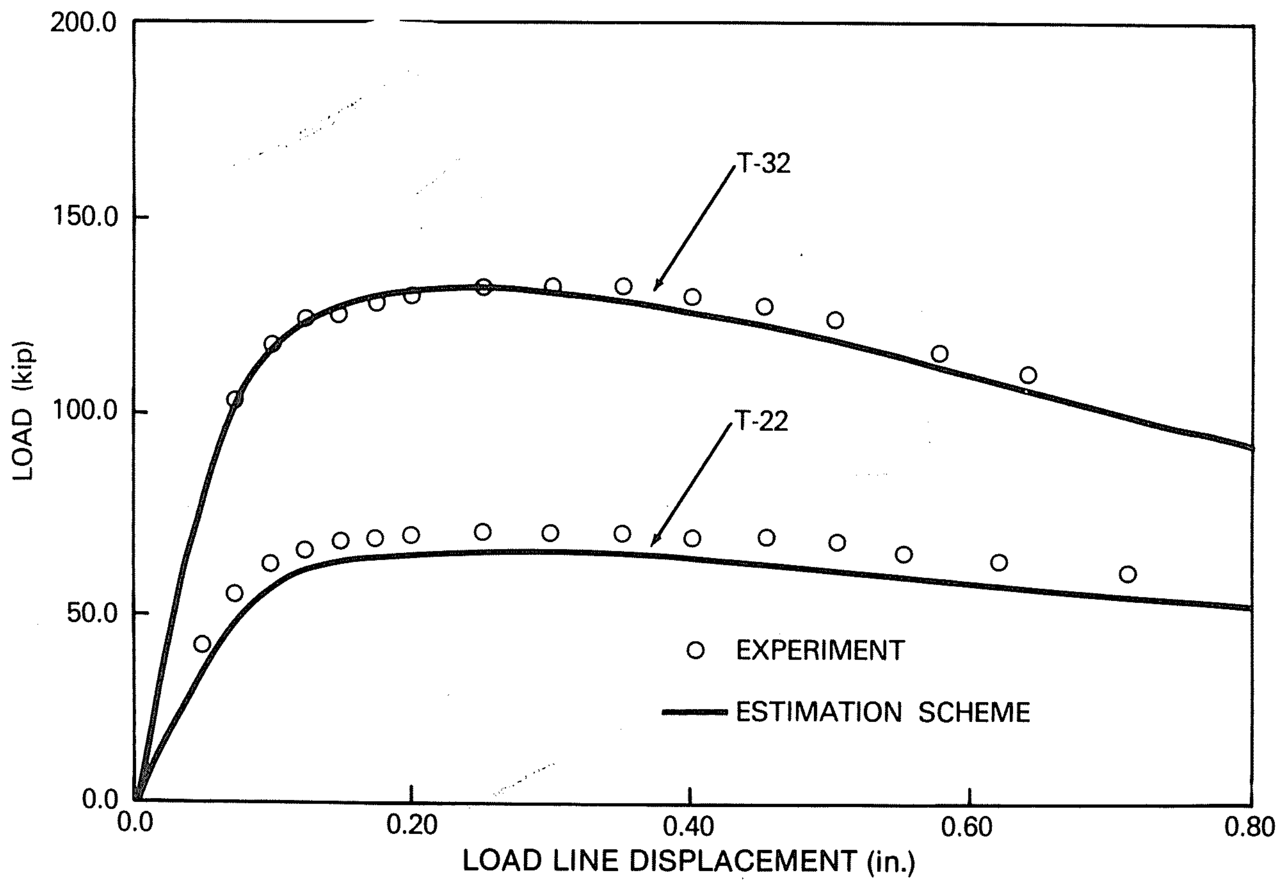

Figure 6-7. Comparison of predicted and experimentally measured load-line displacement relationship for two 4T compact specimens in plane strain with 12.5% side-grooves. $a_o/b = 0.615$ for T-32 and $a_o/b = 0.718$ for T-22.

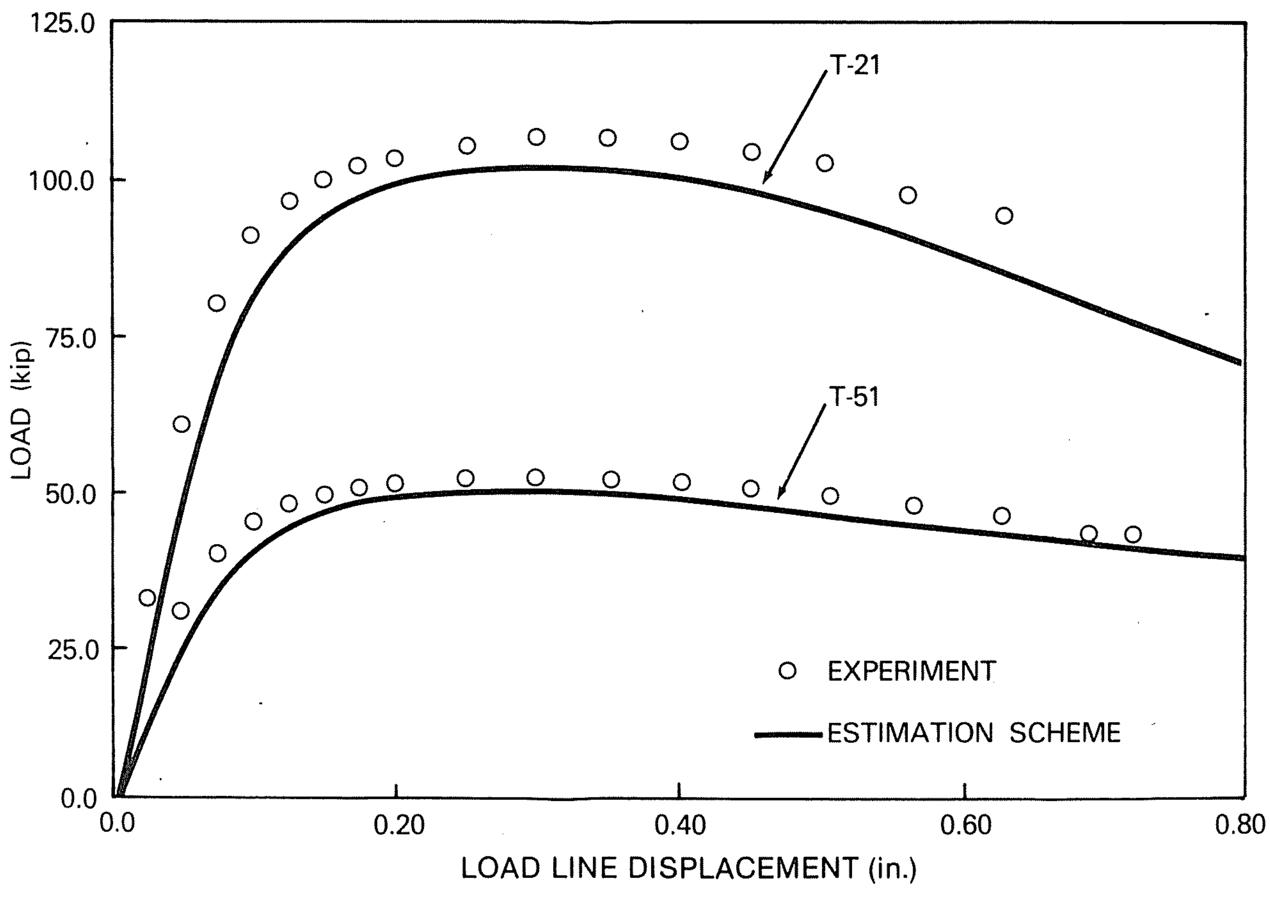

Figure 6-8. Comparison of predicted and experimentally measured load-displacement relationship for two 4T compact specimens in plane strain. T-21 has $a_o/b = 0.527$ and 12.5% side-groove, and T-51 has $a_o/b = 0.736$ and 25% side-groove.

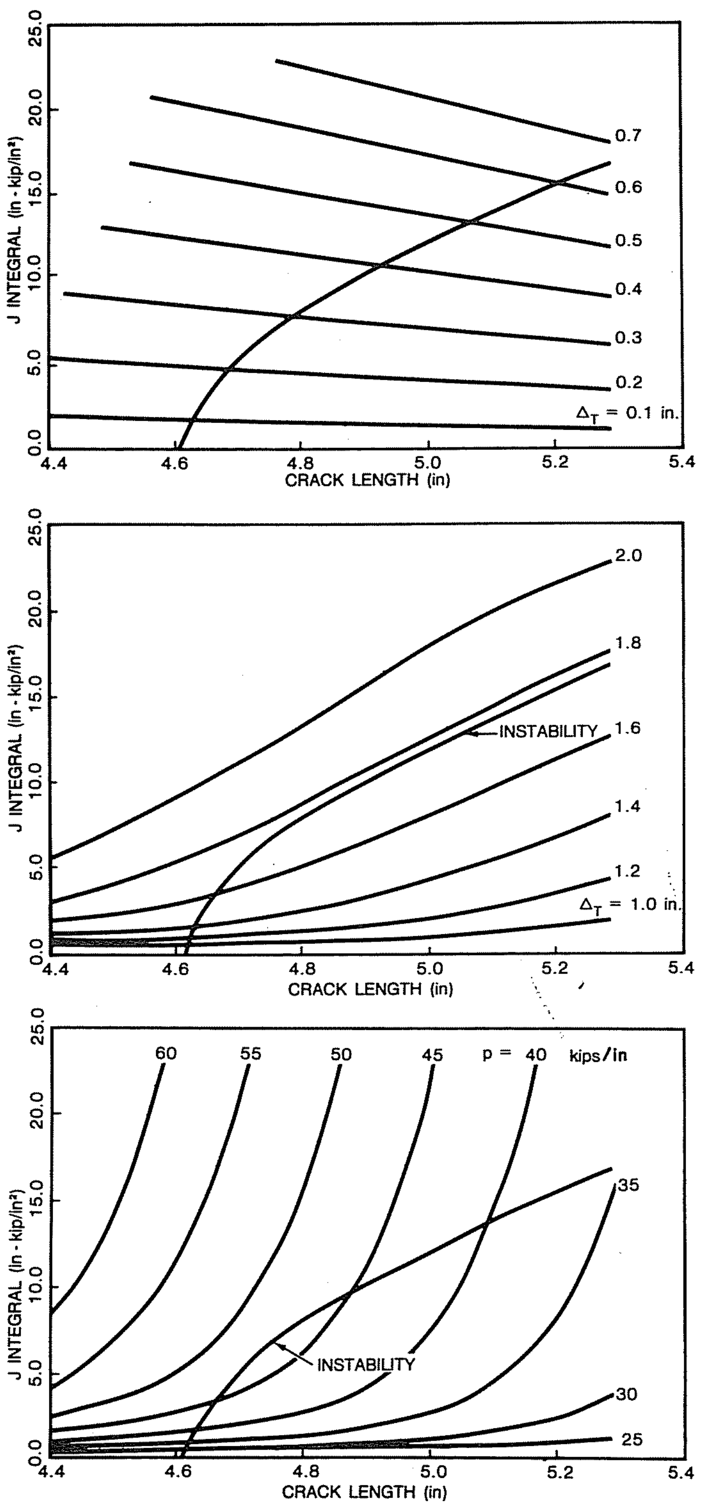

Figure 6-9. J-integral crack driving force diagrams for A533B steel, 4T, 25% side-grooves, plane strain compact specimen with initial crack length of 4.615 inches. (a) Displacement controlled situation, $\overline{C}_M$ = 0, (b) soft loading system, $\overline{C}_M$ = 1000, and (c) load-controlled situation, $\overline{C}_M$ = ∞.

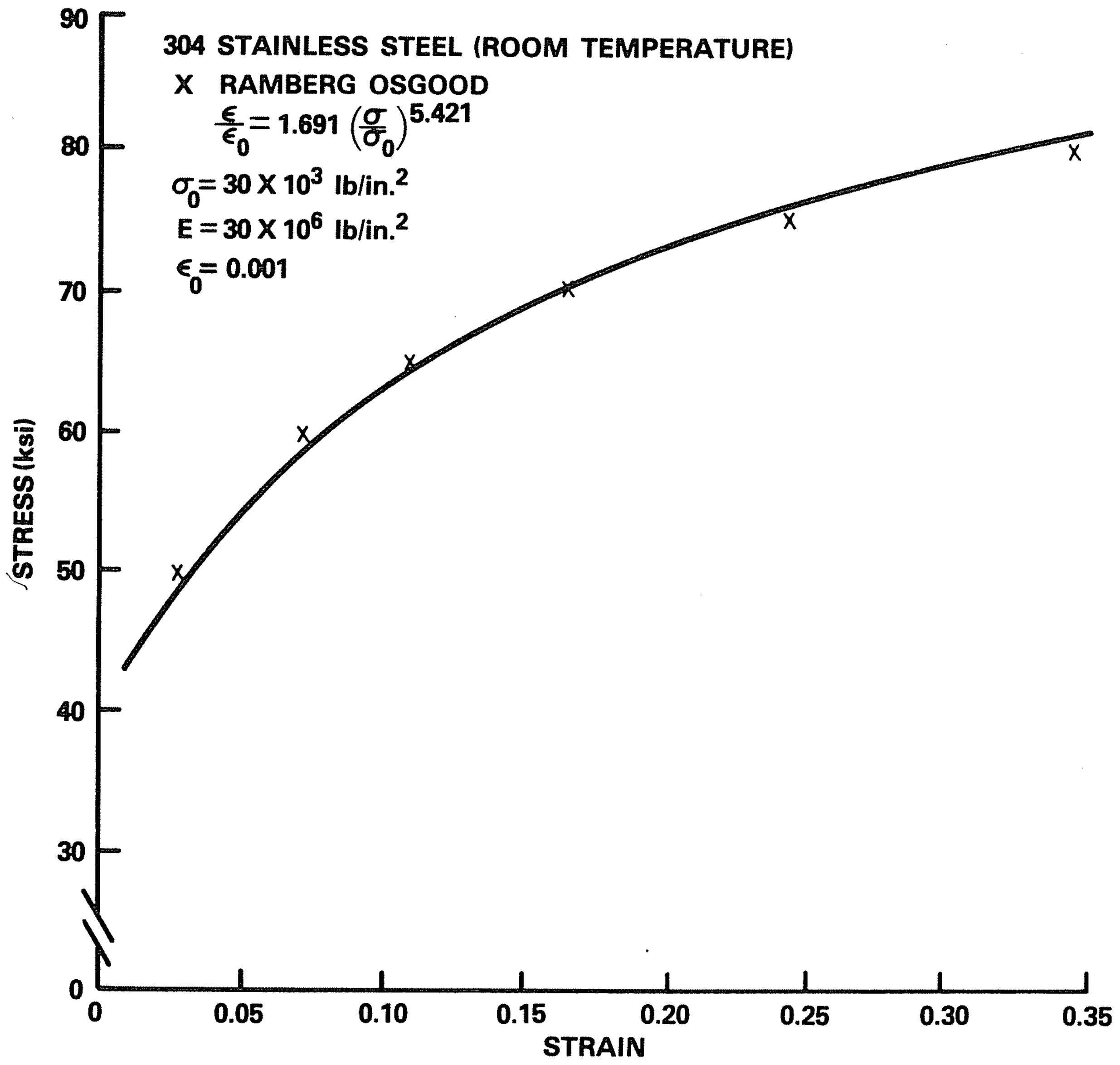

Figure 6-10. Ramberg-Osgood characterization stress-strain curve for 304 stainless steel at room temperature.

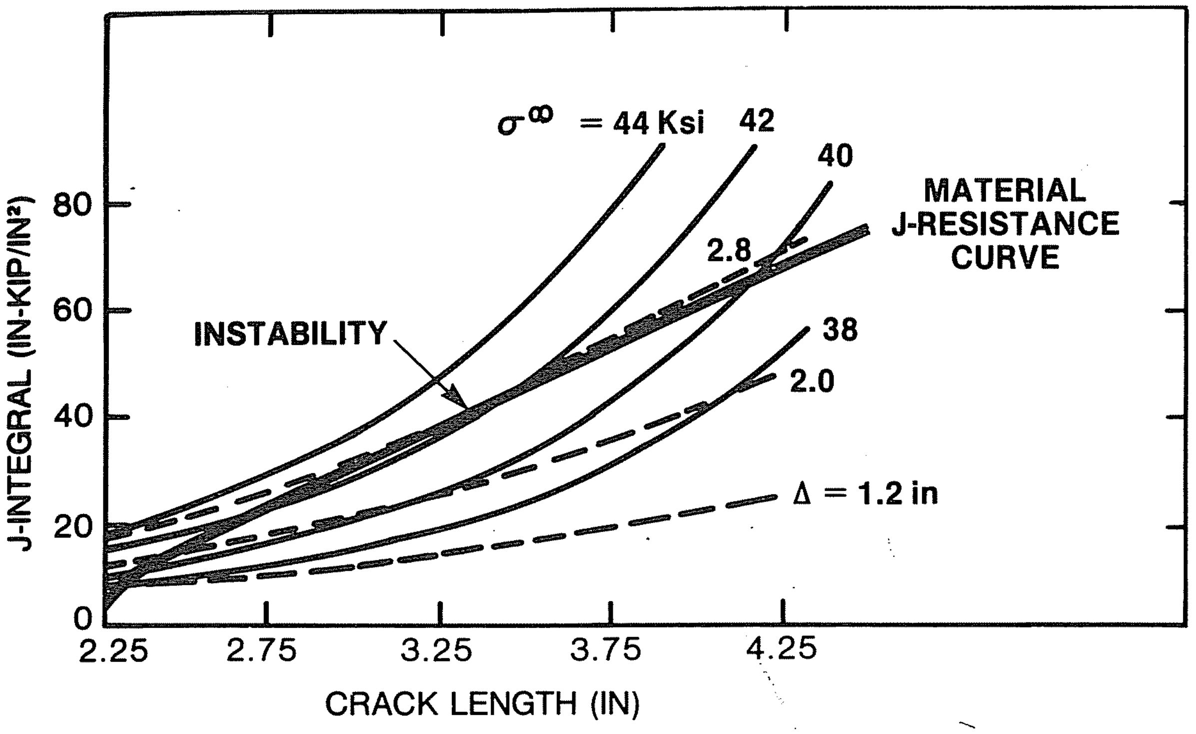

Figure 6-11. J-integral crack driving force diagram for a circumferentially cracked cylinder of 304 stainless steel.

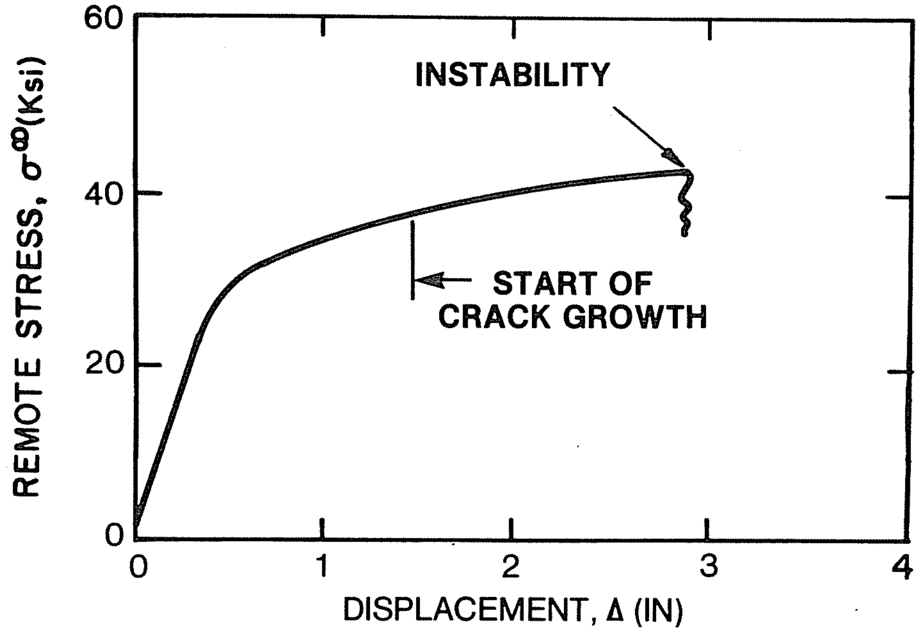

Figure 6-12. Load-displacement behavior of a circumferentially cracked cylinder of 304 stainless steel.

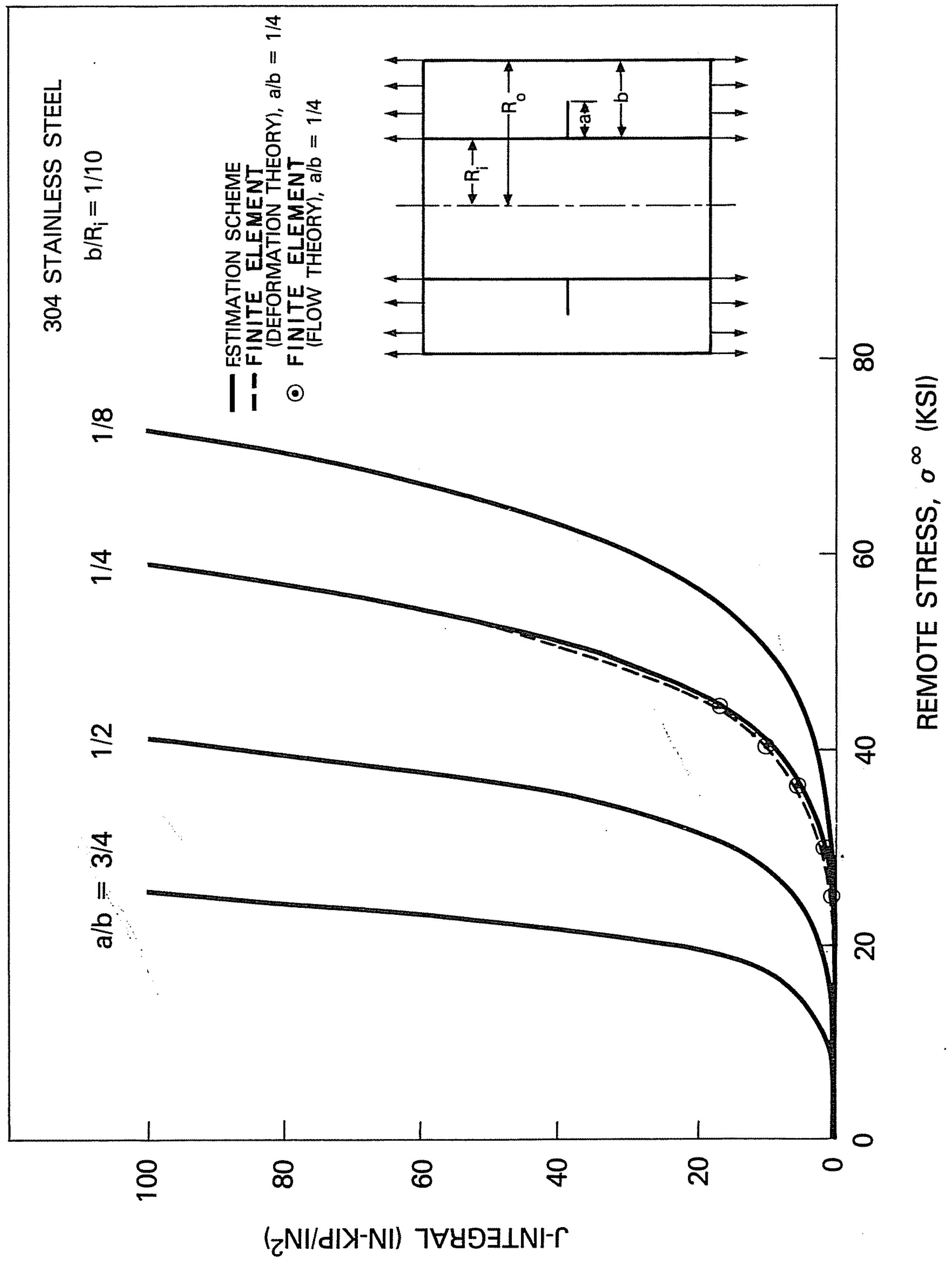

Figure 6-13. J-integral crack driving force diagram for a circumferentially cracked cylinder of 304 stainless steel with b = 9 inches. For a/b = 1/4 the estimation method results are also compared with detailed finite element calculations based on flow and deformation theories of plasticity.

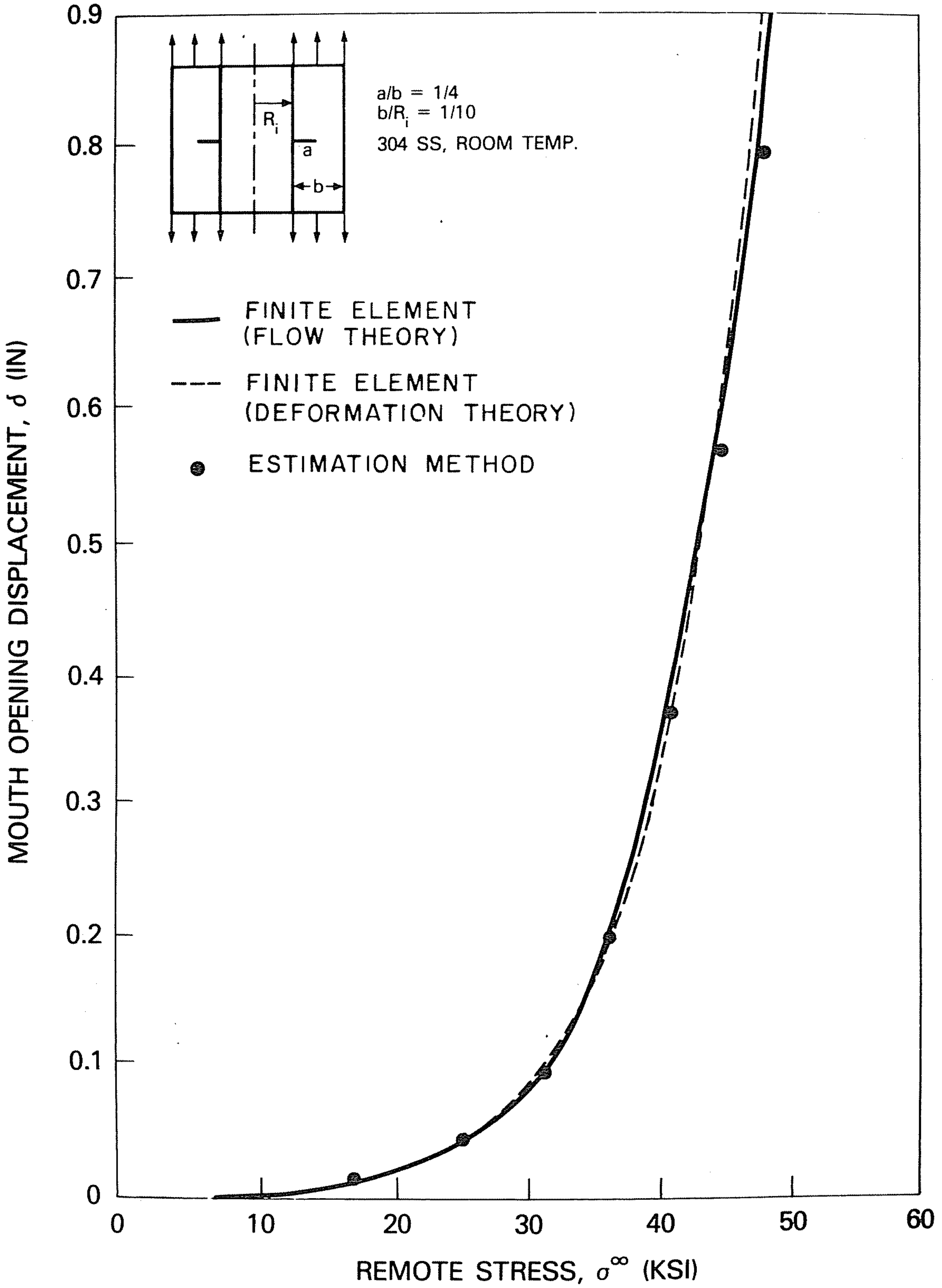

Figure 6-14. Comparison of the estimation method and finite element results for mouth opening displacement versus applied load for a circumferentially cracked cylinder of 304 stainless steel.

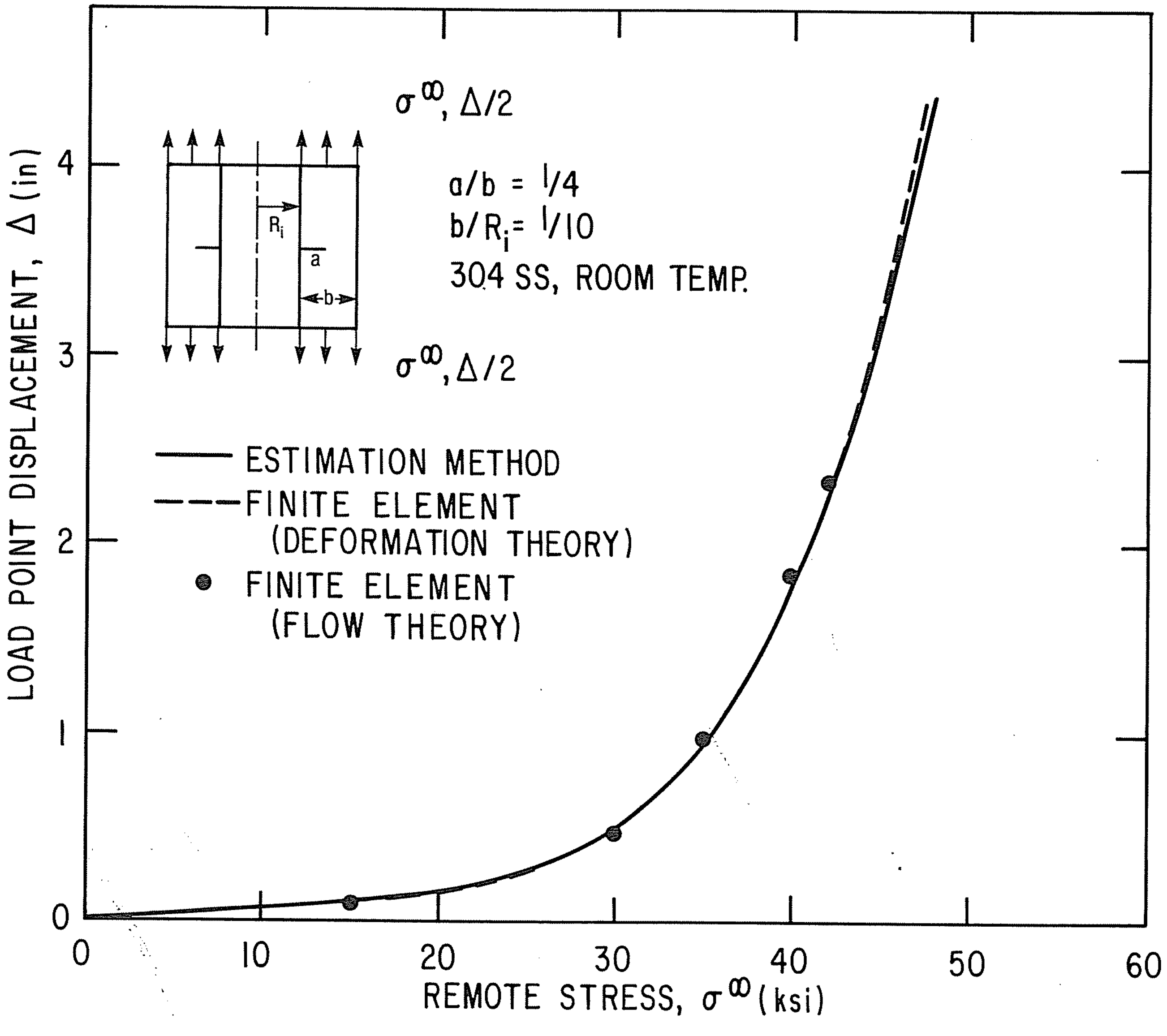

Figure 6-15. Comparison of the estimation method predictions and the finite element computations for the load-displacement behavior of a circumferentially cracked cylinder of 304 stainless steel.

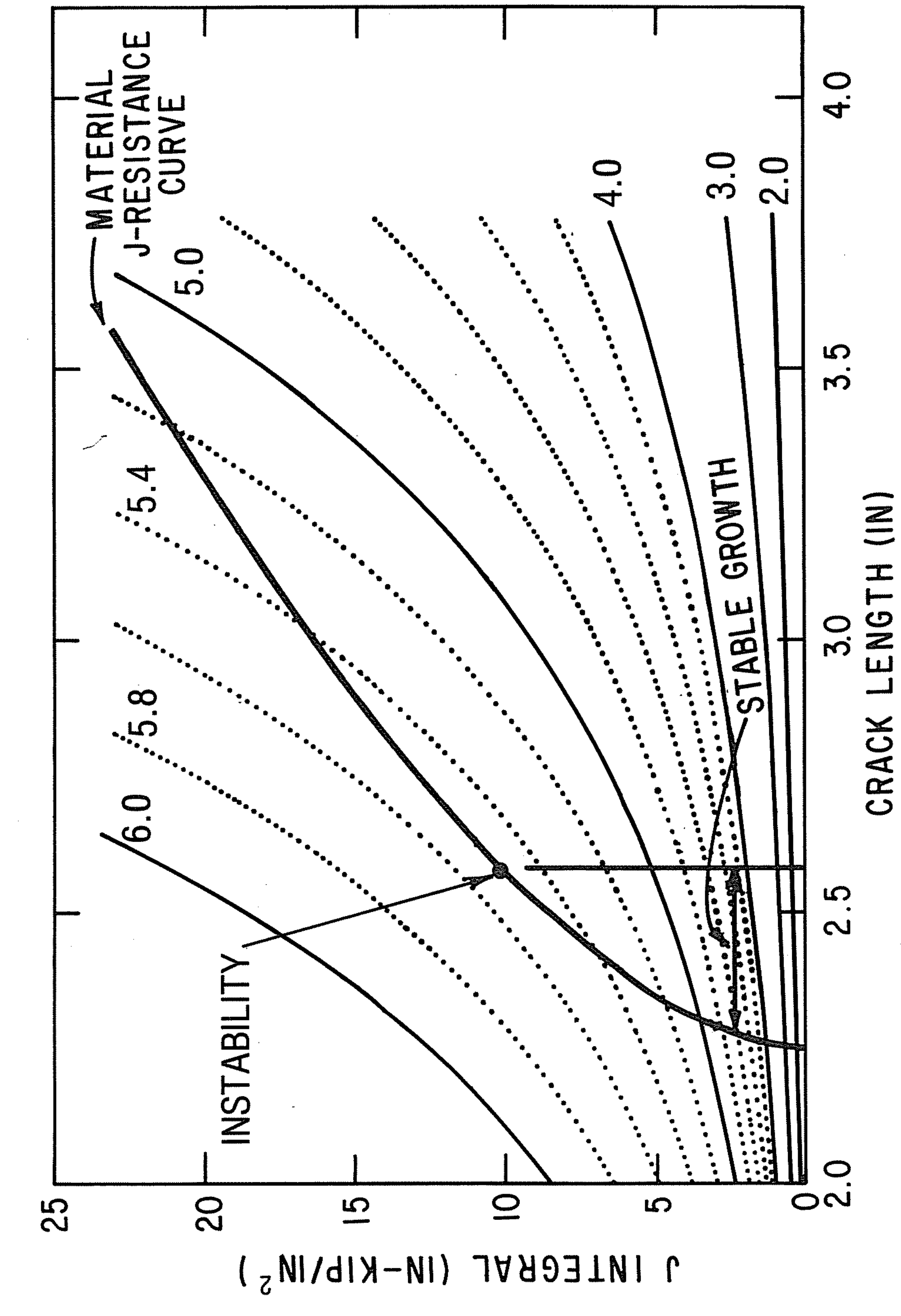

Figure 6-16. Crack driving force diagram for an axially cracked cylinder of A533B steel under internal pressure loading and with b = 9 inches. The material J_R curve is shown by the heavy solid line and the instability point is also clearly indicated.

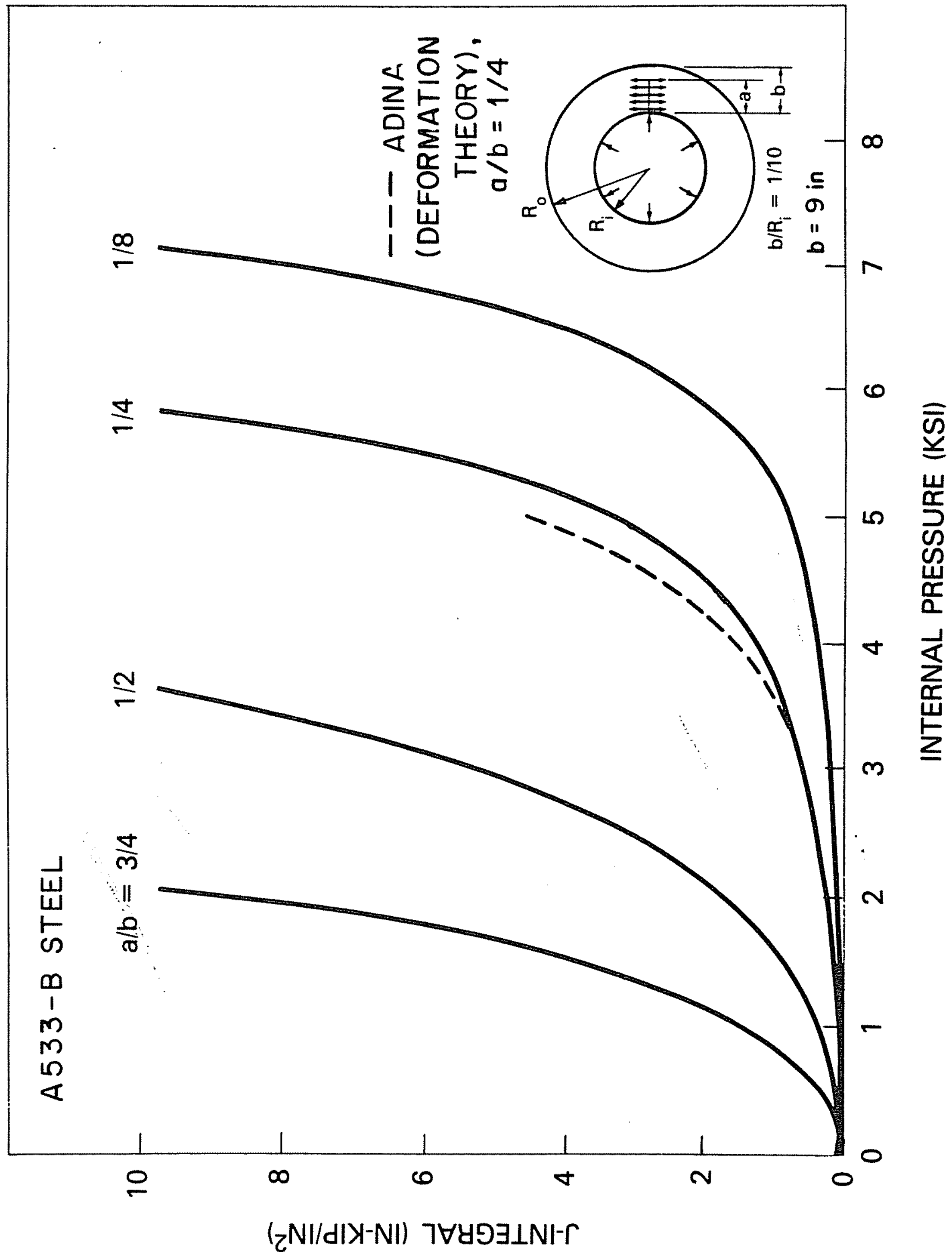

Figure 6-17. J-integral crack driving force diagram for an internally pressurized, axially cracked cylinder of A533B steel. For a/b = 1/4 the estimation method results are also compared with detailed finite element calculations.

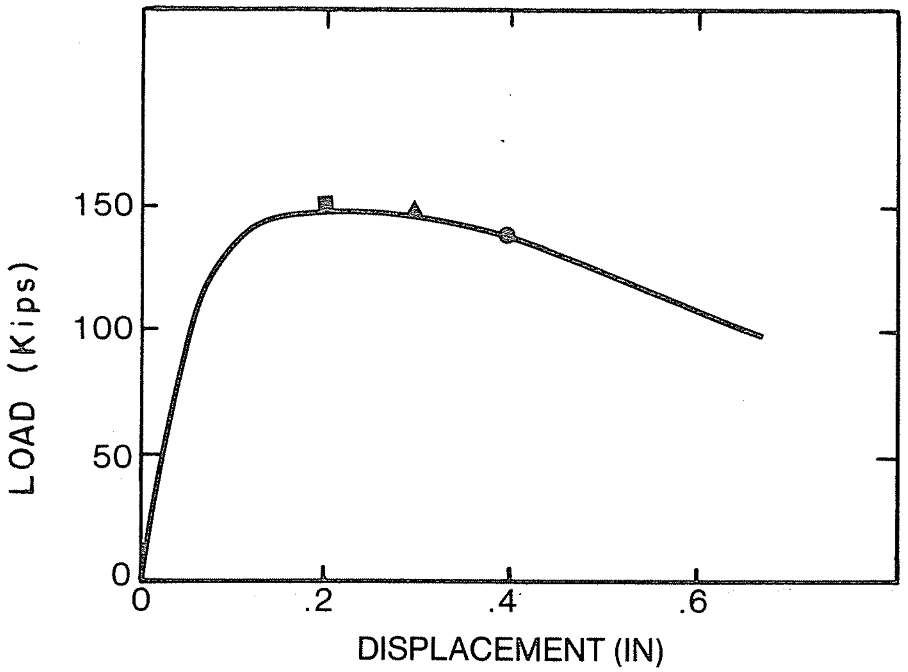

Figure 6-18. Measured load-displacement behavior of a 4T, T-52, 25% side-grooved compact specimen of A533B steel.

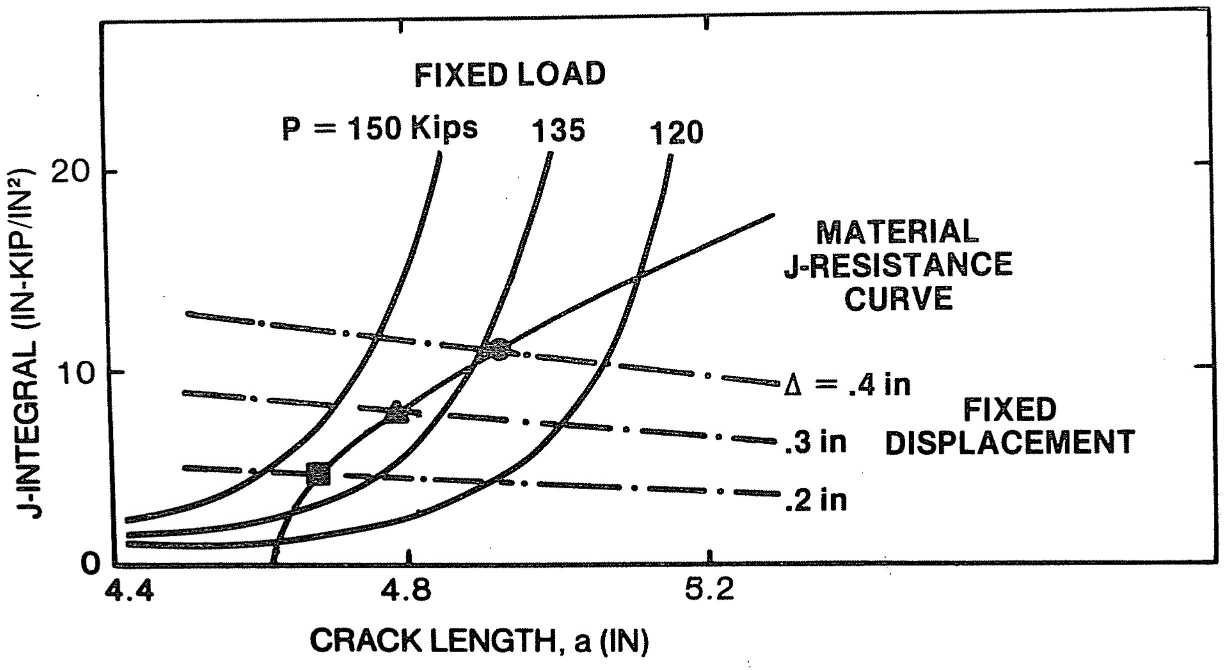

Figure 6-19. Crack driving force diagram for a 4T, T-52, 25% side-grooved, plane strain compact specimen of A533B steel.

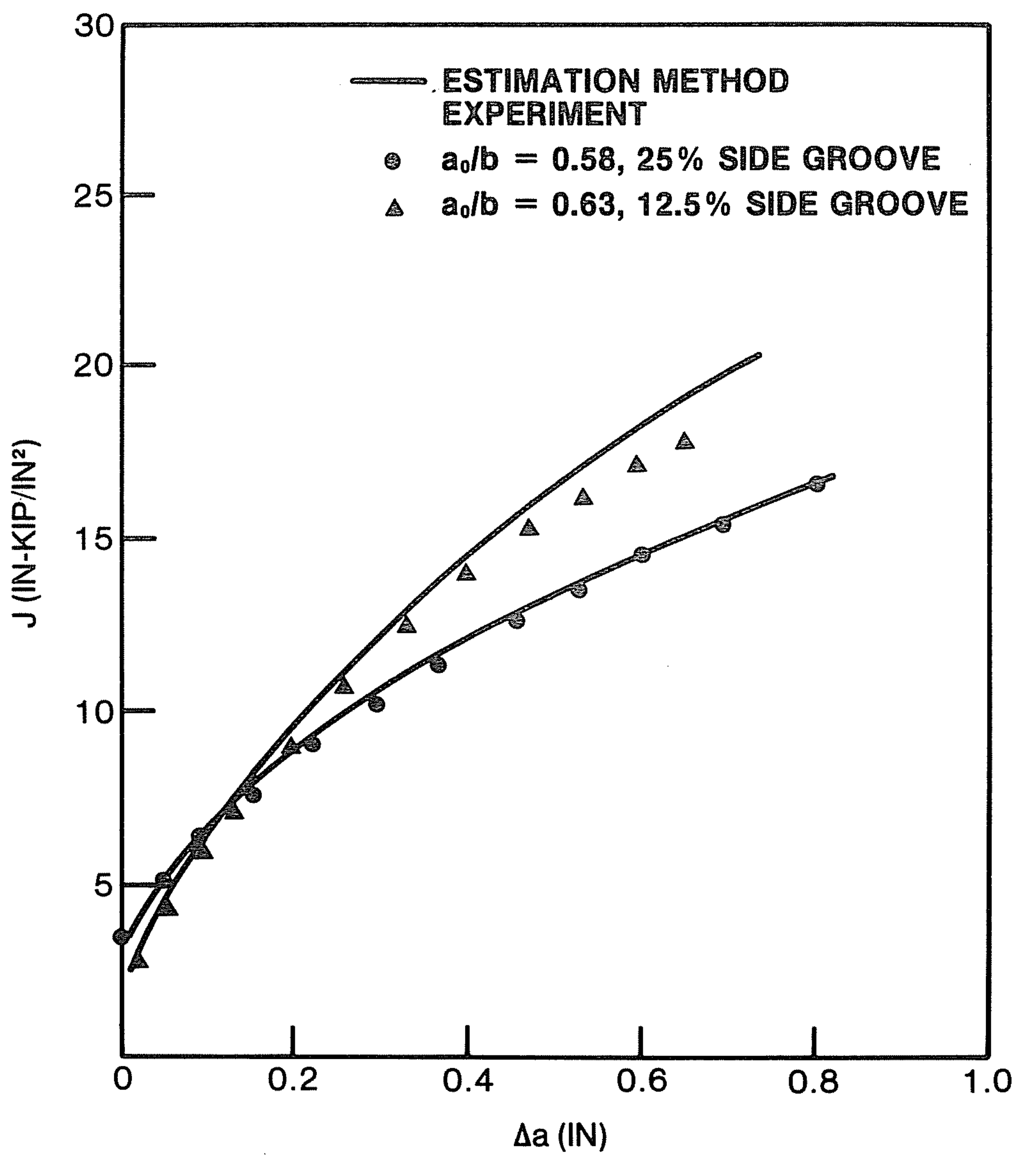

Figure 6-20. J_R curve predicted from the measured load-displacement records and crack driving force diagrams for T-52 and T-32 compact specimens of A533B steel. The experimentally measured J_R curves for the two specimens are also indicated.

SECTION 7
STABILITY ASSESSMENT DIAGRAMS

Section 7
STABILITY ASSESSMENT DIAGRAMS

7.1 INTRODUCTION

The discussion in the previous section showed how the stability of a flawed structure can be analyzed through the use of a crack driving force diagram. In some applications it is convenient to calculate the tearing modulus explicitly and plot it as a function of the relevant flaw and structure parameters. Such curves are termed stability assessment diagrams, and are basically a compression of the information contained in the crack driving force diagram. This section discusses a procedure for computing stability assessment diagrams and their applications to examining stability of crack growth in flawed structures.

The concept of tearing modulus was introduced in Section 2 and will be expanded upon here. Tearing modulus based on the J-integral was proposed by Paris, et al. [7-1], and was developed further by Hutchinson and Paris [7-2]. In the latter work, a theoretical basis and conditions for use of the J-integral during crack growth were formulated. The tearing modulus T_J is defined as

$$T_J = \frac{E}{\sigma_o^2} \left(\frac{\partial J}{\partial a}\right)_{\Delta_T} \qquad (7\text{-}1)$$

where Δ_T denotes total displacement, to be defined subsequently. The material resistance to instability is represented by T_{JR} and is defined by

$$T_{JR} = \frac{E}{\sigma_o^2} \frac{dJ_R}{da} \qquad (7\text{-}2)$$

The stability conditions are stated as

$$T_J < T_{JR} \text{ (stable)} \qquad (7\text{-}3)$$

$T_J \geq T_{JR}$ (unstable)

The subscript in Eq. (7-1) denotes a partial derivative with the total displacement Δ_T held fixed; Δ_T is defined by

$$\Delta_T = \Delta + C_M P \qquad (7\text{-}4)$$

where C_M denotes compliance of the system and can be identified with the compliance of a linear spring placed in series with a cracked body as shown in Fig. 7-1. It represents stored energy in the system containing a cracked body. Length of a circumferentially cracked pipe, diameter of an axially cracked pressure vessel and size of a vessel containing a nozzle corner flaw are typical examples of system compliance. A general expression for $(\partial J/\partial a)_{\Delta_T}$ appearing in Eq. (7-1) was derived in Reference [7-2] and is given by

$$\left(\frac{\partial J}{\partial a}\right)_{\Delta_T} = \left(\frac{\partial J}{\partial a}\right)_P - \left(\frac{\partial J}{\partial P}\right)_a \left(\frac{\partial \Delta}{\partial a}\right)_P \left[C_M + \left(\frac{\partial \Delta}{\partial P}\right)_a\right]^{-1}. \qquad (7\text{-}5)$$

It is evident from the above discussion that for given material properties and a given crack configuration the tearing modulus is a function of a, P and C_M, i.e., $T_J = T_J(a, P, C_M)$. C_M has a strong influence on the instability behavior. There are two limiting situations: (1) $C_M = 0$, corresponding to a displacement controlled situation, for example a rigid test machine and (2) $C_M = \infty$, representing a load controlled situation, exemplified by a dead load or infinitely soft system. For the latter case, Eq. (7-5) simplifies to

$$\left(\frac{\partial J}{\partial a}\right)_{\Delta_T} = \left(\frac{\partial J}{\partial a}\right)_P \qquad (7\text{-}6)$$

In a given problem if the system compliance cannot be easily evaluated or modeled, C_M can be taken to be ∞ since it represents the worst case behavior and would yield a conservative estimate of the extent of stable crack growth.

The problem of calculating tearing modulus reduces to finding the partial derivatives of J and Δ on the right-hand sides of Eq. (7-5) or (7-6). The discussion in earlier sections showed that J and Δ are functions of a and P only. This is

$$J = J(a, P) \qquad (7\text{-}7)$$

$$\Delta = \Delta(a, P) \qquad (7\text{-}8)$$

where the explicit functional forms for a Ramberg-Osgood material were given in Sections 3 through 5. (Similar expressions for other uniaxial stress-strain property representations are given in Appendix A.) The derivatives in Eq. (7-5) or (7-6) can be evaluated by performing analytical or numerical differentiation on detailed expressions for J and Δ. An example of the analytical differentiation procedure is illustrated in Reference [7-3] to derive a tearing modulus expression for a circumferentially cracked cylinder in tension. T_J formulae for other crack configurations can be obtained in this manner by following the algebraic manipulation procedure illustrated.

Numerical evaluation of the derivatives can be carried out using forward or centered-difference differentiation schemes [7-4]. To illustrate this, consider the forward-differentiation scheme applied to Eqs. (7-7) and (7-8):

$$\begin{aligned}
\left(\frac{\partial J}{\partial a}\right)_P &= \frac{J(a + \Delta a,\ P) - J(a,\ P)}{\Delta a} \\
\left(\frac{\partial J}{\partial P}\right)_a &= \frac{J(a,\ P + \Delta P) - J(a,\ P)}{\Delta P} \\
\left(\frac{\partial \Delta}{\partial a}\right)_P &= \frac{\Delta(a + \Delta a,\ P) - \Delta(a,\ P)}{\Delta a} \\
\left(\frac{\partial \Delta}{\partial P}\right)_a &= \frac{\Delta(a,\ P + \Delta P) - \Delta(a,\ P)}{\Delta P}
\end{aligned} \qquad (7\text{-}9)$$

By choosing suitable values for Δa and ΔP and employing Eq. (7-9) with the explicit expressions for J(a, P) and $\Delta(a, P)$ in Sections 3 through 5, the various terms in Eq. (7-5) can be computed. Once $(\partial J/\partial a)_{\Delta_T}$ has been obtained, the tearing modulus T_J can be computed via Eq. (7-1) for any desired value of a, P and C_M. Depending upon the problem being analyzed, it may be more suitable in some cases to use a centered-difference scheme; Eq. (7-9) are then appropriately modified [7-4].

Given the material properties E, ν, α, σ_o and n and the system's compliance C_M, the applied tearing modulus for a flawed structure can be calculated for the entire range of a and P values of interest. The corresponding crack driving force (J-integral) can be computed by using the estimation formulae described in the earlier sections. Having obtained this information, the stability assessment diagram can be easily constructed on coordinates of T_J versus J or T_J versus a for constant values of the other relevant parameters. It has become customary to plot T_J versus J with a/b and C_M as parameters, but other combinations may be more appropriate for the problem of interest. By superposing the material resistance (T_{JR} versus J_R) curve, the regions of stable and unstable behavior can be identified through the instability criterion, Eq. (7-3). In subsequent discussion, example stability assessment diagrams are presented for a compact specimen, an axially cracked cylinder under internal pressure and a circumferentially cracked cylinder under remotely applied tension.

If it is desired to employ the crack tip opening displacement δ_t as the characterizing parameter in place of J, the foregoing analysis is suitably modified via the relationship between δ_t and J, Eq. (2-4). Following Reference [7-5], the tearing modulus T_δ based on δ_t is defined

$$T_\delta = \frac{E}{\sigma_o}\left(\frac{\partial \delta}{\partial a}\right)_{\Delta_t} \quad \text{and} \quad T_{\delta R} = \frac{E}{\sigma_o}\frac{d\delta_R}{da} \tag{7-10}$$

and the condition of Eq. (7-3) is restated as

$$T_\delta < T_{\delta R} \ \text{(stable)} \tag{7-11}$$

$$T_\delta \geq T_{\delta R} \ \text{(unstable)}$$

Eqs. (7-5) - (7-9) still hold except that J is now replaced by δ_t. The calculational procedure for T_δ is identical to that described above for T_J. An example stability diagram in terms of T_δ is presented in Reference [7-6].

7.2 STABILITY ASSESSMENT DIAGRAM FOR A COMPACT SPECIMEN

The compact specimen illustrated in Fig. 3-3 is used in this example. The material is A533B steel with the uniaxial stress-strain properties summarized in Section 6 (see Fig. 6-1). Both plane strain and plane stress conditions are considered. The crack length-to-specimen width ratio a/b is taken to be 0.75. The specimen size corresponds to 4T specifications. The relevant elastic-plastic expressions for J and Δ_L are given by Eqs. (3-12) and (3-14). The partial derivative in the definition of T_J was obtained numerically in this case by the forward-difference scheme, Eq. (7-9). A wide range of $\overline{C}_M$ ($\overline{C}_M = E\ C_M$) values are

utilized to represent various loading situations ranging from a typically rigid to a soft testing machine. The diagrams presented are also given in Reference [7-7].

Figure 7-2 shows the curves of T_J versus J (normalized by c σ_o^2/E) for various values of $\overline{C}_M$. The solid lines correspond to plane strain and dashed lines to plane stress. $\overline{C}_M$ varies from 10 to 100 for a typical test machine and T_J is less than 5 over this range. For A533B steel T_{JR} typically ranges from 50 to 200 [7-8]. Thus, $T_J < T_{JR}$ in these cases and crack growth in deeply cracked compact specimens will be stable. However, it can be concluded from this discussion that a dead load or an extremely soft testing machine is required to induce instability in this specimen. It is also noted that in this example T_J associated with plane strain conditions is larger than that for plane stress. This observation was also made in Reference [7-2].

An alternate form of the stability diagram is illustrated in Fig. 7-3. Here T_J is plotted against crack length at several constant load levels for a soft testing system ($\overline{C}_M$ = 1000) and plane strain conditions. The dependence of T_J on applied load and crack length is clearly demonstrated. Again, since $T_J < T_{JR}$ the crack growth will be stable. Such diagrams are useful in obtaining various combinations of a and P at which an instability condition will develop.

7.3 STABILITY ASSESSMENT DIAGRAM FOR AN AXIALLY CRACKED CYLINDER UNDER INTERNAL PRESSURE

The axially cracked cylinder (subject to internal pressure) illustrated in Fig. 4-1 is used in this example. The material is A533B steel and material stress-strain and fracture properties are given in Section 6-2. The analysis assumes plane strain conditions. Since internal pressure in this case behaves as a dead load, $C_M = \infty$ and Eq. (7-6) is applicable. The pertinent elastic-plastic formulae for J are given in Section 4.3. The cylinder dimensions are chosen to correspond to a typical reactor pressure vessel, namely R_i = 90 in., R_o = 99 in. and b = $R_o - R_i$ - 9 inches. This example is identical to that discussed in Section 6. The tearing modulus was computed numerically by the forward-difference method, Eq. (7-9).

Figure 7-4 gives the stability assessment diagram. The solid lines represent applied J versus applied T_J for several crack length-to-wall thickness ratios. The material J_R-T_{JR} curve, obtained from the material J_R curve via Eq. (7-2) is shown by the dashed line. As stated by Eq. (7-3), the dashed curve separates the stable and unstable regions. In the stable region, T_J is less than T_{JR}, and in the unstable regime T_J exceeds T_{JR}. For a given a/b, the critical value of J corresponding to instability is given by the point of intersection of the J_R-T_{JR} curve with a J-T_J curve. The critical value of J thus obtained can be used to enter the crack driving force diagram of Fig. 6-17 to predict the instability pressure.

7.4 STABILITY ASSESSMENT DIAGRAM FOR A CIRCUMFERENTIALLY CRACKED CYLINDER SUBJECTED TO REMOTE TENSION

This example considers a circumferentially cracked cylinder of 304 stainless steel subjected to remote uniform tension. The crack configuration is illustrated in Fig. 4-2. The material properties are taken from Section 6.4, and cylinder dimensions are the same as employed in Section 6. A worst case analysis was performed by taking the compliance C_M as infinity; Eq. (7-6) applies. The appropriate elastic-plastic formulae for J are given in Section 4.3. The tearing modulus was computed through Eq. (7-9) for this example, but it could as well have been calculated from the analytical expression for T_J derived in Reference [7-3].

The tearing modulus thus obtained is plotted in Fig. 7-5 on J versus T_J coordinates with crack depth as the parameter. The material resistance relationship obtained from the J_R curve via Eq. (7-2) is represented by the dashed line. The safe and unsafe regions are indicated on the figure. The critical values of J and a corresponding to instability can be readily obtained and used with an associated crack driving force diagram (Fig. 6-13) to predict the instability load.

7.5 REFERENCES

[7-1] P. C. Paris, H. Tada, A. Zahoor, and H. Ernst, "The Theory of Instability of the Tearing Mode of Elastic-Plastic Crack Growth," in Elastic-Plastic Fracture, ASTM Special Technical Publication 668, 1979, pp. 5-36 and 251-265.

[7-2] J. W. Hutchinson and P. C. Paris, "Stability Analysis of J-Controlled Crack Growth," in Elastic-Plastic Fracture, ASTM Special Technical Publication 668, 1979, pp. 37-64.

[7-3] V. Kumar, H. G. deLorenzi, W. R. Andrews, C. F. Shih, M. D. German, and D. F. Mowbray, "Estimation Techniques for the Prediction of Elastic-Plastic Fracture of Structural Components of Nuclear Systems," 4th Semiannual Report to EPRI, Contract No. RP1237-1, General Electric Company, Schenectady, New York, July 1, 1980 - January 31, 1981.

[7-4] S. D. Conte and C. deBoor, Elementary Numerical Analysis, Second Edition, McGraw-Hill Book Company, New York, 1972.

[7-5] C. F. Shih, H. G. deLorenzi, and W. R. Andrews, "Studies on Crack Initiation and Stable Crack Growth," in Elastic-Plastic Fracture, ASTM Special Technical Publication 668, 1979, pp. 65-120.

[7-6] C. F. Shih and V. Kumar, "Estimation Technique for the Prediction of Elastic-Plastic Fracture of Structural Components of Nuclear Systems," 1st Semiannual Report to EPRI, Contract No. RP1237-1, General Electric Company, Schenectady, New York, July 1, 1978 - January 31, 1979.

[7-7] V. Kumar and C. F. Shih, "Fully Plastic Crack Solutions, Estimation Scheme and Stability Analyses for Compact Specimen," in Fracture Mechanics, ASTM Special Technical Publication 700, 1980, pp. 406-438.

[7-8] W. R. Andrews and C. F. Shih, "Thickness and Side-Groove Effects in J-Resistance Curves," in Elastic-Plastic Fracture, ASTM Special Technical Publication 668, 1979, pp. 426-450.

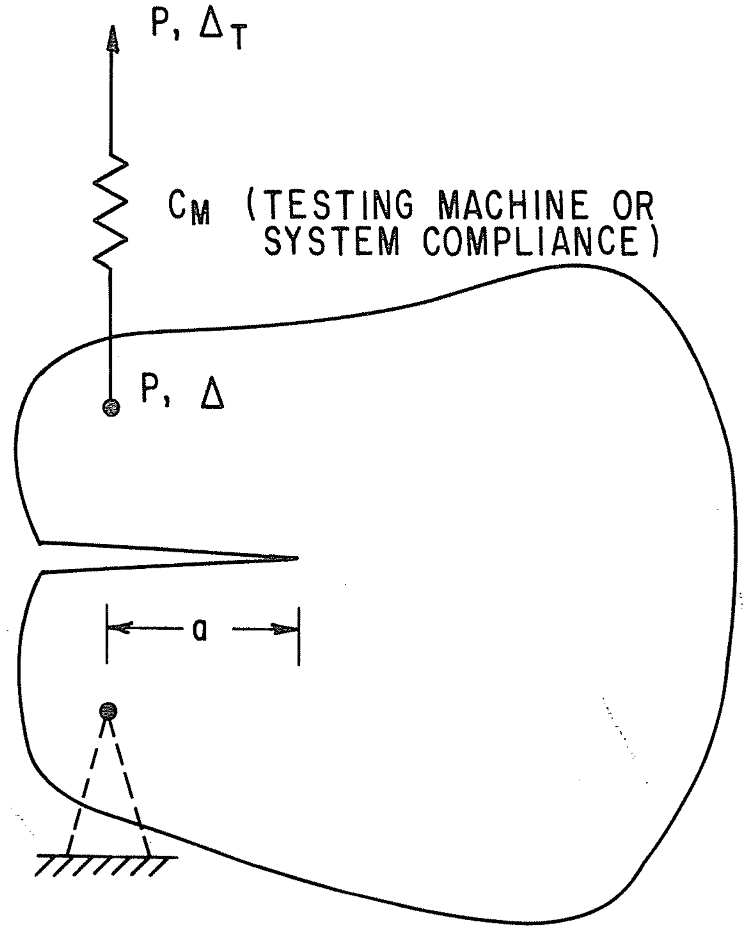

Figure 7-1. Schematic of a cracked body with a linear spring in series which represents the compliance of testing machine or loading system.

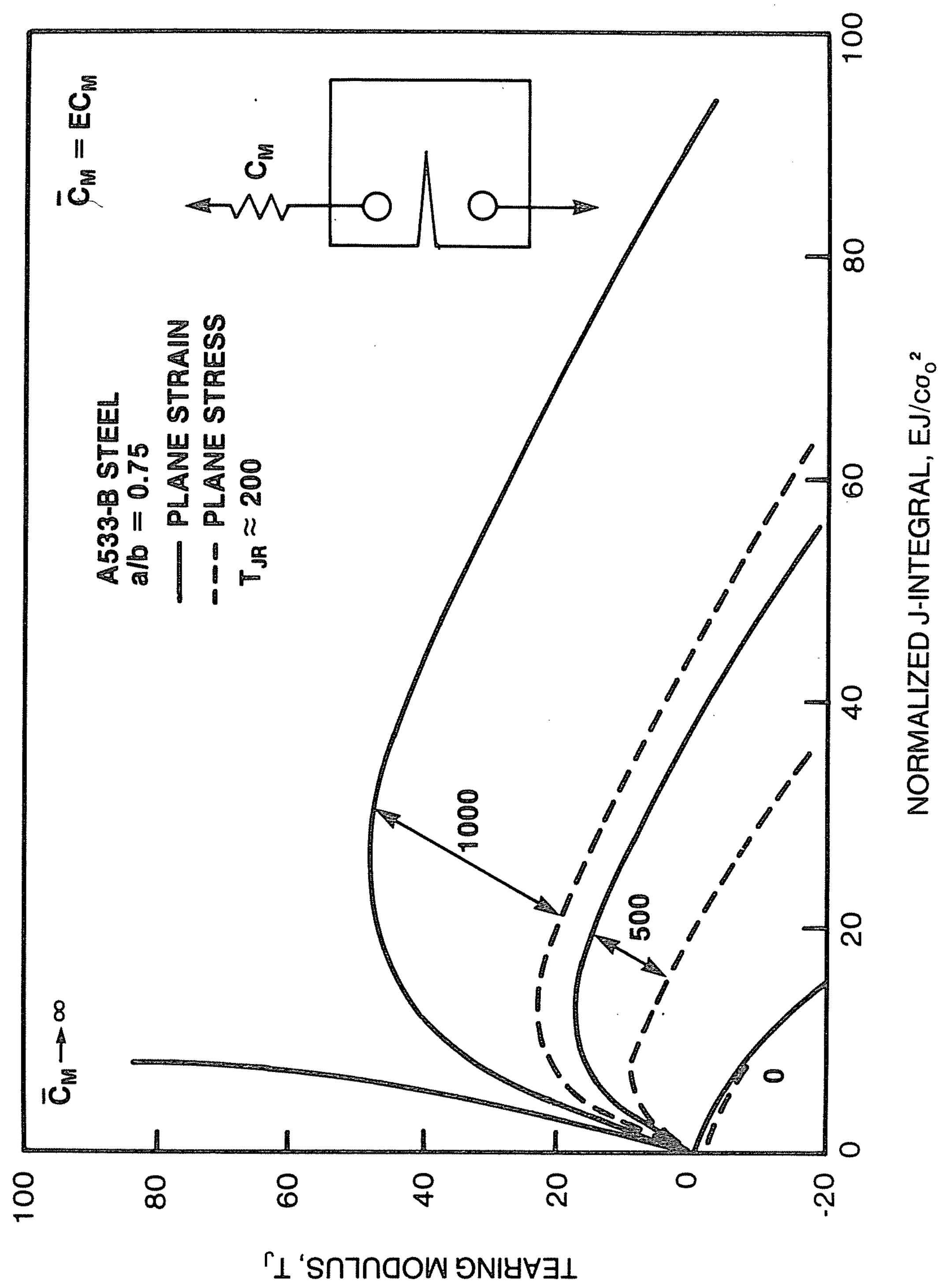

Figure 7-2. Stability diagram for a deeply cracked compact specimen of A533B steel.

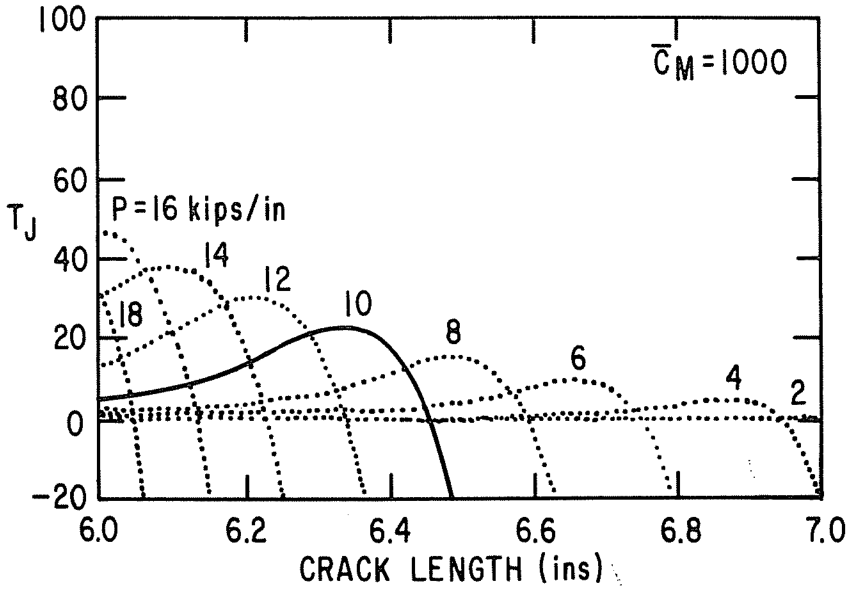

Figure 7-3. Variation of T_J with crack length at several values of applied load for a 4T, A533B steel, plane strain compact specimen. $\bar{C}_M = 1000$.

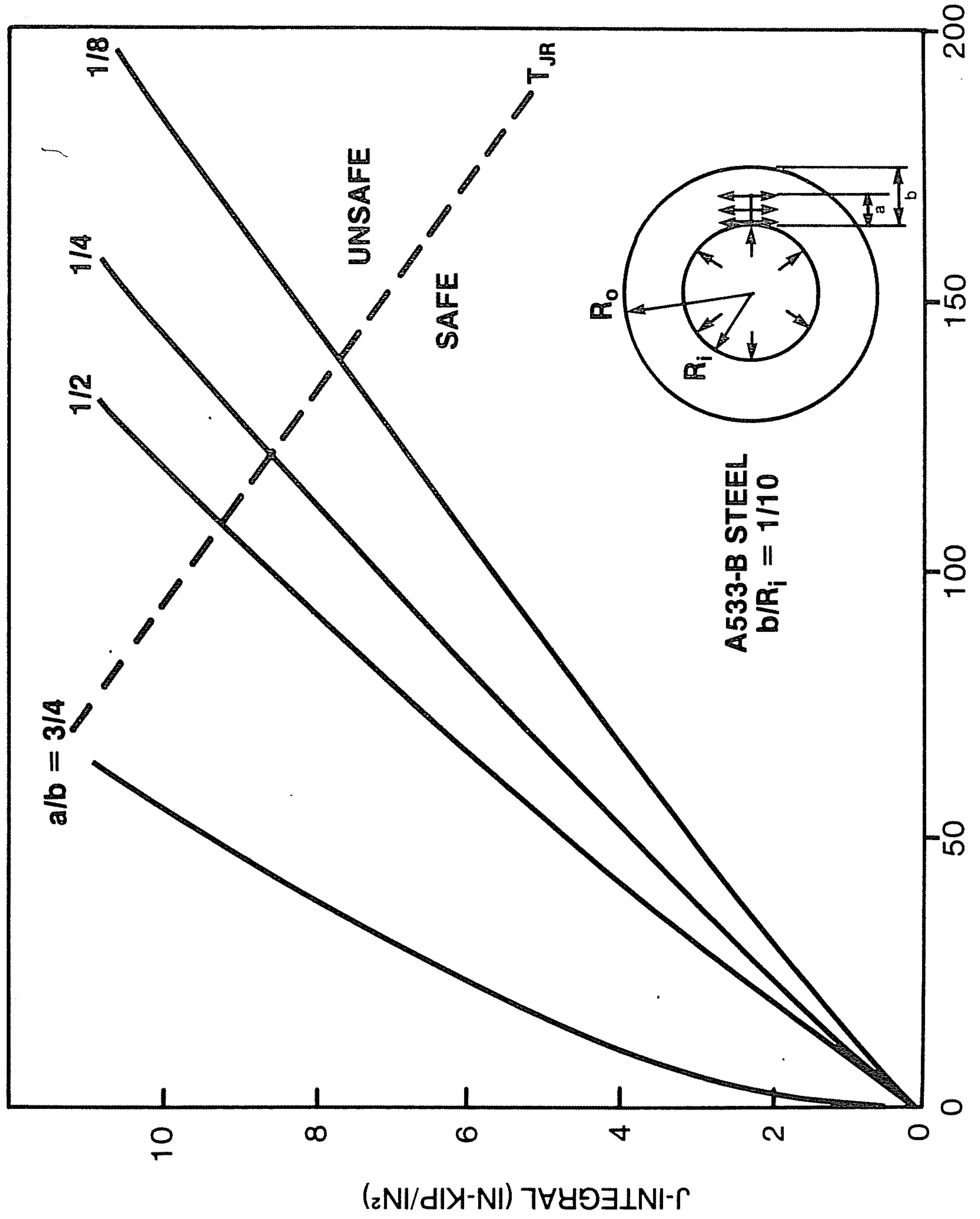

Figure 7-4. J versus T_J stability diagram for an internally pressurized, axially cracked cylinder of A533B steel. The material J_R - T_{JR} curve is shown by the dashed line.

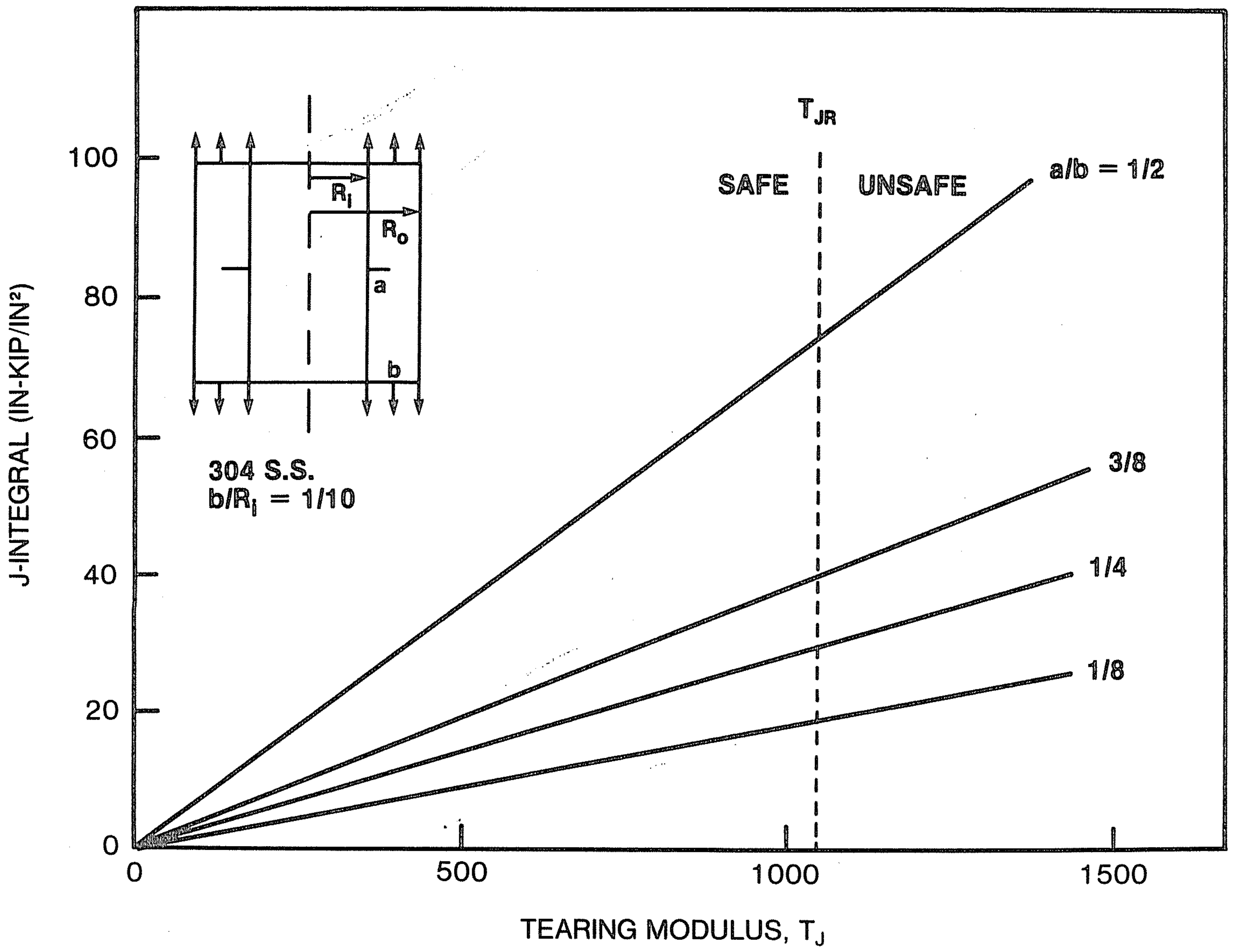

Figure 7-5. J versus T_J stability diagram for a circumferentially cracked cylinder of 304 stainless steel. The material $J_R - T_{JR}$ curve is shown by the dashed line.

Section 8
FAILURE ASSESSMENT DIAGRAM

8.1 INTRODUCTION

The failure assessment diagram, introduced in Section 2,will be discussed in detail in this section. These diagrams are convenient in a preliminary investigation of the safety margin of a flawed structure. The concept of a failure assessment diagram has mainly evolved from work at the Central Electricity Generation Board (CEGB) of the United Kingdom, and is based on the "two criteria" approach of Dowling and Townley [8-1]. The present form, also referred to as the R-6 diagram, is due to Harrison, Loosemore and Milne [8-2]. It was generalized to include consideration of thermal and residual stresses and crack growth by Chell [8-3] and Milne [8-4], respectively.

In essence, a failure assessment or R-6 diagram represents a transition curve or interpolation between two distinctly separate mechanisms of failure: brittle fracture as governed by the LEFM defined fracture toughness, K_{Ic}, and plastic collapse governed by the limit load, P_o. In the CEGB approach, the interpolation curve between these two cases is obtained by using the Dugdale solution for the plane stress problem of a finite crack in an infinite sheet of elastic-perfectly plastic material subject to remote tension. The coordinates employed in such a diagram are K_r and S_r, which are defined as follows:

$$K_r = \frac{K_I(a,\ P)}{K_{Ic}}$$

$$S_r = \frac{P}{P_o}$$

$K_I(a,\ P)$ is the elastic stress intensity factor. A typical R-6 diagram is illustrated in Fig. 8-1. The region bounded by the axes and the failure (R-6) line is the safe regime. Any load and crack size combination that falls beyond the failure line may lead to failure of the structure being analyzed. In marginal situations where the point defining load and crack size lies in close vicinity of the failure line, a more detailed evaluation using the crack driving force diagram or stability diagram will yield a more precise estimate of the safety margin.

The failure assessment diagram can be derived using the J-controlled crack growth concept [8-5, 8-6], which shows that the failure line depends on the geometry of the cracked body and the type of loading and material deformation properties. The R-6 line, though independent of these factors, is observed to be a useful approximation to the actual failure lines for configurations examined with the present elastic-plastic solutions. This is particularly so for ferritic steels, as will be observed in some of the ensuing examples. Incorporation of the material strain-hardening into the failure assessment diagram has also been carried out by Bloom [8-7].

8.2 DERIVATION OF THE FAILURE ASSESSMENT DIAGRAM BASED ON J-CONTROLLED GROWTH

As discussed in Section 2, under J-controlled crack growth conditions the equilibrium of crack growth requires the driving force to equal the resisting force, i.e.,

$$J(a,\ P) = J_R(\Delta_a) \tag{8-1}$$

From the estimation procedure, the crack driving force is expressed as

$$J = J^e(a_e) + J^p(a,\ n)$$

or

$$J = \hat{J}(a_e)\left[\frac{P}{P_o}\right]^2 + \hat{J}(a,\ n)\left[\frac{P}{P_o}\right]^{n+1} \tag{8-2}$$

The equality of Eq. (8-1) then becomes

$$\hat{J}(a_e)\left[\frac{P}{P_o}\right]^2 + \hat{J}(a,\ n)\left[\frac{P}{P_o}\right]^{n+1} = J_R(\Delta a) \tag{8-3}$$

The latter equation can be rearranged to yield

$$\frac{J^e(a,\ P)}{\hat{J}(a_e)\left[\frac{P}{P_o}\right]^2 + \hat{J}(a,\ n)\left[\frac{P}{P_o}\right]^{n+1}} = \frac{J^e(a,\ P)}{J_R(\Delta a)} \tag{8-4}$$

where J^e is the elastic crack driving force and has the form

$$J^e(a,\ P) = \bar{J}(a)\left[\frac{P}{P_o}\right]^2 . \tag{8-5}$$

Note that the functional forms of J and $\bar{J}$ are not identical because P_o is defined based on a rather than a_e.

By definition J^e is related to K by

$$J^e = K^2/E' \tag{8-6}$$

where E' = E for plane stress problems and E' = E/(1 − v^2) for plane strain problems. $\hat{J}(a)$ can of course be determined directly from available solutions for K. A consequence of J-controlled growth is

$$E'\ J_R(\Delta a) = K_R^2(\Delta a) \tag{8-7}$$

where the K_R curve is obtained under small-scale yielding conditions. The equality (or identity) holds at the same amount of physical crack growth as long as J-controlled growth conditions are met.

The following dimensionless ratios for stress and crack driving force are defined:

$$S_r = \frac{P}{P_o} \tag{8-8}$$

$$K_r = K_I(a,\ P)/K_R(\Delta a) \tag{8-9}$$

$$J_r = J^e(a,\ P)/J_R(\Delta a) \tag{8-10}$$

It follows from Eqs. (8-6) and (8-7) that

$$K_r^2(a,\ P,\ \Delta a) = J_r(a,\ P,\ \Delta a) \tag{8-11}$$

Substituting Eqs. (8-8) through (8-11) into (8-4) gives

$$\frac{S_r^2}{H_e\ S_r^2 + H_n\ S_r^{n+1}} = J_r = K_r^2 \tag{8-12}$$

where

$$H_e = \hat{J}(a_e)/\overline{J}(a) \tag{8-13}$$

and

$$H_n = \hat{J}(a,\ n)/\overline{J}(a) \tag{8-14}$$

Eq. (8-12) describes a curve in the space of K_r and S_r where the crack driving force (under dead load condition) is in equilibrium with the material resistance. The shape and location of the equilibrium curve depends on the crack configuration and material properties including the hardening exponent since H_e and H_n depend on these quantities. The curve defines the equilibrium crack growth state in terms of the applied load, P, and the crack length, a, for a given amount of crack extension. For example, if crack initiation is defined as failure (i.e., setting $\Delta a = 0$ in the above considerations), then $K_R = K_{Ic}$ and $J_R = J_{Ic}$ and the elastic driving force terms in Eqs. (8-9) and (8-10) are normalized by the respective crack initiation resistance. In this case Eq. (8-12) defines the equilibrium state for crack initiation in terms of P and a. By considering several values of Δa, Eq. (8-12) specifies the equilibrium states for a given crack configuration undergoing crack extension.

The R-6 line can be derived in this fashion to express the crack driving force. That is, in place of Eq. (8-1),

$$J(a,\ \sigma^\infty) = \frac{8}{\pi}\,\sigma_o\ \varepsilon_o\ a\ \ln\left[\sec\left(\frac{\pi}{2}\,\frac{\sigma^\infty}{\sigma_o}\right)\right]\ . \tag{8-15}$$

On substituting Eq. (8-15) into Eq. (8-1), rearranging and applying the definitions Eqs. (8-8) - (8-11), the equilibrium curve, Eq. (8-12), becomes the failure line of Harrison, Loosemore and Milne [8-2] for crack initiation and Milne [8-3]

for crack growth:

$$\frac{S_r^2}{\frac{8}{\pi^2}\ \ln\left[\sec\left(\frac{\pi}{2}\ S_r\right)\right]} = J_r = K_r^2 \tag{8-16}$$

Eqs. (8-12) and (8-16) are a restatement of the equilibrium condition for crack growth in terms of the stress ratio S_r and elastic force K_r or J_r. A graphical interpretation of the developments is given in Fig. 8-2. Part a shows J as a function of crack length with applied load held fixed for a given crack configuration. J_1 denotes the value of J at crack initiation. From the diagram, it is possible to identify the values $(a_1,\ P_1)$, $(a_2,\ P_2)$ and $(a_3,\ P_3)$ that will cause the crack to initiate. The pairs $(a_1,\ P_1)$, $(a_2,\ P_2)$, $(a_3,\ P_3)$ form a curve in the space of a and P, as shown in Part b of the figure. This is the crack initiation curve. Any combination of a and P which falls on the curve will cause crack initiation in the configuration under consideration. The process can be repeated for different levels of J, e.g., J_2, J_3 and so forth, corresponding to different amounts of crack growth. This generates the family of crack growth curves indicated in Fig. 8-2b. By normalizing the ordinate and abscissa of the diagram through the parameters K_r and S_r, the family of curves collapses into a single crack growth curve for the configuration under consideration, as indicated in Fig. 8-2c.

Failure lines can be derived in similar fashion for other stress-strain laws. One example pursued in the present work [8-5, 8-6] applies to very ductile materials which strain harden and eventually reach a saturation stress σ_s; 304 stainless steel is an example of such a material [8-8 - 8-10]. The stress-strain law is expressed in the form

$$\frac{\varepsilon}{\varepsilon_o} = \frac{\sigma}{\sigma_o} + \alpha\left(\frac{\sigma}{\sigma_o}\right)^n + \beta\left(\frac{\sigma}{\sigma_s}\right)^m \tag{8-17}$$

where α and β are material constants and $m/n >> 1$. In the range between σ_o and σ_s, the primary contribution to the strain comes from the strain-hardening term, but beyond σ_s the strain is dominated by the last term in Eq. (8-17) and the material behaves like a perfectly plastic material.

In deriving an expression for the failure curve, the following definitions are made:

$$\mu = \frac{\sigma_s}{\sigma_o} \tag{8-18}$$

$$P_s = \Lambda c \sigma_s \tag{8-19}$$

$$S_r = \frac{P}{P_s} \tag{8-20}$$

where Λ is the constraint factor and c, the uncracked ligament. Using the estimation procedure the failure line for a material obeying Eq. (8-17) is [8-5, 8-6]

$$\frac{S_r^2}{H_e S_r^2 + H_n(\mu S_r)^{n+1} + H_m S_r^{m+1}} = J_r = K_r^2 \tag{8-21}$$

where

$$H_m = \hat{J}(a, m)/\bar{J}(a) \tag{8-22}$$

and H_e and H_n are as given by Eqs. (8-13) and (8-14).

8.3 FAILURE ASSESSMENT DIAGRAMS FOR SEVERAL CRACK CONFIGURATIONS

8.3.1 Failure Curves Considering No Crack Growth

The basic input for construction of failure assessment diagrams are the linear elastic and the fully plastic crack solutions for the relevant structural configuration. The fully plastic solutions given in Sections 3 and 4 will be used in the present examples. The elastic solutions are taken from Reference [8-11].

The failure line for a strain-hardening material described by the Ramberg-Osgood stress-strain relationship is given by Eq. (8-12). As discussed previously, the shape and position of the failure line in the space of K_r and S_r is dependent on crack configuration, deformation properties and state of stress. This is illustrated with the series of failure assessment diagrams shown in Figs. (8-3)

through (8-6).

Fig. (8-3) shows failure lines for the center-cracked panel in plane stress as a function of strain-hardening exponent. The R-6 curve is also indicated. All the curves intersect the ordinate at unity, and in the case of the R-6 curve, they intersect the abscissa at unity. The strain-hardening solutions approach the abscissa asymptotically at $S_R > 1.0$. The curves for strain-hardening materials will shift closer to the R-6 curve if S_r is defined from the limit load based on the flow stress σ_f. In any event, the R-6 curve appears to provide a reasonable lower bound.

The dependence of the failure curves on the crack length-to-width ratio is shown in Fig. 8-4. The curves are only slightly dependent on relative crack lengths, suggesting that in the analysis of small amounts of crack growth, a failure assessment curve based on the original crack length may yield information within acceptable accuracy.

The dependence of the failure line on stress-state and applied loading is illustrated in Fig. 8-5, which shows curves for plane stress and plane strain in the CCP and CS for single n and a/b values. The differences are not large, and again the R-6 curve appears a reasonable lower bound.

Failure assessment diagrams for axially and circumferentially cracked cylinders are shown in Fig. 8-6 for A533B steel and 304 stainless steel. The crack length-to-wall thickness ratio was chosen to match the deepest relative crack depth for the maximum postulated flaw size in the ASME Pressure Vessel and Piping Code. The R-6 curve is also indicated in the diagram. It can be observed that the examples for 304 SS do lie in part below the R-6 curve.

Examples of failure assessment diagrams based on the saturation stress model, Eq. (8-21), are presented in References [8-5, 8-6].

8.3.2 Failure Curves for Changing Crack Size

The failure curves in Figs. 8-3 through 8-6 were constructed for fixed crack length-to-width ratios. As was noted in the example of Fig. 8-4, the variation in the curves for small amounts of crack growth is relatively insignificant.

When there are substantial amounts of crack growth, the failure line can be reconstructed for varying crack length. This point is illustrated in Fig. 8-7 with the plane strain compact specimen, which undergoes substantial stable crack growth. In Fig. 8-7, the dashed lines correspond to failure curves for crack length-to-width ratio (a/b) of 0.25, 0.50 and 0.75. When there is sufficient crack growth, the relative crack length is changing and therefore the equilibrium curve will shift. This is illustrated by the solid curves in Fig. 8-7 for a/b of 0.25 and 0.50. These curves were calculated for a 4T compact specimen of A533B steel using the mean J_R curve reported in Reference [8-5]. The solid curves in Fig. 8-7 are obtained by adjusting the values of the quantities H_e and H_n in Eq. (8-12) according to the "updated" crack length determined from the J_R curve.

8.4 APPLICATIONS OF THE FAILURE ASSESSMENT DIAGRAM

To employ the failure assessment diagram for structural integrity analysis, the following steps should be taken:

1. The failure line for the specific crack configuration should be constructed using Eq. (8-12), (8-16) or (8-21), whichever is considered most appropriate for the material and structure of interest.

2. For the given crack configuration, and initial crack length a_o, K (or J^e) is computed using a handbook such as Reference [8-11]. The values of K are normalized by K_{Ic} (or J_{Ic}) to obtain K_r. The stress ratio S_r is obtained by normalizing the applied load P by the limit load for the crack configuration being examined.

3. The point K_r, S_r is now placed on the failure assessment diagram. There are two possible situations. If the point lies inside the region bounded by the axes and the failure curve, the structure is safe. If the point falls on or beyond the failure curve, the crack in the structure will initiate. If failure is defined on the basis of crack initiation, then the structure is unsafe or has failed. If the design or safety analysis tolerates crack growth, the load carrying capacity of the structure can be evaluated further.

4. For the case where the load point falls beyond the safe region, the crack in the structure is incremented by an amount Δa. The limit load for the structure is computed for the current crack length $a_o + \Delta a$. The applied load normalized by the limit load defines the updated stress ratio S_r. Based on the current load and crack length, the updated K (or J^e) is computed. The value of K_R (or J_R) corresponding to crack growth of Δa is obtained from the resistance curve for the material; K_r is given by the ratio $K(a_o + \Delta a)$ and $K_R(\Delta a)$.

5. The updated point K_r, S_r is again placed on the diagram and the preceding steps (3) and (4) are repeated.

By the above process, the crack growth behavior and the load carrying capacity of the structure can be determined. If there is substantial stable crack growth, then the failure curve (or equilibrium curve) itself should be updated to correspond to the updated crack lengths. In general, changes in the failure curve itself are negligible for small amounts of crack growth. The above analysis procedure is based on load-controlled conditions. The diagram can also accommodate displacement-controlled conditions with finite compliance. However the procedure becomes more complex for displacement-controlled systems, and it may be easier to obtain similar information directly from a crack driving force diagram analysis discussed in Section 6.

8.5 REFERENCES

[8-1] A. R. Dowling and C. H. A. Townley, "The Effects of Defects on Structural Failure: A Two-Criteria Approach," International Journal of Pressure Vessel and Piping, Vol. 3, 1975, pp. 77-137.

[8-2] R. P. Harrison, K. Loosemore, and I. Milne, "Assessment of the Integrity of Structures Containing Defects," CEGB Report No. R/H/R6, Central Electricity Generating Board, United Kingdom, 1976.

[8-3] G. G. Chell, "A Procedure for Incorporating Thermal and Residual Stresses into the Concept of a Failure Assessment Diagram," in Elastic-Plastic Fracture, ASTM Special Technical Publication 668, 1979, pp. 581-605.

[8-4] I. Milne, "Failure Analysis in the Presence of Ductile Crack Growth," Materials Science and Engineering, Vol. 39, No. 1, 1979, pp. 65-79.

[8-5] C. F. Shih, M. D. German, and V. Kumar, "An Engineering Approach for Examining Crack Growth and Stability in Flawed Structures," General Electric Company TIS Report No. 80CRD205, September 1980; also in press, International Journal of Pressure Vessels and Piping.

[8-6] C. F. Shih, V. Kumar, and M. D. German, "Studies on the Failure Assessment Diagram Using the Estimation Scheme and J-Controlled Crack Growth Approach," General Electric Company TIS Report, 1981, to appear.

[8-7] J. M. Bloom, "Prediction of Ductile Tearing Using a Proposed Strain Hardening Failure Assessment Diagram," International Journal of Fracture, Vol. 6, 1980, pp. R73-R77.

[8-8] C. S. Hartley, D. A. Jenkins, and J. J. Lee, "Tensile Properties of Zircaloy 4 and 304 Stainless Steel at Constant True Strain Rates," in Transactions of 5th International Conference on Structural Mechanics in Reactor Technology, Vol. C, Paper C3/13, 1979.

[8-9] D. M. Norris, Jr., private communication, 1979.

[8-10] D. M. Norris, Jr., B. Moran, J. K. Scudder, and D. F. Quinones, "A Computer Simulation of the Tension Test," Journal of Mechanics and Physics of Solids, Vol. 26, 1978, pp. 1-19.

[8-11] H. Tada, P. C. Paris, and G. R. Irwin, "The Stress Analysis of Cracks Handbook," Del Research Corporation, Hellertown, Pennsylvania, 1973.

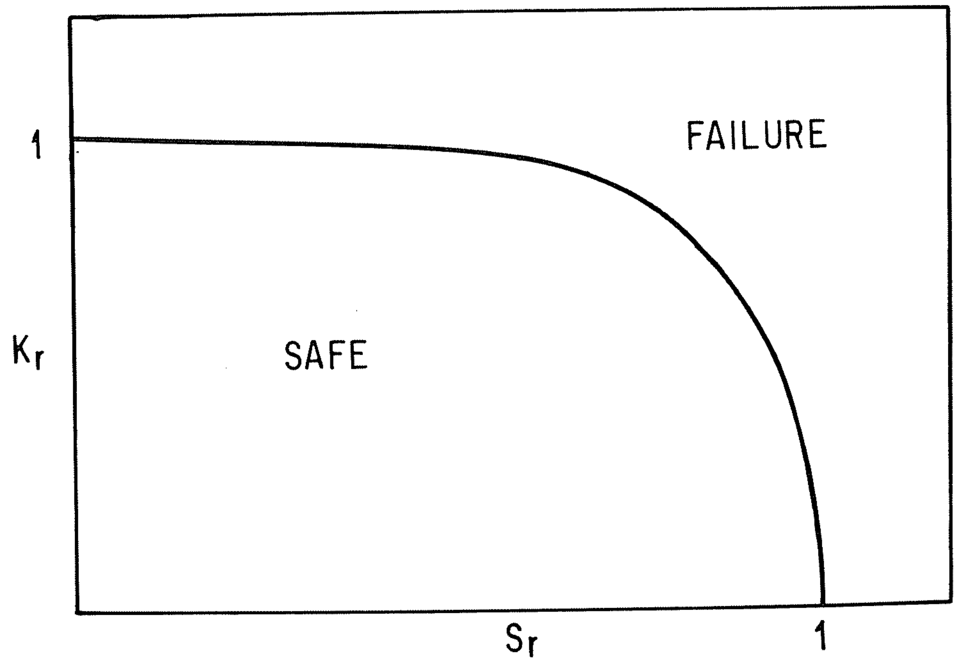

Figure 8-1. Schematic of a failure assessment diagram based on the British two-parameter approach.

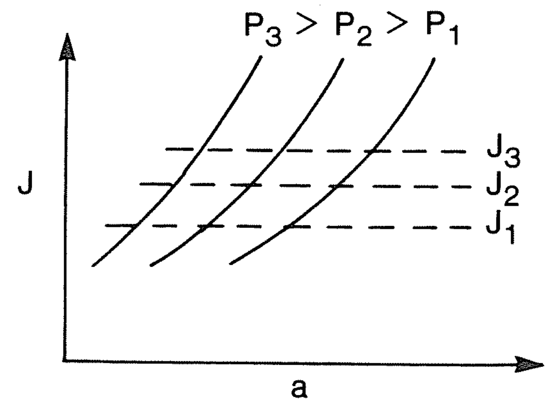

(a)
Crack Driving Force

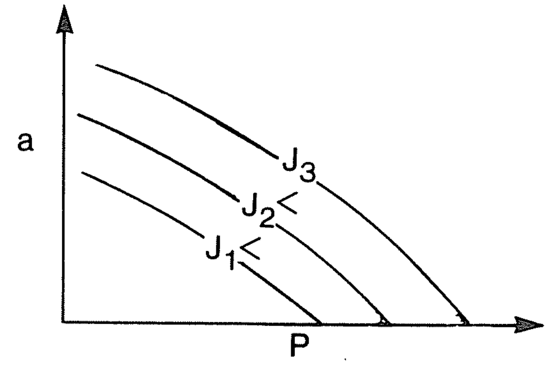

(b)
Equilibrium Curves
at Various Levels
of J

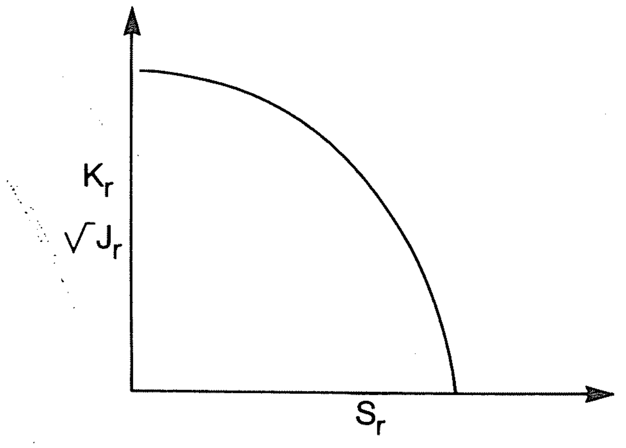

(c)
Single Failure Curve
where

$K_r = K/K_R = J^e/J_R$

$S_r = P/P_f$

Figure 8-2. Construction of failure assessment diagram from J-integral crack driving force. Generalized coordinates K_r and S_r collapse crack growth curves into single failure curve.

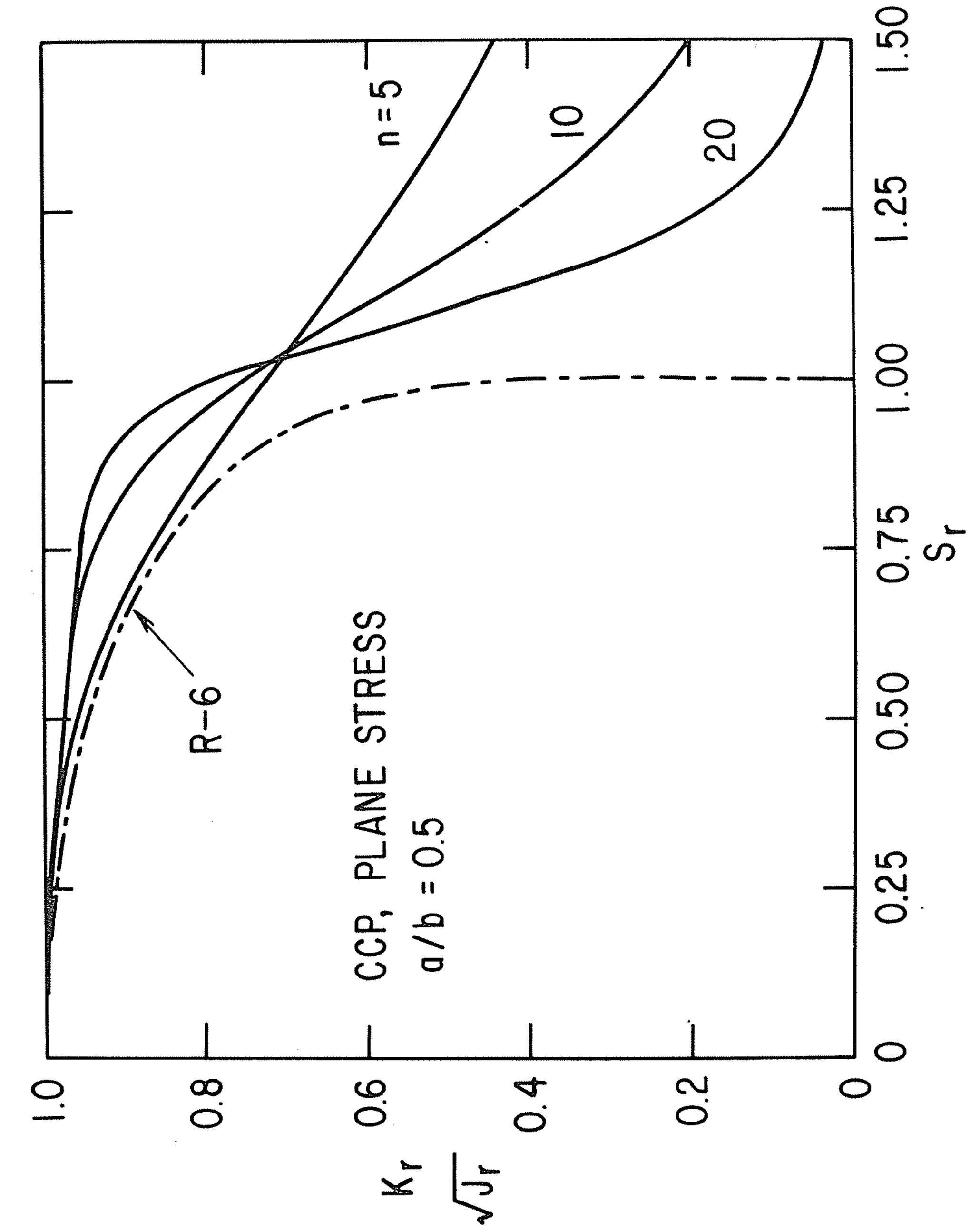

Figure 8-3. Plane stress failure curves for center-cracked plate for several values of strain-hardening exponent.

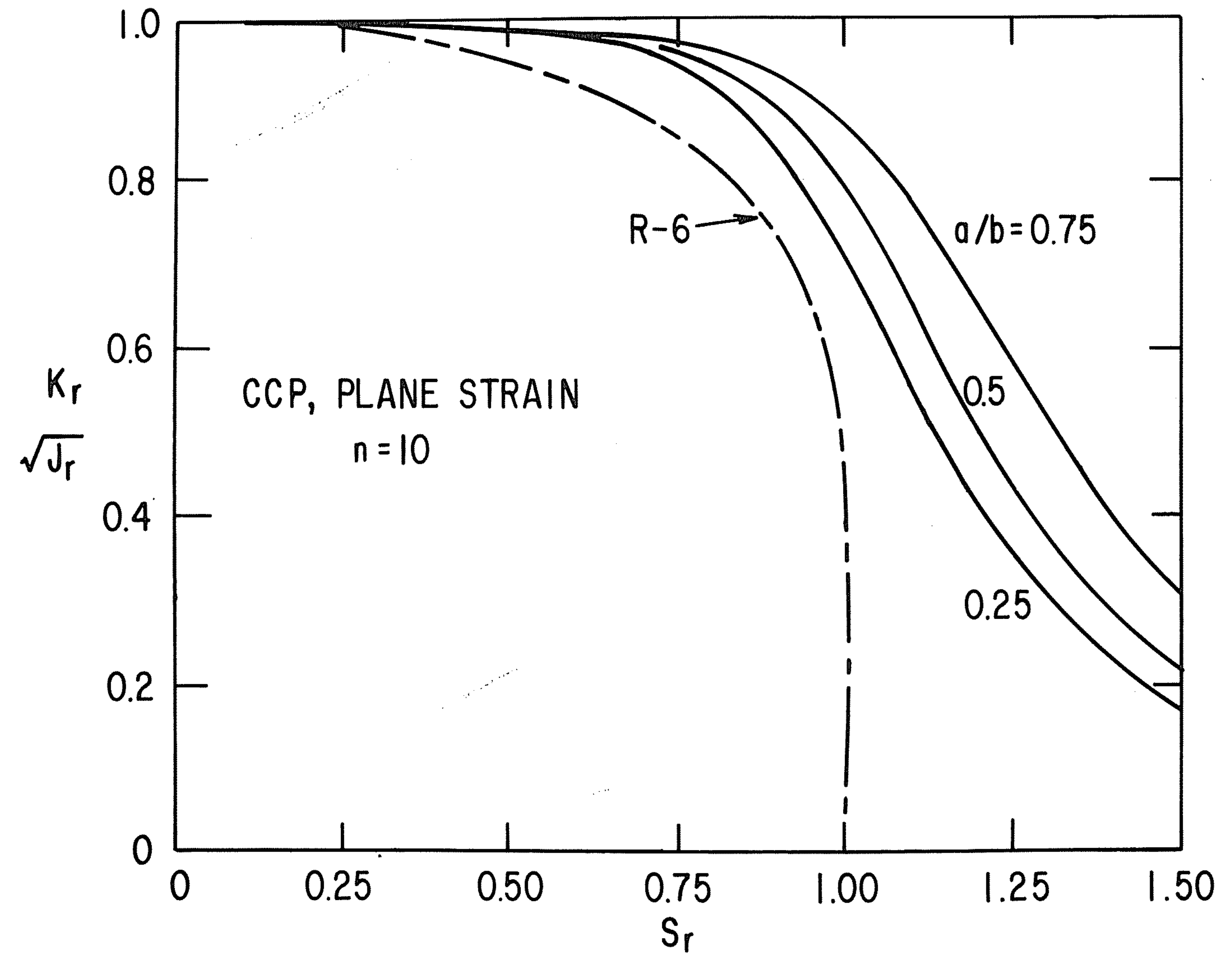

Figure 8-4. Plane strain failure curves for center-cracked plate for several crack length-to-width ratios.

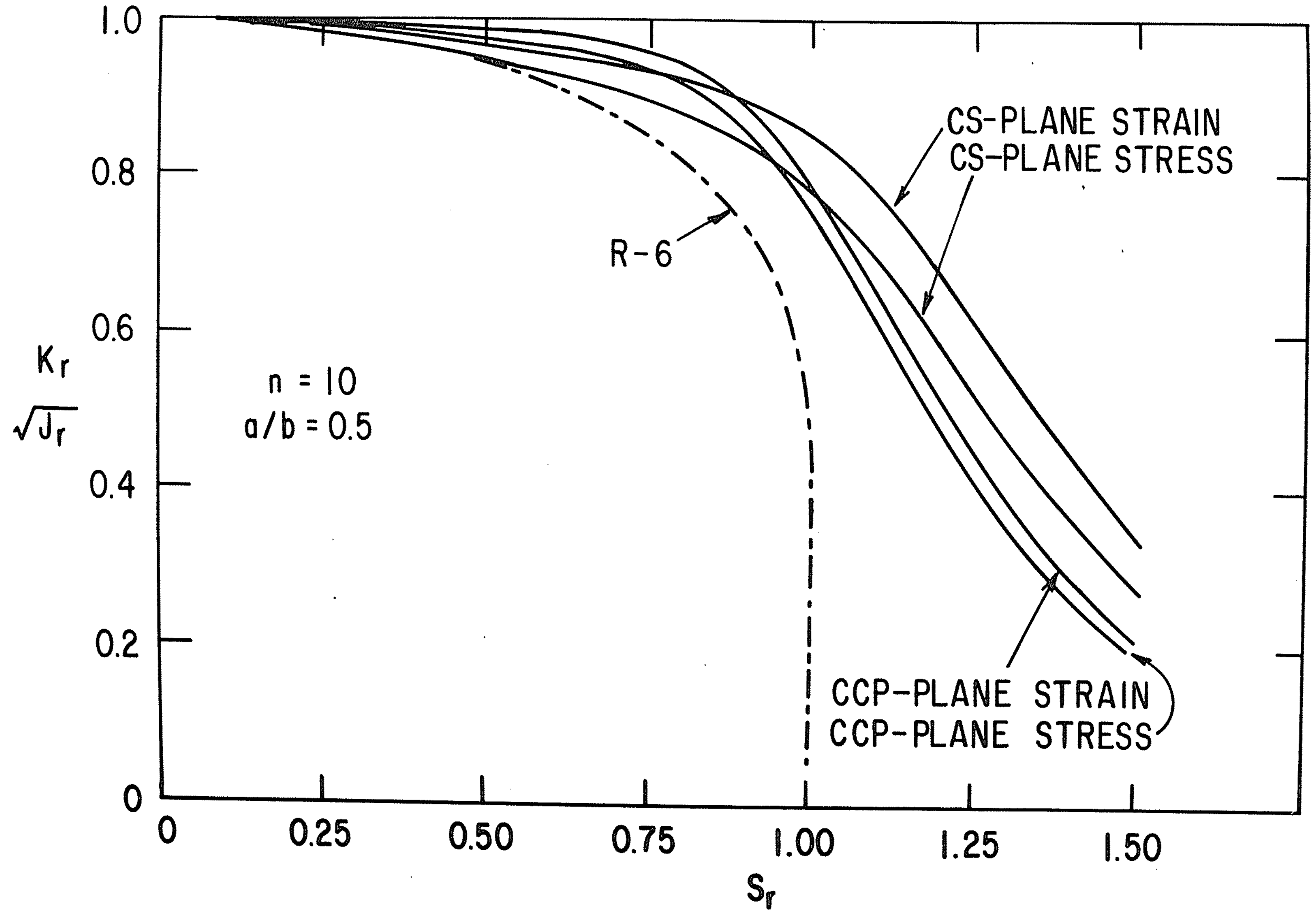

Figure 8-5. Plane strain and plane stress failure curves for center-cracked plate and compact specimen.

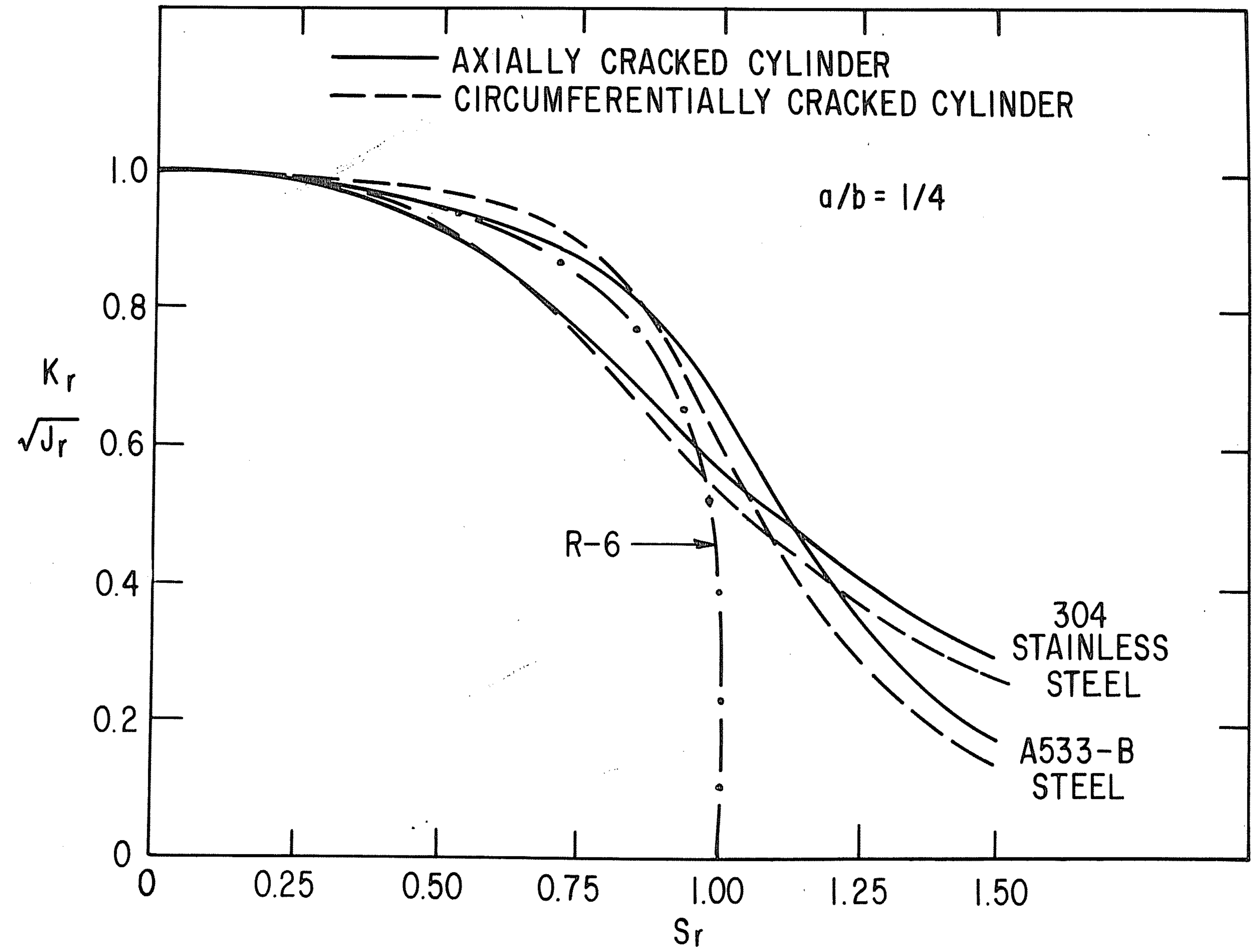

Figure 8-6. Failure curves for axially and circumferentially cracked cylinders.

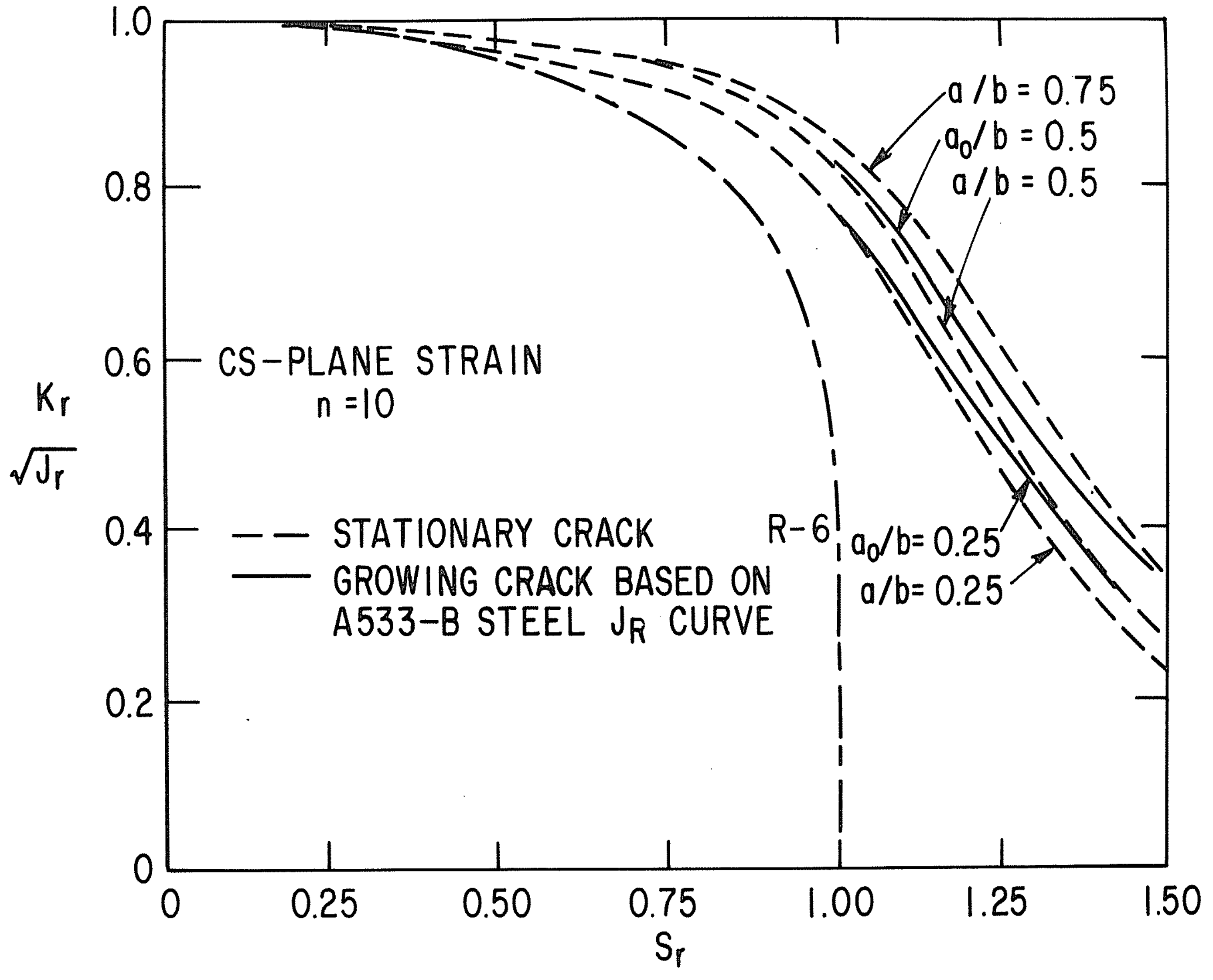

Figure 8-7. Plane strain crack growth curves for A533B steel, plane strain compact specimen with initial crack length-to-width ratios of 0.25 and 0.5.

APPENDIX A
ESTIMATION FORMULAE FOR SEVERAL STRESS-STRAIN
LAWS

Appendix A

ESTIMATION FORMULAE FOR SEVERAL STRESS-STRAIN LAWS

Estimation formulae were developed in Reference [A-1] for two variations of the Ramberg-Osgood stress-strain relationship. These will be defined in this appendix, together with two additional stress-strain relationships.

A.1 RAMBERG-OSGOOD RELATIONSHIP (ROR)

In the ROR the uniaxial strain is related to the uniaxial stress by

$$\frac{\varepsilon}{\varepsilon_o} = \frac{\sigma}{\sigma_o} + \alpha\left(\frac{\sigma}{\sigma_o}\right)^n \tag{A-1}$$

The estimation formulae for J, δ and Δ_c are

$$\begin{aligned} J &= J(a_e)\left[\frac{P}{P_o}\right]^2 + J(a,\ n)\left[\frac{P}{P_o}\right]^{n+1} \\ \delta &= \delta(a_e)\left[\frac{P}{P_o}\right] + \delta(a,\ n)\left[\frac{P}{P_o}\right]^2 \\ \Delta_c &= \Delta_c(a_e)\left[\frac{P}{P_o}\right] + \Delta_c(a,\ n)\left[\frac{P}{P_o}\right]^n \end{aligned} \tag{A-2}$$

As discussed in Reference [A-1], the formulae in Eq. (A-1) can be shown to be exact for the infinitely wide slab with a semi-infinite slit. For several finite crack configurations, Eq. (A-2) has been shown to be in excellent agreement with results from complete numerical calculations as discussed in Section 6 and in References [A-1, A-2].

A.2 PIECEWISE POWER LAW (PWPL)

In the PWPL representation, the uniaxial stress-strain relations are

$$\frac{\varepsilon}{\varepsilon_o} = \frac{\sigma}{\sigma_o} \qquad \sigma \leq \sigma_o \tag{A-3}$$

$$\frac{\varepsilon}{\varepsilon_o} = \left(\frac{\sigma}{\sigma_o}\right)^n \qquad \sigma > \sigma_o$$

The estimation formulae for J have the form

$$J = \hat{J}(a_e)\left[\frac{P}{P_o}\right]^2 \qquad P \leq P_o \tag{A-4}$$

$$J = J(a_e) + \hat{J}(a,\, n)\left\{\left[\frac{P}{P_o}\right]^{n+1} - 1\right\} \qquad P > P_o$$

where P_o is the limit load based on the material reference stress and the plastic constraint factor for the relevant crack configuration. Eq. (A-4) is also exact for the infinitely wide slab with semi-infinite slit. Similar formulae have been derived for δ and Δ_c. They can be inferred directly from the form for J in Eq. (A-4) and the scaling law [A-1]. These formulae were shown to be in good agreement with complete numerical calculations [A-1].

A.3 GENERALIZED RAMBERG-OSGOOD RELATIONSHIP (GROR)

The ROR can be generalized to include the concept of a material saturation stress denoted by σ_s. This generalized relationship is especially useful for the derivation of failure assessment diagrams for very ductile materials. The uniaxial stress-strain relationship for the GROR is

$$\frac{\varepsilon}{\varepsilon_o} = \frac{\sigma}{\sigma_o} + \alpha\left(\frac{\sigma}{\sigma_o}\right)^n + \beta\left(\frac{\sigma}{\sigma_s}\right)^m \tag{A-5}$$

where σ_o is the yield stress and σ_s is the saturation stress; σ_s is chosen to ensure that $m/n >> 1$. There are three regimes of deformation for the material described by Eq. (A-5). For applied stress σ less than σ_o, the strain is essentially elastic. In the range between σ_o and σ_s, the primary contribution to the strain comes from the strain-hardening term. For σ greater than σ_s, the strain

is dominated by the last term in Eq. (A-5); in the latter regime the material behaves like a perfectly plastic material. The estimation formula for J which is compatible with Eq. (A-5) is

$$J = \hat{J}(a_e)\left[\frac{P}{P_o}\right]^2 + \hat{J}(a,\, n)\left[\frac{P}{P_o}\right]^{n+1} + \hat{J}(a,\, m)\left[\frac{P}{P_s}\right]^{m+1} \tag{A-6}$$

where

$$P_s = \Lambda\, c\, \sigma_s. \tag{A-7}$$

Equation (A-6) can also be shown to be exact for the infinitely wide slab with a semi-infinite slit. By examining the functional forms for δ and Δ_c, estimation formulae similar to Eq. (A-6) can be derived for δ and Δ_c.

A.4 IMPROVED PIECEWISE POWER LAW (IMWPL)

There are many materials where the piecewise power law representation of the deformation behavior is more appropriate. However the representation using Eq. (A-3) introduces a sharp discontinuity in the slope of the stress-strain relationship at the yield stress. This discontinuity causes analytical difficulties in the analysis of crack growth stability. To circumvent these difficulties, the IPWPL representation of deformation behavior is employed. This representation gives a strictly linear behavior up to the yield stress σ_o and nonlinear behavior beyond σ_o with a continuous slope at all points in the stress-strain curve. Specifically,

$$\frac{\varepsilon}{\varepsilon_o} = \frac{\sigma}{\sigma_o} \qquad \sigma \leq \sigma_o \tag{A-8}$$

$$\frac{\varepsilon}{\varepsilon_o} = \frac{1}{n}\left(\frac{\sigma}{\sigma_o}\right)^n + \left(1 - \frac{1}{n}\right) \qquad \sigma \geq \sigma_o$$

The estimation formulae corresponding to Eq. (A-8) are

$$J = \hat{J}(a_e)\left[\frac{P}{P_o}\right]^2 \qquad P \leq P_o \tag{A-9}$$

$$J = J(a_e) + \hat{J}(a,\ n)\left\{\frac{1}{n}\left[\frac{P}{P_o}\right]^{n+1} - \frac{1}{n}\right\} \qquad P \geq P_o$$

Equation (A-9) can be shown to be exact for the infinitely wide slab with semi-infinite slit. Similar estimation formulae for δ and Δ_c can be obtained by appealing to their corresponding functional forms.

A.5 REFERENCES

[A-1] C. F. Shih, "J-Integral Estimates for Strain Hardening Materials in Antiplane Shear Using Fully Plastic Solutions," in Mechanics of Crack Growth, ASTM Special Technical Publication 590, 1976, pp. 3-22.

[A-2] C. F. Shih and J. W. Hutchinson, "Fully Plastic Solutions and Large-Scale Yielding Estimates for Plane Stress Crack Problems," Transactions of ASME, Journal of Engineering Materials and Technology, Series H, Vol. 98, No. 4, October 1976, pp. 289-295.

MODIFIED J-INTEGRAL EXPRESSIONS

APPENDIX B
MODIFIED J-INTEGRAL EXPRESSIONS

Appendix B

MODIFIED J-INTEGRAL EXPRESSIONS

B.1 J-INTEGRAL EXPRESSION FOR LOADED CRACK SURFACES

A modified expression for the J-integral to account for crack face loading has been derived by Karlsson and Backlund [B-1]. For the case of a constant pressure p on the crack surface, it is given by

$$J = \int_{\Gamma} (W\,dy - T \cdot \frac{\partial U}{\partial x}\,ds) + p\,U_y(-d,\ 0) \tag{B-1}$$

where the symbols are illustrated in Fig. B-1. For further details on the derivation the reader is referred to Reference [B-1].

B.2 J-INTEGRAL EXPRESSION FOR AXISYMMETRIC BODIES

Astiz, et al. [B-2], and Bergquist and Lan Huong [B-3] obtained modified expressions for energy release rate or the J-integral in problems of axial symmetry. In this case the J-integral, interpreted as energy release rate per unit crack advance in the radial direction and per unit length along the circumferential direction, is given by

$$J = \frac{1}{R_i + a} \{ \int_{\Gamma} r \left[W\,dz - (T_r \frac{\partial U_r}{\partial r} + T_z \frac{\partial U_z}{\partial r}) ds \right] - \int_S (W - T_{\theta} \frac{U_r}{r}) dS \} \tag{B-2}$$

where the coordinate system and other notations in the above equation are described in Fig. (B-2).

B.3 REFERENCES

[B-1] A. Karlsson and J. Backlund, "J-Integral at Loaded Crack Surfaces," International Journal of Fracture, Vol. 14, 1978, pp. R311-R314.

[B-2] M. A. Astiz, M. Elices, and V. Sanchez Galrez, "On Energy Release Rates in Axisymmetric Problems," in Fracture 1977, Vol. 3, ICF4, Waterloo, Canada, June 19-24, 1977, pp. 395-399.

[B-3] H. Bergkvist and G.-L. Lan Huong, "J-Integral Related Quantities in Axisymmetric Cases," International Journal of Fracture, Vol. 13, 1977, pp. 556-558.

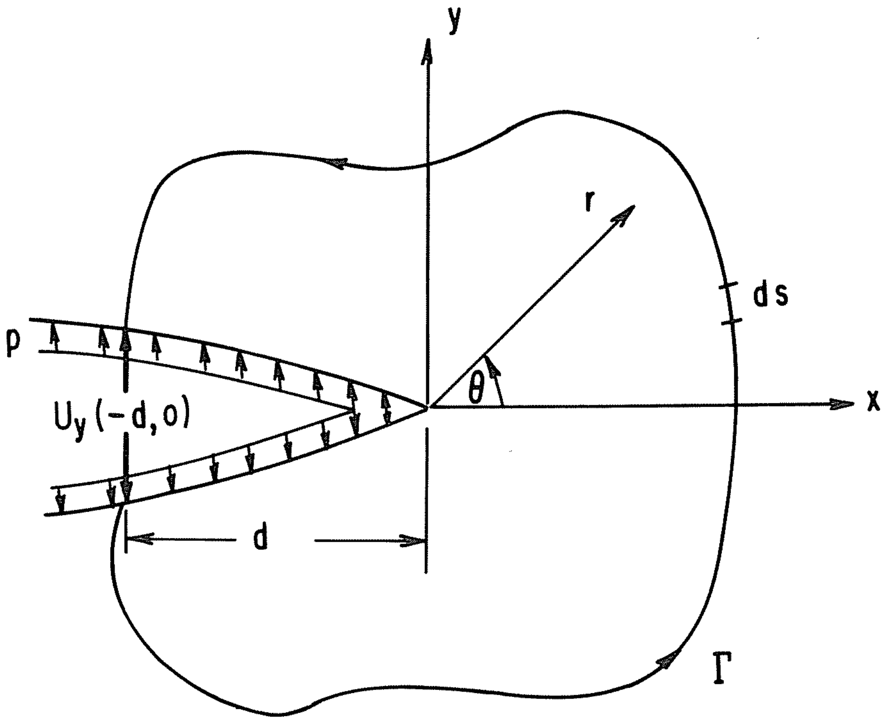

Figure B-1. Schematic of a cracked body with uniform pressure on the crack surface.

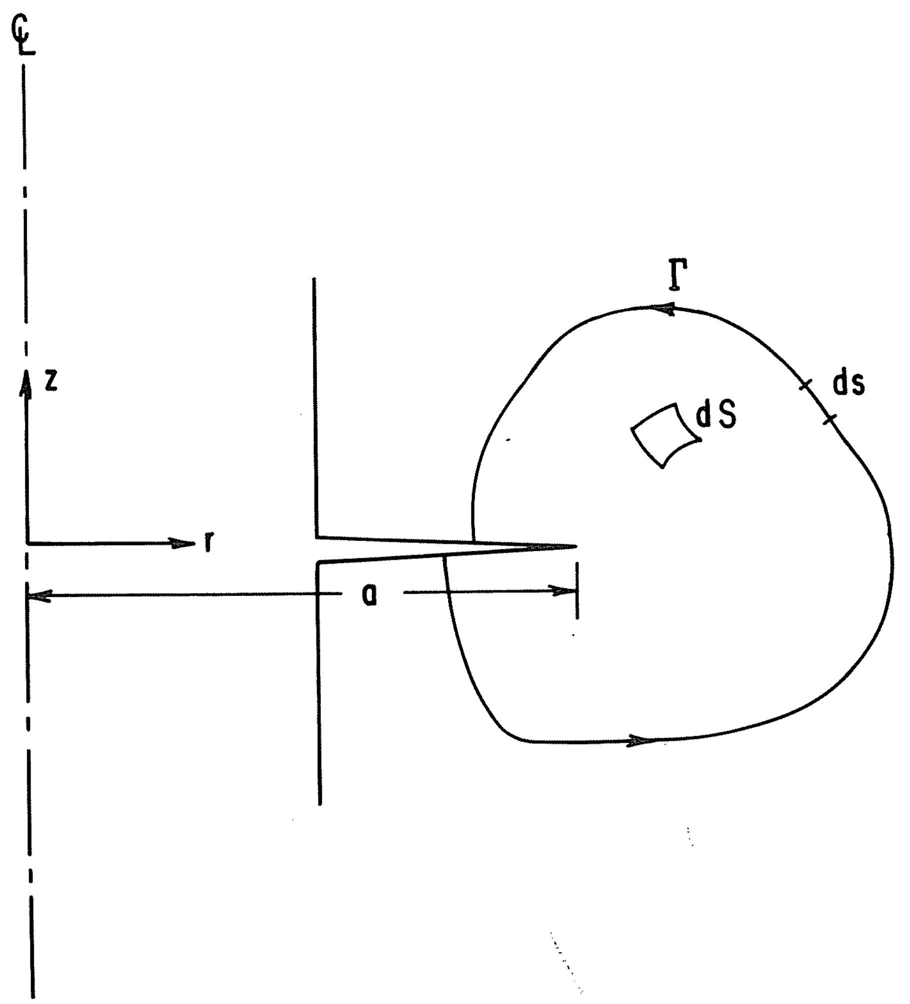

Figure B-2. Coordinate system and nomenclature employed in definition of J-integral for an axisymmetric crack. S is the area enclosed by contour Γ.

PLOTS OF h FUNCTIONS VERSUS 1/n

APPENDIX C
PLOTS OF h FUNCTIONS VERSUS 1/n

Appendix C

PLOTS OF h FUNCTIONS VERSUS 1/n

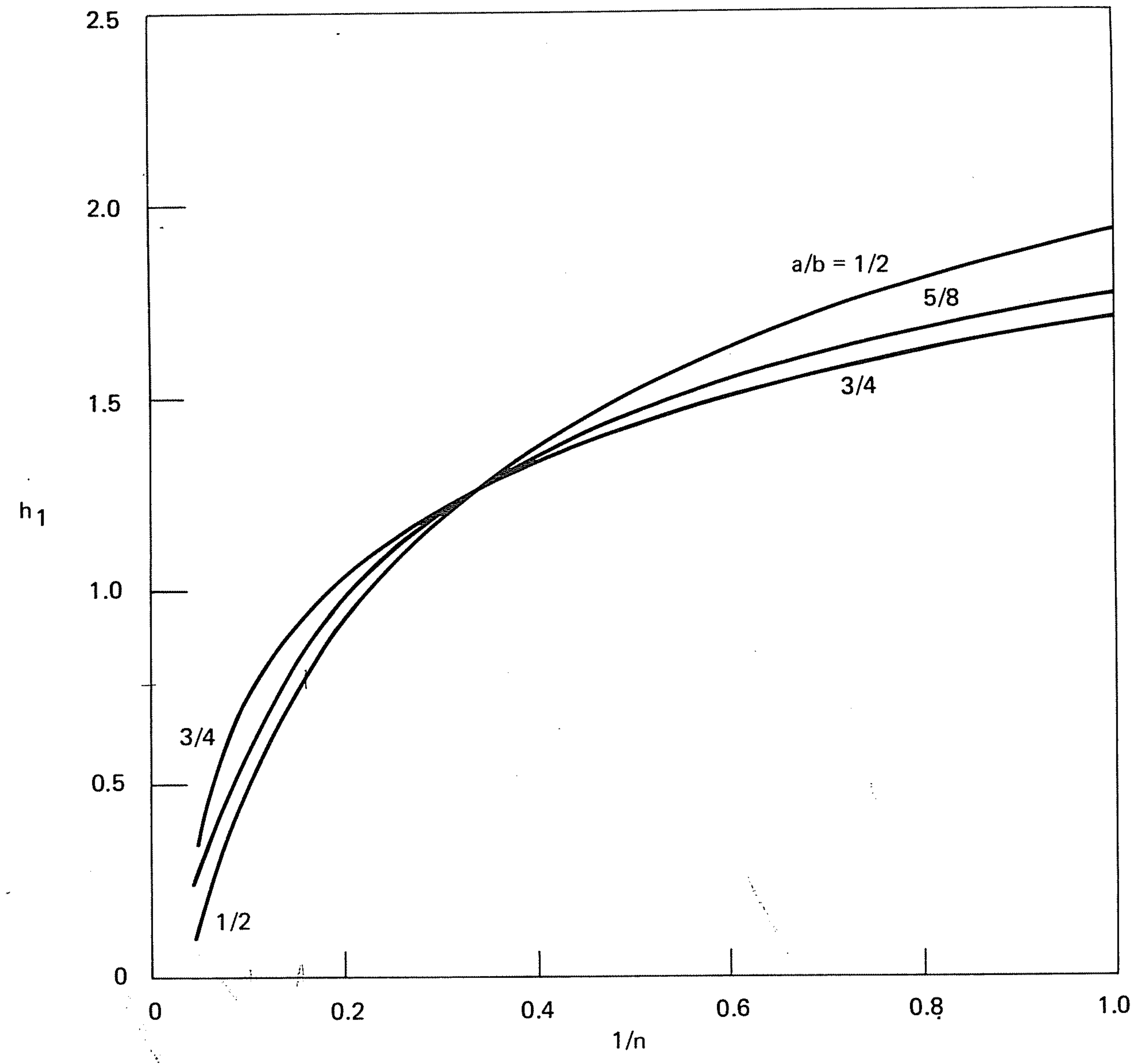

Figure C-1. h_1 versus 1/n for a compact specimen in plane strain.

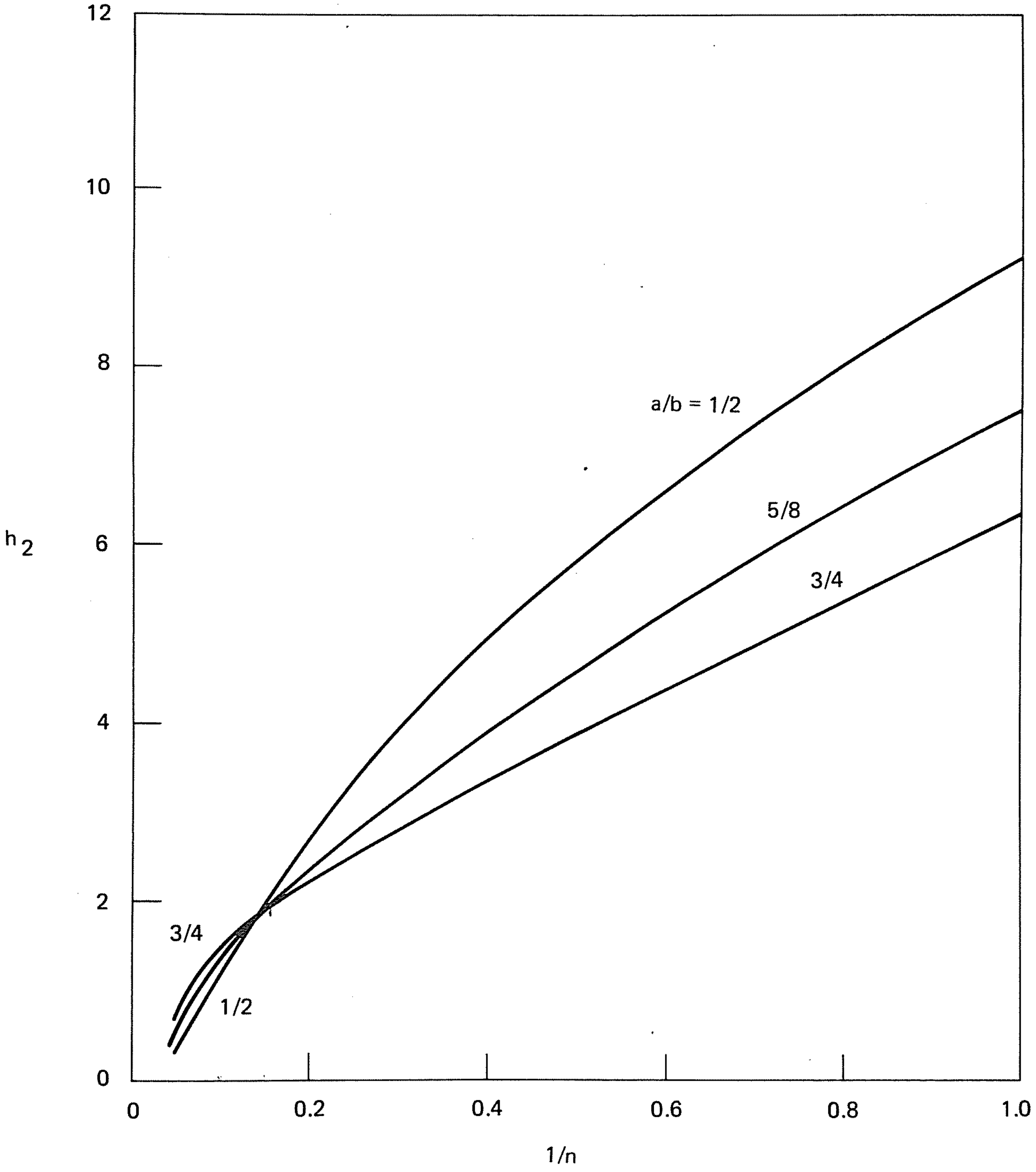

Figure C-2. h_2 versus 1/n for a compact specimen in plane strain.

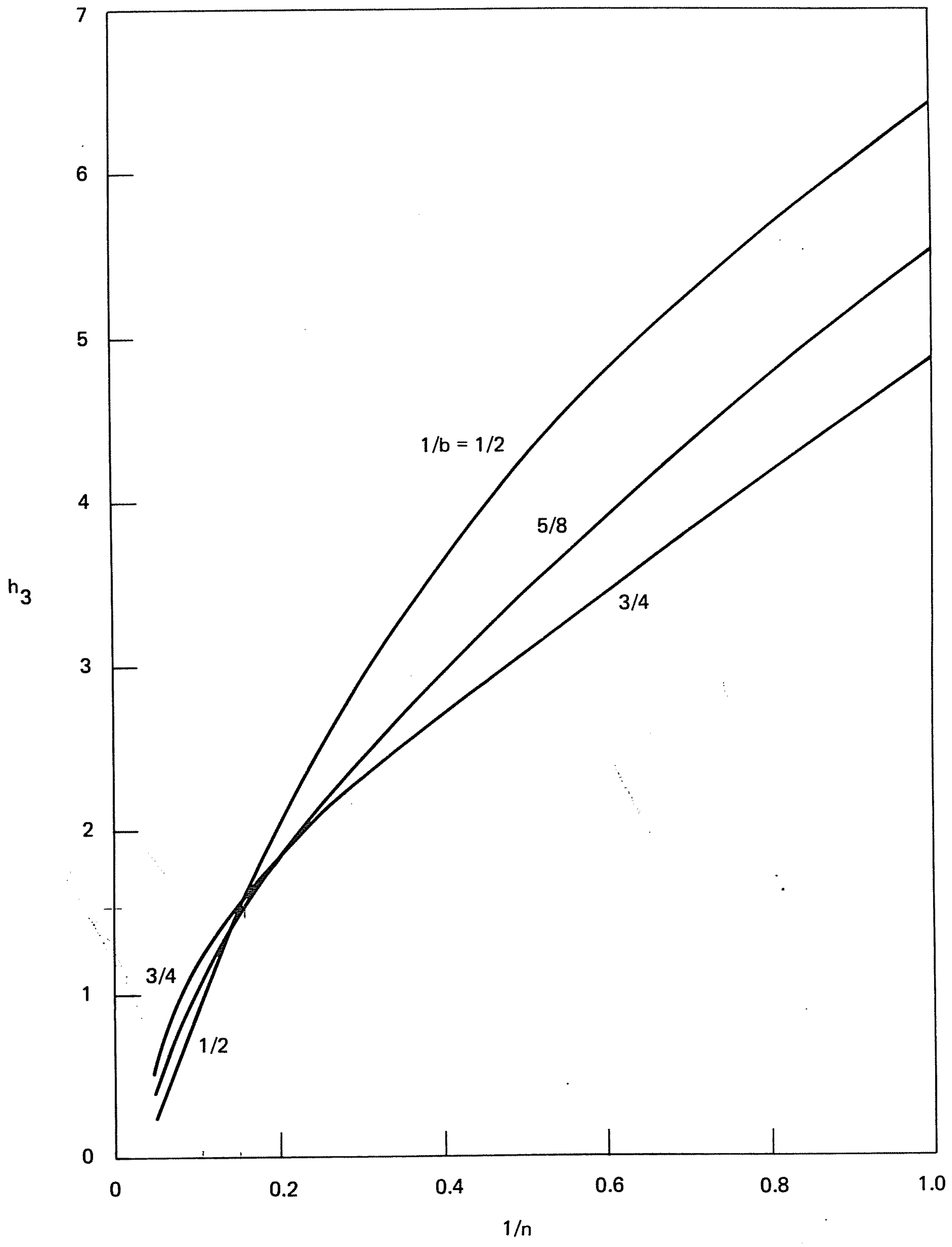

Figure C-3. h_3 versus 1/n for a compact specimen in plane strain.

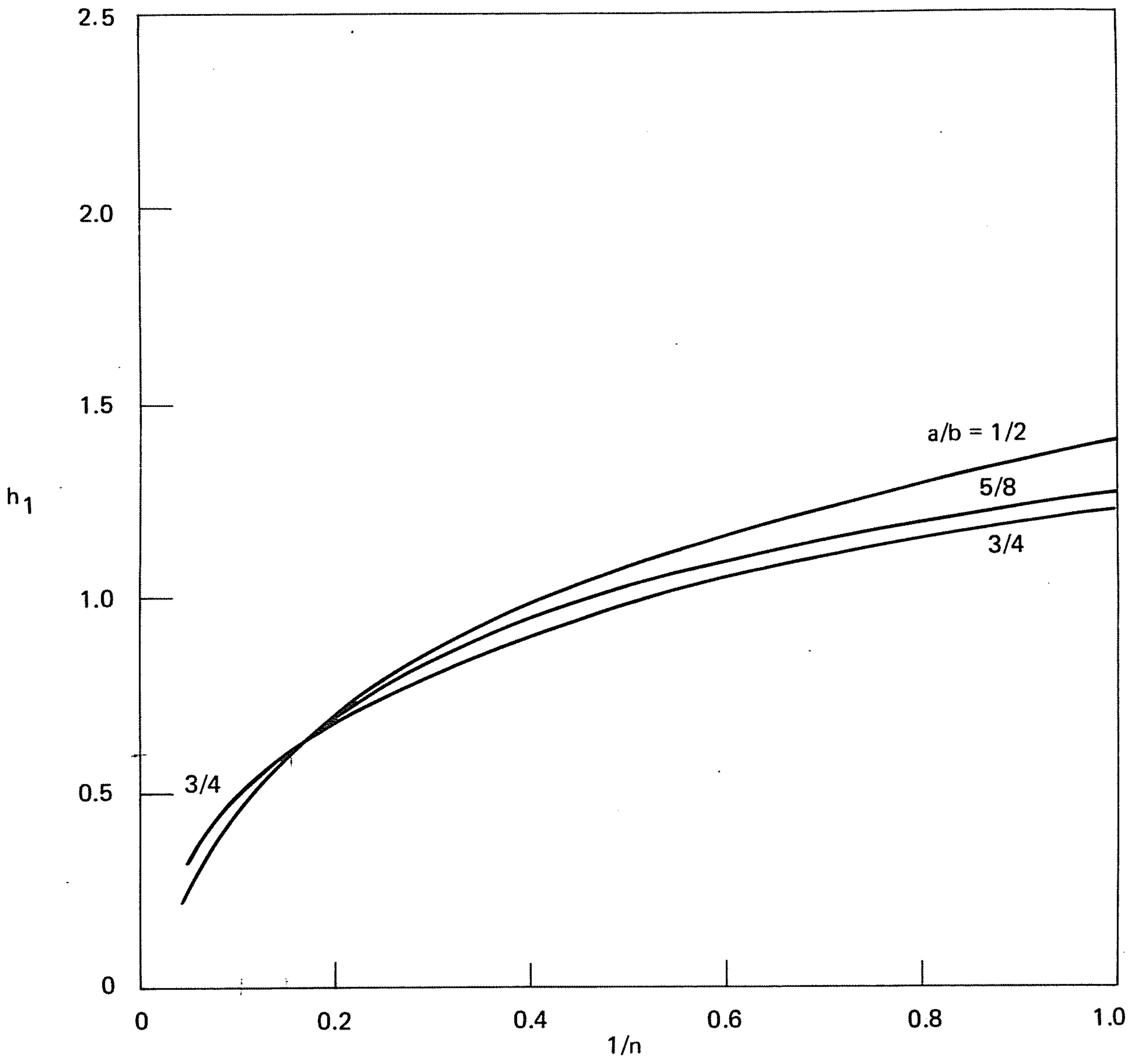

Figure C-4. h_1 versus 1/n for a compact specimen in plane stress.

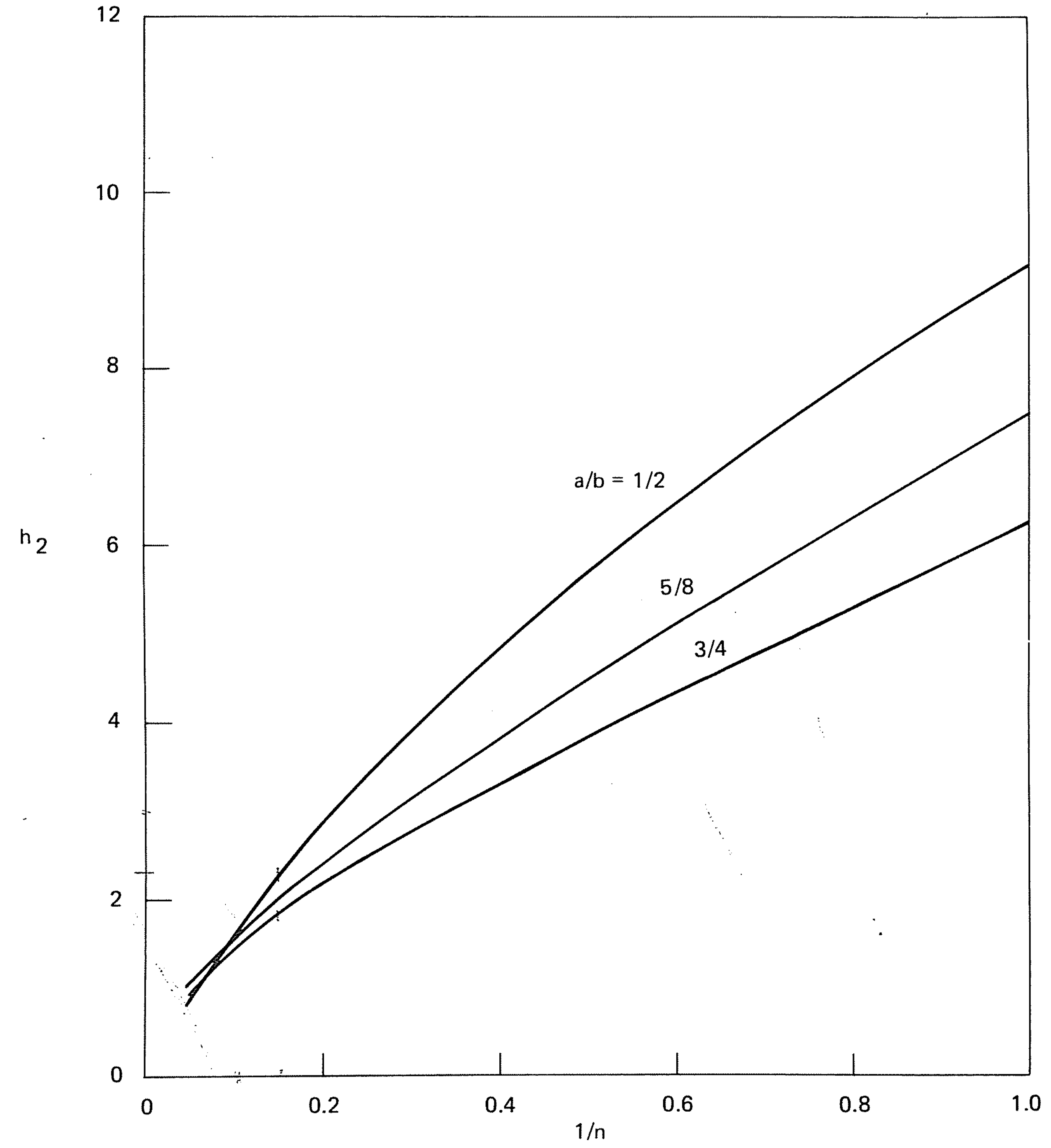

Figure C-5. h_2 versus 1/n for a compact specimen in plane stress.

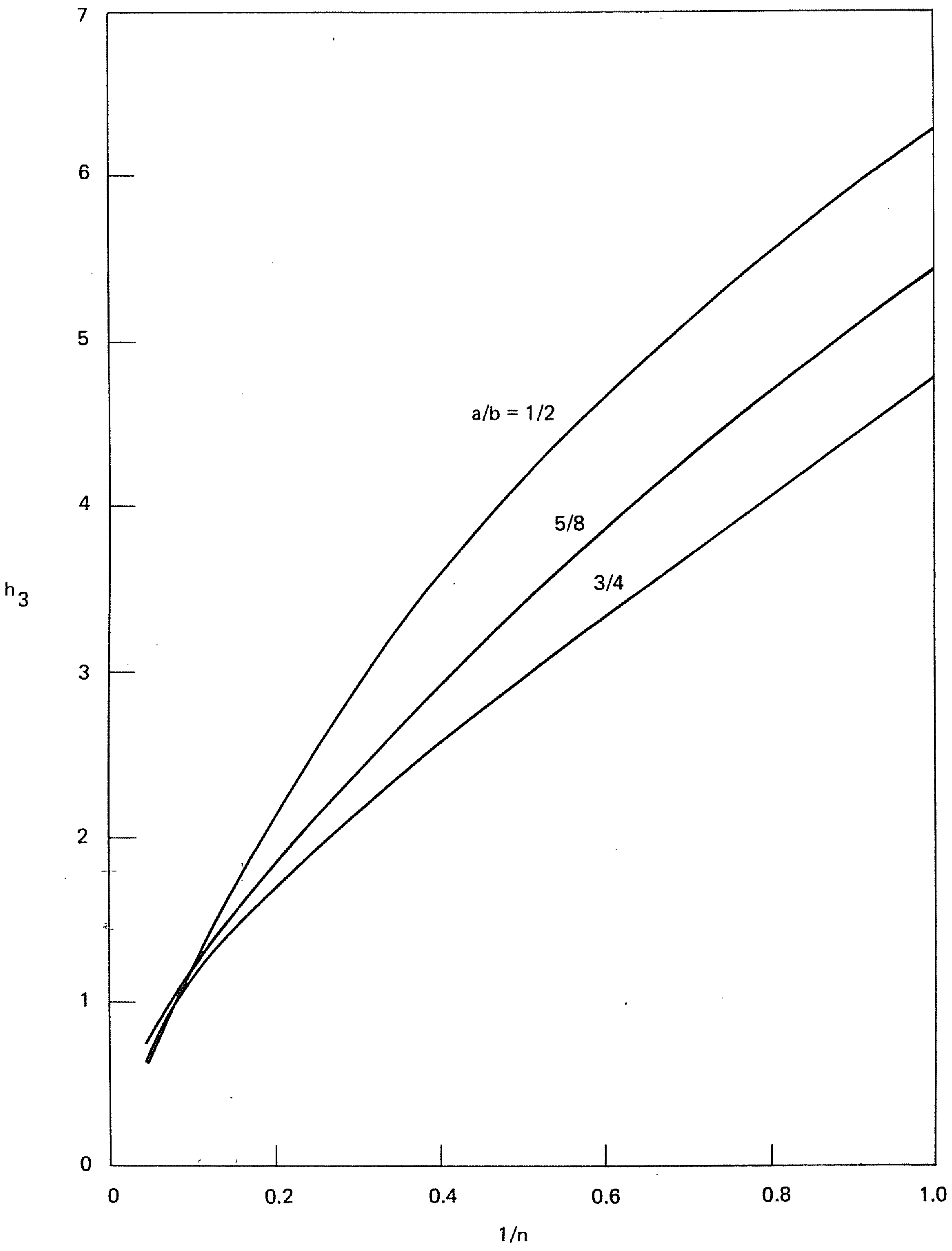

Figure C-6. h_3 versus 1/n for a compact specimen in plane stress.

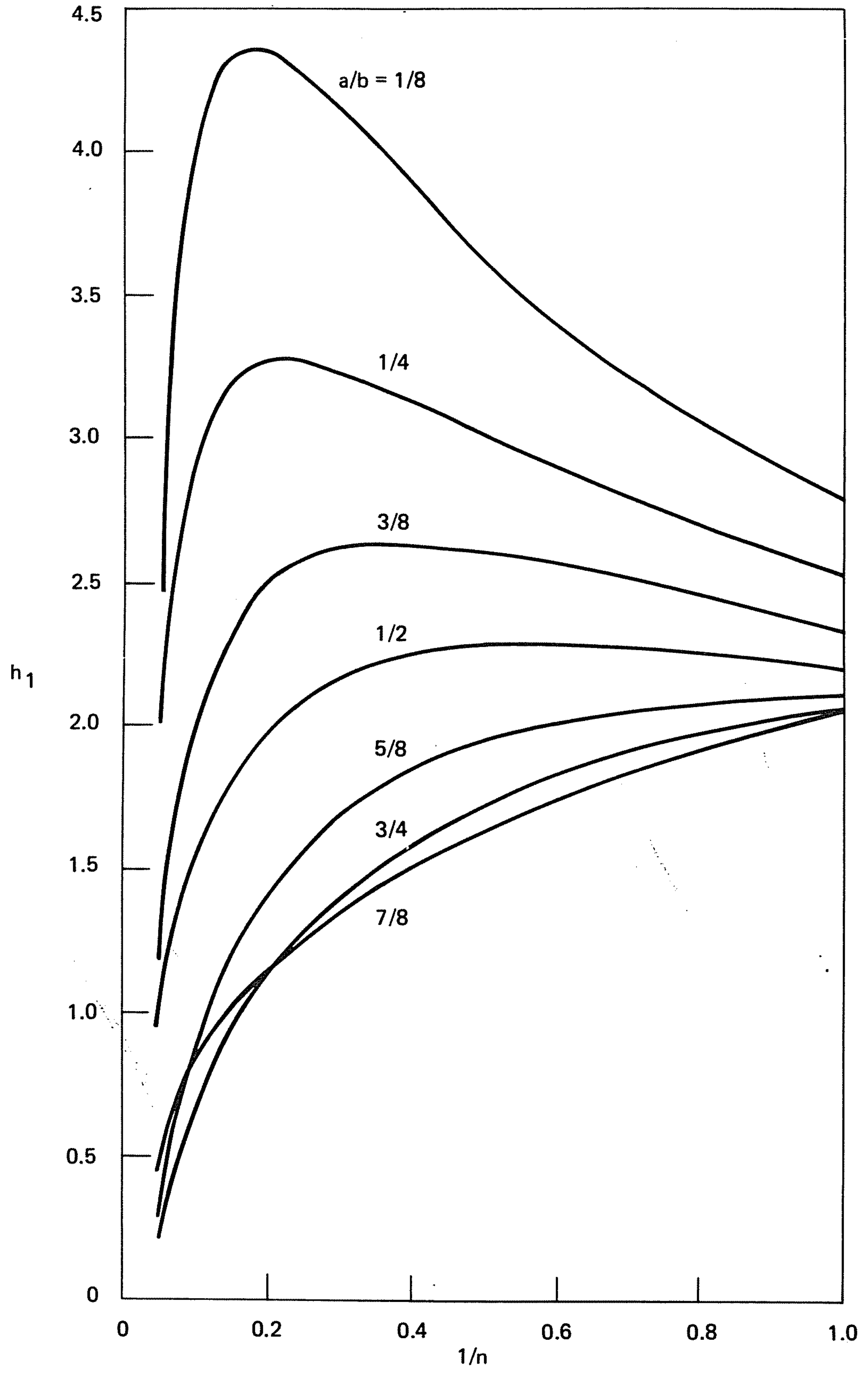

Figure C-7. h_1 versus 1/n for a center-cracked panel in tension – plane strain.

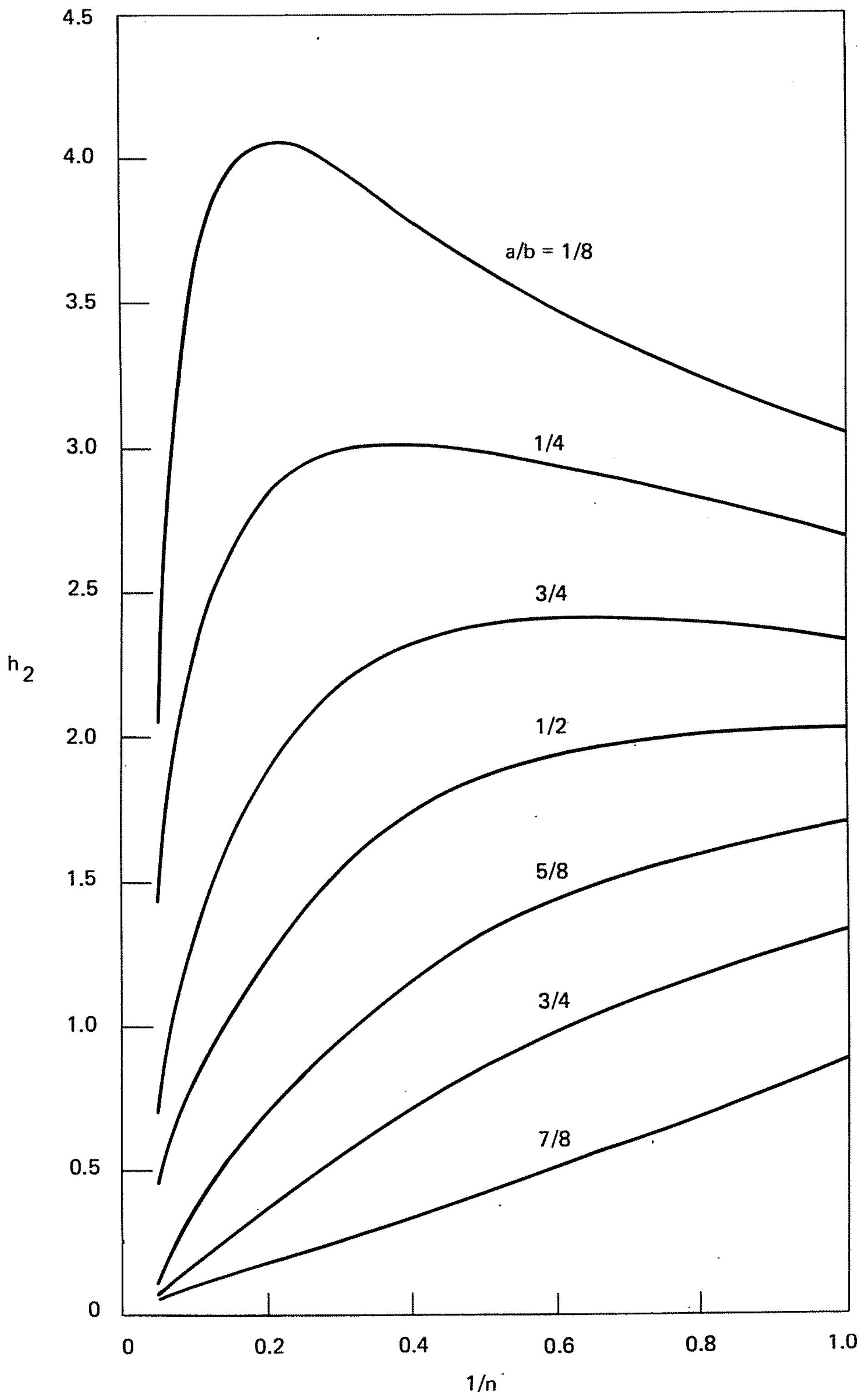

Figure C-8. h_2 versus 1/n for a center-cracked panel in tension – plane strain.

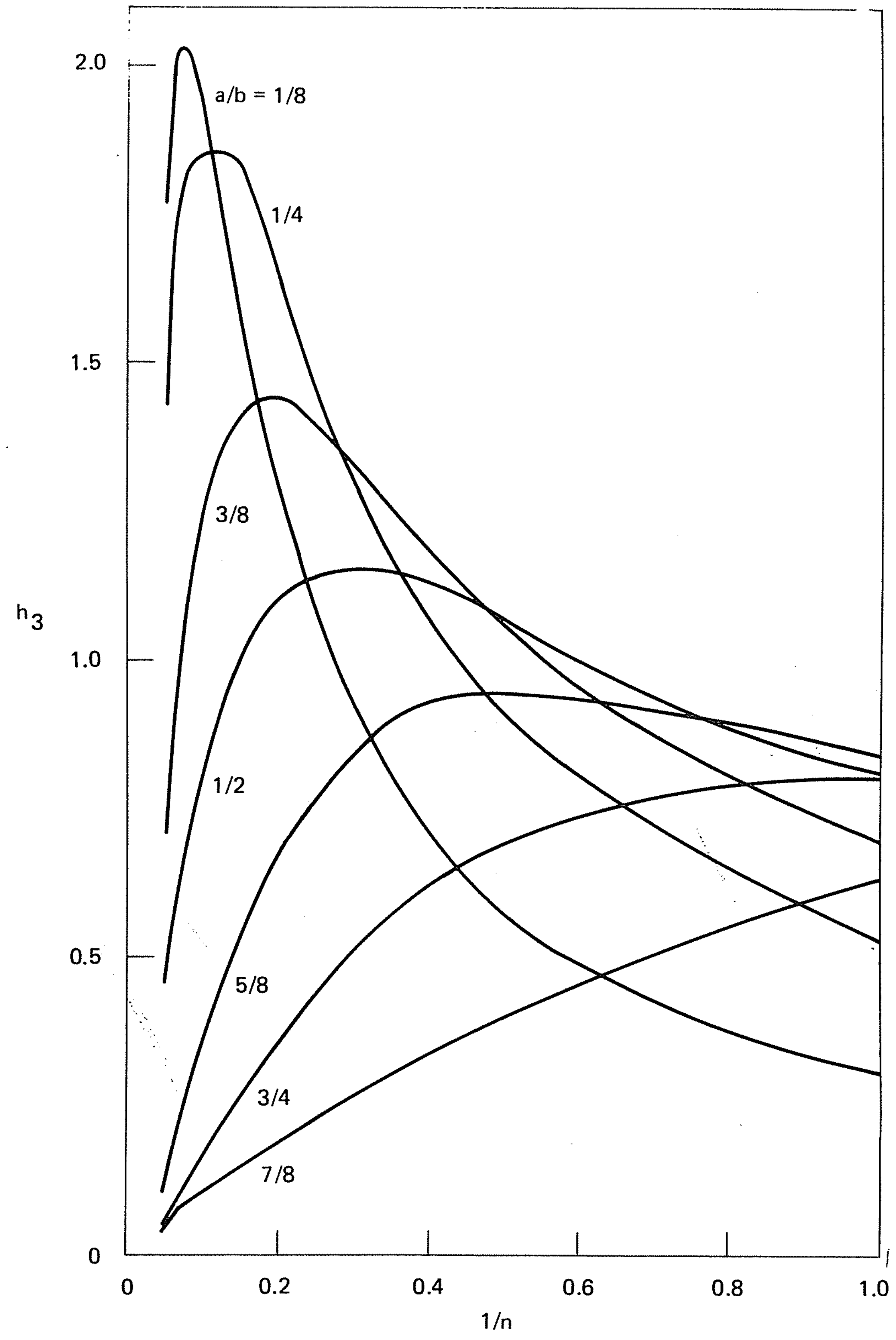

Figure C-9. h_3 versus 1/n for a center-cracked panel in tension - plane strain.

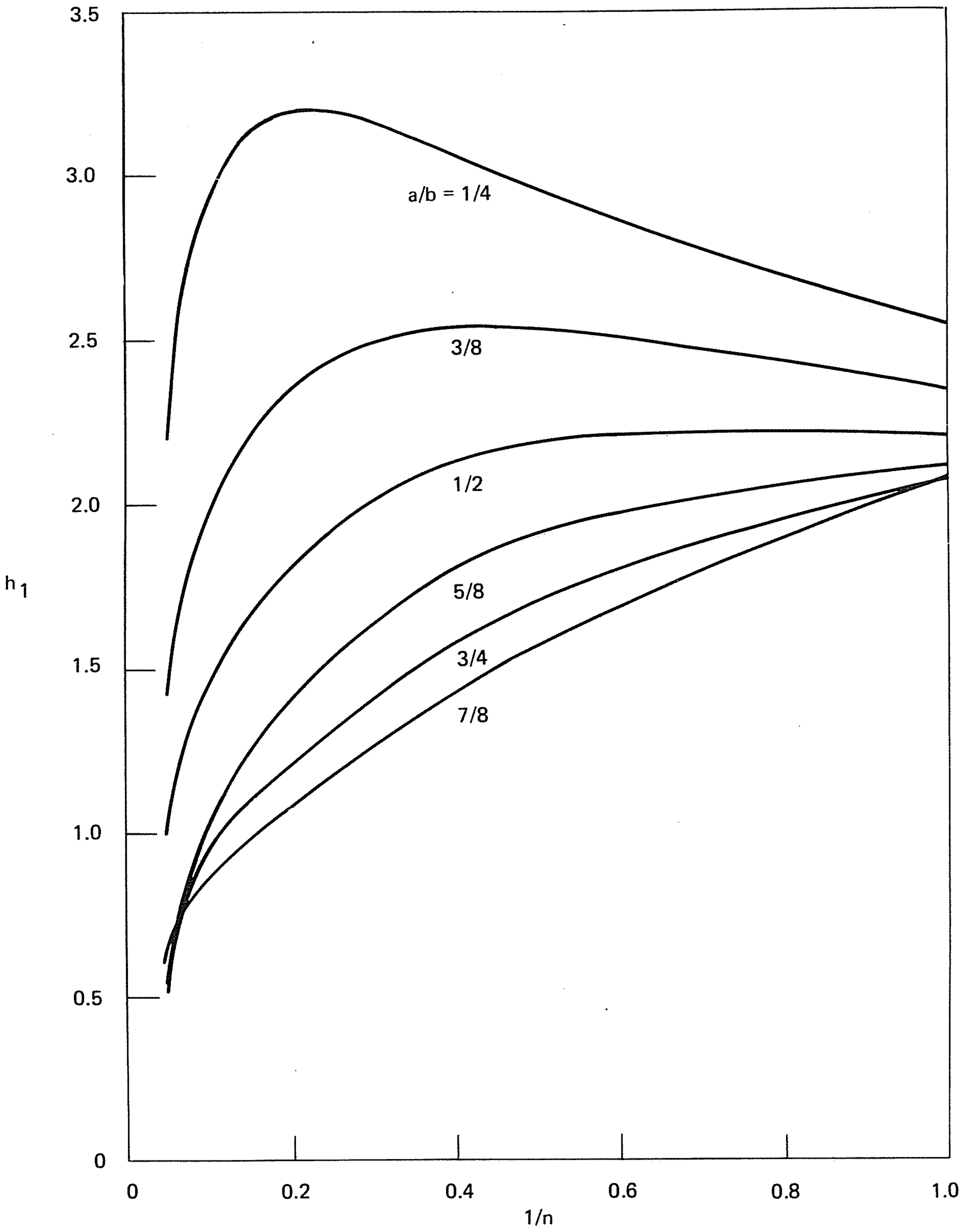

Figure C-10. h_1 versus 1/n for a center-cracked panel in tension - plane stress.

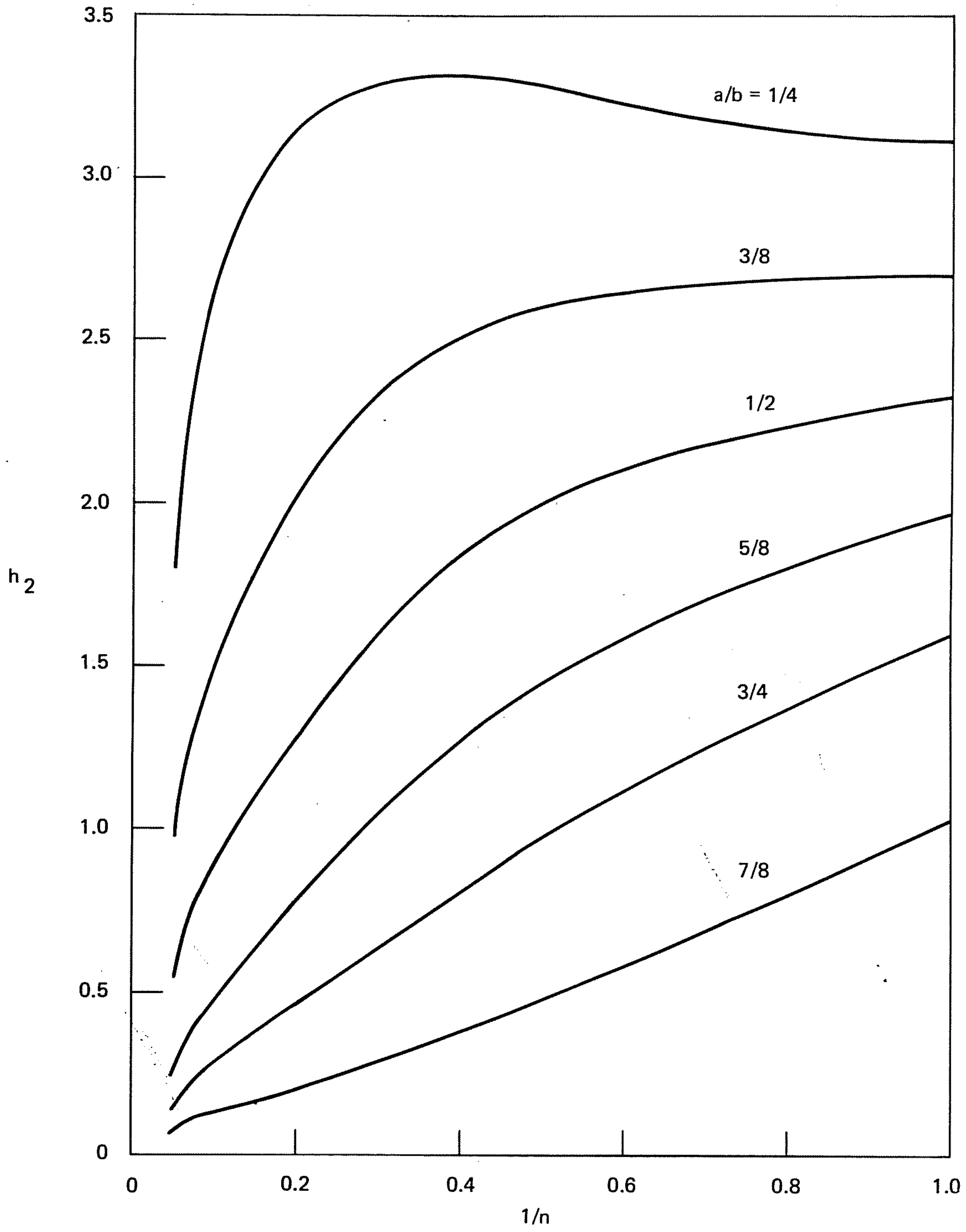

Figure C-11. h_2 versus 1/n for a center-cracked panel in tension - plane stress.

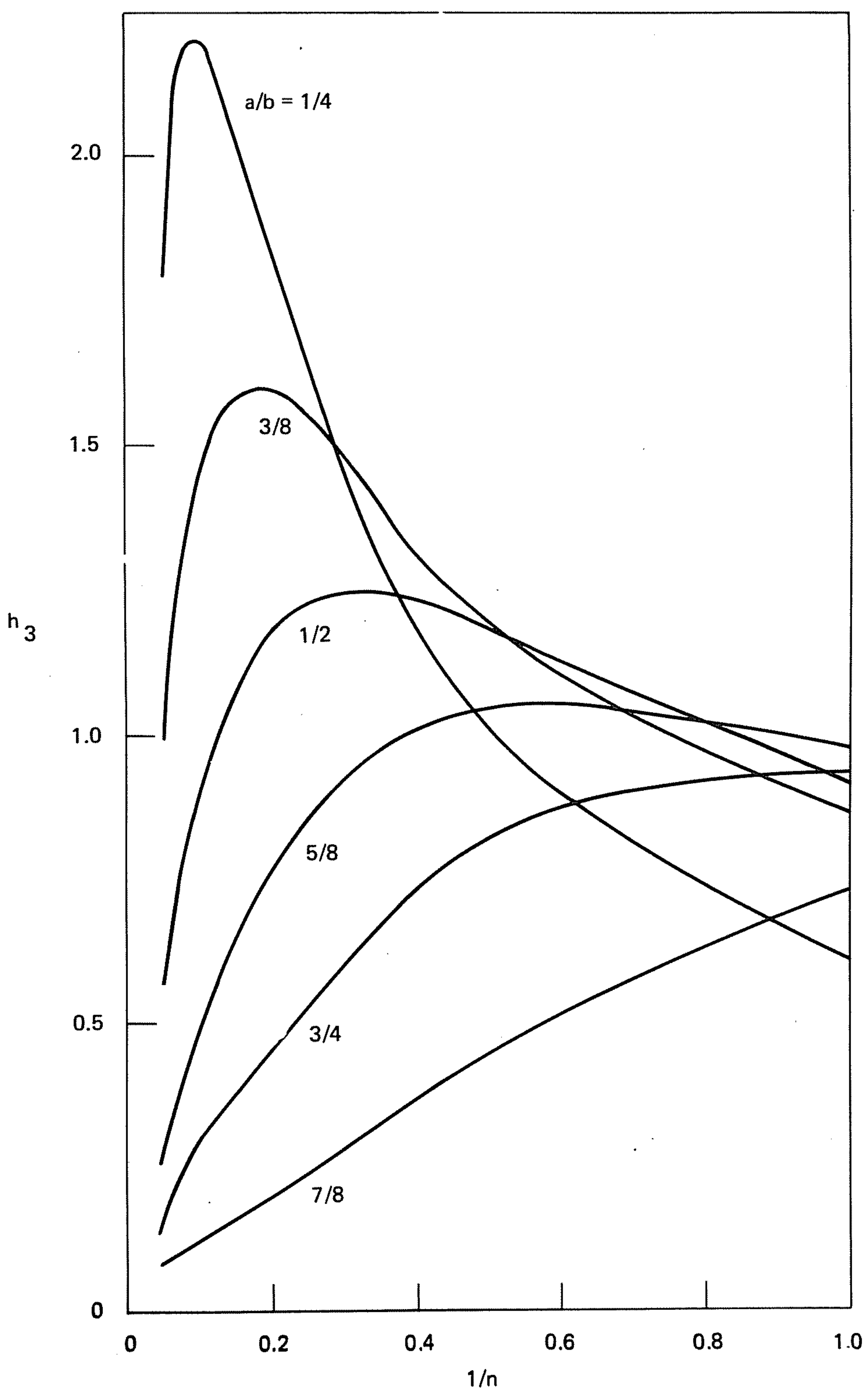

Figure C-12. h_3 versus 1/n for a center-cracked panel in tension - plane stress.

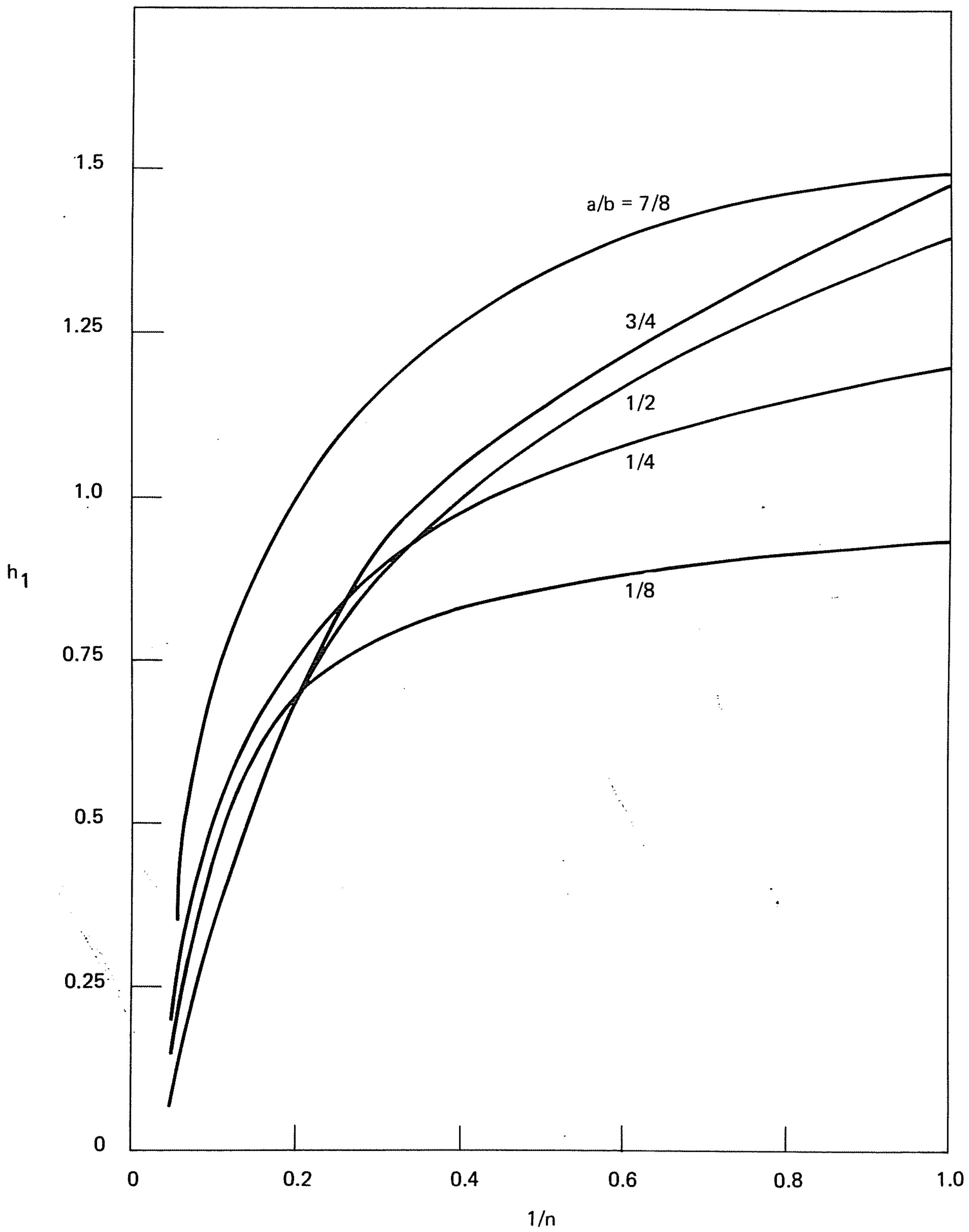

Figure C-13. h_1 versus 1/n for a single-edge cracked panel in three-point bending - plane strain.

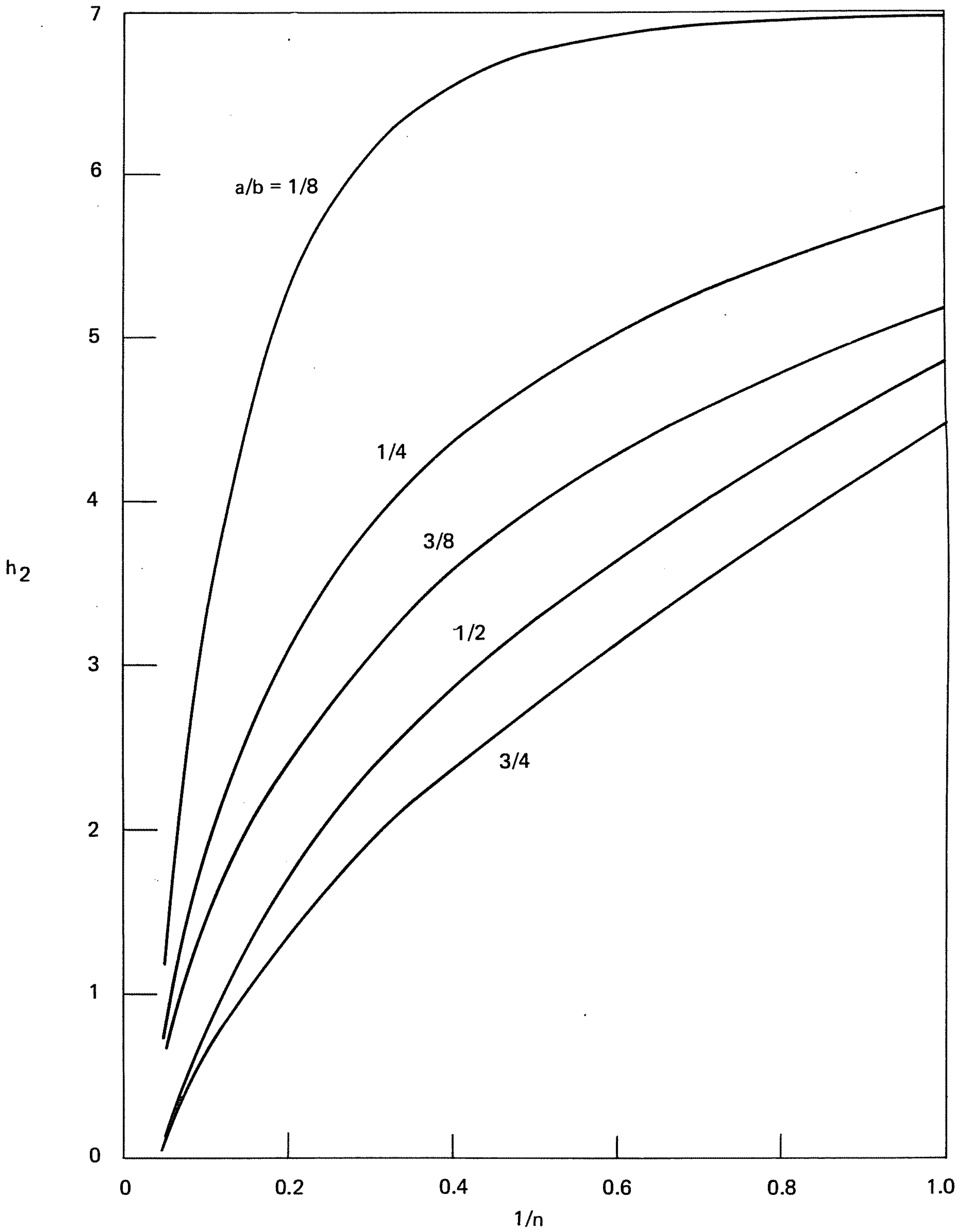

Figure C-14. h_2 versus 1/n for a single-edge cracked panel in three-point bending - plane strain.

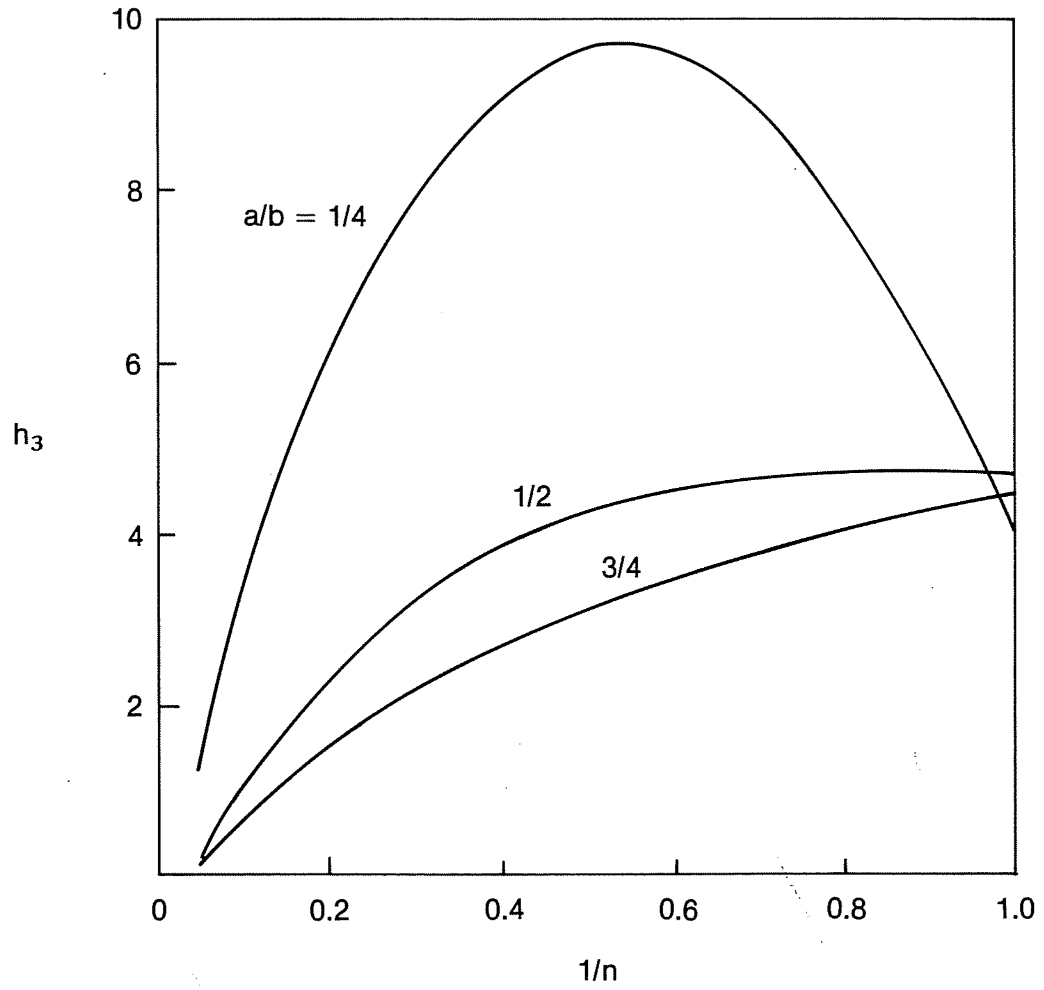

Figure C-15. h_3 versus 1/n for a single-edge cracked panel in three-point bending - plane strain.

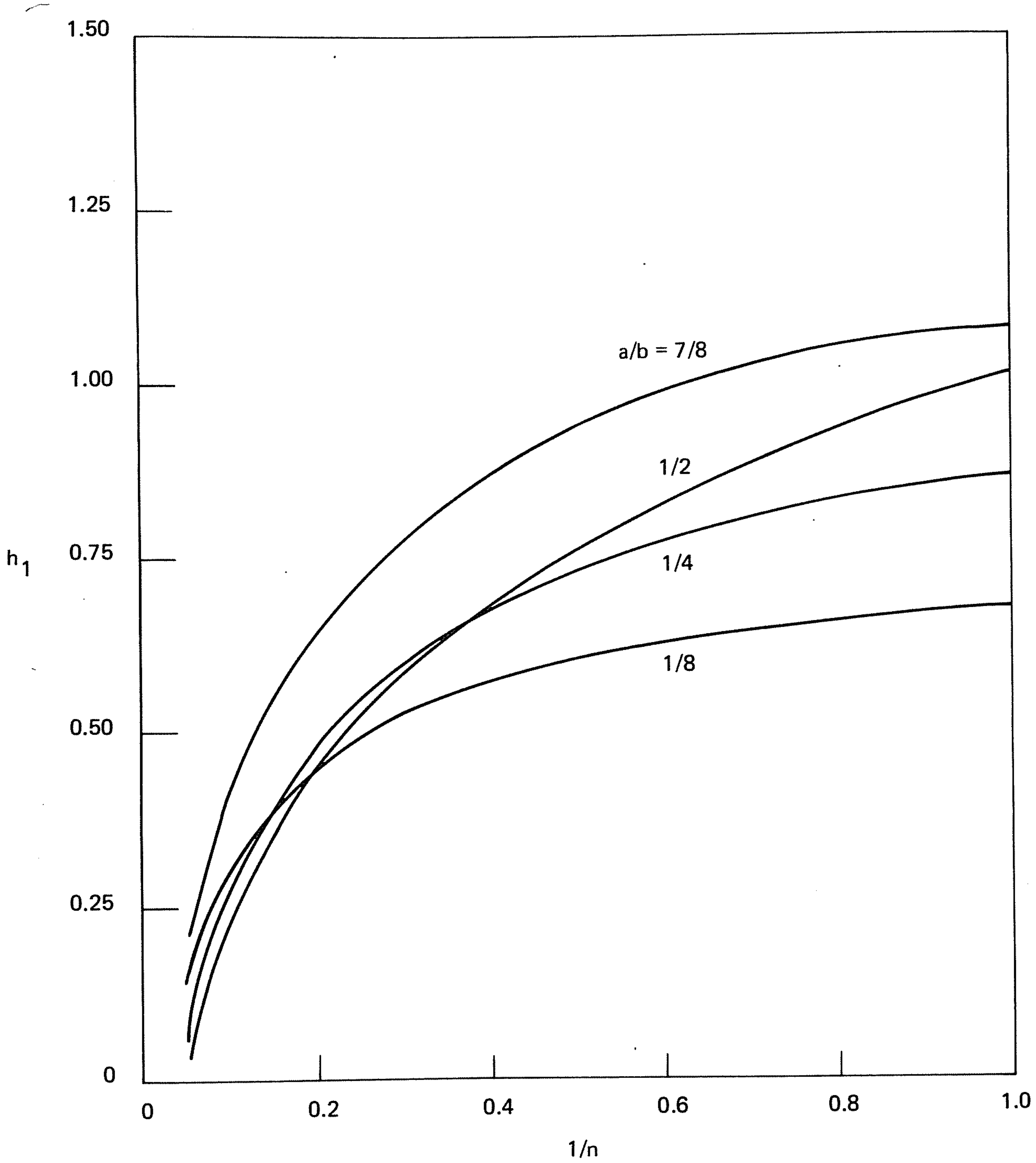

Figure C-16. h_1 versus 1/n for a single-edge cracked panel in three-point bending - plane stress.

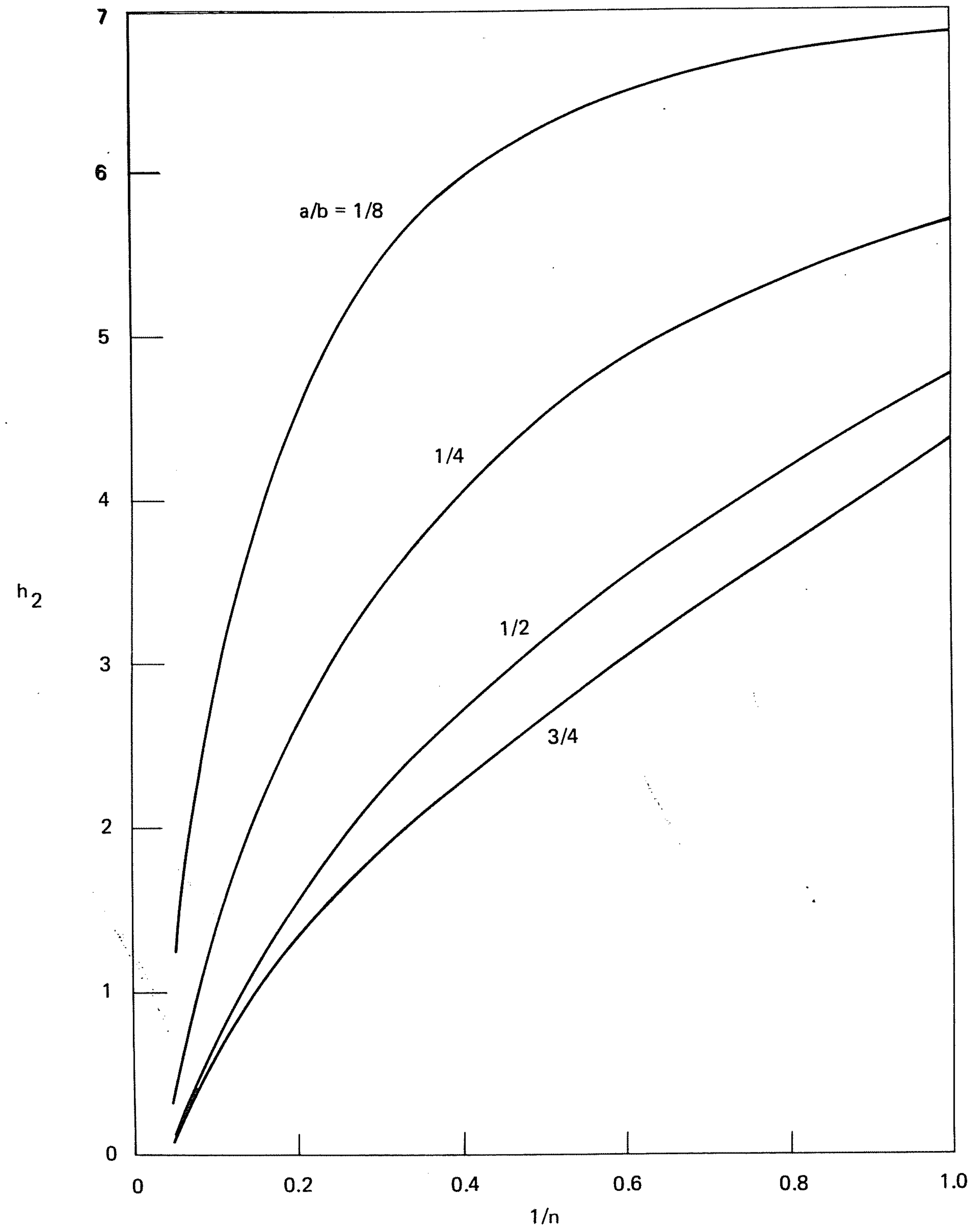

Figure C-17. h_2 versus 1/n for a single-edge cracked panel in three-point bending - plane stress.

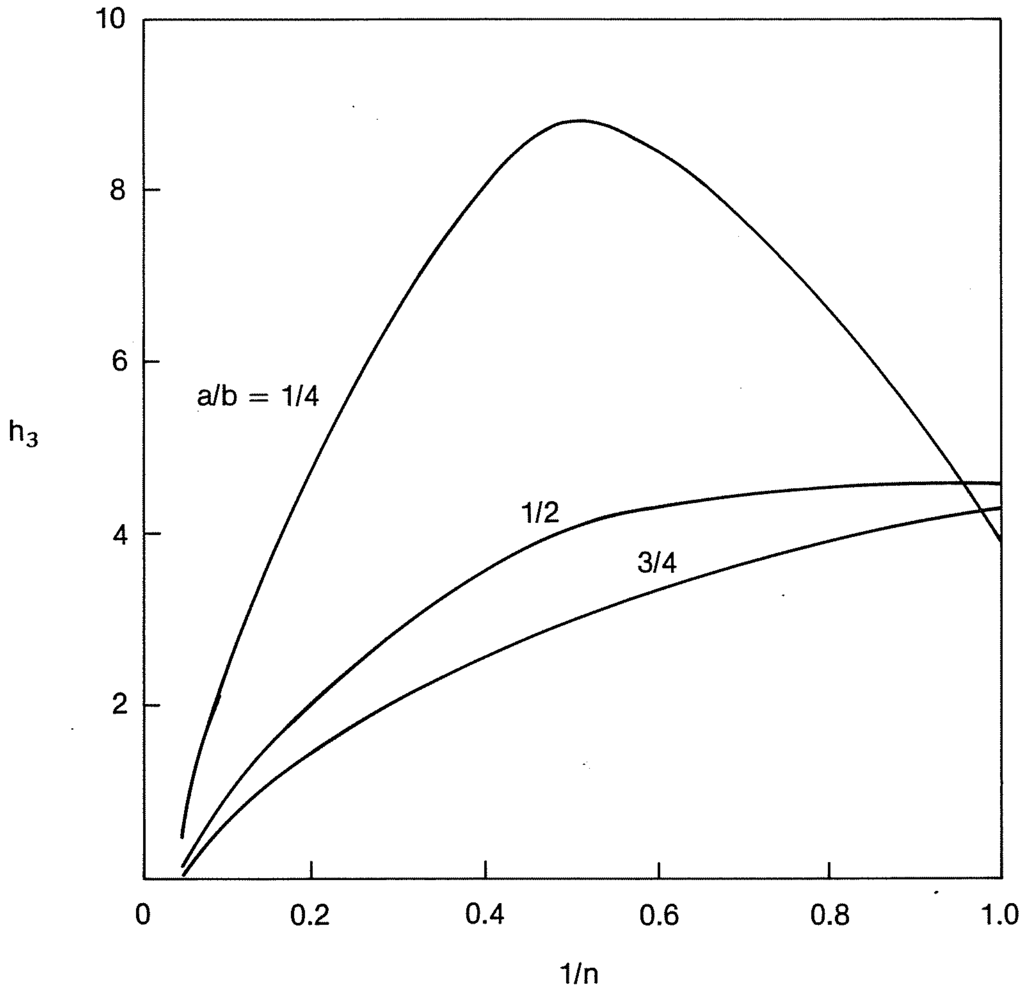

Figure C-18. h_3 versus 1/n for a single-edge cracked panel in three-point bending - plane stress.

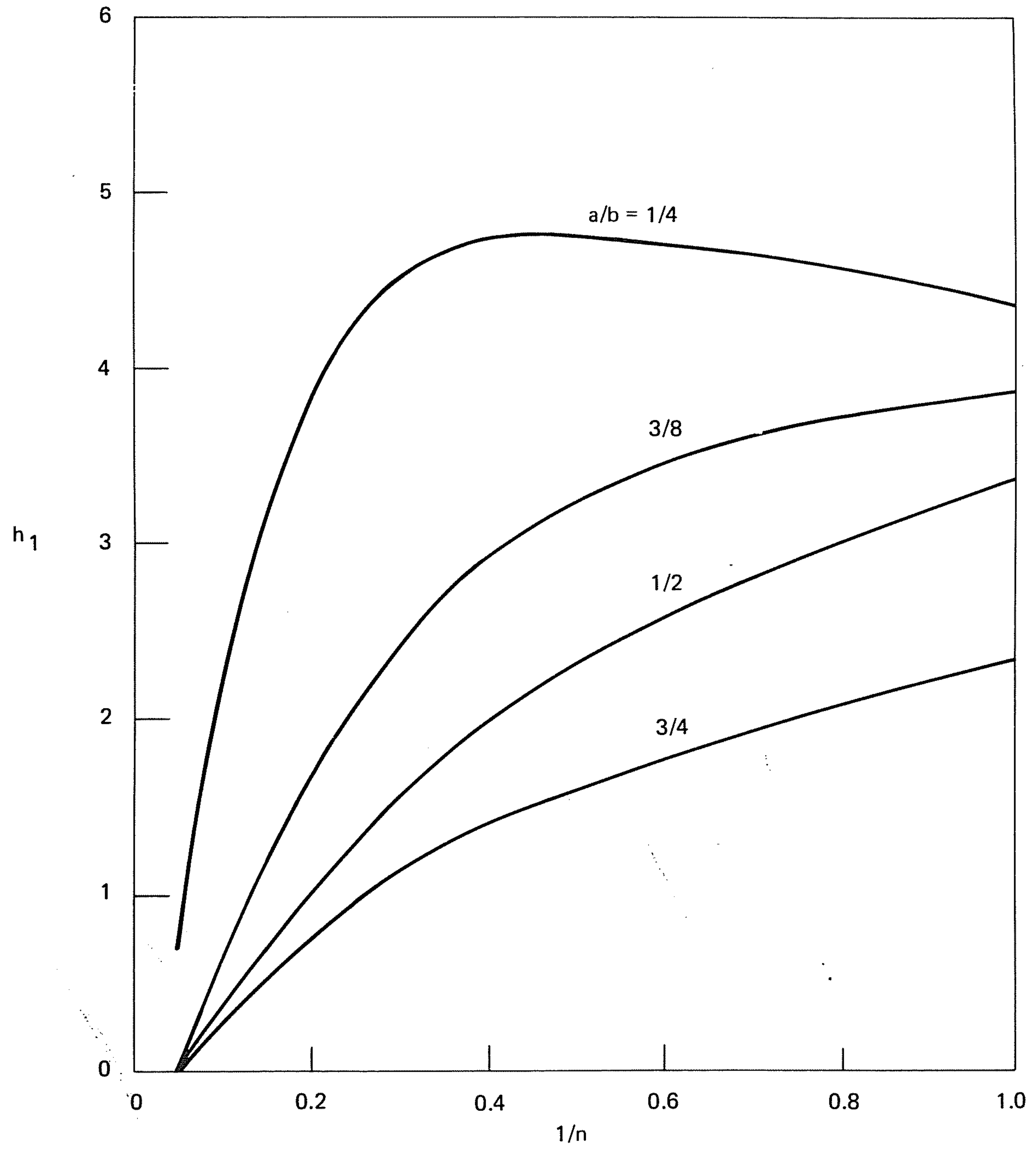

Figure C-19. h_1 versus $1/n$ for a single-edge cracked panel in tension – plane strain.

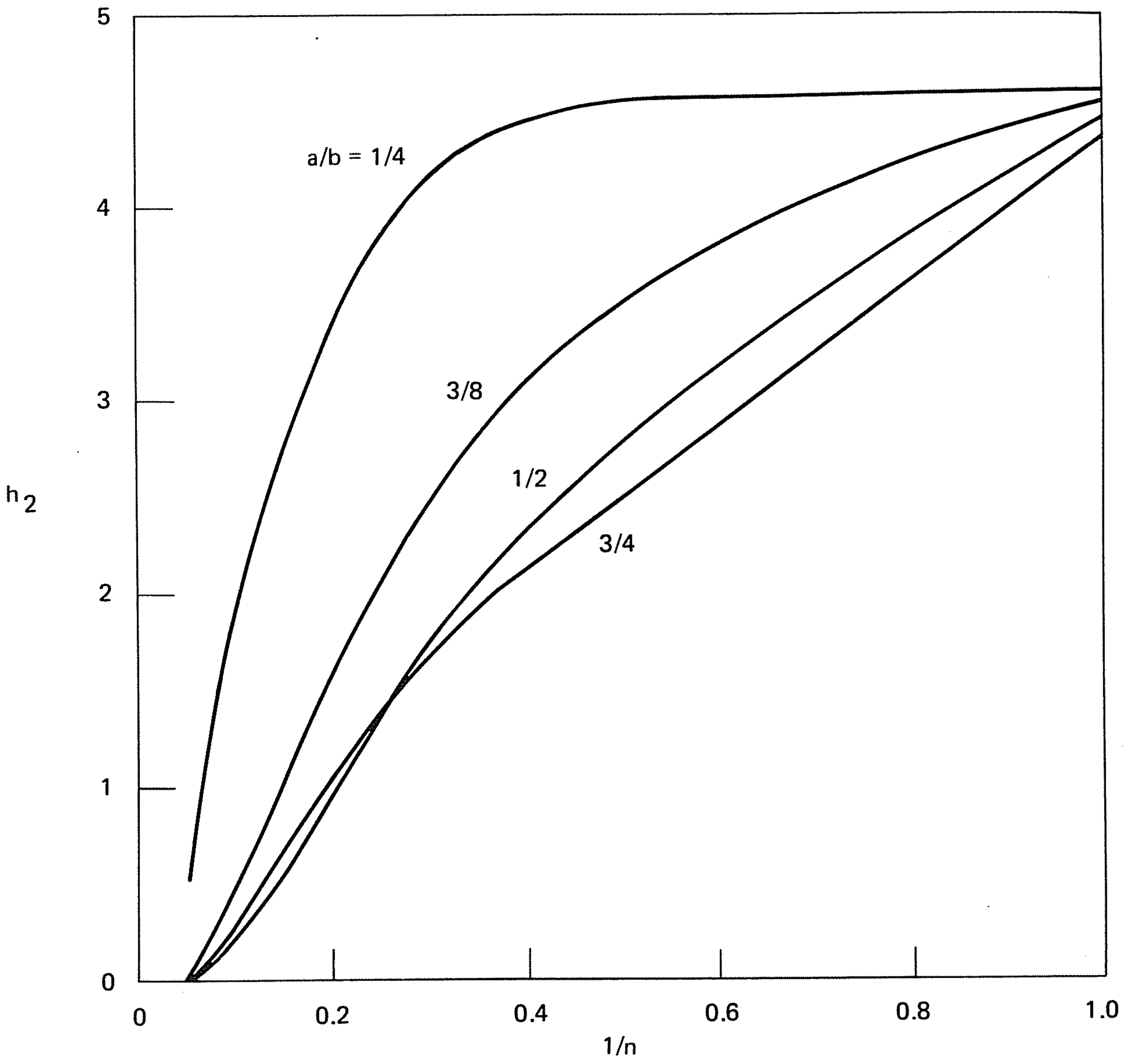

Figure C-20. h_2 versus $1/n$ for a single-edge cracked panel in tension – plane strain.

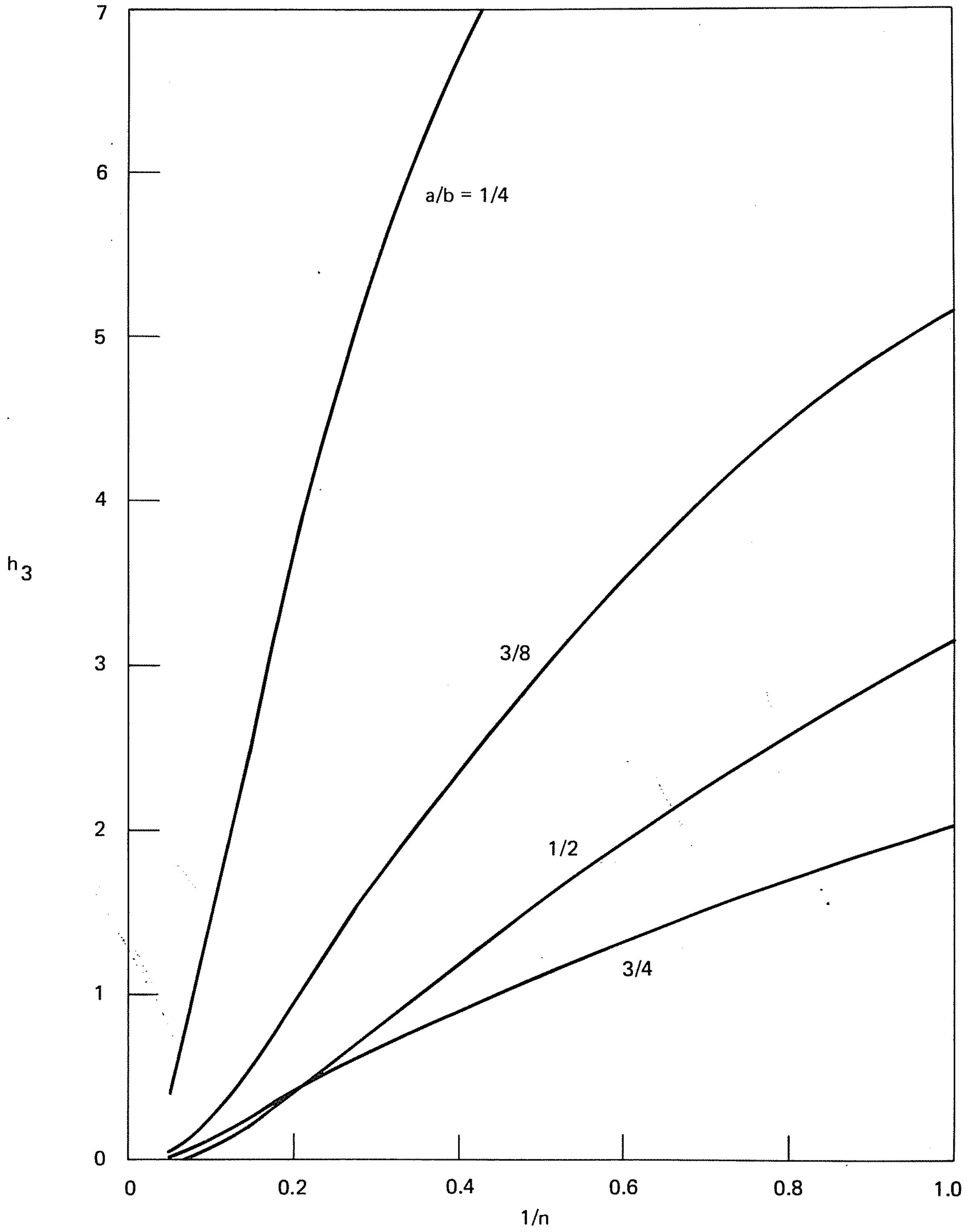

Figure C-21. h_3 versus 1/n for a single-edge cracked panel in tension – plane strain.

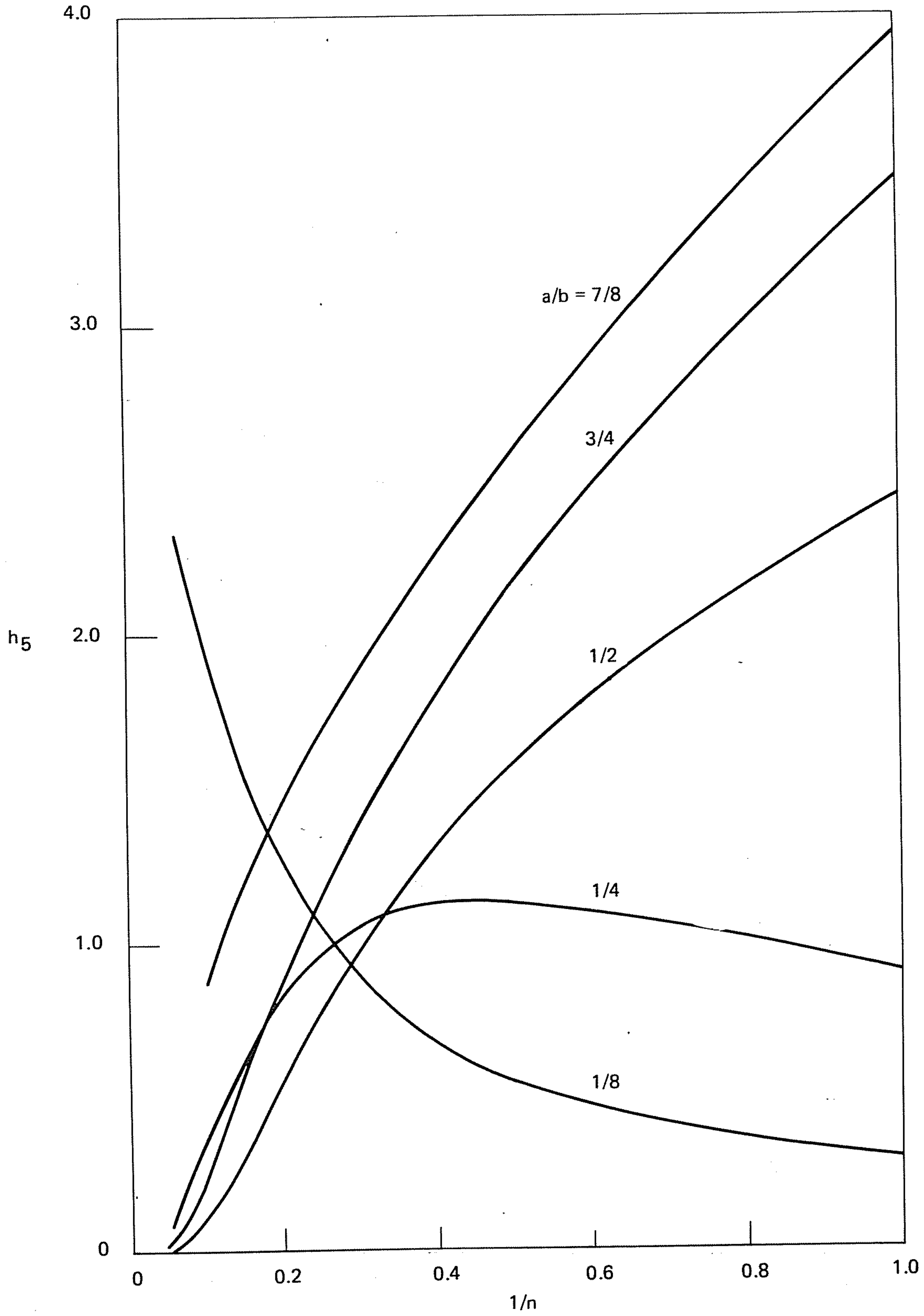

Figure C-22. h_5 versus 1/n for a single-edge cracked panel in tension – plane strain.

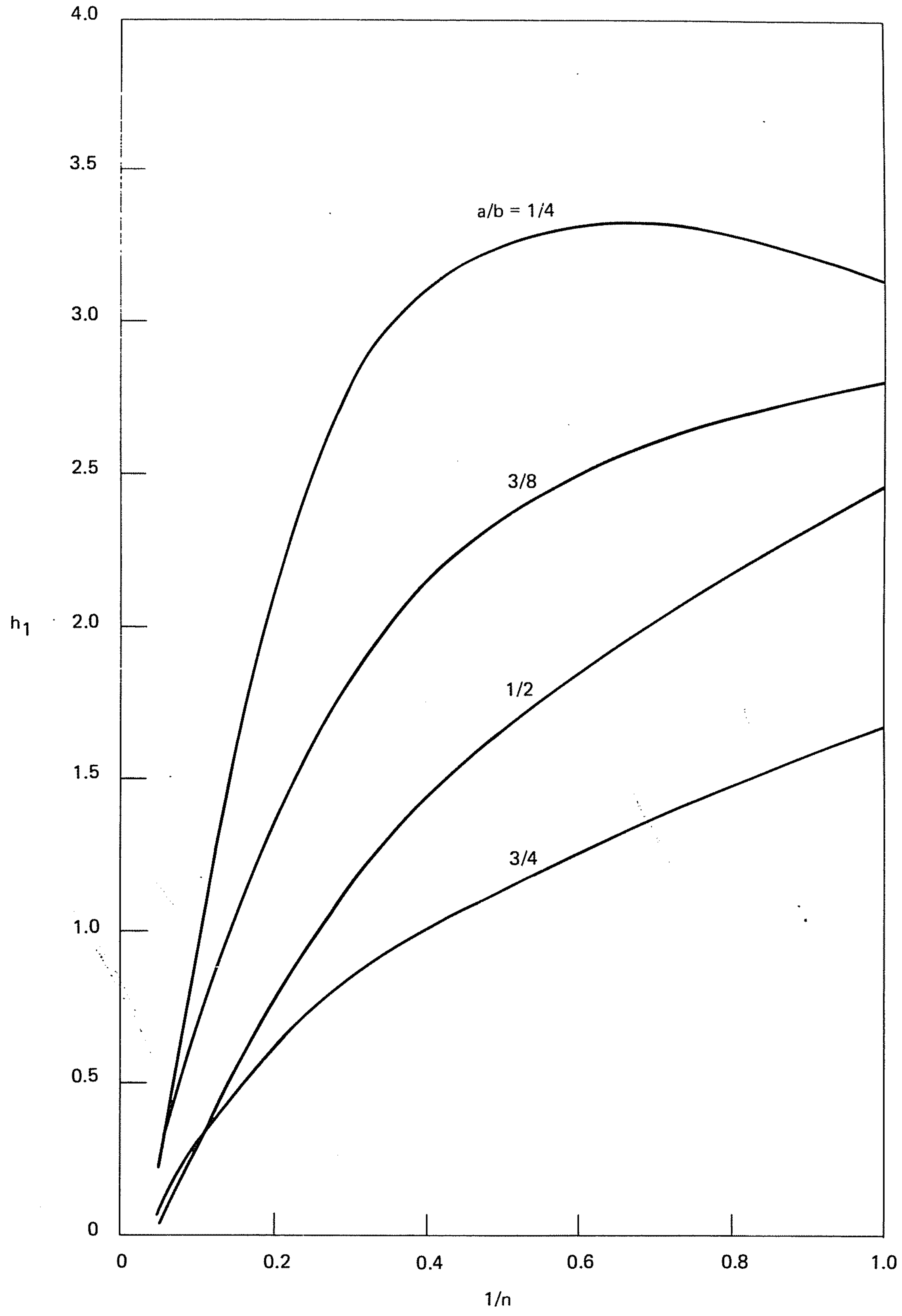

Figure C-23. h_1 versus 1/n for a single-edge cracked panel in tension – plane stress.

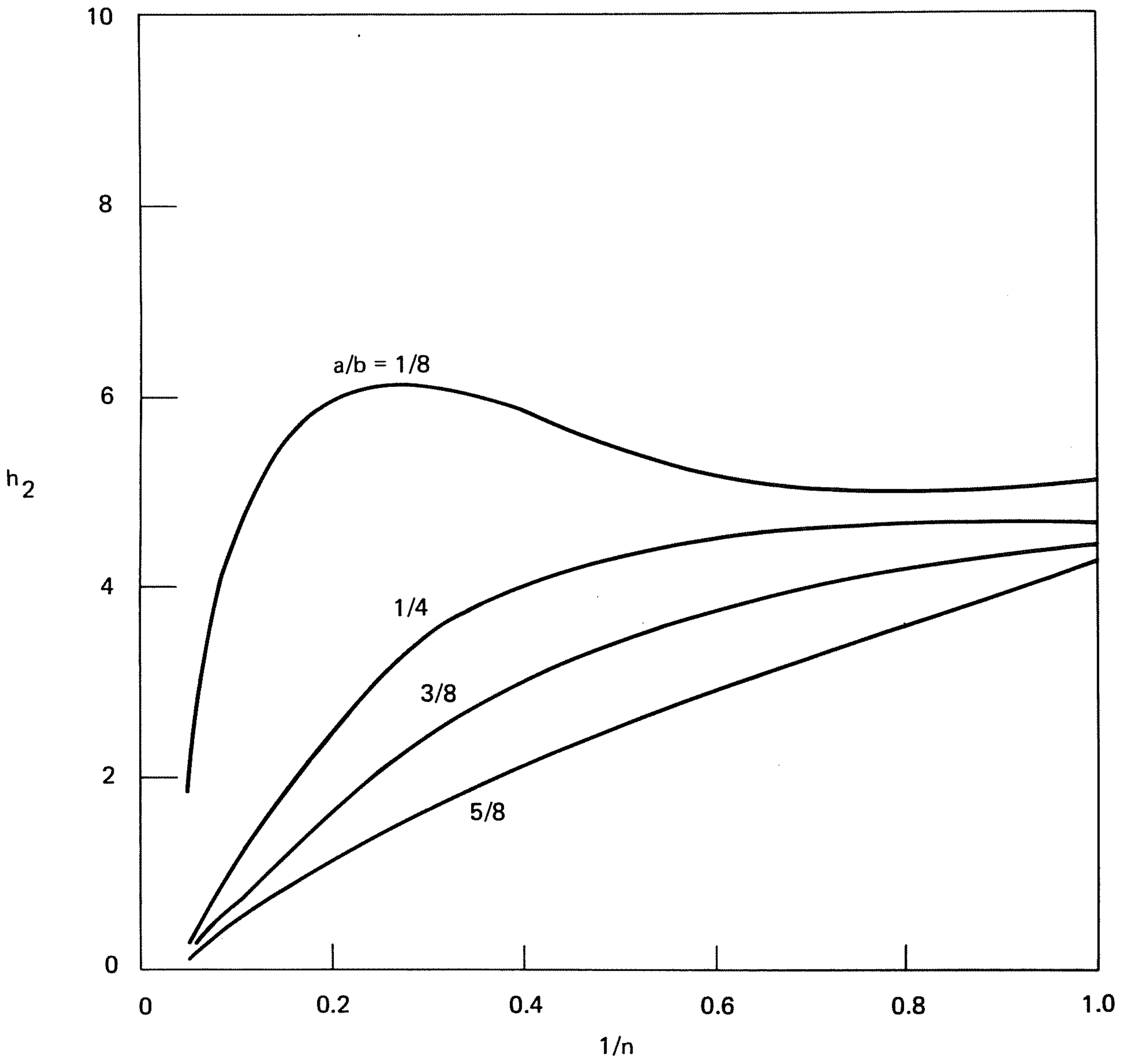

Figure C-24. h_2 versus 1/n for a single-edge cracked panel in tension – plane stress.

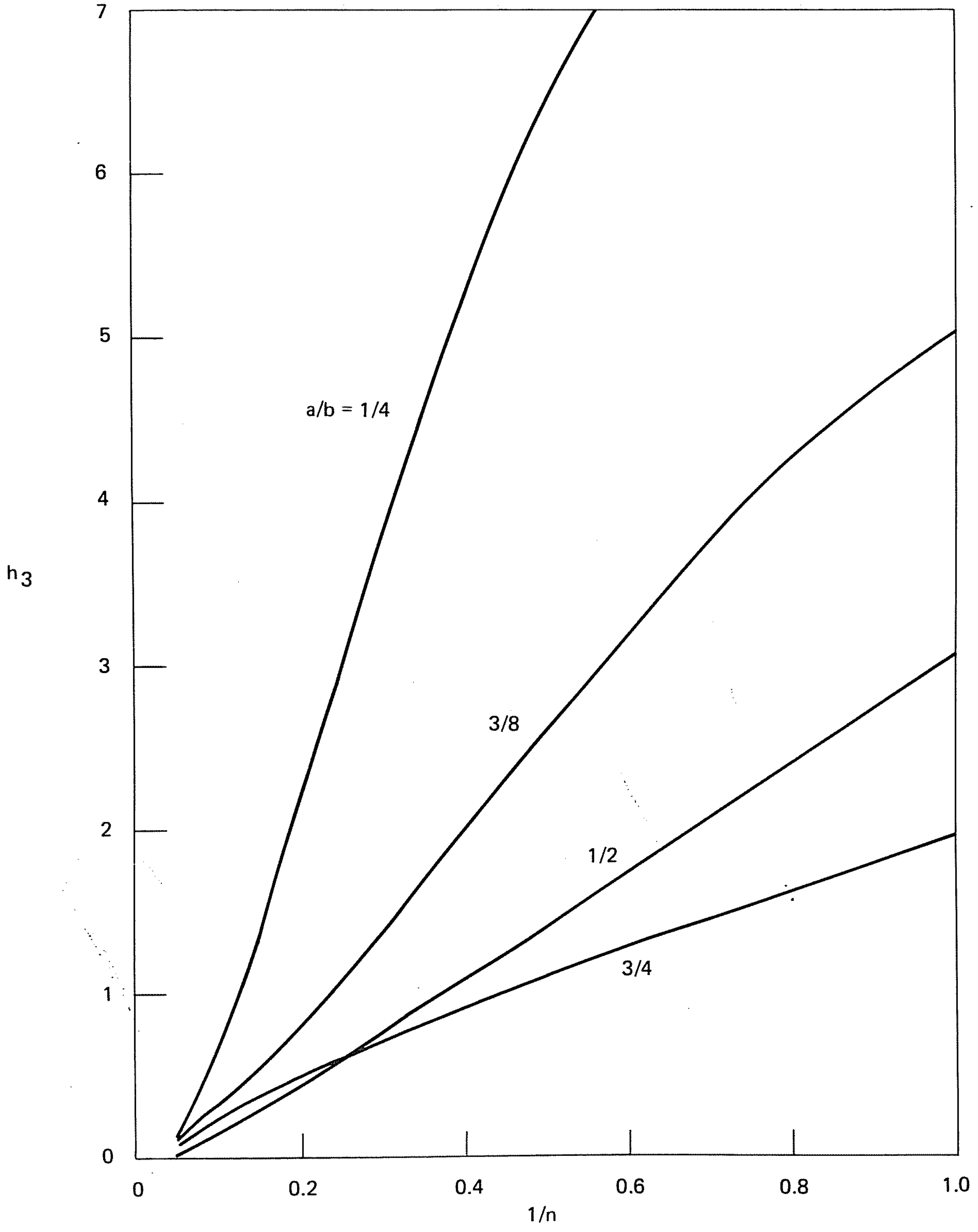

Figure C-25. h_3 versus 1/n for a single-edge cracked panel in tension - plane stress.

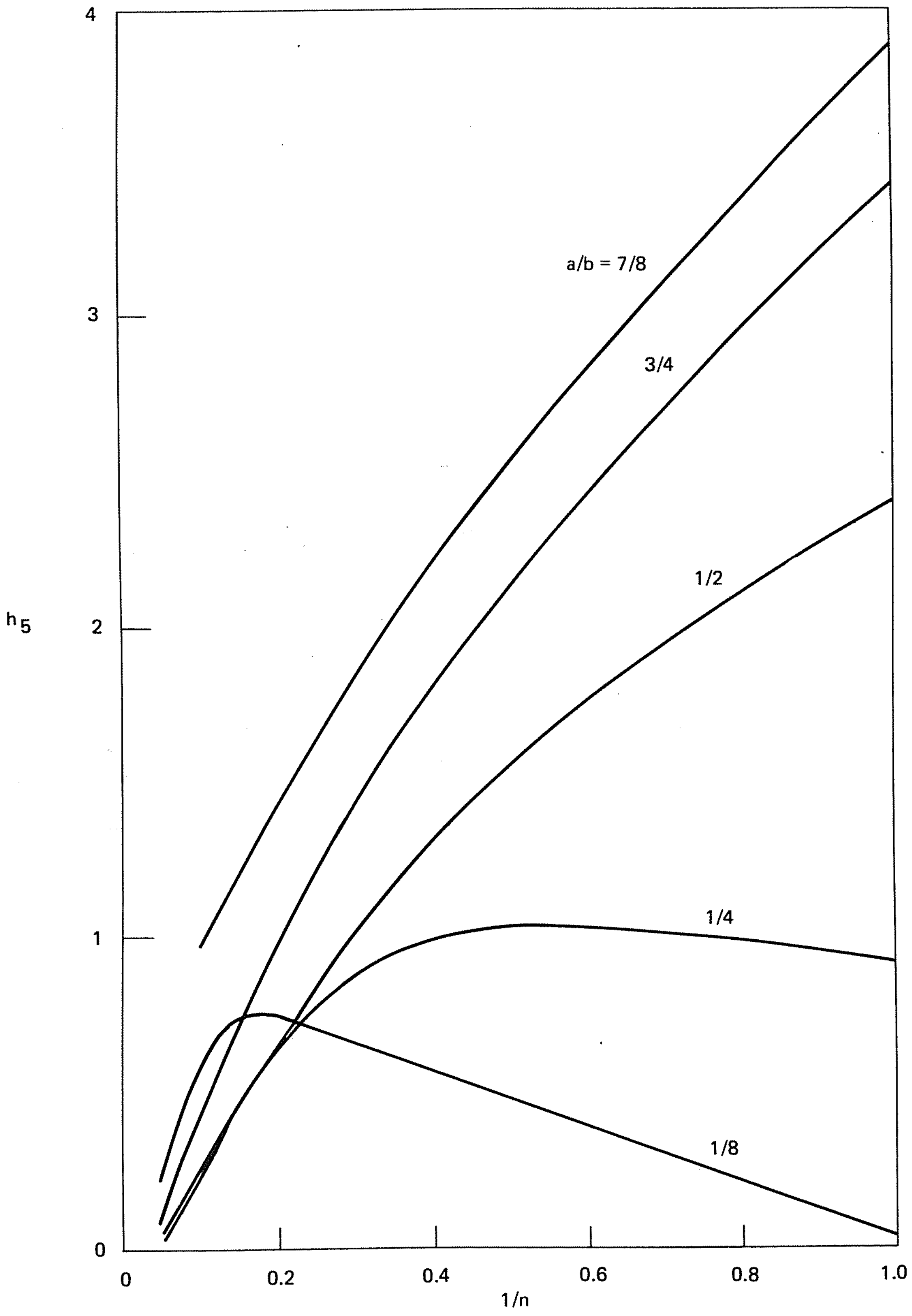

Figure C-26. h_5 versus 1/n for a single-edge cracked panel in tension - plane stress.

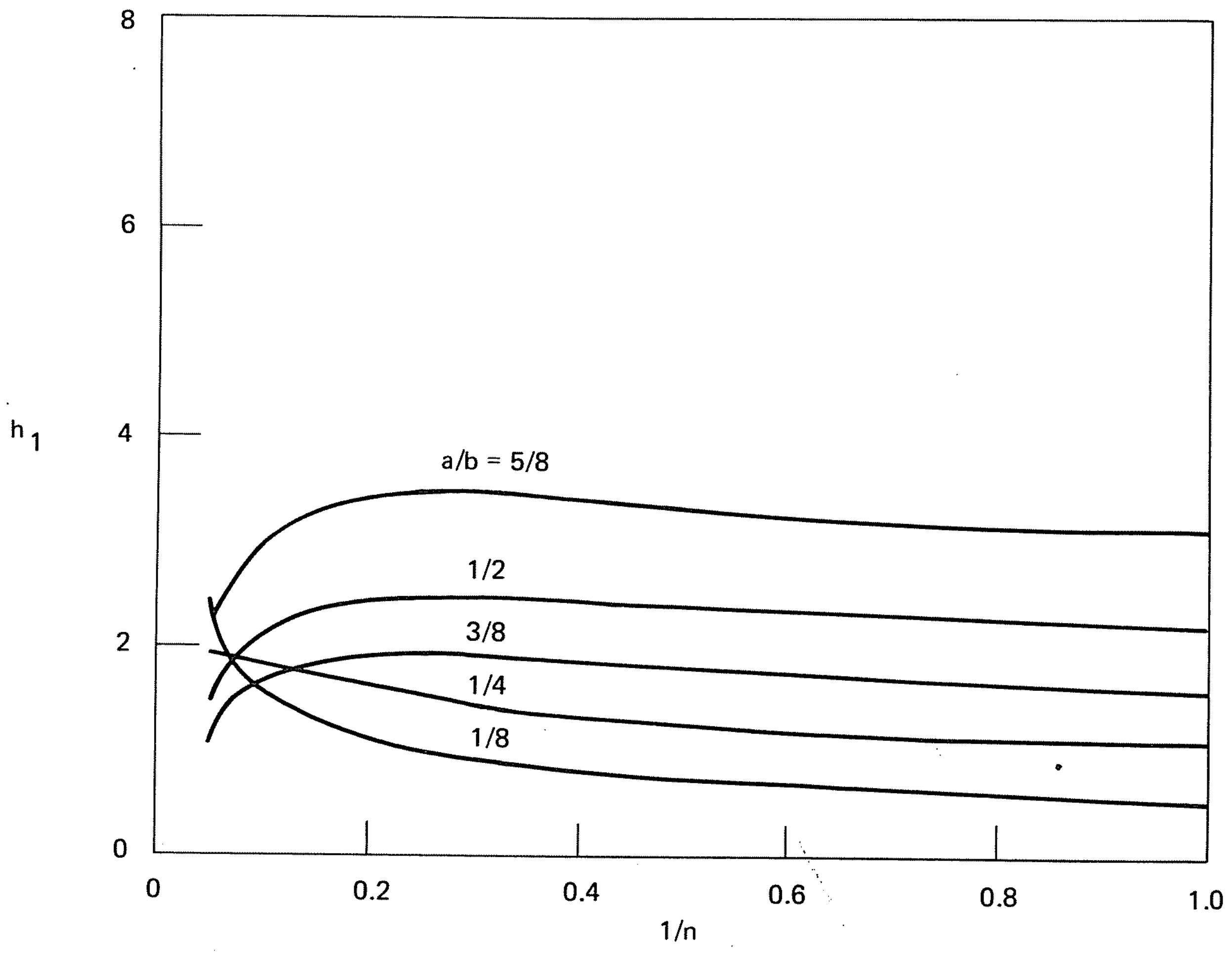

Figure C-27. h_1 versus 1/n for a double-edge cracked panel in tension – plane strain.

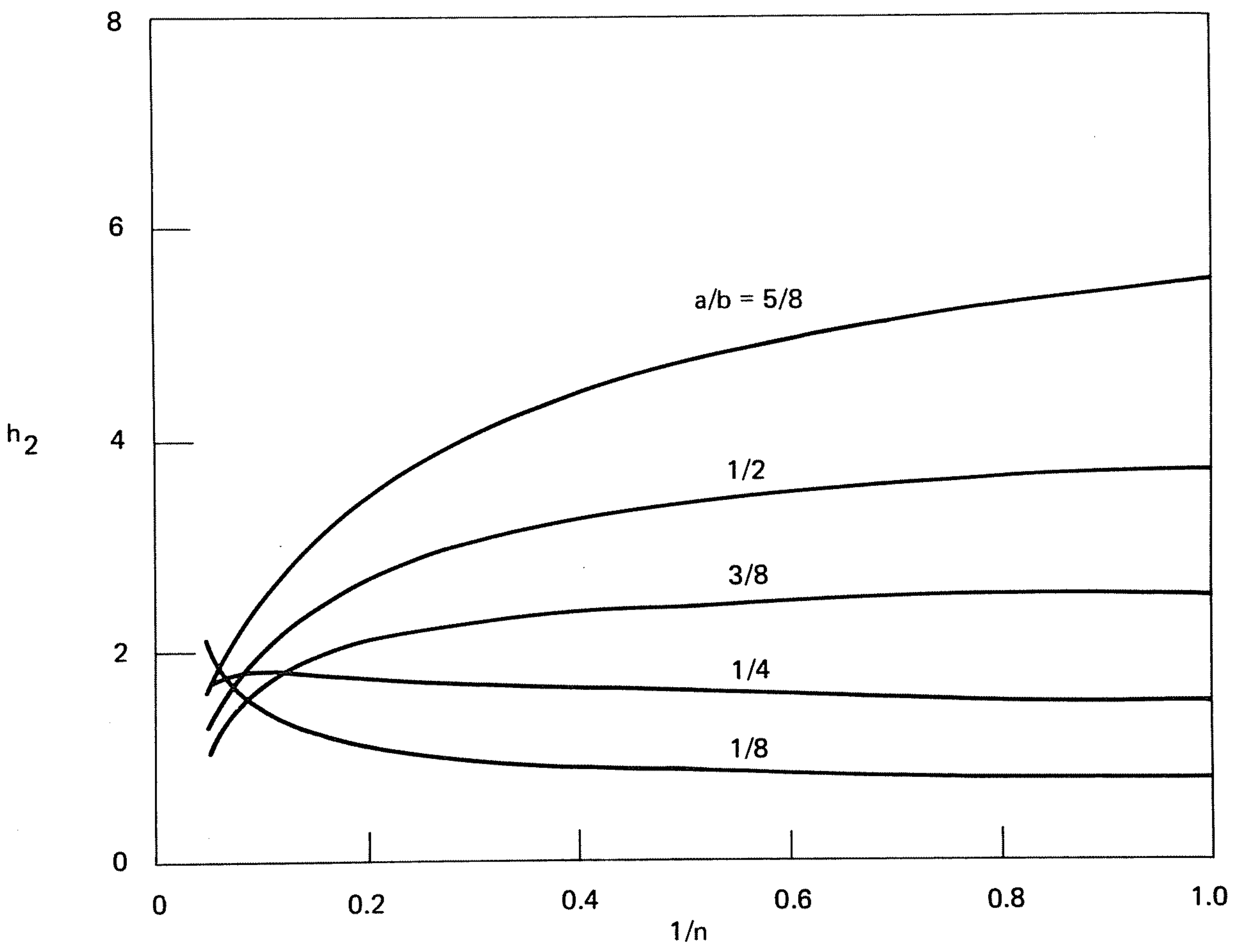

Figure C-28. h_2 versus 1/n for a double-edge cracked panel in tension – plane strain.

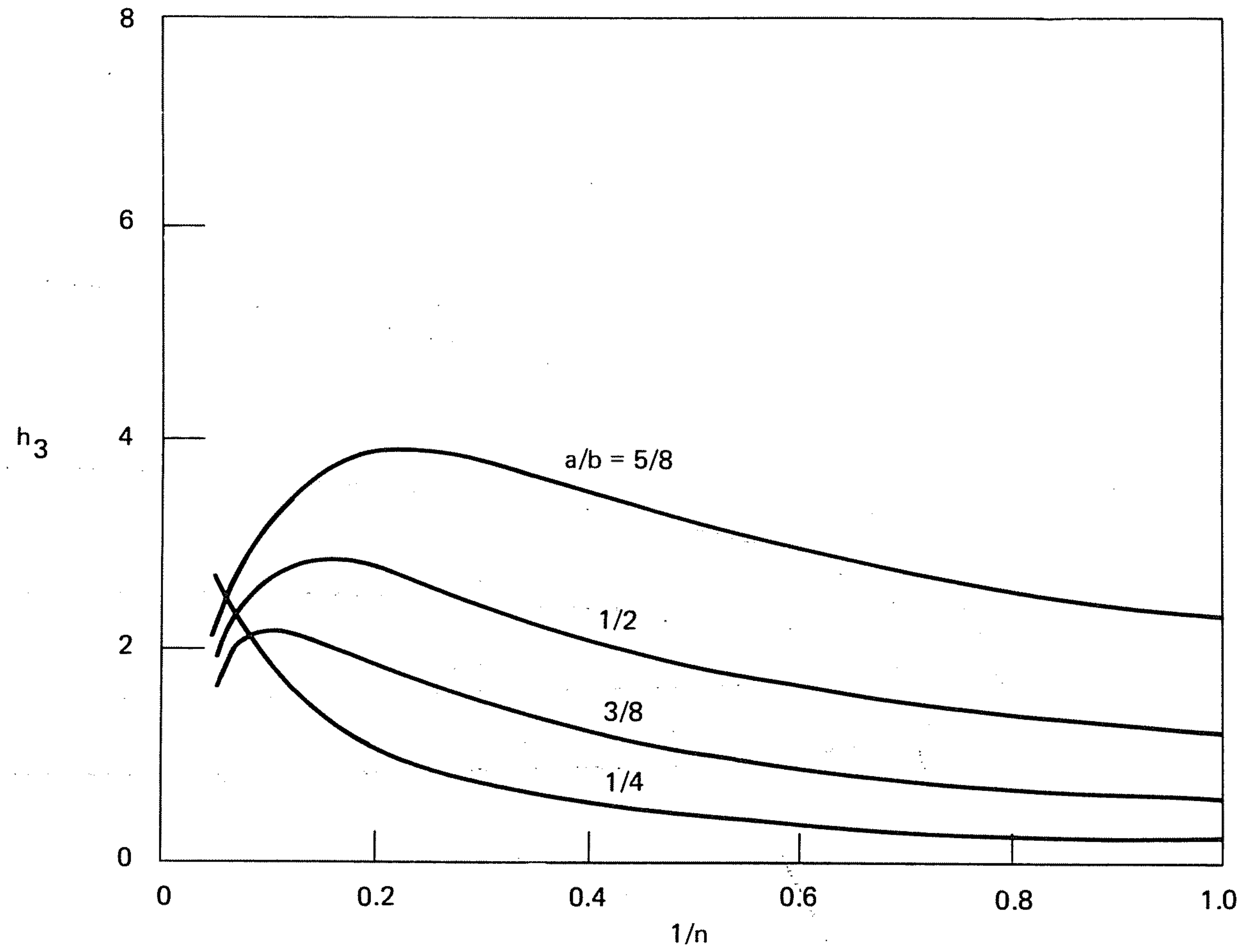

Figure C-29. h_3 versus 1/n for a double-edge cracked panel in tension - plane strain.

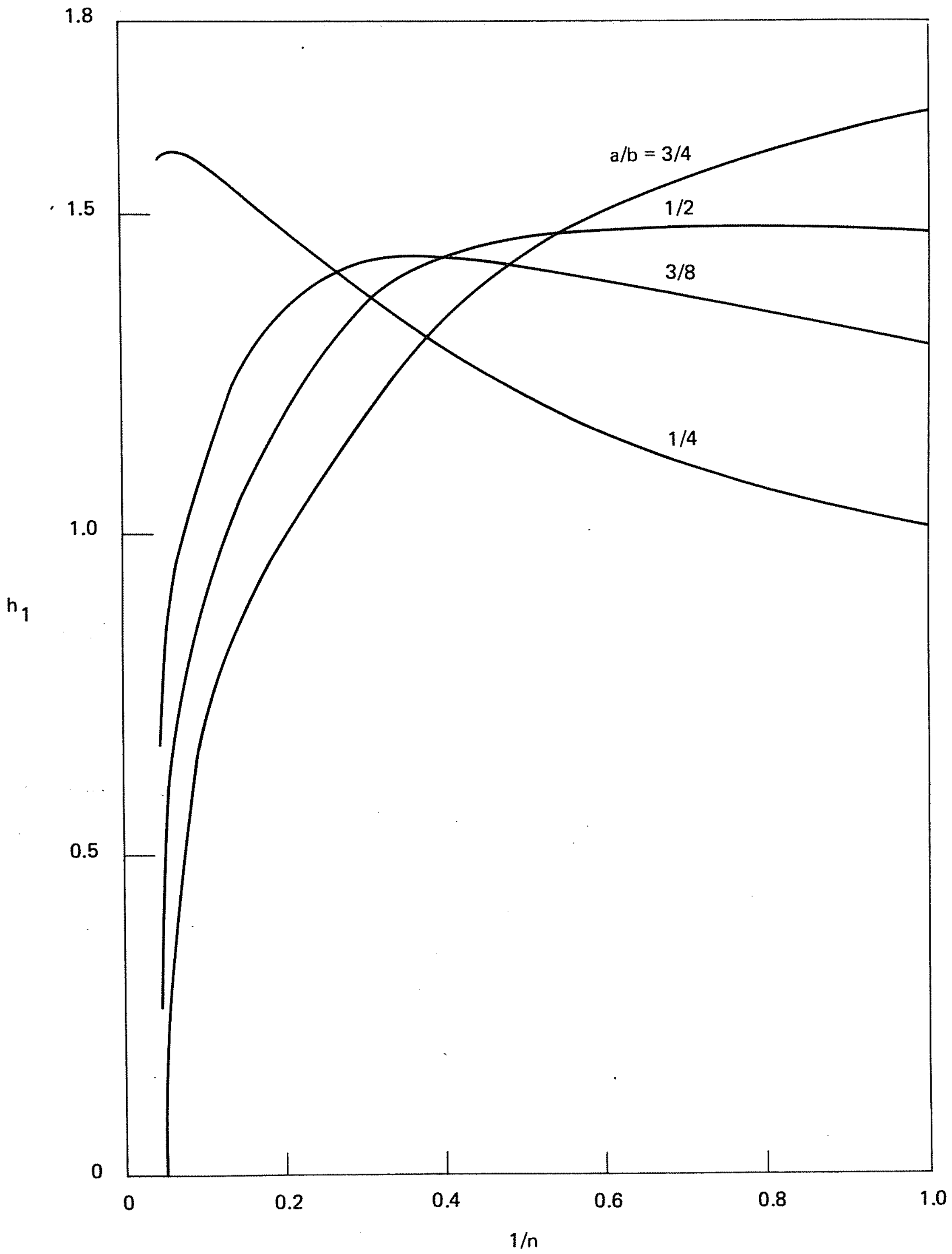

Figure C-30. h_1 versus 1/n for a double-edge cracked panel in tension - plane stress.

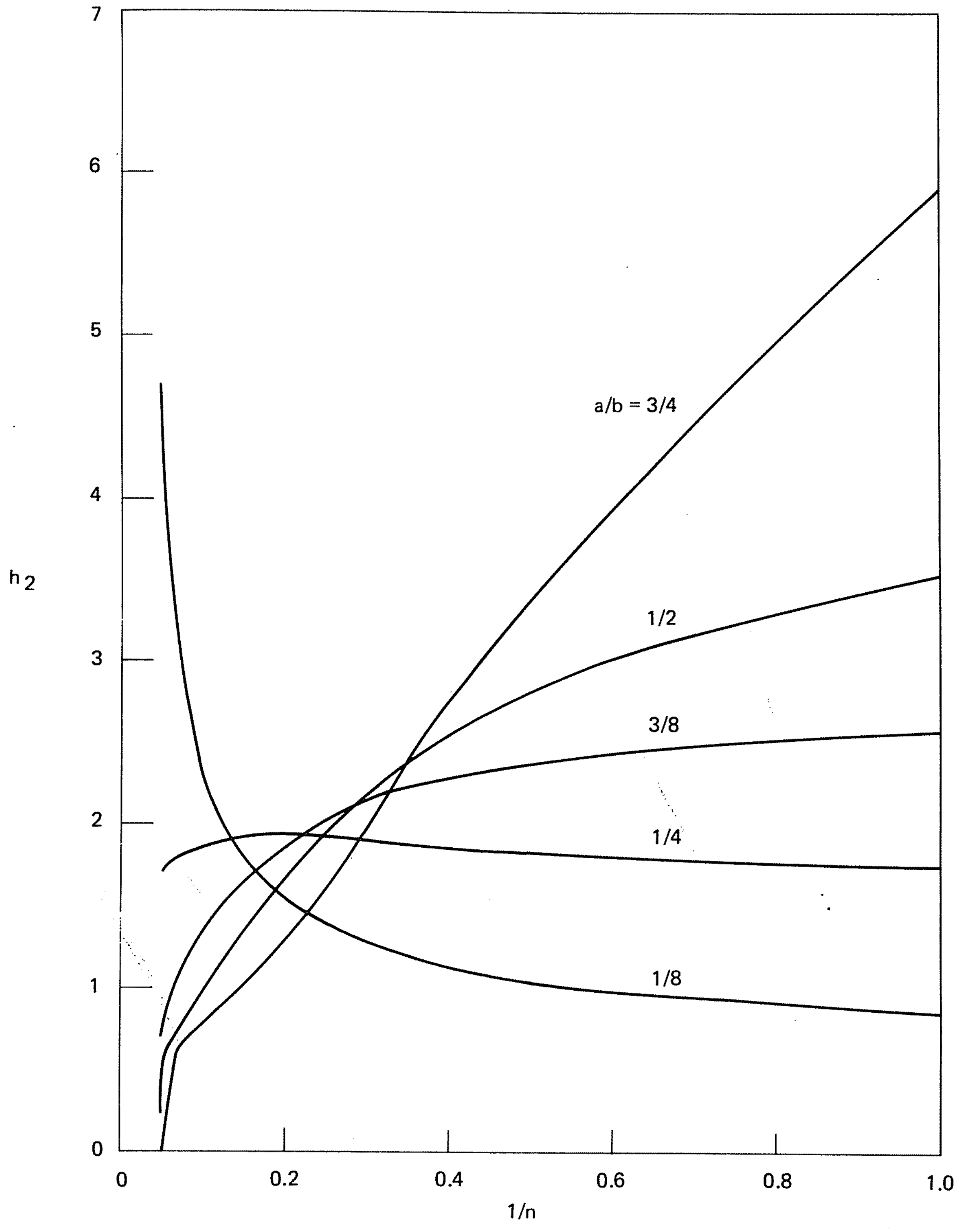

Figure C-31. h_2 versus 1/n for a double-edge cracked panel in tension – plane stress.

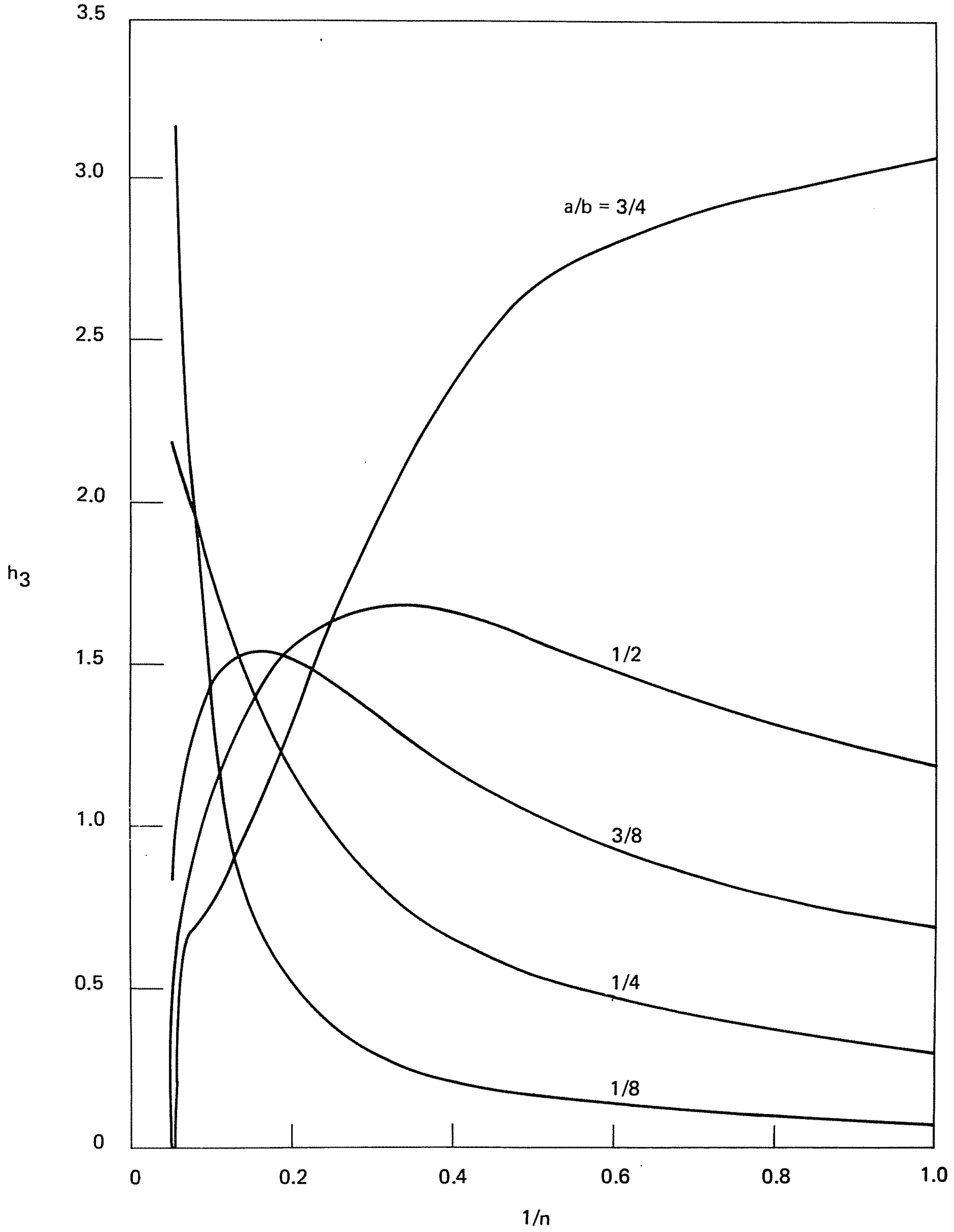

Figure C-32. h_3 versus 1/n for a double-edge cracked panel in tension – plane stress.

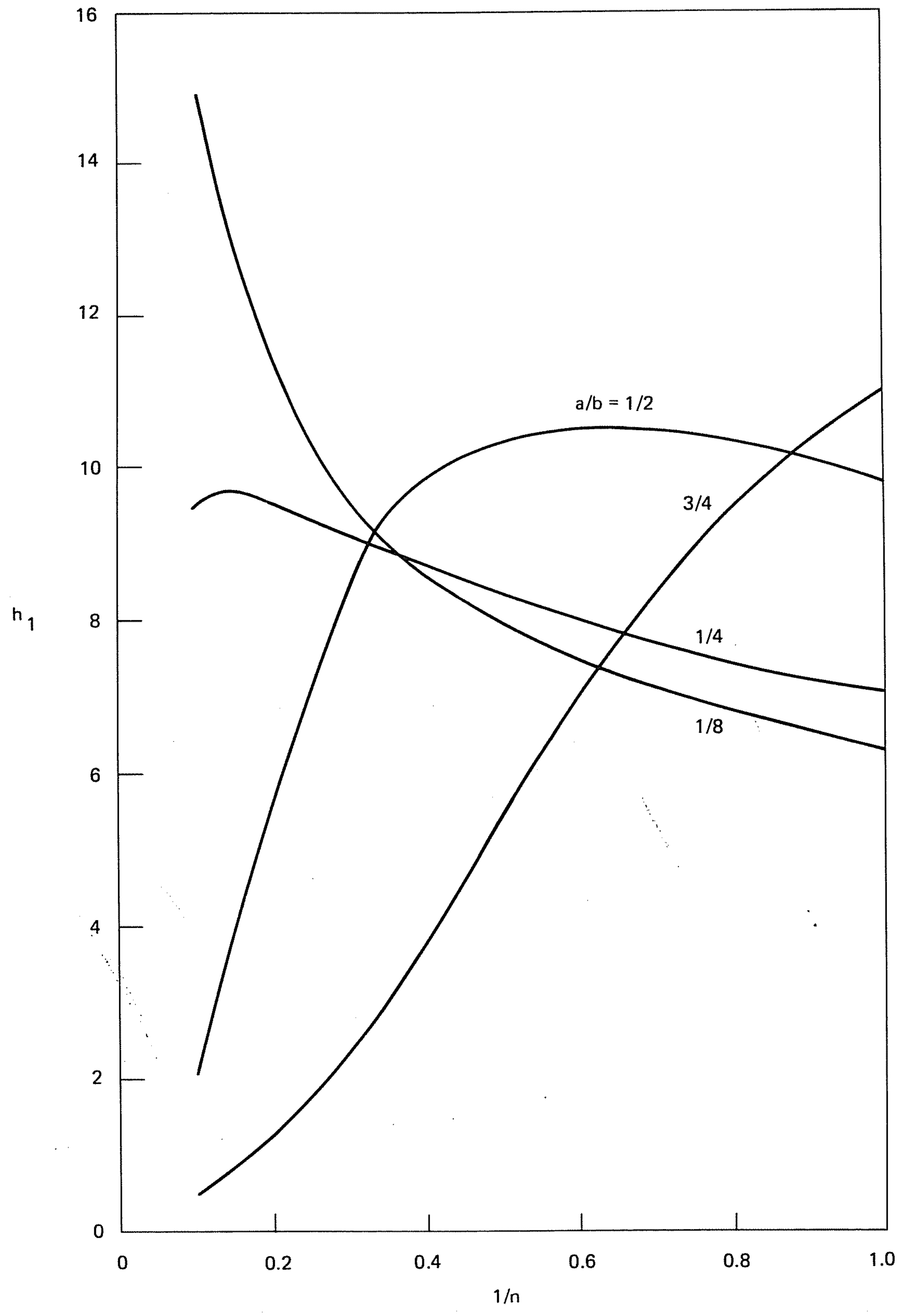

Figure C-33. h_1 versus 1/n for an axially cracked cylinder with $R_i/b = 5$.

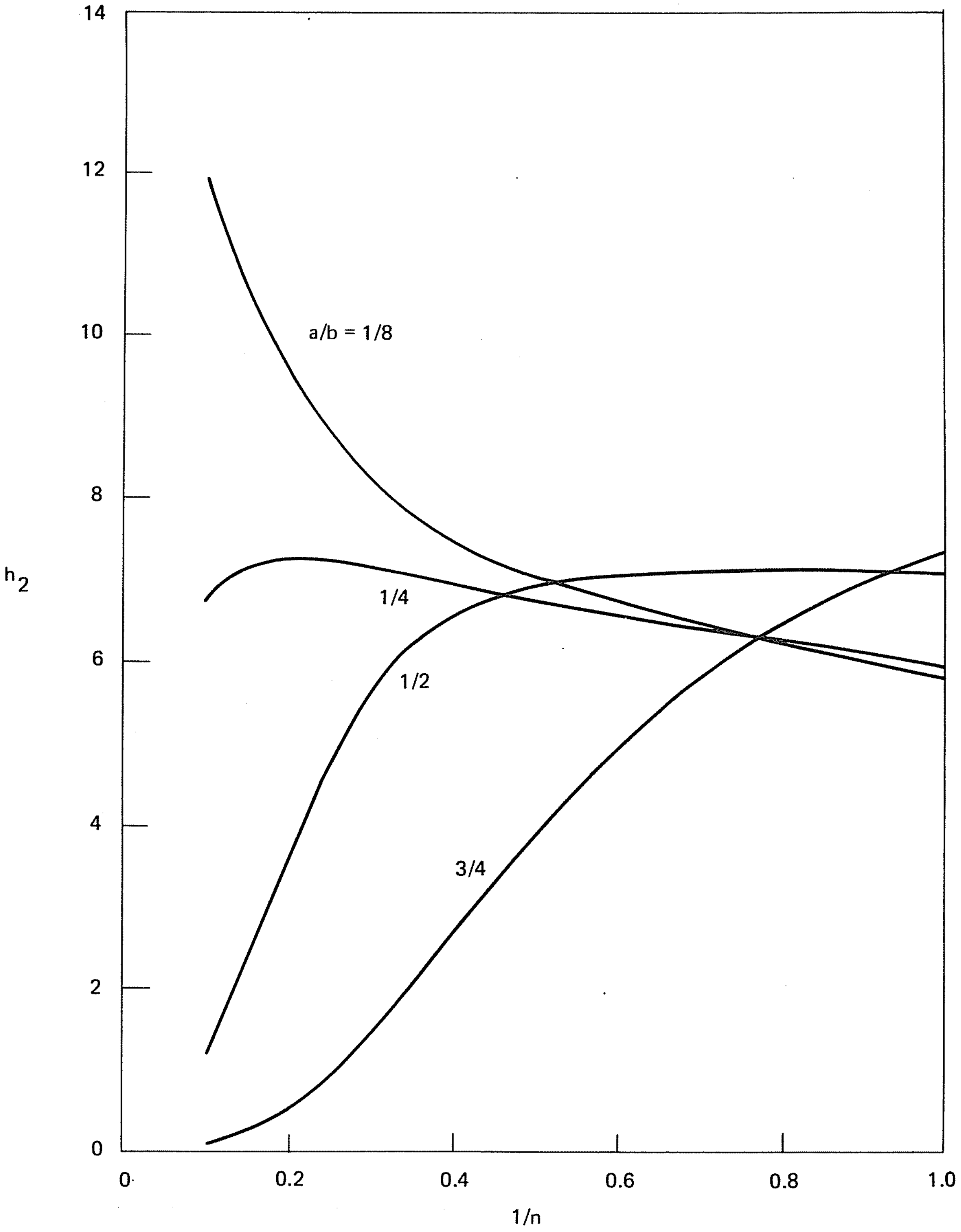

Figure C-34. h_2 versus 1/n for an axially cracked cylinder with $R_i/b = 5$.

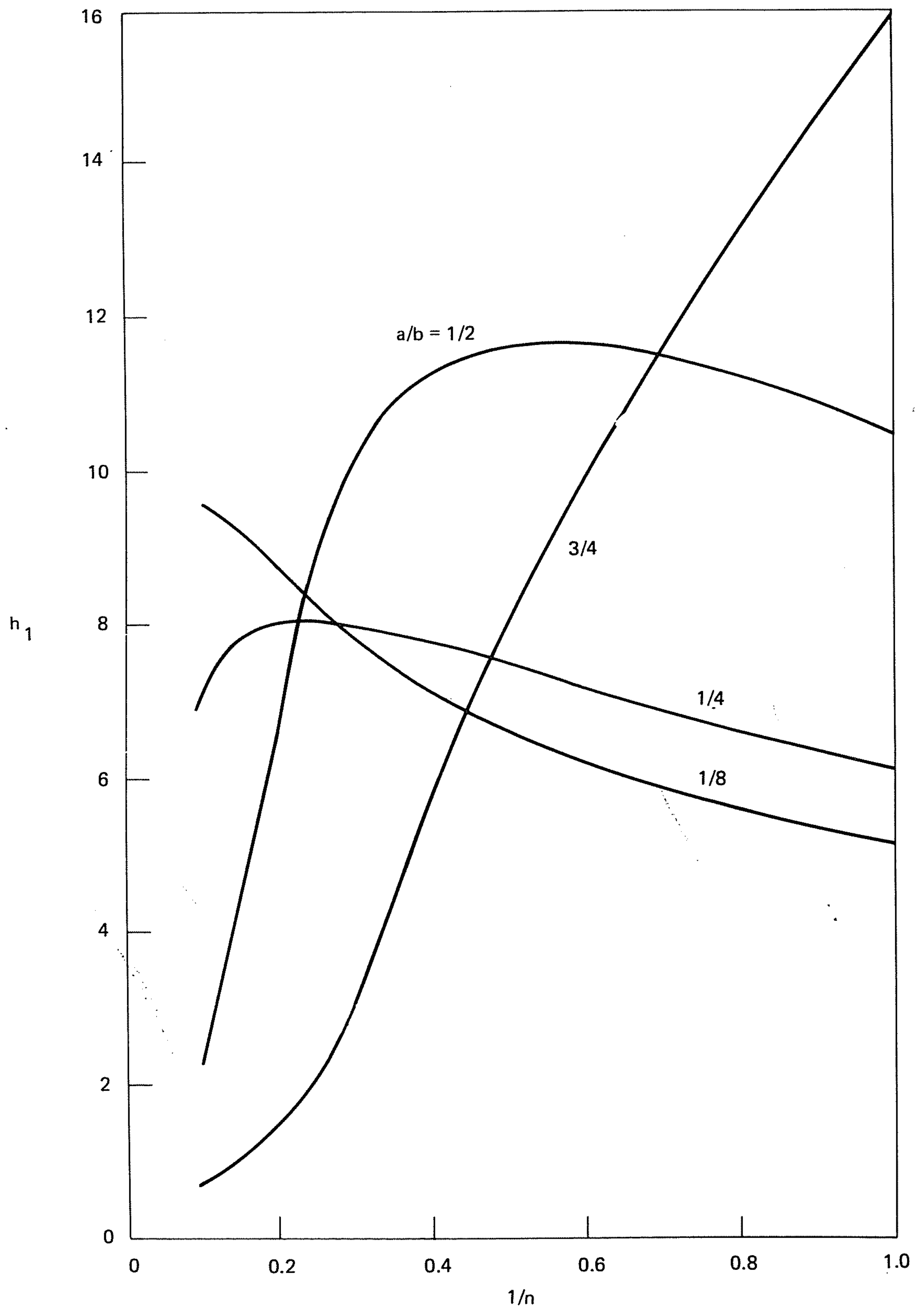

Figure C-35. h_1 versus 1/n for an axially cracked cylinder with $R_i/b = 10$.

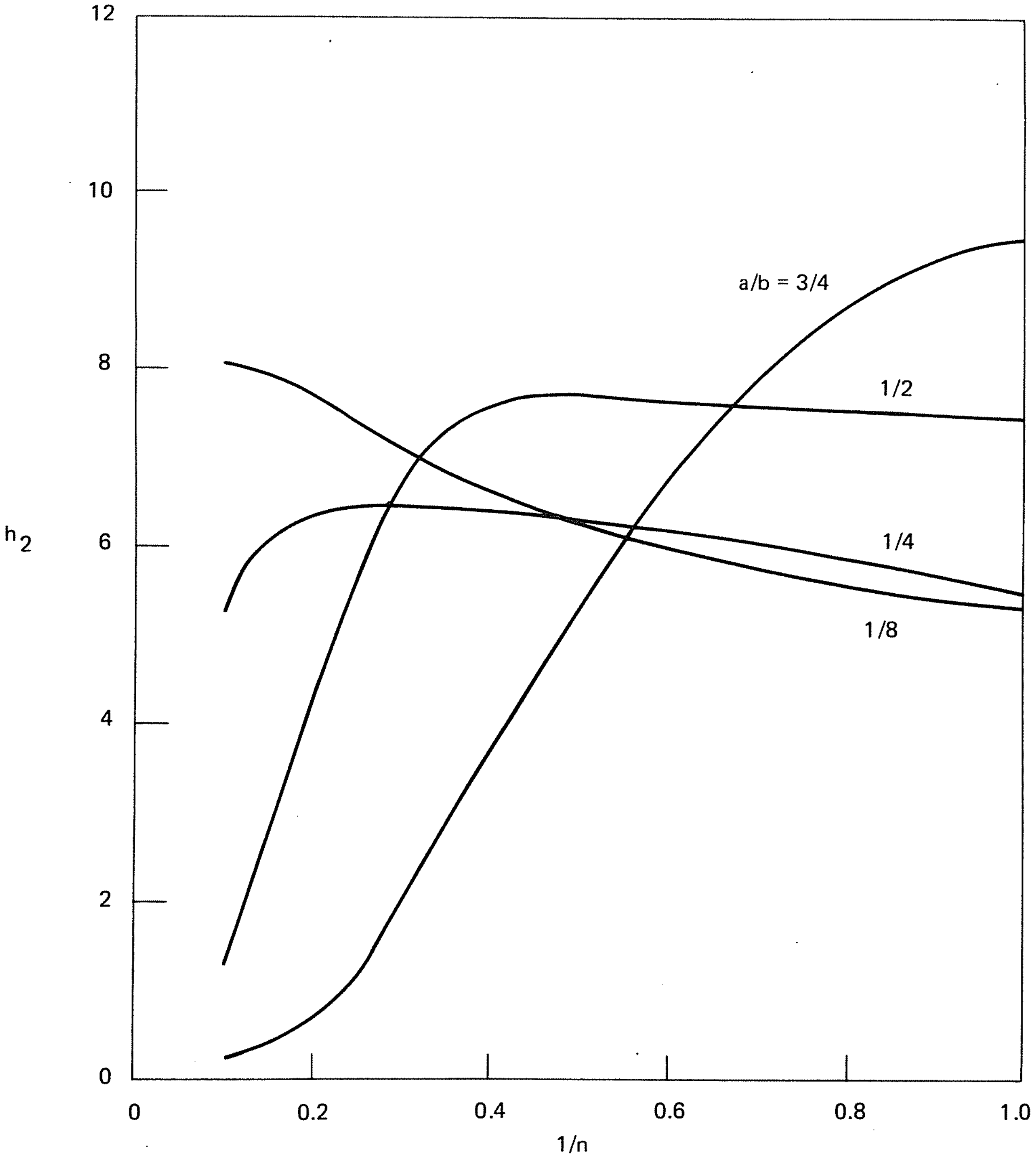

Figure C-36. h_2 versus 1/n for an axially cracked cylinder with $R_i/b = 10$.

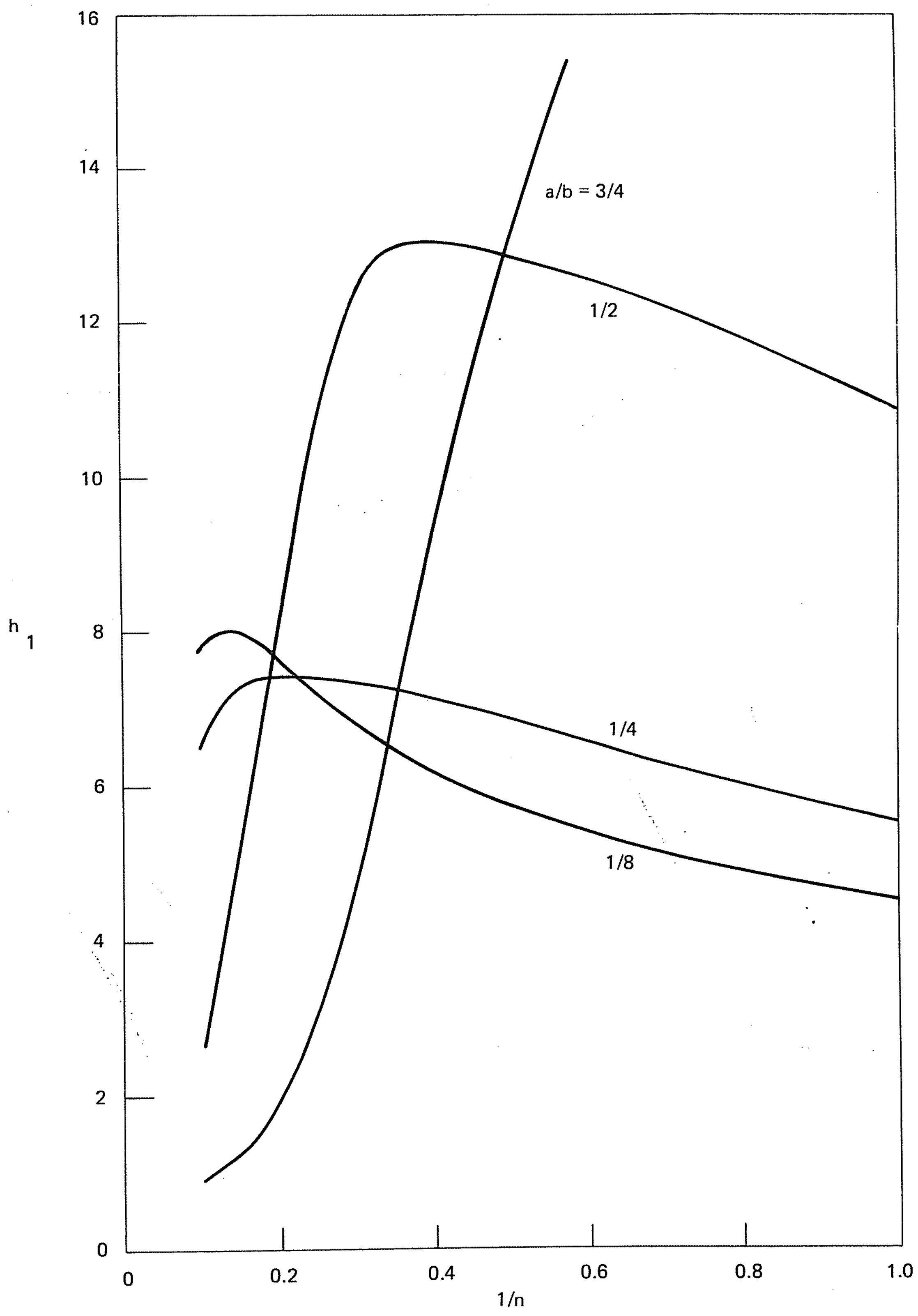

Figure C-37. h_1 versus 1/n for an axially cracked cylinder with R_i/b = 20.

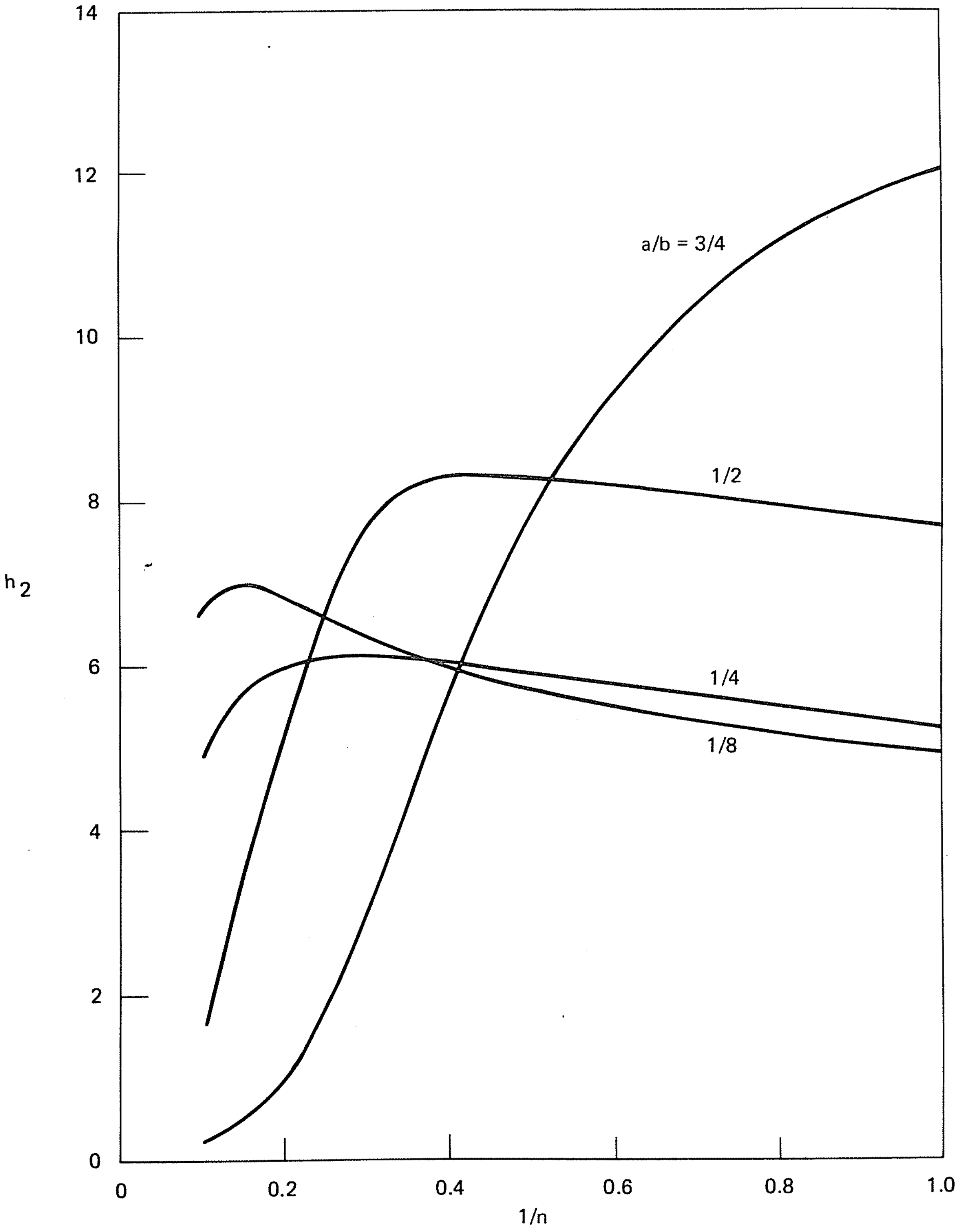

Figure C-38. h_2 versus 1/n for an axially cracked cylinder with R_i/b = 20.

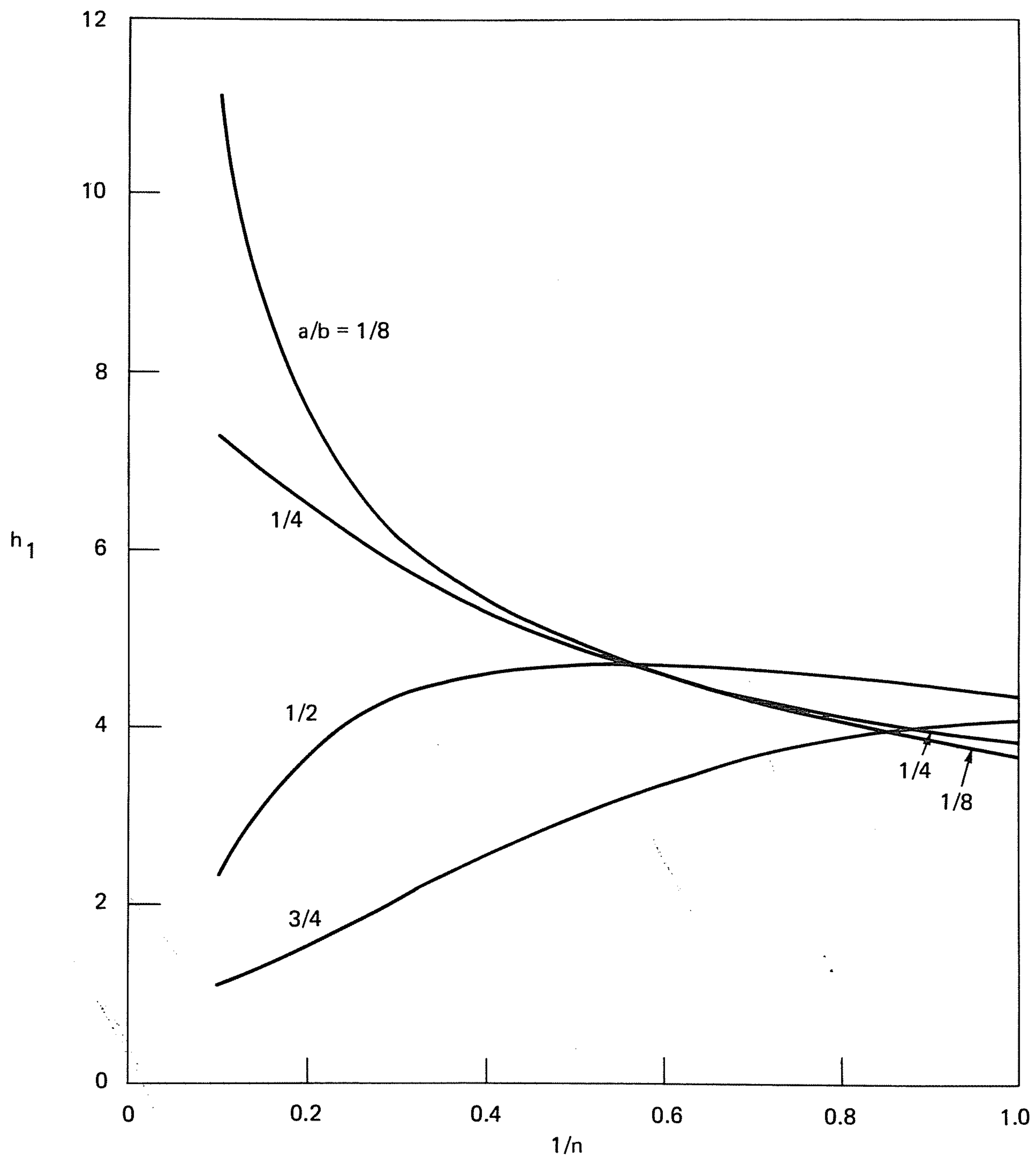

Figure C-39. h_1 versus 1/n for a circumferentially cracked cylinder with R_i/b = 5.

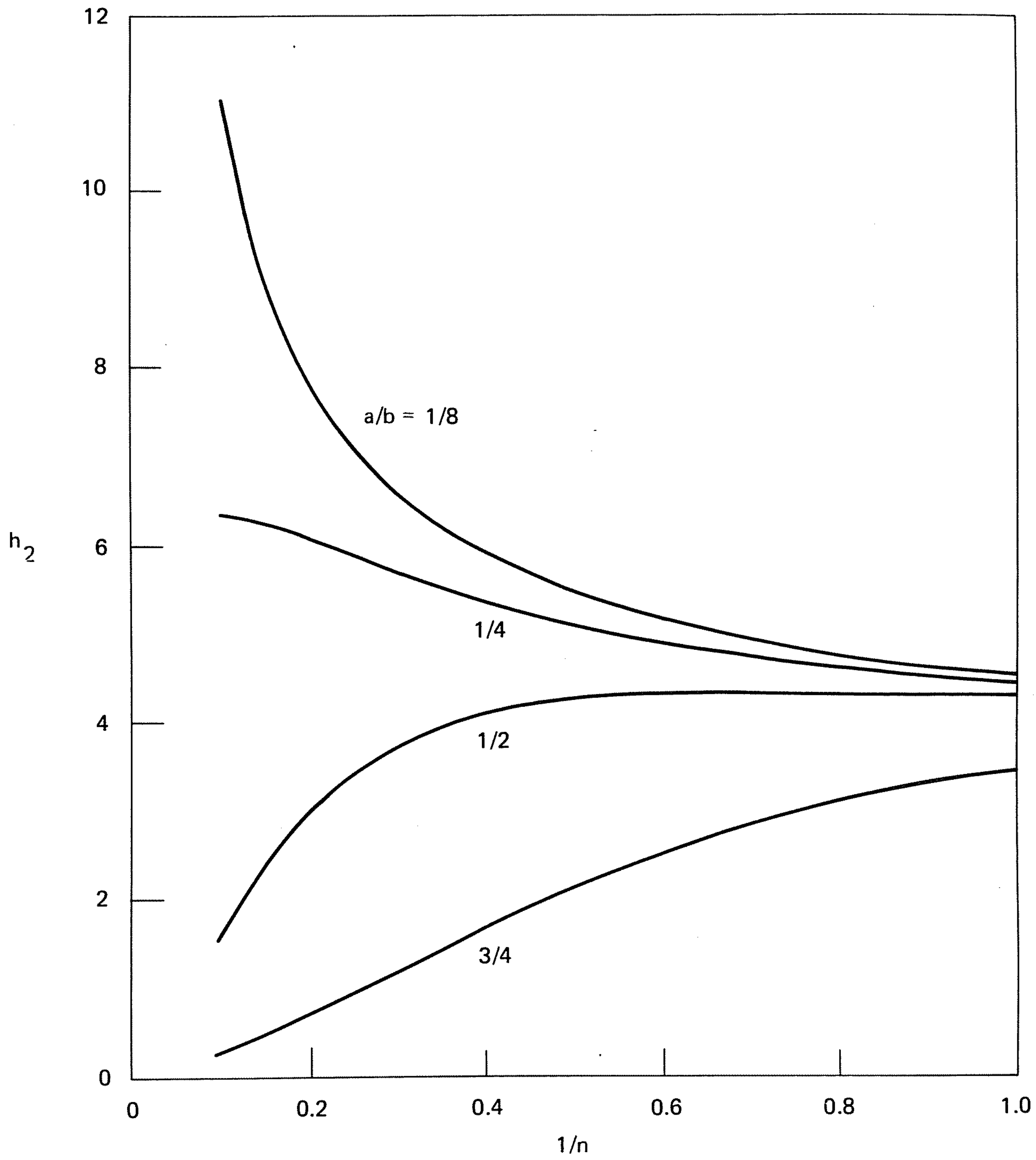

Figure C-40. h_2 versus 1/n for a circumferentially cracked cylinder with R_i/b = 5.

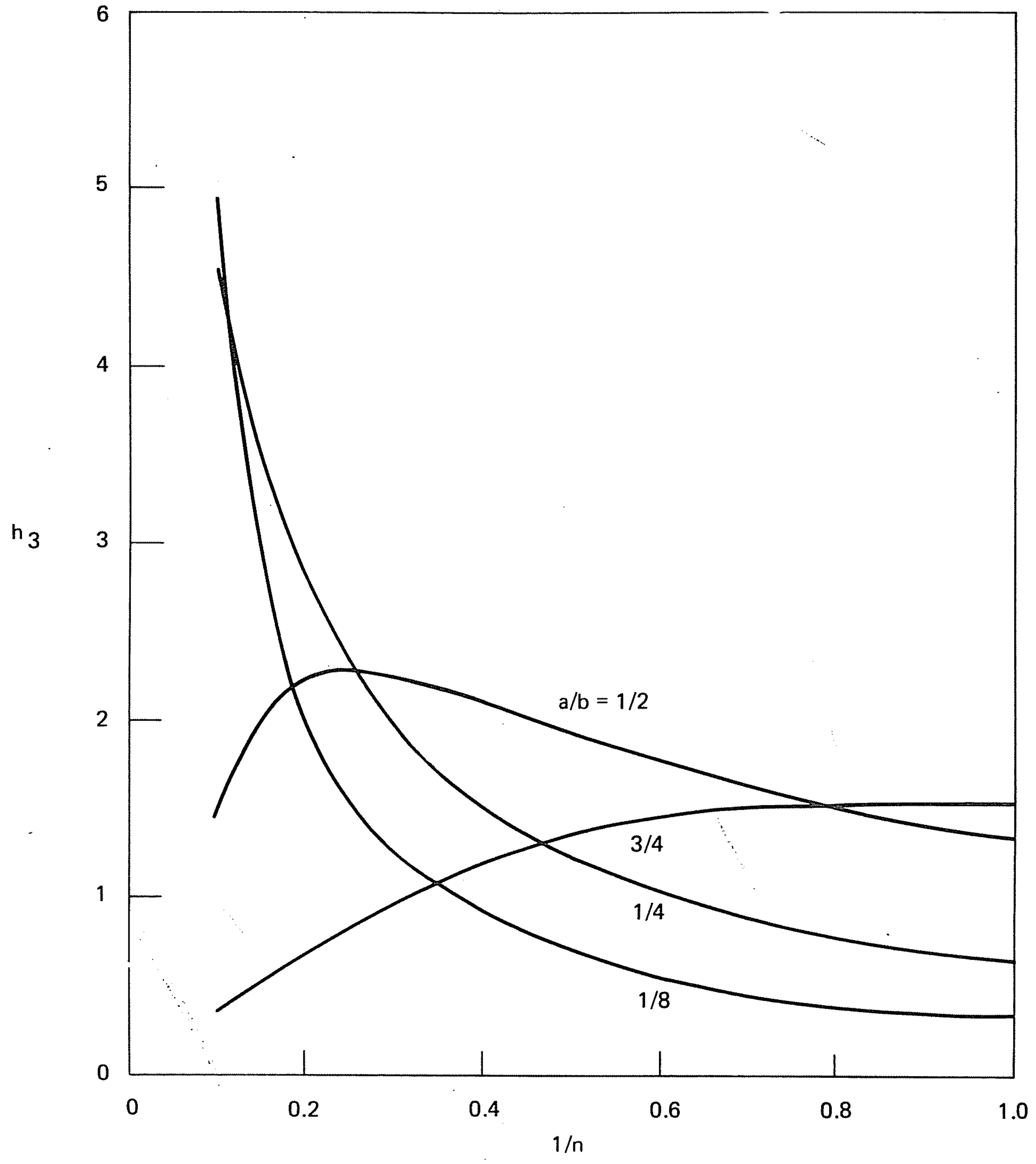

Figure C-41. h_3 versus 1/n for a circumferentially cracked cylinder with R_i/b = 5.

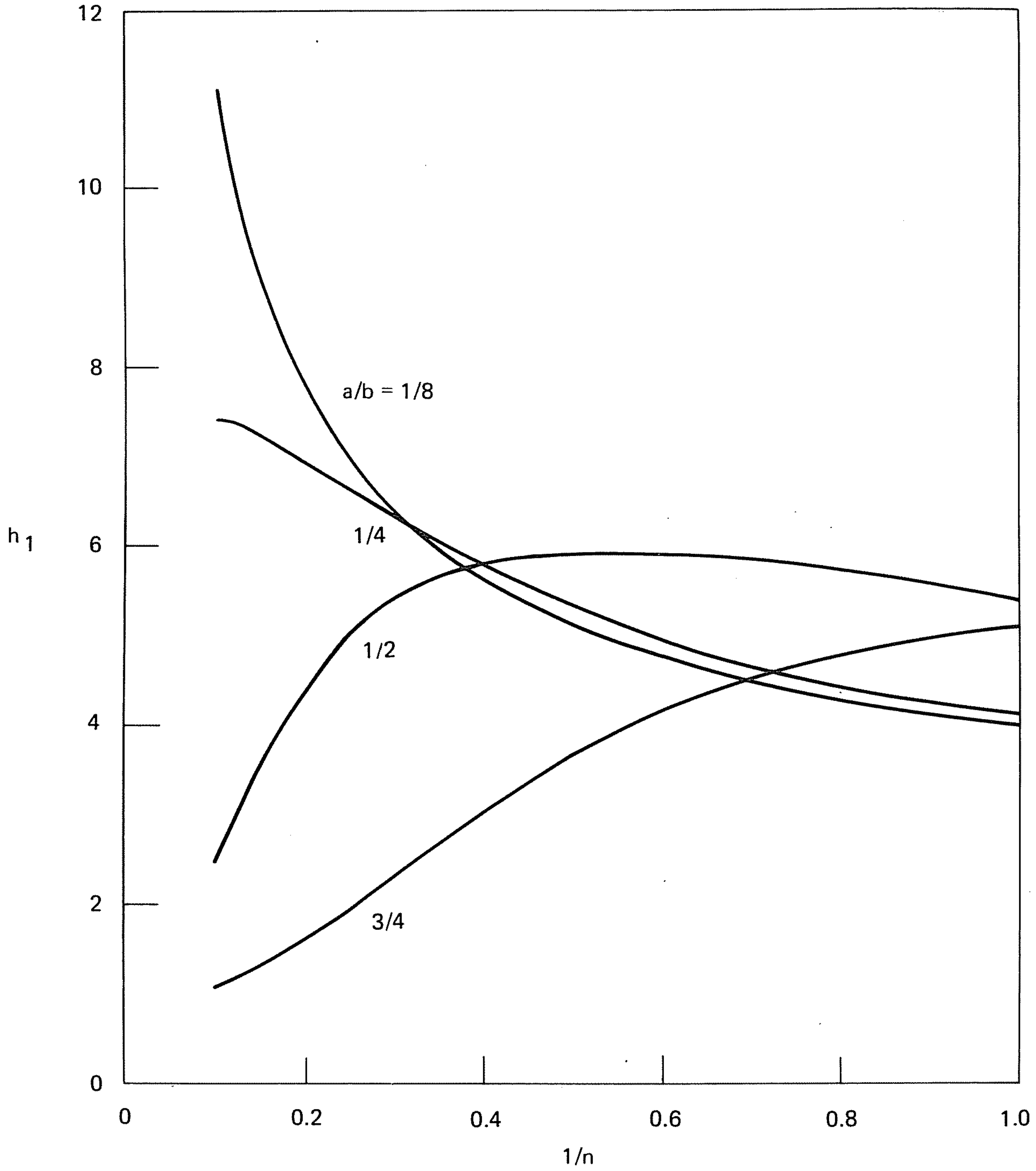

Figure C-42. h_1 versus 1/n for a circumferentially cracked cylinder with R_i/b = 10.

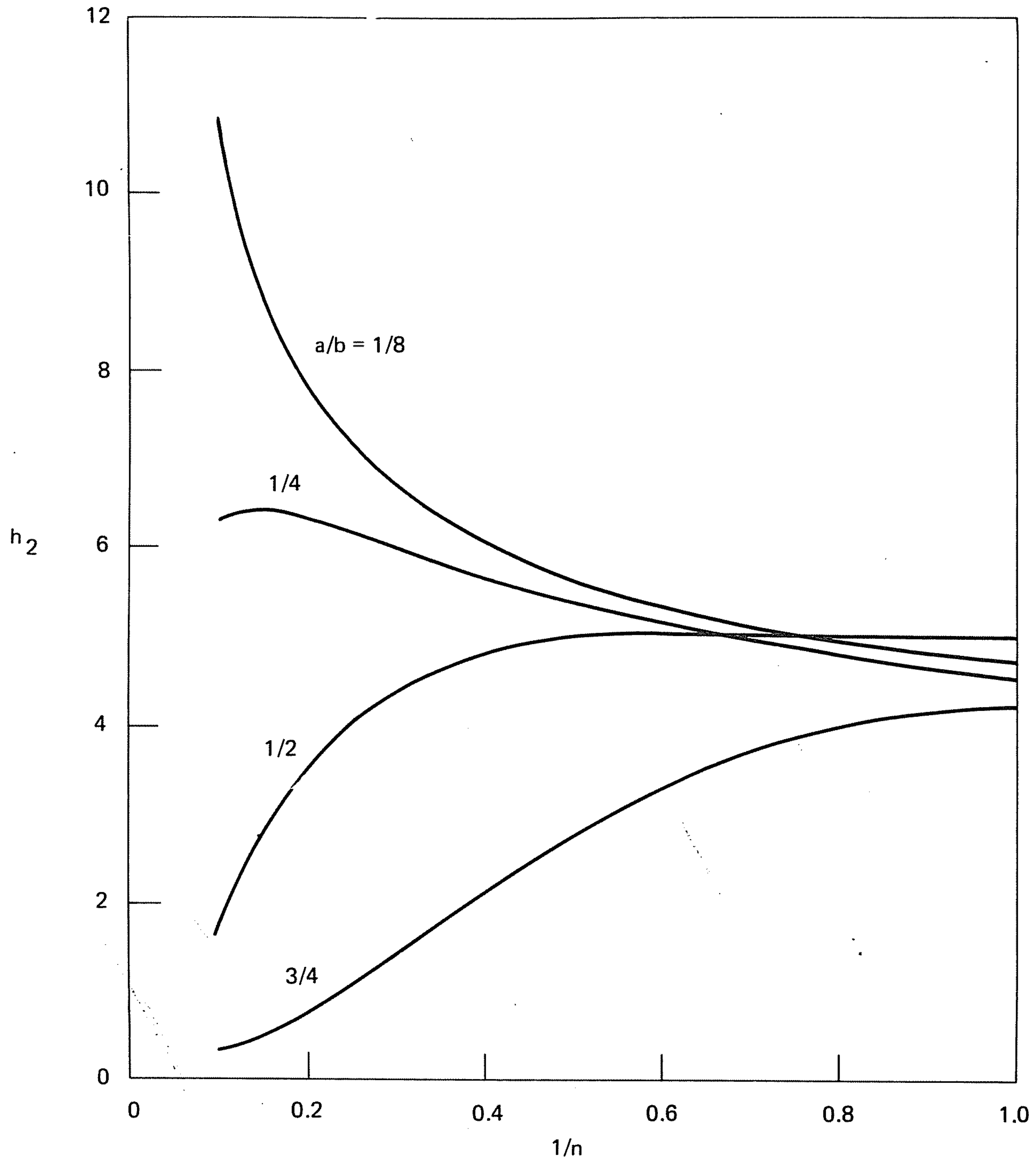

Figure C-43. h_2 versus 1/n for a circumferentially cracked cylinder with R_i/b = 10.

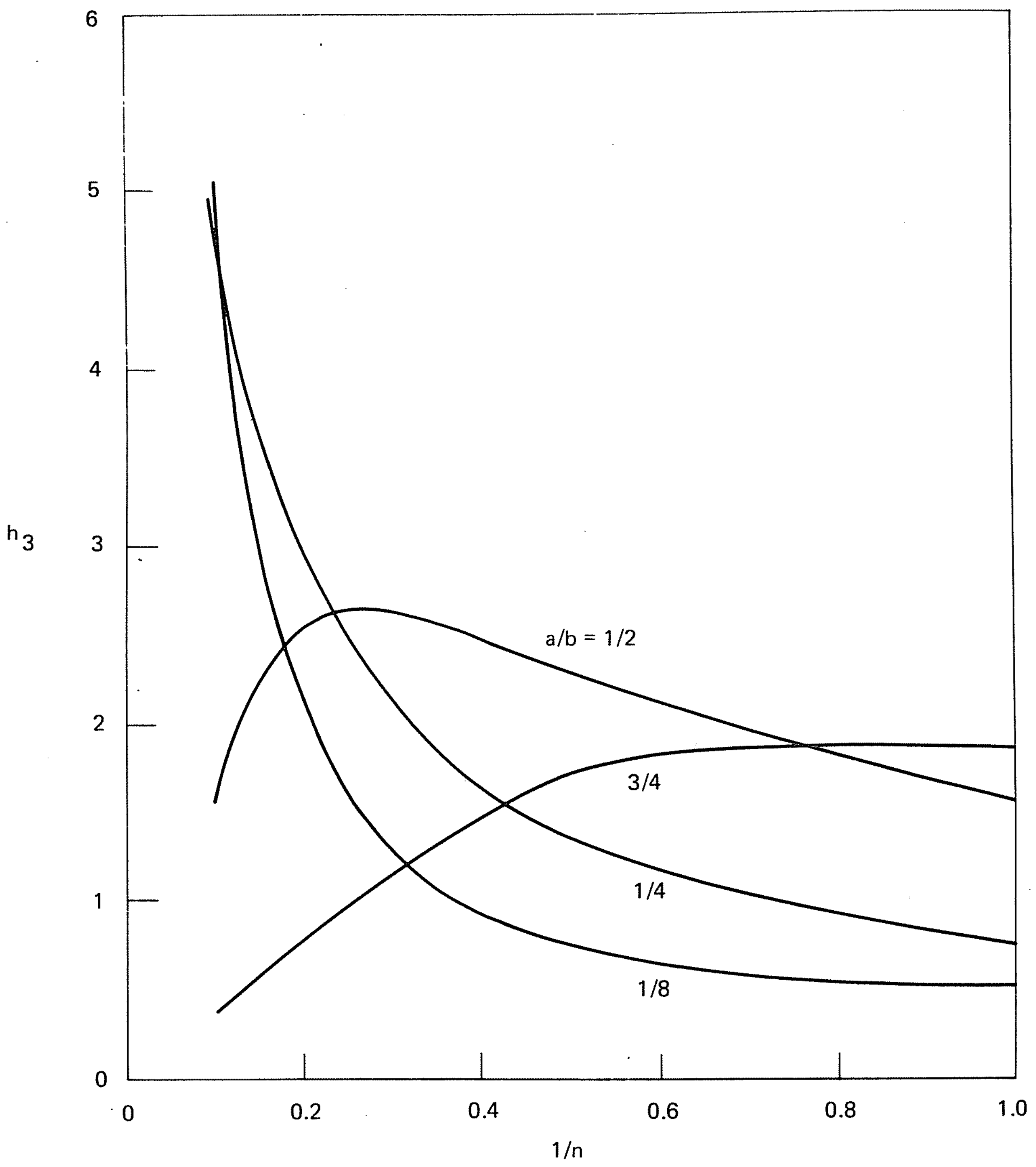

Figure C-44. h_3 versus 1/n for a circumferentially cracked cylinder with R_i/b = 10.

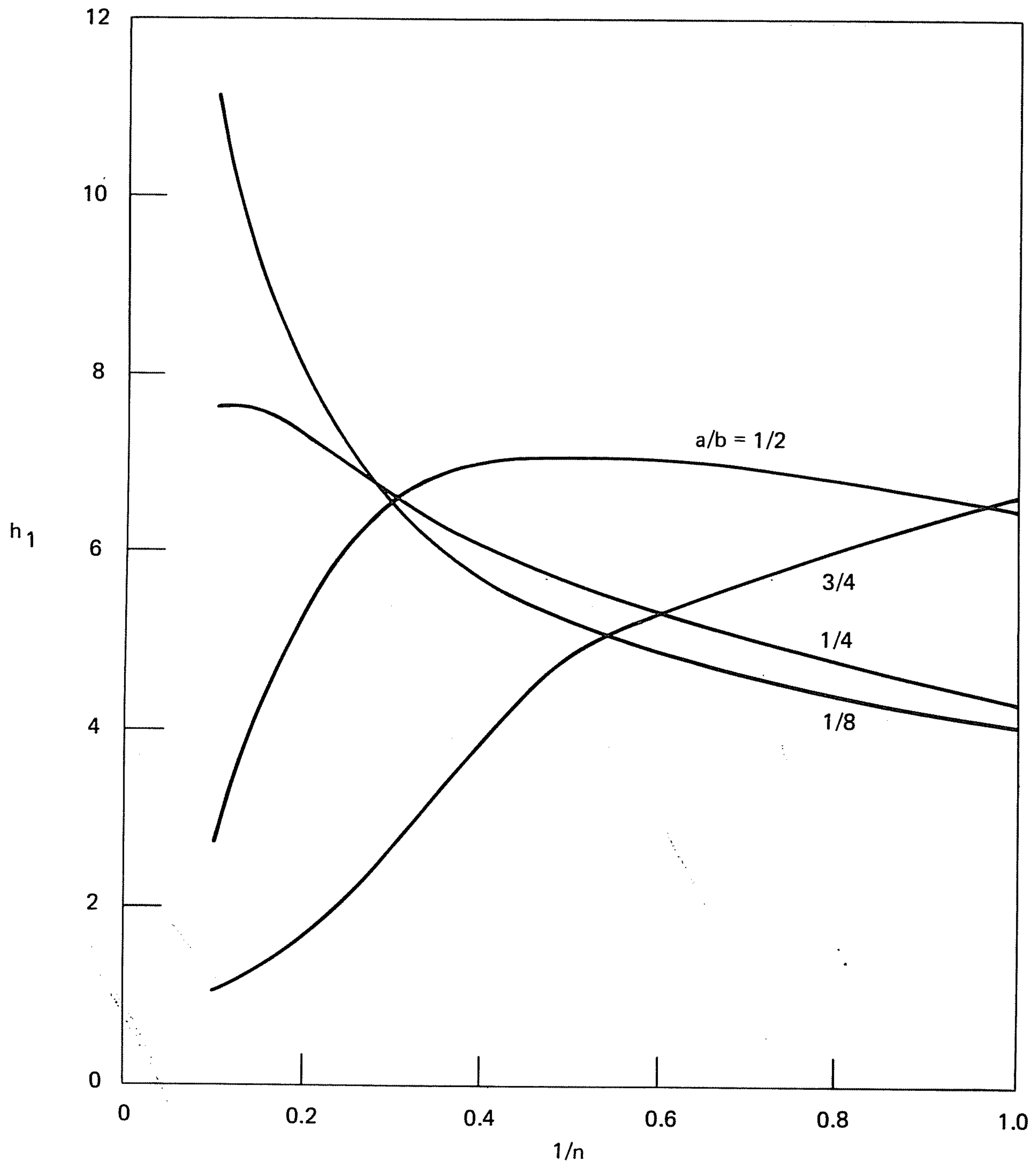

Figure C-45. h_1 versus 1/n for a circumferentially cracked cylinder with $R_i/b = 20$.

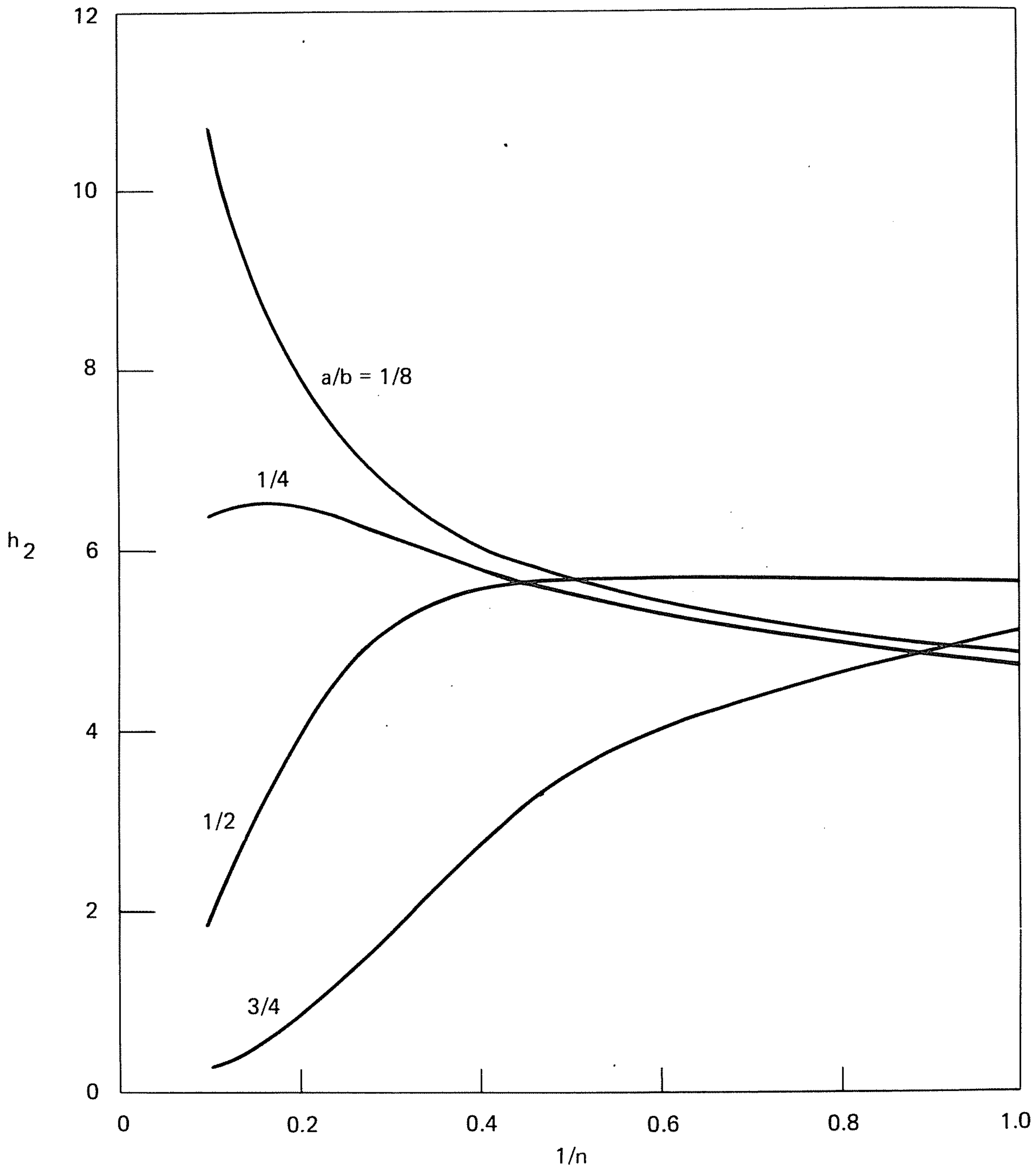

Figure C-46. h_2 versus 1/n for a circumferentially cracked cylinder with $R_i/b = 20$.

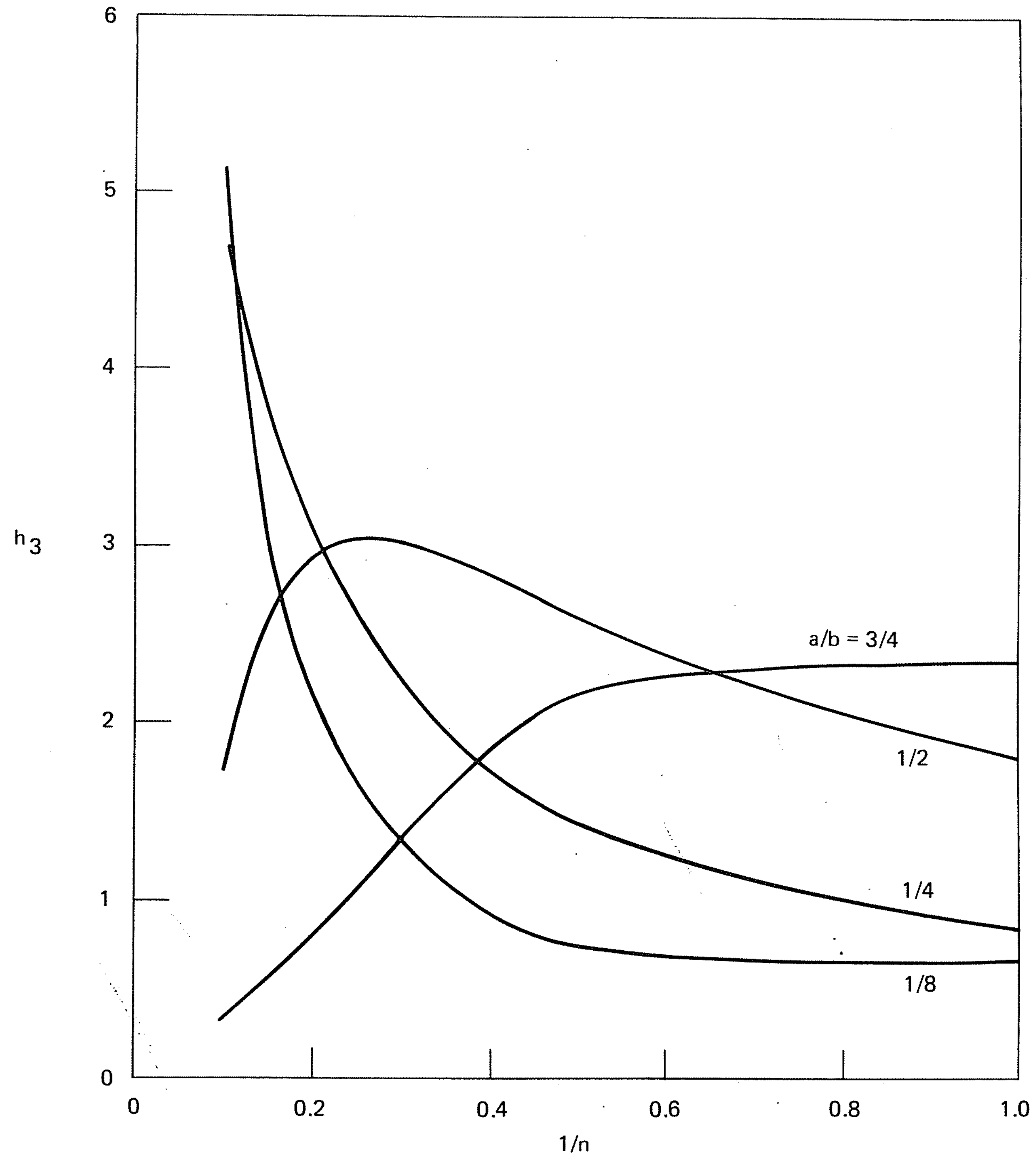

Figure C-47. h_3 versus 1/n for a circumferentially cracked cylinder with R_i/b = 20.